

Andrzej M. Pawlak

# SENSORS AND ACTUATORS IN MECHATRONICS

## Design and Applications



# **SENSORS AND ACTUATORS IN MECHATRONICS**

---

Design and Applications



# SENSORS AND ACTUATORS IN MECHATRONICS

---

Design and Applications

Andrzej M. Pawlak



Taylor & Francis

Taylor & Francis Group

Boca Raton London New York

---

CRC is an imprint of the Taylor & Francis Group,  
an Informa business

CRC Press  
Taylor & Francis Group  
6000 Broken Sound Parkway NW, Suite 300  
Boca Raton, FL 33487-2742

© 2007 by Taylor & Francis Group, LLC  
CRC Press is an imprint of Taylor & Francis Group, an Informa business

No claim to original U.S. Government works  
Printed in the United States of America on acid-free paper  
10 9 8 7 6 5 4 3 2 1

International Standard Book Number-10: 0-8493-9013-3 (Hardcover)  
International Standard Book Number-13: 978-0-8493-9013-5 (Hardcover)

This book contains information obtained from authentic and highly regarded sources. Reprinted material is quoted with permission, and sources are indicated. A wide variety of references are listed. Reasonable efforts have been made to publish reliable data and information, but the author and the publisher cannot assume responsibility for the validity of all materials or for the consequences of their use.

No part of this book may be reprinted, reproduced, transmitted, or utilized in any form by any electronic, mechanical, or other means, now known or hereafter invented, including photocopying, microfilming, and recording, or in any information storage or retrieval system, without written permission from the publishers.

For permission to photocopy or use material electronically from this work, please access [www.copyright.com](http://www.copyright.com) (<http://www.copyright.com/>) or contact the Copyright Clearance Center, Inc. (CCC) 222 Rosewood Drive, Danvers, MA 01923, 978-750-8400. CCC is a not-for-profit organization that provides licenses and registration for a variety of users. For organizations that have been granted a photocopy license by the CCC, a separate system of payment has been arranged.

**Trademark Notice:** Product or corporate names may be trademarks or registered trademarks, and are used only for identification and explanation without intent to infringe.

---

**Library of Congress Cataloging-in-Publication Data**

---

Pawlak, Andrzej M.  
Sensors and actuators in mechatronics : design and applications / Andrzej M. Pawlak.  
p. cm.  
Includes bibliographical references and index.  
ISBN-13: 978-0-8493-9013-5 (alk. paper)  
ISBN-10: 0-8493-9013-3 (alk. paper)  
1. Mechatronics. 2. Optical detectors. I. Title.

TJ163.12.P39 2006  
621--dc22

2006004129

---

Visit the Taylor & Francis Web site at  
<http://www.taylorandfrancis.com>

and the CRC Press Web site at  
<http://www.crcpress.com>

*To my wife Ewa*



---

## *The Author*

---



**Andrzej M. Pawlak, Ph.D.**, (Fellow IEEE), was born and educated in Poland. He obtained his M.S. in 1971 from the Technical University of Poznan. He did postgraduate study at the Warsaw University of Technology and obtained his Ph.D. in electrical engineering in 1981 from the Silesian University of Technology, Gliwice. His years of engineering and technology experience stem from his work at the Hitachi Poland and Japan manufacturing plants and his 20 years of research on electromechanical and electromagnetic devices at General Motors and subsequently Delphi, all of which contributed to his solid background of industrial expertise. His works on stepper motors, magnetic sensors, rotary actuators, and fast-acting solenoids are frequently cited worldwide.

Most of Dr. Pawlak's 70 scientific publications, patents, and patent applications are related to sensors and actuators. A number of them have found industrial applications in mechatronic systems with significant scientific, engineering, and economical impact on the automotive industry and beyond, with tremendous overall business value to Delphi and General Motors. Dr. Pawlak was honored with one of the highest number of individual awards in General Motors and Delphi history, including four prestigious "Boss" Kettering Awards for his accomplishments. He was the first individual from the automotive industry to receive the Respectable Achievement Award of the Industrial Research Institute.

Dr. Pawlak has contributed to the initial scientific analysis and design of several unique electromagnetic and electromechanical devices. An actuator he invented for the Magnasteer® system led to the development and the first industrial application of neodymium-boron-iron ring magnets with radial orientation, which are now commonly found in a variety of industrial applications and consumer products. Dr. Pawlak is a frequent invited keynote speaker and panelist at professional conferences and congresses worldwide. This book is the culmination of his research findings and award-winning solutions for industrial applications over the last 20 years.



---

## **Preface**

---

The importance of mechatronic devices — both the application of electromagnetic and electromechanic devices in industry and their impact on emerging technologies — has increased dramatically in recent years. Significant advances in control technologies based on microprocessors and the substantial cost reduction of high-performance hard and soft magnetic materials have changed the face of the world of technology.

In particular, the automotive industry has shifted from mechanical and hydraulic systems and components to mechatronic systems based on electromagnetic and electromechanical devices. Servo motor design and optimization techniques used in industrial applications are well established and described elsewhere in the literature. This book discusses several perhaps less-elaborate families of modern electromechanical actuators and magnetic sensors in industrial applications: magnetic sensors, linear and latching solenoid actuators, stepper motors, rotary actuators, and other special magnetic devices. This book is intended to fill the gap in devising and designing optimization of mechatronic devices in modern industry applications. Each chapter examines a variety of magnetic sensors and electromechanical actuator analyses and designs, supported by numerical problems for mechatronic system applications in the automotive industry and beyond. The primary focus is on automotive applications, with more general discussions of studies of electromagnetic and electromechanical designs, analyses, optimization, and tests, including material and application aspects.

This book will be valuable to all those whose interests and job responsibilities are related to mechatronic systems and, in particular, magnetic sensors and electromechanical actuators. The intention of this book is to bring readers closer to the state of the art, to help them understand device functions and features, and to provide design guidance to meet specific, and sometimes extreme, industrial requirements. The focus on electromagnetic and electromechanical devices is natural because they are based on my inventions. I share my unique experiences as a design and manufacturing engineer, a researcher, and an inventor to help explain my way of thinking, which led to the development and successful industrial implementation of hundreds of millions of sensors and actuators in modern industrial mechatronic systems. I hope that this book will serve as a textbook for students and as a design handbook for engineers and will stimulate innovations in the field. I also want to share business and social aspects of the technology development process to help explain what it takes to successfully develop world-class technology.

Most of the research content of this book was developed at General Motors and Delphi Corporation in collaboration with divisional and outside partner teams. Much of the content of this book was published previously in the form of professional papers and conference presentations and is now used with the kind permission of Delphi Corporation. I would like to express my gratitude to those who contributed to those papers, including Dr. Alex Alexandridis, David Graber, Dr. Bruno Lequesne, and Takeshi Shirai, as well as to all the researchers, technicians, draftsmen, and other individuals from product lines for their support, constructive comments, and excellent work. I also thank my daughter Patrycja for her efforts to make this book reader-friendly and my wife Ewa for the impressive cover concept. Finally, this book would not have been possible without fruitful discussions with Dr. Thomas Nehl of Delphi and the continuous encouragement of Professor Tadeusz Glinka of the Silesian University of Technology.

**Andrzej M. Pawlak**



---

## ***Symbols and Abbreviations***

---

### **Symbols**

$a$	Acceleration.
$a_o$	The polynomial component.
$a_1$	The dimension of the tooth; polynomial component.
$a_2$	The dimension of the tooth; polynomial component.
$a_3$	The dimension of the tooth; polynomial component.
$\underline{a}_n$	The polynomial component.
$\underline{a}_x$	A unit vector in the vertical ( $x$ ) direction.
$A$	The area of each component; the active sensor surface area.
$\overline{A}$	The magnetic vector potential.
$A_f$	The peak value of the line current density.
$A_g$	The effective surface of a tooth.
$A_m$	The magnet surface area.
$A_m'$	The effective magnet surface area.
$A_{T_{avg}}$	The average tooth cross-section area.
$A_\delta$	The area of the main air gap.
$A_{\delta b}$	The area of the back air gap.
$AT_2$	The magnet's value of magnetomotive force at the working point.
$AT_4$	The magnet's maximum value of magnetomotive force.
$AT_D$	The value of magnetomotive force drop in the back walls.
$AT_{Fe}$	The value of magnetomotive force drop in the iron.
$AT_L$	The value of magnetomotive force drop in the side walls.
$AT_{L1}$	The value of magnetomotive force drop in the side walls of external lap-joint stator.
$AT_{L2}$	The value of MMF drop in the side walls of internal lap-joint stator.
$AT_T$	The value of magnetomotive force drop in the claw poles.
$AT_\delta$	The value of magnetomotive force drop in the main air gap.
$AT_{\delta b}$	The value of magnetomotive force drop in the parasitic air gaps.
$b_{p1}$	The tooth width at the tip.
$b_{p2}$	The tooth width at the bottom.
$B$	The magnetic field density.
$B_D$	The flux density in the back walls.
$B_g$	The flux density in the air gap.
$B_L$	The flux density in the side walls.

$B_{in}$	The flux density in the inner gap.
$B_{\max}$	The maximum flux density.
$B_{mean}$	The mean value of the flux density.
$B_{\min}$	The minimum flux density.
$B_{out}$	The flux density in the outer air gap.
$B_r$	The remanent flux density of the magnet.
$B_{rx}$	The remanent magnetic flux density in the radial direction.
$B_{ry}$	The remanent magnetic flux density in the tangential direction.
$B_t$	The total flux density.
$B_T$	The flux density in the tooth.
$B_\delta$	The flux density in the air gap.
$B_{\delta b}$	The flux density in the back air gap.
$c$	The viscous damping coefficient.
$C$	The maximum value of load that can be applied.
$d$	A skin depth.
$D$	The viscous damping coefficient.
$D_c$	The cylinder inside diameter.
$D_m$	The magnet outside diameter.
$D_{pm}$	The magnet outside diameter.
$D_{RI}$	The rotor inside diameter.
$D_{RO}$	The rotor outside diameter.
$D_{SI}$	The stator inside diameter.
$D_{SO}$	The stator outside diameter.
$D_{SO1}$	The lap-joint stator outside diameter.
$D_{SO2}$	The lap-joint inside stator outside diameter.
$D_\delta$	The average diameter of the air gap.
$e$	The voltage generated in the coil.
$e_s$	The applied voltage.
$E$	The sensor signal.
$E_{V1}$	The back electromotive force coil 1.
$E_{V2}$	The back electromotive force coil 2.
$f$	The frequency.
$f_{el}$	The electrical frequency of the sensor signal.
$f_{mech}$	The mechanical frequency of the sensor signal.
$f_p$	The cycle frequency.
$F$	The uniform flux in the magnetic core.
$F$	A new function as defined in Equation 5.80.
$F$	The Lorentz forces.
$F_a$	The force developed in the armature.
$F_{AR}$	The armature reaction.
$F_{pl}$	The spring preload.

$F_{m1}$	The magnetic force component.
$F_{m2}$	The magnetic force component.
$F_{mag}$	The magnetic force.
$F_{mech}$	The net mechanical accelerating force.
$F_{spg}$	The total spring force.
$F_t$	The one-pole-pitch (tooth-pitch) magnetic force.
$F_T$	The magnetic force. The total magnetic force.
$F_{vdg}$	The viscous damping force.
$g$	Acceleration.
$g_b$	The back air gap.
$G_u$	The motor permeance.
$h$	The valve height.
$h_c$	The coil height.
$h_s$	The magnet stroke.
$H_c$	The coercive force of the permanent magnet.
$H_D$	The field strength in the back walls.
$H_L$	The field strength in the side walls.
$H_T$	The field strength in the tooth.
$i$	The winding current.
$i_k$	The current in the $k$ coil.
$i_s$	A current in the coil.
$i(t)$	The winding current that is a function of time.
$I$	The current in the stepper motor coils.
$I_1$	The supplied current (constant) in coil 1.
$I_2$	The supplied current (constant) in coil 2.
$I_c$	The coil thickness.
$I_f$	The root-mean-square value of the phase current.
$I_n$	The nominal current in the coil.
$I_S$	The current in the coil.
$I_{S1}$	The current in coil 1.
$I_{S2}$	The current in coil 2.
$I_{Sk}$	The current in the $k$ coil.
$I_w$	The current in an equivalent coil.
$J$	The rotor inertia.
$J_{add}$	The additional inertia.
$J_c$	The coupling inertia.
$J_M$	The motor (rotor) inertia.
$\overline{J}_{pm}$	The equivalent permanent magnet current density.
$\overline{J}_s$	The external source current density.
$k$	The thermal dissipation coefficient of the material; a spring constant; a force constant.

$k_{1F}$	The ratio of the tooth-to-pole active areas at one coil energized.
$k_{2F}$	The ratio of the tooth-to-pole active areas for both coils energized.
$k_a$	The effective magnet area factor.
$k_m$	The effective flux length in the magnet factor.
$K$	A static torque coefficient at constant nominal voltage.
$K_{1T}, K_1$	The static torque coefficient that is a function of flux $\phi_1$ .
$K_{2T}, K_2$	The static torque coefficient that is a function of flux $\phi_2$ .
$K_m$	The mutual torque constant.
$K_{V1}$	The static torque coefficient that is a function of flux $\phi_1$ .
$K_{V2}$	The static torque coefficient that is a function of flux $\phi_2$ .
$l$	The length of each component.
$l_2$	The dimensions of the tooth dimension.
$l_a$	The dimensions of the tooth dimension.
$l_d$	The stator dimension.
$l_{d0}$	The stator two pole-pair section length.
$l_{d1}$	The stator dimension.
$l_{d2}$	The stator dimension.
$l_{Fe}$	The length of the magnetic path in the iron.
$l_m$	The average flux length in the magnet.
$l_m'$	The effective flux length in the magnet.
$l_{mat}$	The material thickness of the stator elements.
$l_o$	The total stator thickness.
$l_{o1}$	The total length of the tooth.
$l_{pm}$	The length of the permanent magnet.
$l_{pm}'$	The effective length of the permanent magnet.
$l_{s1}$	The lap-joint inside stator length.
$l_{s2}$	The lap-joint outside stator length.
$l_{s3}$	The overlap length.
$l_{ST}$	The tooth length.
$l_{ST}'$	The effective tooth length.
$L$	A self-inductance of coils.
$L_1$	A self-inductance coil 1.
$L_2$	A self-inductance coil 2.
$L_{sk}$	A self-inductance of the $k$ coil.
$L_{sw}$	A mutual inductance.
$L_y$	The rectangular core of length in the $y$ direction.
$L_w$	A self-inductance of an equivalent coil.
$L_{ws}$	A mutual inductance.
$m$	The total mass of all moving parts; the number of subdivisions in the coil region; the reciprocal of the skin depth.
$m$	The iron (real) permeability; the electron mobility; viscosity.

$m_f$	The multiplying factor for the International System of Units unit A/cm.
$m_\phi$	The multiplying factor for the International System of Units unit Wb/cm.
$M_c$	The closing moment due to pressure.
$M_m$	The closing magnetic moment.
$M_{m1}$	Component 1 of the closing magnetic moment.
$M_{m2}$	Component 2 of the closing magnetic moment.
$M_{m3}$	Component 3 of the closing magnetic moment.
$M_o$	The opening moment due to pressure.
$M_p$	The total pressure moment.
$n$	The number of stator coils.
$n_o$	The velocity of rotor in r/min.
$N$	The number of turns of the coil.
$N_1$	The number of turns of stator coil 1.
$N_2$	The number of turns of stator coil 2.
$N_f$	The number of turns per phase.
$N_i$	The magnetomotive force.
$N_o$	A fixed number of pulses applied to the motor.
$N_t$	The number of teeth of the exciter wheel.
$p$	The number of magnet pole pairs or sensor sections; pressure.
$P$	The number of poles; permeance of the magnetic circuit.
$P_1$	The pole head end leakage permeance.
$P_2$	The pole side leakage permeance.
$P_3$	The pole body permeance.
$P_4$	The semicircular cylinder leakage permeance.
$P_5$	The corner pole head leakage permeance.
$P_6$	The pole body permeance.
$P_7$	The back air gap semicircular cylinder leakage permeance.
$P_8$	The pole body leakage permeance.
$P_{\max}$	The maximum permeance.
$P_{\min}$	The minimum permeance.
$P_b$	The butt-joint permeance.
$P_c$	The power loss due to the winding resistance.
$P_e$	The eddy current loss.
$P_{em}$	The rate of energy conversion (electromagnetic power).
$P_{em}$	The electromagnetic power.
$P_{Fe}$	The iron permeance.
$P_{Fea}$	The apparent iron permeance.
$P_g$	The lap-joint back air gap permeance.
$P_{mech}$	The net mechanical power.
$P_r$	The rate of change in the stored magnetic energy (reactive power).
$P_s$	The source power.

$P_{spg}$	The eddy spring power.
$P_t$	The total power.
$P_\delta$	The main air gap permeance.
$P_{vdg}$	The viscous damping power.
$P1$	The elementary section permeance.
$P(\theta)$	The permeance.
$q$	The electron charge.
$r$	The disk radius.
$r_1$	The dimensions of the tooth.
$r_2$	The dimensions of the tooth.
$R$	The resistance of coils.
$R_1$	The resistance of coil 1.
$R_2$	The resistance of coil 2.
$R_b$	The reluctance of the back air gap.
$R_c$	The total ohmic resistance.
$R_{c1}$	The core reluctance.
$R_{c2}$	The core reluctance.
$R_{c3}$	The core reluctance.
$R_e$	The reflected resistance due to induced eddy current.
$R_{ex}$	The exciter wheel radius.
$R_{Fe}$	The reluctance of the iron.
$R_{g1}$	The air gap reluctance.
$R_{g2}$	The air gap reluctance.
$R_H$	The Hall constant of the material.
$R_p$	The plunger reluctance.
$R_{peak}$	The magnet-width/tooth-pitch ratio.
$R_\delta$	The reluctance of the main air gap.
$R1$	The elementary section reluctance.
$s$	The distance, deflection, or position of the moving armature.
$\dot{s}$	The velocity of the armature.
$s_v$	The sensor signal sensitivity.
$s_\phi$	The electromagnetic efficiency of the sensor configuration.
$S$	The stepping rate; the surface of integration or the device sensitivity; the surface of the electromagnet.
$S_D$	The cross section area of the one-pole-pair section.
$S_{pm}$	The magnet surface.
$S_{T_{avg}}$	The average cross section of the tooth.
$t$	Time.
$t_2$	The armature opening time.
$t_3$	The bottom plate thickness.
$t_4$	The armature closing time.

$t_4$	The disk armature thickness or start of armature motion.
$t_{45}$	The time for armature to reach force of 200N.
$t_o$	The voltage pulse width.
$t_{rp}$	The total travel time of solenoid.
$T$	The total static torque developed by the stepper motor; the period equal to the tooth pitch; temperature.
$\bar{T}$	The Maxwell stress tensor in dyadic form.
$T_1$	The stepper motor torque due to coil 1.
$T_2$	The stepper motor torque due to coil 2.
$T_A$	The reluctance torque, part A.
$T_B$	The reluctance torque, part B.
$T_C$	The synchronous torque.
$T_d$	The stall torque at zero speed.
$T_D$	The torque developed by the stepper motor.
$T_F$	The torque due to a friction.
$T_L$	The load torque.
$T_{Li}$	The load torque at $i$ position.
$T_{\max}$	The maximum torque developed by the stepper motor.
$T_{1\max}$	The maximum torque due to coil 1.
$T_{2\max}$	The maximum torque due to coil 2.
$T_N$	The available net torque.
$T_T$	The total torque.
$T_t$	The pole-pitch (tooth-pitch) torque.
$U_1$	The voltage applied to coil 1.
$U_2$	The voltage applied to coil 2.
$V$	The electric voltage; volume.
$\bar{V}$	The velocity of the field point.
$V_c$	The volume of the cylinder for one cycle.
$V_H$	The voltage across the chip.
$V_r$	The total required volume.
$V_s$	The sensor volume.
$W$	The magnet width; magnetic energy.
$W_m$	The coenergy stored in the air gap.
$W_{mag}$	The total magnetic energy.
$x(t)$	The position of the moving part.
$\alpha$	The electrical angle; the mechanical angle between two stators; the angle between flux and magnetizing force; pivot offset.
$\alpha_u$	The magnet load line angle.
$\beta$	The temperature coefficient for the magnet material.
$\dot{\gamma}$	The sheer rate.
$\delta$	The size of air gap; a position error; the Hall angle.

$\delta_b$	The size of back air gap (parasitic).
$\Delta B$	The flux density difference.
$\Delta S$	The stepping rate.
$\Delta t_n$	The zero crossing time interval.
$\Delta\alpha$	The change in the rotor position.
$\Delta\theta$	The temperature rise.
$\Delta\phi$	The flux linkage change.
$\xi$	The $B/A$ ratio of maximum torque values A and B of two consecutive steps.
$\theta$	The mechanical angle position; sensor or rotor position.
$\theta(t)$	The location of the trailing edge of the core at time $t$ .
$\lambda_t$	The total flux linkage of the winding.
$\lambda(i, x)$	The equivalent flux linkage of the winding.
$\mu_0$	The permeability of the air equals $4\pi \times 10^{-7}$ H/m.
$\rho$	The resistivity of the iron.
$s$	The location of any point on the active sensor surface area.
$\sigma$	The material conductivity.
$\tau$	The sheer stress; the stator pole pitch.
$\tau_o$	The pole pitch; yield stress.
$v$	The material reluctivity.
$v$	The sensor signal; voltage generated in a sensor coil.
$v_1$	The sensor signal; signal component of coil 1.
$v_2$	The sensor signal; signal component of coil 2.
$v_d$	The voltage generated in a coil of the distributed sensor.
$v_{\max}$	The sensor signal characterized by the maximum flux density $B_{\max}$ .
$v_{\min}$	The sensor signal characterized by the minimum flux density $B_{\min}$ .
$v_n$	The noise signal.
$v_s$	The sensor signal.
$v_s$	The induced signal in the sensor coil.
$\phi$	The magnetic flux embraced by the coil; flux in the air gap with the armature reaction.
$\phi_1$	The magnetic flux in air gap 1.
$\phi_1$	The magnetic flux embraced by coil 1.
$\phi_{1m}$	The magnetic flux embraced by coil 1 for a single pole-pair section.
$\phi_2$	The magnetic flux in air gap 2.
$\phi_2$	The magnetic flux embraced by coil 2.
$\phi_{2m}$	The magnetic flux embraced by coil 2 for a single pole-pair section.
$\phi_i$	The flux linkage in any of the $N$ turns of the coil.
$\phi_k$	The flux linkages of the $k$ coil.
$\phi_m$	The median magnetic flux embraced by the coil for a single pole-pair section.
$\phi_m$	The maximum magnetic flux in the air gap without an armature reaction.
$\phi_{\max}$	The flux linkage for the maximum permeance position.

$\phi_{\min}$	The flux linkage for the minimum permeance position.
$\phi_o$	The total flux developed by permanent magnet without an armature reaction.
$\phi_p$	The magnetic flux embraced by the $p$ single pole-pair section.
$\phi_s$	The flux linkages in the stator.
$\phi_{T^{\circ}C}$	The magnetic flux in the air gap at temperature $T^{\circ}C$ .
$\phi_w$	The flux linkages in the rotor.
$\phi_{ws}$	The flux per pair of teeth.
$\Phi_k(x'', y'')$	The $k$ th magnetic vector potential of one coil side.
$\Phi_k(x', y')$	The $k$ th magnetic vector potential of the other coil side.
$\psi$	The flux linkage; the rotor position in electrical degrees.
$\Psi_{c1}$	The rotor command position for step 1.
$\Psi_{c2}$	The rotor command position for step 2.
$\Psi_c$	The rotor command position.
$\Psi_i$	The rotor $i$ position in electrical degrees.
$\Psi_k$	The flux linkages of the $k$ coil.
$\Psi_s$	The flux linkage in the stator.
$\Psi_w$	The flux linkage in the rotor.
$\omega$	The angular speed.
$\omega_{el}$	The electrical angle speed of the motor (rotor).
$\omega_{mech}$	The mechanical angle speed of the motor (rotor).
$\dot{\omega}_{mech}$	The mechanical angular acceleration of the motor (rotor).

---

## Subscripts

$a$	Area.
$avg$	Average.
$A$	Part A.
$AR$	Armature reaction.
$ASIC$	Application specific integration circuit.
$b$	Back air gap.
$B$	Part B.
$c$	Coercive, winding resistance.
$C$	Part C.
$d$	Distributed; stall at zero speed.
$D$	Back walls; developed.
$e$	Eddy current.
$el$	Electrical.
$em$	Electromagnetic.
$ex$	Exciter wheel.
$f$	Magnetomotive force.

$1F$	One coil energized factor.
$2F$	Two coils energized factor.
$F$	Friction.
$Fe$	Ferromagnetic.
$g$	Tooth, claw pole.
$H$	Across the chip.
$i$	By $i$ turn (any of the turns).
$k$	The $k$ coil.
$L$	Load; side walls.
$L1$	Side walls of external lap-joint stator.
$L2$	Side walls of internal lap-joint stator.
$Li$	Load at $i$ position.
$m$	Maximum; magnetic; median.
$mag$	Magnetic.
$\max$	Maximum.
$1_{\max}$	Maximum at coil 1.
$2_{\max}$	Maximum at coil 2.
$mech$	Mechanical.
$\min$	Minimum.
$N$	Net.
$o$	In the air; without armature reaction; per pole pair.
$p$	Single pole-pair section.
$p1$	Width at the tip.
$p2$	Width at the bottom.
$pl$	Preload.
$pm$	Permanent magnet.
$RI$	Rotor inside.
$RO$	Rotor outside.
$r$	Remanence; reactive.
$rx$	In the tangential direction.
$ry$	In the radial direction.
$sk$	The stator $k$ coil.
$s$	Stator; spring.
$s3$	Stator overlap.
$spg$	Spring.
$sw$	Rotor stator.
$S1$	Stator (coil) 1.
$S2$	Stator (coil) 2.
$SI$	Stator inside.
$SO$	Stator outside.
$SO1$	Joint stator inside.

<i>SO2</i>	Joint stator outside.
<i>ST</i>	Stator tooth.
<i>t</i>	Total, teeth.
<i>T</i>	Tooth; claw poles.
<i>T<sub>avg</sub></i>	Average tooth area.
<i>T°C</i>	At temperature of.
<i>v</i>	Sensor signal.
<i>w</i>	Rotor; rotor's equivalent coil.
<i>ws</i>	Stator rotor.
<i>V1</i>	Electromagnetic force coil 1.
<i>V2</i>	Electromagnetic force coil 2.
$\delta$	Air gap.
$\delta_b$	Back (parasitic) air gap.
<i>vdg</i>	Viscous damping.
$\phi$	Flux; magnetic.
<i>x</i>	In the <i>x</i> direction.

---

## Abbreviations

<b>ABS</b>	Antiskid braking system.
<b>AC</b>	Alternating current.
<b>AWG</b>	American wire gauge.
<b>BH</b>	Magnetization curve.
<b>DC</b>	Direct current.
<b>EGR</b>	Exhaust gas recirculation.
<b>EMF</b>	Electromotive force.
<b>FE</b>	Finite element.
<b>GM</b>	General Motors.
<b>GMR</b>	Giant magnetoresistive.
<b>H</b>	Samarium-cobalt magnets.
<b>HDDR</b>	Hydrogenation-disproportionation-desorption-recombination.
<b>HS</b>	Neodymium magnets.
<b>HVAC</b>	Heating, ventilating, air-conditioning.
<b>ID</b>	Inside diameter.
<b>IP</b>	Intellectual property.
<b>IPO</b>	Initial public offering.
<b>MMF</b>	Magnetomotive force.
<b>MOSFET</b>	Metal oxide semiconductor field effect transistor.
<b>MQ1</b>	Magnequench 1.
<b>MQ2</b>	Magnequench 2.

MQ3	Magnequench 3.
MR	Magnetoresistive.
NI	Ampere-turns.
OD	Outside diameter.
p-p	Signal peak-to-peak.
PM	Permanent magnet.
PSSM	Passive solid-state magnetic.
PWM	Pulse-width modulation.
rpm	Revolutions per minute.
R&D	Research and development.
TC	Traction control.
TFM	Transverse flux motors.
VC	Venture capital.
VR	Variable reluctance.
VSM	Vibrating sample magnetometer.
YBM	Ferrite magnets.
YCM	Alnico magnets.
2D	Two-dimensional.
3D	Three-dimensional.

---

# *Contents*

---

<b>1</b>	<b>Introduction .....</b>	<b>1</b>
1.1	Classification of Sensors and Actuators .....	2
1.1.1	Magnetic Sensors .....	2
1.1.2	Linear and Latching Solenoid Actuators .....	3
1.1.3	Stepper Motors .....	5
1.1.4	Special Magnetic Devices .....	7
1.1.5	Rotary and Linear Actuators .....	8
1.2	Magnetic Materials and Technology .....	8
1.2.1	Soft Magnetic Materials .....	9
1.2.2	Hard Magnetic Materials .....	12
1.2.3	Coating Technologies .....	15
1.2.4	Magnetic Materials Market and Applications .....	16
<b>2</b>	<b>Magnetic Sensors.....</b>	<b>21</b>
2.1	Theory of Magnetic Sensors .....	23
2.2	Magnetic Sensor Analysis .....	24
2.3	VR Sensors .....	26
2.3.1	Conventional VR Sensors .....	27
2.3.2	High Performance VR Sensors .....	32
2.3.3	Sensors with Inserted Magnets .....	36
2.3.4	Front-Mounted-Magnet Sensors .....	43
2.3.5	Sensors with E-Shaped Magnetic Structure .....	45
2.3.6	Sensors with U-Shaped Magnetic Structure .....	46
2.3.7	Multiple Magnets VR Sensors .....	53
2.3.8	Dual-Magnet Sensors .....	53
2.3.9	Dual Sensor Arrangement .....	61
2.3.10	Distributed VR Sensors .....	63
2.4	Solid-State Sensors .....	70
2.4.1	Solid-State Sensor Analysis .....	71
2.4.2	Solid-State Sensor Design .....	72
2.4.3	Solid-State Sensor Test Results .....	75
2.5	Magnetic Sensor Applications .....	77
2.5.1	Magnetic Speed Sensor Requirements .....	77
2.5.2	Magnetic Speed Sensor Applications .....	78
2.5.3	Magnetic Position Sensor Applications .....	79
2.6	VR Sensor Noise .....	81
2.6.1	Math Model and Noise Analysis .....	81
2.6.2	Noise Problem Solutions .....	82
	Example 2.1 .....	85
	Example 2.2 .....	86
	Example 2.3 .....	88

<b>3</b>	<b>Linear Actuators .....</b>	<b>89</b>
3.1	Mathematical Model for Linear Actuators .....	89
3.1.1	Symmetrical Analysis of Electromagnetic Devices.....	90
3.1.2	Electrical Network Equations.....	92
3.1.3	Mechanical Equations .....	94
3.1.4	Magnetic Forces .....	96
3.1.5	PWM Analysis.....	97
3.1.6	Solenoid Analysis and Simulations .....	102
3.2	Fast-Acting Actuators.....	106
3.2.1	Disk Solenoids.....	106
3.2.2	Plunger Solenoids.....	108
3.2.3	Ball Solenoids .....	110
3.2.4	Conical Solenoids .....	112
3.2.5	Optimization of Fast-Acting Actuators.....	115
3.3	Applications of Solenoid Actuators .....	118
3.3.1	Long Stroke Solenoid Fuel Pump .....	118
3.3.2	Gasoline Injectors .....	121
3.3.3	Natural Gas Injectors .....	125
3.3.4	Diesel Fuel Injectors .....	131
3.3.5	Compressor Solenoid Valves .....	137
3.3.6	Transmission Solenoids .....	140
Example 3.1 .....	149	
Example 3.2 .....	151	
<b>4</b>	<b>Latching Linear Actuators .....</b>	<b>155</b>
4.1	Latching Relays .....	155
4.1.1	Dynamics of Latching Relays .....	157
4.1.2	Bipolar Latching Relays.....	159
4.1.3	Unipolar Latching Relays.....	163
4.1.4	Latching Relay Analysis .....	165
4.1.5	Latching Relay Analysis and Tests .....	168
4.2	Latching Solenoids.....	173
4.2.1	Latching Solenoids with Moving Magnets .....	174
4.2.2	Latching Solenoids with Stationary Magnets .....	182
4.3	Latching Solenoid Applications.....	189
Example 4.1 .....	190	
<b>5</b>	<b>Stepper Motors .....</b>	<b>191</b>
5.1	Principles of Operation .....	191
5.2	Static Analysis of Stepper Motor.....	196
5.2.1	Static Torque Analysis.....	196
5.2.2	Magnetic-Circuit Analysis.....	201
5.2.3	Magnet Operating Point.....	207
5.2.4	Temperature Effect .....	210
5.2.5	Armature Reaction Effect .....	210
5.2.6	Experimental Results of Static Performance .....	211
5.3	Dynamic Analysis of Stepper Motor .....	217
5.3.1	Math Model of the Dynamic Operation.....	218
5.3.2	Stepper Motor Dynamic Simulation .....	221
5.3.3	Validation of the Dynamic Model .....	223

5.3.4	Effects of Various Parameters on Stepper Motor Performance .....	226
5.3.5	Experimental Results of Dynamic Performance .....	231
5.3.6	Evaluation of Viscous Damping Coefficient .....	233
5.3.7	Effects of Load Torque on Stepper Motor Performance .....	237
5.3.8	Stepper Motor Inductance in Dynamic Operation .....	242
Example 5.1:	Magnetic-Circuit Calculations.....	250
Example 5.2:	Static Torque Calculations .....	256
Example 5.3:	Magnetic Flux Calculations .....	257
<b>6</b>	<b>Special Magnetic Devices.....</b>	<b>261</b>
6.1	Magnetic Valves .....	261
6.1.1	Background.....	262
6.1.2	Heart Valve Requirements .....	262
6.1.3	Heart Valve Design Concept .....	265
6.1.4	Mathematical Model and Simulations .....	265
6.1.5	Optimized Design.....	269
6.1.6	Comparison and Test Results .....	272
6.2	Heart Pump.....	273
6.2.1	Heart Pump Requirements .....	274
6.2.2	Heart Pump Design Concept.....	275
6.2.3	Analytical Simulations and Optimized Design.....	275
6.3	Magnetorheological Fluid Solenoids .....	281
6.3.1	Background.....	281
6.3.2	Magnetorheological Fluid Solenoid Actuator.....	283
6.3.3	MR Fluid Applications .....	284
Example 6.1	.....	287
Example 6.2	.....	288
Example 6.3	.....	288
<b>7</b>	<b>Rotary Actuators .....</b>	<b>291</b>
7.1	Disk Rotary Actuators .....	292
7.1.1	Disk Rotary Actuator Analysis.....	293
7.1.2	Disk Rotary Actuator Design .....	298
7.1.3	Disk Rotary Actuator Excitation Electromagnetic Circuit.....	298
7.1.4	Disk Rotary Actuator Toothed Magnetic Part .....	299
7.1.5	Disk Rotary Actuator PM.....	300
7.1.6	Disk Rotary Actuator Test Results.....	302
7.2	Claw Pole Rotary Actuators.....	304
7.2.1	Claw Pole Rotary Actuator Analysis.....	306
7.2.2	Claw Pole Rotary Actuator Design .....	309
7.2.3	Claw Pole Rotary Actuator Excitation Electromagnetic Circuit.....	309
7.2.4	Claw Pole Actuator Toothed Magnetic Part .....	310
7.2.5	Claw Pole Actuator PM.....	310
7.2.6	Claw Pole Rotary Actuator Test Results.....	313
7.3	Cylindrical Rotary Actuators .....	316
7.3.1	Cylindrical Rotary Actuator Analysis .....	317
7.3.2	Cylindrical Rotary Actuator 2D Analysis.....	318
7.3.3	Cylindrical Rotary Actuator 3D Analysis and Test Results .....	322
7.3.4	Cylindrical Rotary Actuator Design.....	325
7.3.5	Cylindrical Rotary Actuator PM.....	326

7.3.6	Cylindrical Rotary Actuator Excitation Electromagnetic Circuit .....	332
7.3.7	Cylindrical Rotary Actuator Toothed Magnetic Structure.....	332
7.4	Rotary Actuator Applications .....	333
7.4.1	Disk Rotary Actuator Application .....	335
7.4.2	Claw Pole Rotary Actuator Application.....	336
7.4.3	Cylindrical Rotary Actuator Application .....	338
	Example 7.1 .....	342
	Example 7.2 .....	343
	Example 7.3 .....	343
<b>8</b>	<b>Addendum.....</b>	<b>345</b>
8.1	Technology Development .....	345
8.1.1	Partnership.....	345
8.1.2	Competitiveness.....	346
8.1.3	Persistence.....	347
8.1.4	Technical Growth.....	348
8.2	Technology Valuation .....	349
8.2.1	Technical Attributes.....	349
8.2.2	Business Attributes.....	353
8.2.3	Financial Attributes .....	354
8.2.4	Technology Ranking.....	355
	<b>Bibliography.....</b>	<b>357</b>
	<b>Index.....</b>	<b>363</b>

# 1

---

## *Introduction*

---

Mechatronics is the synthesis of mechanical engineering and electronics, two distinct technology areas that overlap in the design of complex systems. It is a synergetic combination of precision mechanical engineering, electronic control, and system thinking in the design of product and process (Alciatore and Histand 2003, Baumann et al. 2000, Bishop 2002, Triantafyllou et al. 1999). Sensors and actuators convert energy in mechatronics systems and the magnetic circuit seems to be the best medium for such a conversion (White and Woodson 1959). Therefore, the magnetic sensors and electromechanical actuators, with electromagnetic circuits that are electronically controllable, such as stepper motors, magnetic sensors, rotary actuators, linear solenoids, and other special devices with smart materials chosen for and described in this book, are critical components of mechatronic systems (Delphi 2002). This book discusses several families of modern electromagnetic and electromechanical devices in industrial applications and is devised to guide the reader in analysis and design optimization (Baumann et al. 2000, Bishop 2002, Box et al. 1969, Dąbrowski 1977, Fletcher 1987, Geras and Wing 1994, Kuester et al. 1973, Navarra 1990, Pawlak 1989, Piron et al. 1999, Yoon et al. 1999). The presentation of prototypes and test results along with their analyses should allow for a better understanding of the progression from concept to mass production.

The first part of this chapter categorizes and describes several key families of electromechanical and electromagnetic devices utilized in mechatronic applications. With a focus on variable reluctance (VR) sensors, it describes and categorizes different types of magnetic sensors, linear and latching solenoids, stepper motors, and different types of rotary actuators (Pawlak et al. 1997, Pawlak 1996). Special magnetic devices also are introduced, including devices with smart materials with an emphasis on biomedical applications.

Because of their simplicity, low cost, controllability, and high performance, modern electromechanical and electromagnetic sensors and actuators are finding increasing use in industrial applications (Aftonin et al. 1999, Ellis and Collins 1980, Hanitsch 1994). Proper selection of magnetic materials is a key element in electromagnetic-circuit design. Because of this, both soft and hard magnetic materials are described in the second part of this chapter (Carpenter 1989, Daido 2003, Furlani 2001, Hitachi 1999, Kasai 1992). A review of soft and hard magnetic materials includes a recommendation for different applications (Dąbrowski 1980, Geras and Wing 2002, Glinka 1995, Macoit 1999, Pawlak et al. 1999, Pawlak 2000a, Pawlak 1996, Rashidi 1982). New advancements in high-energy magnets are indicated; however, all of the applications discussed are based on commercially available magnetic materials. Furthermore, the magnetic material manufacturing technologies that should help the reader understand both the advantages and the magnetic material limitations are also discussed in this chapter.

---

## 1.1 Classification of Sensors and Actuators

The electromechanical and electromagnetic sensors and actuators such as stepper motors, sensors, rotary actuators, linear solenoids, which are electronically controllable in mechatronic systems, and other special devices with smart materials, are described and categorized in this chapter.

### 1.1.1 Magnetic Sensors

The magnetic sensors that are most commonly used in mechatronics systems today are VR and solid-state sensors [Hall-effect devices and magnetoresistive (MR)]. They are quickly making their way to the world market (Foster 1988, Ohshima and Akiyama 1989a, Ohshima and Akiyama 1989b, Podeswa and Lachman 1989). Over the last 10 years, the number of sensors installed in the average automobile has risen from several up to the current 20. It is expected to exceed 50 units in the near future. Worldwide, the automotive sensor market is valued at \$5 billion and is expected to continue growing at an annual average rate of about 7%. Common applications for magnetic sensors include ignition timing, power sensing, valve position, current sensing, linear or rotary motion detection, speed sensing, length measurement, flow sensing, revolutions per minute (rpm) sensing, security systems, and more. Magnetic sensors are generally used to provide speed, timing, or synchronization data to a display (or control circuitry) in the form of a pulse train. Therefore, sensors for rpm and speed measurement, the two most popular applications, can be found in almost any market:

1. rpm measurement on engines for aircraft, automobiles, boats, buses, agricultural equipment, trucks, rail vehicles, as well as on motors for precision camera, tape recording and motion picture equipment, drills, grinders, lathes, automatic screw machines, etc.
2. speed measurement on processes for food, textile, woodworking, paper, printing, tobacco, and pharmaceutical industry machinery, for pumps, blowers, mixers, exhaust and ventilating fans, electric motors, and generators

Completely self-powered, VR magnetic sensors are simple, robust devices that do not require an external voltage source for operation (Pawlak et al. 1991d). They feature non-contact, error-free conversion of actuator speed to output frequency, as well as simple installation, with no moving parts. They are also usable over a wide speed range and adaptable to a wide variety of configurations. These properties have led to widespread utilization in a number of industries. As a result, VR sensors have become known by many use-related names such as magnetic pickups, speed sensors, motion sensors, pulse generators, variable reluctance sensors, frequency generators, transducers, magnetic probes, timing probes, monopoles, and pickoffs.

The drawback of VR sensors is that they generate a signal proportional to the magnetic field's rate of change. Therefore, the signal strength decreases with decreasing speed and, below a certain flux change rate, the signal disappears into the noise. At high-frequency magnetic fields, the excess output voltage of the coil also causes problems for circuit designers. The generated voltage for VR sensors is up to 4000 V, for air gaps from  $0.25 \times 10^{-3}$  to  $3.0 \times 10^{-3}$  m with coils of resistance ranging from 200 to 4000  $\Omega$  over the wide range of temperatures from -40 to +165°C.

Analog VR sensors are passive sensors and do not require any external power source. Such a sensor generates a typically sinusoidal-like output voltage proportional to the speed of the exciter wheel. A signal level is a function of the air gap between the sensor and a toothed exciter wheel. Digital output VR speed sensors produce a digital (square wave) pulse that is directly proportional to exciter-wheel speed. The active solid-state signal conditioning integral with the sensor converts the analog VR output to digital pulses. The exciter-wheel speed sensing range is from 0.5 m/s to 40 m/s at frequencies up to 50,000 Hz.

In most applications, it is sufficient to have one voltage output; however, when speed sensor redundancy is required, multiple coil configurations are recommended. Instead of using two separate single coil sensors, multiple coil sensors accommodate redundancy needs while minimizing system costs and weight. Sensor coil options include single, dual, triple, or quad coil configurations for both redundancy and multiple readout needs, i.e., two coils for redundant speed detection and a third independent coil for ground trim, cockpit readout, etc. For multiple coil applications, output voltages for redundant applications are maintained in the event of a sensor or system fault, such as a short in the sensor harness or associated electronics, while maintaining speed detection integrity.

Neither the Hall-effect nor the magnetoresistive (MR) sensors can generate a signal voltage on their own and must have an external power source. Therefore, they are called active sensors. Solid-state sensors produce either a digital or an analog output. Digital output sensors are in one of two states — OFF or ON. Analog sensors provide a continuous voltage output, which increases with the strength of the magnetic field. There are three types of digital sensors: bipolar, unipolar, and omnipolar. Bipolar sensors require a positive magnetic field strength (south pole) to operate and a negative one (north pole) to release. Omnipolar sensors operate with either north or south poles. Unipolar sensors require a single magnetic pole (south pole) to operate; the sensor is released when the pole is removed. Analog sensors operate in proximity of either magnetic pole (Rowley and Stolfus 1990).

Hall-effect sensors are zero speed, noncontact sensors that can provide constant amplitude output over typical target speed ranges from 0 Hz to 50 kHz and even up to 100 kHz with air gaps up to  $3.0 \times 10^{-3}$  m. Hall-effect circuitry measures speed accurately to true zero, direction of rotation or travel, and true angular position of gear. Hall-effect devices generate a very small raw signal because of low field sensitivities (0.5 to 5.0 mV/100 Oe applied field) and the device performance is strongly temperature dependent. Hall-effect sensors feature true zero speed sensing, a wide operating voltage range from 5.0 to 24.0 V, an open collector output with sinking currents to 35 mA, and an operating temperature range up to 150°C.

Giant magnetoresistive (GMR) metal multilayer sensors, which have recently been introduced, offer improvements over galvanometric MR sensors. A new passive solid-state magnetic (PSSM) sensor technology is based on a combination of two phenomena: the magnetostrictive effect and the piezoelectric effect. In response to a magnetic field, the magnetostrictive component imparts a strain on the piezoelectric element that in turn produces an electrical output signal of the PSSM sensor. It has the potential to replace existing sensors, provided that the technology is cost-effective in mass production and would work in the harsh environment of the final product. These sensors combine the advantages of the miniature size of Hall sensors and the passive nature of VR coil devices because the PSSM sensors consume no electrical power. Both solid-state and VR sensors are described in Chapter 2.

### 1.1.2 Linear and Latching Solenoid Actuators

Solenoid actuators are common industrial components used in almost every industrial motion control (Boldea and Nasar 2001). Solenoids can be found in applications that

require a pinch, lock, divert, move, latch, or kicking type of functionality in a variety of industries, such as factory automation, material handling, transportation, automotive, food processing, medical equipment, agricultural equipment, vending machines, laundry equipment, construction equipment, marine, space, and aircraft. In addition, solenoid actuators are widely used in consumer markets.

A solenoid consists of a coil with magnetic wire wound on a bobbin with a moving armature and a return spring encapsulated within the housing. Depending on an armature's shape, solenoids can be categorized as plunger, disk, ball, or conical types. When electricity is applied to the coil, the resulting magnetic field attracts the armature and pulls it into the solenoid body against an armature stop, contracting a return spring. When electricity is removed, the solenoid plunger is allowed to return to its original position due to a return spring or gravity. Solenoids are typically classified as alternating current (AC) or direct current (DC), linear or rotary, or on-off vs. variable positioning. A linear solenoid can be found in either an open frame solenoid configuration, which is used for lower-cost, less-efficient applications, or a tubular solenoid, which is most often used for longer-life, higher-force applications.

Linear solenoids convert electrical energy into mechanical work via a plunger with an axial stroke in either a push or pull action. The electromotive force (EMF) is supplied by the current applied to the coil and is limited by the heat dissipation capacity of the coil. The duty cycle, or the percentage of time that the solenoid is powered, is therefore a crucial factor in solenoid selection; the less time a solenoid needs to be powered, the more time it has to cool, and thus it can be used with a higher rated current, providing more force. The same solenoid design can have widely varying force ratings associated with different duty cycles. Continuous duty solenoids are rated for a 100% duty cycle. In general, this duty cycle will have the lowest force ratings.

Industrial work solenoids can be designed to accept the attachment of the load to the pulling or pushing end of the plunger. For some applications, the plunger assembly is designed to accept load attachments at both ends. The method of connecting the load to the industrial work solenoid must be developed with the consideration that side loads will be detrimental to solenoid life if not properly accounted for. Furthermore, if the installation causes a binding condition anywhere within the required operating stroke, excessive wear and reduced operating life will result.

Solenoid actuators transform electrical energy into mechanical energy. Depending on function, there are three types of solenoid actuators: rotary solenoid with shaft rotary motion, linear solenoid with linear motion, and holding solenoid with holding force. A rotary solenoid is an electromechanical device that converts linear motion to rotary motion by virtue of three ball bearings that travel down inclined raceways. When the coil is energized, the armature assembly is pulled toward the stator and rotated through an arc determined by the coining of the raceways. Linear solenoids are subdivided into:

- Single-acting linear solenoids — solenoid force developed in one direction, return action is effected mechanically, e.g., with a coil
- Two-directional linear solenoids — motion is effected by specifically energizing the respective coil
- Bistable solenoids — switching is effected with a current impulse of varying polarity, the end positions are maintained without current

A linear solenoid has three important characteristics: stroke, pull-in force, and relative duty cycle. Stroke is the distance by which the armature should be moved. The pull-in force is defined as the force available before the movement starts. The relative duty cycle

represents the relation of switch-on time to operational cycle time. A solenoid rated for a 100% duty cycle may be energized at its rated voltage (current) continuously, because its total coil temperature will not exceed the maximum allowable ratings (Class A 105°C, Class B 130°C, Class F 155°C, and Class H 200°C, all at an ambient temperature of 25°C). Less than a 100% duty cycle falls into the category of intermittent duty cycle that has an associated allowable “on” time, which must not be exceeded. For the same solenoid, intermittent duty coils provide considerably higher forces than continuous duty coils.

Linear solenoids are available in various types and sizes for the widest range of stroke lengths, force capabilities, and duty cycles (Pawlak et al. 1988). The line of linear solenoids includes specially engineered types for standard, intensive, heavy-duty applications, as well as bistable linear solenoids and self-holding latching solenoids designed for low energy consumption. Rotary solenoids provide rotation angles of 45°–90°.

A proportional solenoid is a linear actuator with a fixed range of travel where the value of the input signal corresponds to the solenoid travel distance. The proportional solenoids can control position in a precise manner. Solenoids also may be designed for simple on-off applications, acting much like relays. For example, they are used this way in starters and door locks. Pulse-width modulated (PWM) linear solenoids are used to operate pistons and valves for accurate control of fluid pressure or flow in applications such as transmissions and fuel injection. Transmissions require accurate and smooth control of pressure on clutches to change gears and to control the locking torque converter. Electronically controlled transmissions may contain more than eight linear solenoids, all of which require smooth, accurate control. Common-rail diesel fuel-injection applications, with pressures in excess of  $13.8 \times 10^3$  kPa, may require one linear solenoid per cylinder — and one at the fuel pump — to adjust pressure accurately to maintain predictable injector fuel flow. The linear solenoid’s position is controlled in a feedback loop. For example, a valve’s downstream pressure can be monitored and used as a feedback signal to compare with the set point, adjusting the PWM duty cycle to control the solenoid. However, it may be difficult, impractical, or very costly to measure the downstream pressure. A practical alternative is to establish the position of the solenoid by measuring the current through the solenoid. This is possible because the force imposed by the mechanical load on a solenoid is directly proportional to the magnetic field, which, in turn, is directly proportional to the current through the coil. Proportional control of the solenoid is achieved by a balance of the forces between the spring-type load and the solenoid’s magnetic field, which can be determined by measuring the current through the solenoid. Linear solenoids are described in Chapter 3.

A solenoid can also be made in a magnetic latching style (Pawlak et al. 1999). In this case, a magnet is used inside the solenoid body. When the coil is energized and the armature is pulled into the solenoid body, the magnet holds the armature in position even after the power is removed. A reverse voltage is then applied to release the armature from the solenoid body to allow it to return to the starting position. Bistable solenoids have two stable end positions that are maintained without current. Switching is effected with a current impulse of varying polarity between the two end positions. In contrast to standard linear solenoids, bistable solenoids feature three characteristic forces: pull-in force (as with standard linear solenoids), holding force with the armature fully in the home position, and holding force with the armature at start position. Latching solenoids are introduced in Chapter 4.

### 1.1.3 Stepper Motors

A stepper motor is an electronically operated rotary electric motor that converts electrical pulses into a mechanical rotary motion with limited-angular increments called “steps.” Each revolution of the stepper motor’s shaft is made up of a series of discrete individual

steps. A step is defined as the angular rotation produced by the output shaft each time the motor receives a step pulse. These types of motors are very popular in digital control circuits, such as robotics, because they are ideally suited for receiving digital pulses for step control. These motors are popular because they are compatible with modern digital controls. Stepper motors, also called step motors or stepping motors, have a wide presence; they are popular in machine tools, process control systems, tape and disk drive systems, and programmable controllers, to name a few (Ellis and Collins 1980, Furlani 2001).

There are three distinctive stepper motor families that vary in their design based on magnetic material selection. Perhaps the most popular family is the permanent-magnet (PM) stepper motor, which operates on the interaction between a multipole ring or thin-disk PM rotor and electromagnetic field of the stator. The rotary torque is produced the same way as in a synchronous motor with an interaction of a rotating stator flux and electromagnetically corresponding PM flux.

A claw pole stepper motor, also known as a thin-can or can-stack motor, is the most commonly used motor for low torque and low speed applications because of its low cost, simplicity, high reliability, and relatively low inertia. This motor consists of a coil, multipole ring magnet, and a claw pole stator. The teeth on the stator surface and the rotor pole faces are offset so that there will be only a limited number of rotor teeth aligning themselves with an energized stator pole. The number of teeth on the rotor and stator determine the step angle that will occur each time the step pulse is applied and the polarity of the winding is reversed. The greater the number of teeth, the smaller the step angle with typical angles of 7.5° or 15°. Claw pole stepper motors are described in Chapter 5.

The VR stepper motors have reluctance-type ferromagnetic rotors that produce reluctance torque. Unlike PM stepper motors, VR stepper motors have no residual torque to hold the rotor at one position when turned off. When the stator coils are energized, the rotor teeth will align with the energized stator poles. The dynamic behavior of magnetic flux is based on the search for a path with minimum reluctance. Therefore, this motor tends to align the rotor's center of the pole with the axis of symmetry of the stator's salient pole. By alternating the windings that are energized in the stator, the stator field changes and the rotor is moved to a new position. Usually a rotor of the reluctance motor is made out of soft iron, and the stator has multiphase windings. In order to improve the motor's performance, a stack of three motors are connected and shifted from each other to obtain a large number of steps with small angular displacements.

The structure of the hybrid stepper motor combines both the VR and active PM design and is operated under the combined principles of the PM and VR stepper motors (Crnosija 2000, Croat 1985, Russell and Lenhouts 1980). The stator core structure of a hybrid motor is essentially the same as that of a VR stepper motor. The main difference is that in the VR motor, only one of the two coils of one phase is wound on one pole. However, a typical hybrid motor has coils of two different phases wound on the same pole. The two coils at a pole are wound in a configuration known as a bifilar connection. Each pole of a hybrid motor is covered with uniformly spaced teeth made of soft steel. The teeth on the two sections of each pole are misaligned with each other by a half-tooth pitch. A typical design presents a cylindrical PM sandwiched between two VR end rotors with an offset. They offer improved performance in comparison with other families, but they are more costly.

The stator winding design can also vary. Therefore, from the controller's point of view, there are several more types of stepper motors. A bipolar stepper motor has a simple winding but a more complex controller with an "H" switch, while a unipolar stepper motor has more complex windings with a simpler controller. The bifilar windings of a stepper motor are applied to the same rotor and stator geometry as a bipolar motor, but instead of winding each coil in the stator with a single wire, two wires are wound in parallel with each other, which doubles the number of wires for the motor. The multiphase

stator winding of a stepper motor is not very popular, while the three-phase winding is. The three-phase winding is connected in the  $\Delta$  and  $y$  configurations that correspond to PM motors with a small number of teeth — in this case, three.

Depending on the mode of operation, stepper motors can perform full steps, half steps, and microsteps. Half steps occur when both windings are excited with identically rated currents at the same time, while microsteps occur when currents in both windings are at different levels (Russell and Pickup 1982). This mode of operation often requires current sensing and limiting that would prevent exceeding the rated current and thermal capacity of the stepper motor. A number of limiting techniques exist, including open loop current limiters, linear current limiters, voltage limiters, one-shot feedback current limiters, or the well-known PWM technique with high frequency, which is described in Chapter 5.

#### 1.1.4 Special Magnetic Devices

Devices with unique medical applications such as an electronically controlled heart valve or a ventricle assist artificial heart pump were selected for this review (Korane 1997, Young and Pawlak 1992, Young and Pawlak 1990, Zhao et al. 1999). The medical environment and its requirements create an unusual design challenge and allow for broadening technological horizons. The key challenges for medical applications are energy supply and heat dissipation. A long-lasting energy supply helps reduce the number of surgeries between implants while a proper heat transfer helps tissues survive longer. Maintaining the temperature rise below 3–5°C above normal body temperature (36.6°C) is critical because such a relatively small temperature increase may permanently damage exposed tissue cells. Another challenge is selecting the device location and its size. The left-ventricular assist device that provides pressures for an artificial heart can be located anywhere along the blood pipeline. Location in the pelvic area would allow anchoring the pressure chamber to the bone structure for convenient energy transfer through the skin. The size of the heart valve for the mitral valve replacement was selected for the mature human heart. Even though the heart valve final design met all the required temperature and blood pressure tests, its design has a number of deficiencies in comparison with a real human mitral valve:

- Excessive noise when in operation
- Blood cell damage, inducing blood clots
- The need to dissipate heat that may damage cells
- Large volume with its sewing ring and electromagnetic circuit
- Requires electrical energy to run
- Need for connections and leads
- Limited durability, up to 10 years

New materials and, in particular, use of smart materials also creates unusual design challenges for an engineer and allows for novel configurations. Piezoelectric, magnetostrictive, rheological, and thermoresponsive materials have perhaps the highest potential for use in mechatronic systems. Piezoelectric ceramic and polymer materials that instantly change the physical shape in response to an electrical field have potential use in actuators that control vibration in precision tools, and improve accuracy and speed of robotics, printers, and injectors. Devices with electrostrictive and magnetostrictive materials that change size in response to either electric or magnetic fields, or that can produce electrical voltage signals when stretched, can be utilized as valves and pumps or sensors.

Electrorheological and magnetorheological fluids that change their states from liquid to almost solid in the presence of electrical or magnetic fields are finding applications in dampers for automotive suspension with great potential for medical, construction, and sport utility applications, among others. Thermoresponsive materials, such as shape memory alloys that change shape in the presence of cold and heat, were found useful for automotive and aircraft parts such as couplers and thermostats. Introducing mass production applications of any of the smart materials is a great challenge and a high risk. The world's first successful industrial application of magnetorheological fluid is described in Chapter 6 (Delphi 2002).

### **1.1.5 Rotary and Linear Actuators**

Rotary actuators, also called torque motors or torque actuators, are electromechanical devices that develop torque with limited-angular travel. Linear actuators are force motors that develop force with limited linear travel. Both linear and rotary actuators are aimed at developing high force density over the limited movement of the armature. For rotary actuators, a PM armature with multipole magnetization is sandwiched between two VR toothed stators for a high-density torque with a magnetic gearing effect. Both the inner and outer armature surfaces effectively collaborate with two active stator surfaces, while the multipole magnetization develops torque that is equivalent to a multiplicity of separate force components in each rotary actuator section (one pair pole). The required angle of rotation determines the allowable number of pole pairs for rotary actuators. A corresponding linear actuator structure with multipole magnet magnetization and an adequate number of pole-pair sections in the stators can also have travel restrictions where limited travel imposes a number of pole pairs on a "transverse flux" linear actuator (Hennenberger and Bork 1997). These structures feature contactless actuation principles with bidirectional functions of magnetic springs as well as high torque and high force density. Some configurations provide a constant torque or force, which is independent of the angular or linear position for a certain current level. Some configurations can be devised with more than one degree of mechanical freedom and inherent position sensing features.

Based on the design structure, there are three types of rotary actuators:

1. Disk rotary actuators with a multipole axially magnetized disk magnet sandwiched between two VR homopolar stators
2. Claw pole rotary actuators with a multipole ring magnet and a claw pole stator homopolar stator
3. Cylindrical rotary actuators with a multipole radially oriented ring magnet with an inside and outside VR monopolar toothed structure

These rotary actuators are well suited for applications with high torque and demanding size requirements (Pawlak 1990, Weh et al. 1990). Such actuators are found in applications in passenger vehicles, computer peripherals, automatic payment machines, laser controls, and pressure and proportional valves, as described in Chapter 7.

---

## **1.2 Magnetic Materials and Technology**

The interaction of matter with an external magnetic field divides magnetic materials into three categories: diamagnets, paramagnets, and ferromagnets. The interaction is due to

the actions exerted by an external magnetic field on the matter's elementary magnetic moments, which are originated by the orbital and spin motion of the electrons. Whereas diamagnets do not respond to the presence of the external magnetic field, paramagnets are materials that weakly magnetize in the same verse as the magnetic field. Ferromagnets are materials that weakly magnetize themselves in opposite verse to the magnetic field.

Only 3 of the 116 elements of the periodic table are ferromagnetic at room temperature — Fe, Co, and Ni. The combination of these elements together or with others, although not magnetic, creates a wide range of materials. Depending on coercivity, there are two types of magnetic materials:

1. *Soft* magnetic materials — when coercivity is lower than 1000 At/m; they have the ability to amplify hundreds of thousands of times the external magnetic field.
2. *Hard* magnetic materials or PMs — when coercivity is higher than 1000 At/m; they have the ability to keep their magnetism permanently and to store in their volume hundreds of kilojoules per cubic meter of energy.

Ferromagnets are substances that can be induced to become magnetized in a magnetic field. Soft ferromagnetic materials become demagnetized spontaneously when removed from a magnetic field with a relatively small remanent magnetization. Hard ferromagnetic materials can retain their magnetism, making them useful in the production of PMs. A magnetized magnet contains a north and a south pole that develop a magnetic field. Similar magnetic poles repel and opposite magnetic poles attract. A magnetic field is a region in space where a magnetic force can be detected. The magnetic field is strongest at the poles of a magnet. Magnetic lines of force are a way of representing a magnetic field. By convention, magnetic lines of force point from north to south outside a magnet and from south to north inside a magnet. Magnetic lines of force form complete loops, which never cross.

### 1.2.1 Soft Magnetic Materials

Soft magnetic materials are mainly utilized in applications in which magnetic materials are needed to amplify the flux generated by an electrical current or by a PM. The principal characteristics of soft magnetic materials are remanence, coercivity, maximum and initial values of permeability, saturation value of flux density  $B$ , and coercive force  $H$  and  $J$ . Properties of different soft magnetic materials are shown in Table 1.1. Figure 1.1 presents a set of first-quadrant hysteresis loops called demagnetization curves (Allegheny 1961).

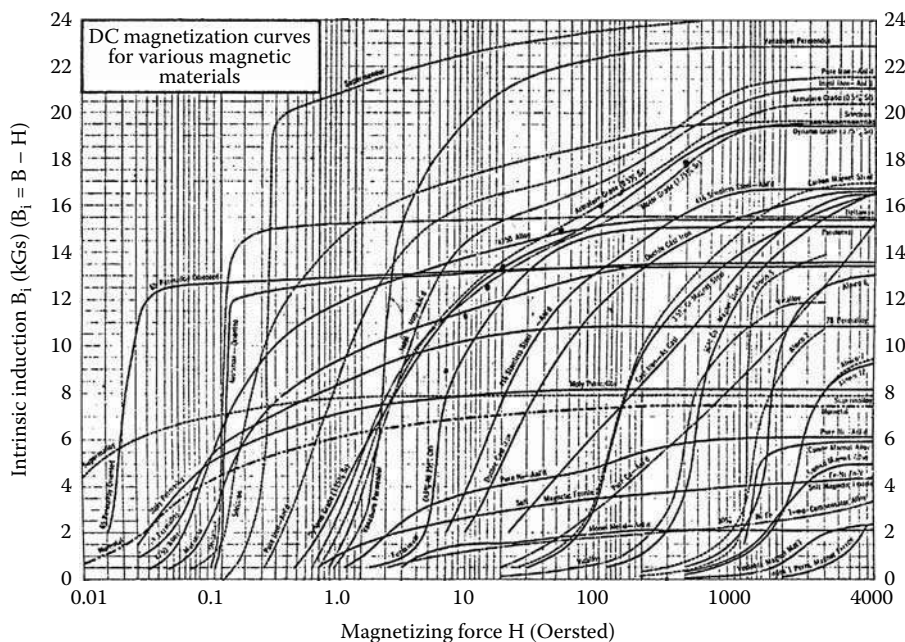
Soft iron is utilized in the form of solid bars, sheets, and, most recently, as a powder. Powder-metal soft magnetic materials also can be used in their sintered form. The development of these materials in the last decade has been spectacular due to advances in powder-metal technology. Sintered soft magnetic materials are most commonly used as pure iron, phosphorus iron, silicon-iron, and nickel-iron forms. They are applied in such devices as peripheral computer devices, printer actuators, brake assembly in disk drives, voice coil actuators, or VR sensors in the automotive industry. There are a number of technical and economic advantages for using sintered powder soft magnetic material:

- Wide range of materials available to designer
- Possibility of obtaining complex and varied shapes
- Process repeatability easily controlled by statistical methods
- Tolerance reliability
- Present magnetic characteristics close to fully dense materials

**TABLE 1.1**

Soft Magnetic Materials Performance Comparison

Material	Composition	$B_{\text{sat}}$ (T)	$H_c$ (A/m)	$\mu_{\text{max}}$ ( $\times 10^{-3}$ )
Pure iron	Fe (100%)	2.15	80	5
Fe-Si (nonoriented)	Fe (96%) Si (4%)	1.97	40	7
Fe-Si (grain-oriented)	Fe (97%) Si (3%)	2	8	40
Permalloy 78	Ni (78%) Fe (22%)	1.08	4	100
Supermalloy	Ni (79%) Fe (16%) Mo (5%)	0.79	0.16	1000
Mumetal	Ni (77%) Fe (16%) Mo (5%) Cr (2%)	0.65	4	100
Permendur	Fe (50%) Co (50%)	2.45	160	5
Soft ferrite	ZnFe <sub>2</sub> O <sub>3</sub>	0.3–0.5	10–100	1.0–10.0

**FIGURE 1.1**

Magnetization curves of various soft magnetic materials. (From Allegheny Ludlum Steel Corp., *Electrical Material Handbook*, 1st ed., Allegheny Ludlum Steel Corp., Pittsburgh, 1961. With permission.)

- Possibility of material composition unattainable by other technologies
- Near integral use of material with little or no machining
- Clean, safe, nonpolluting economic production process
- Flexible production process allowing for good applications of the just-in-time lean manufacturing methods

For the applications requiring maximum induction, cobalt-iron, phosphorus-iron, and pure iron powder metal are recommended. For dynamic applications demanding rapid magnetic flux change, such as relays or injectors, the phosphorus-iron and silicon-iron materials are recommended because of their high-electrical resistivity, which suppresses the eddy currents. For the applications where high magnetic induction must be achieved in a short period of time with a low excitation current, the nickel iron with maximum permeability is recommended. Ferrous stainless steel is recommended for an application, such as wheel speed sensors in automotives, where magnetic requirements are not extreme but corrosion resistance is required. In some cases, surface coatings on nonstainless materials with better magnetic characteristics may be used for corrosion protection, as described in Section 1.2.3. If the main design issue is cost, the recommended materials are pure iron and phosphorus-iron. Complex magnetic structures can be obtained using advanced powder-metal technologies. Using sintered and extrusion methods, a variety of combinations of soft, hard, and nonmagnetic powder structures can be achieved, reducing costs for simple and elegant solutions (Chatterjee et al. 2003, Pawlak et al. 1994a, Pawlak et al. 1991d).

Two categories of soft magnetic materials can be recognized based on the DC and AC applications. DC applications of soft magnetic materials require a low coercivity  $H_c$  and a high permeability  $\mu_{\max}$ . A low coercivity value is necessary to avoid remanence after the magnetic field is applied, when the power switches are off and a high value of permeability is needed to enhance the excitation field  $H$ . The most common DC applications are for electromagnets and yokes, relays, magnetic shields, electrical measuring devices, and magnetic amplifiers.

Typical materials used for DC applications are:

- Iron and low-carbon steels (maximum carbon 0.05%) — During the manufacturing operations of the device, it is necessary to avoid any mechanical deformations during the preparation of the magnetic material. Such deformation must be removed by annealing of the material in elevated temperatures typically between 750 and 900°C.
- Iron-nickel alloys (Permalloy) — Three categories of this alloy are common depending on the Ni content:
  - 36% Ni, which is a high-quality material, suitable for low-distortion transformers
  - 50% Ni, which has the maximum of  $J_{\text{sat}}$  of 1.6 T of Ni alloys and is used for tape-wound cores
  - 80% Ni, which has the higher permeability  $\mu_{\max}$  (up to 300,000)
- Iron-cobalt alloys (Permandur) — Cobalt is the only element that, when alloyed with iron, increases the saturation magnetization (maximum value of 2.45 T for the 50% Fe and 50% Co). The high cost of cobalt limits this application in armatures and relay cores.

AC applications of soft magnetic materials require a low coercivity  $H_c$  and a low power loss, a high permeability  $\mu_{\max}$ , and a high saturation magnetization. In AC applications, the polarity of material changes; therefore, it is important to apply a material with very thin hysteresis loops to minimize losses, with high saturation and low coercivity  $H_c$ . Typical AC applications include transformers, motors, and generators, as well as signal transmitters and receivers.

Typical materials used for AC applications are:

- Iron-silicon alloys — Iron-containing silicon has increased electrical resistivity to reduce eddy currents. A silicon content of 3% quadruples pure iron electrical resistivity. Producing grain-oriented silicon-iron increases the permeability value in the magnetic flux direction. On the other hand, the introduction of silicon in iron reduces the saturation magnetization and increases brittleness. This limits the maximum level of silicon to 4%. Finished fabricated parts must be heat treated to achieve soft magnetic characteristics. Carpenter steel is annealed at various temperatures and atmospheres. One should follow the manufacturer's instructions because the annealing temperature varies from 725°C to 1075°C. With the temperature rise, the maximum permeability of carpenter steel increases and  $H_c$  decreases for a given heat treatment (time and atmosphere). Also, the atmospheres can vary, including nitrogen-hydrogen, vacuum, and dry and wet hydrogen.
- Iron-nickel alloys (Permalloy) can be used for both DC and AC applications.
- Soft ferrites — The conductivity of metal alloys limits their utilization in frequency applications. For high-frequency applications of 1 kHz to 10 MHz Ni-Zn ferrites are utilized. Hexagonal ferrites are utilized for applications beyond 100 MHz.

### 1.2.2 Hard Magnetic Materials

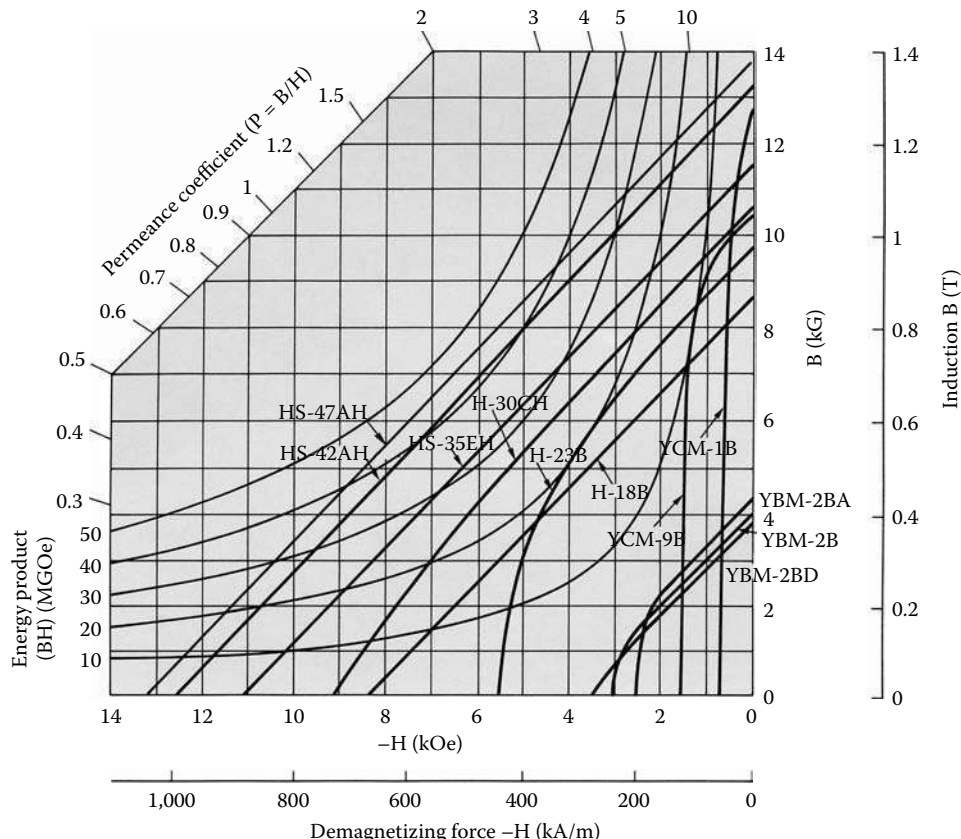
Hard magnetic materials are used as generators of the magnetic field. Hard magnetic materials have both high residual induction and high coercivity. The magnet quality depends not only on remanence  $B_r$ , coercive force  $H_c$ , and the maximum energy product  $BH_{max}$ , but also on its temperature dependence, corrosion resistance, resistivity, brittleness, and cost. Hard magnetic materials include ferrite ceramic magnets, alnico alloys, rare-earth magnets, deformation process magnets, and a bonded magnet category (Coey 1999). The properties of different hard magnetic materials, including magnetic and temperature performance of different families of hard magnet materials, are shown in Table 1.2. Figure 1.2 shows a set of demagnetization curves for different magnet materials coded by the manufacturer (Hitachi 1999): YBM ferrites, YCM alnico magnets, H-samarium-cobalt magnets, and HS-neodymium magnets. The energy product curves identify the maximum energy value for magnet materials from 10.0 to 50.0 MGOe.

Ceramic, also known as ferrite, magnets have been commercialized since the 1950s and continue to be the most widely used magnets today due to their low cost. Ferrites are produced by powder metallurgy, in the form of aggregation of single domain particles (about 1 μm) of barium ferrite  $\text{BaO} \cdot 6\text{Fe}_2\text{O}_3$  or strontium ferrite  $\text{SrO} \cdot 6\text{Fe}_2\text{O}_3$  (Iwasa et al.

**TABLE 1.2**

Magnet Performance Comparison

Material	$B_r$ (T)	$H_c$ (kA/m)	$BH_{max}$ (kJ/m <sup>3</sup> )	$H_{sat}$ (kA/m)	$B_r$ (%/°C)	$H_c$ (%/°C)	$T_{Curie}$ (°C)
Alnico	0.5–1.3	50–120	15–40	300	-0.02	0.02	900
Ferrite	0.4	150–300	25–30	800	-0.2	0.4	450
Bonded ferrite	0.2	50–200	7	800	-0.2	0.4	
NdFeB	1.1–1.2	1000–2000	250	2500	-0.1	-0.5	310
Bonded NdFeB	0.5–0.7	1000	70	2500	-0.08	-0.4	
$\text{SmCo}_5$	0.8–1.0	1500–2500	180	2000	-0.04	-0.04	700
$\text{Sm}_2\text{Co}_{17}$	1.0–1.1	2000	200	3500	-0.03	-0.03	800

**FIGURE 1.2**

Demagnetization curves for different PM materials. (From Hitachi Metals Ltd., Hitachi Rare-Earth Magnets, 1999. With permission.)

1981). Depending on the process, the final product could be isotropic (independent of direction) or anisotropic (having a preferred direction of magnetization). They are well suited for more corrosive environments and provide very good electrical insulation with good resistance to demagnetization. They come in blocks, disks, rings, and segments, as well as custom geometries.

Alnico magnets (general composition Al-Ni-Co) were commercialized in the 1930s and are still used extensively today. These materials span a range of properties that accommodate a wide variety of application requirements. Because alnico alloys can be cast or sintered, a variety of irregular shapes are available. They include horseshoe, pot magnets, button magnets, rotors, and chain castings. Alnico alloys exhibit high induction values, very good resistance to corrosion, excellent electrical conduction, and stability in high temperatures. The main disadvantages of these alloys are the hardness, brittleness, and ease of demagnetization.

Bonded magnets are ferrite or NdFeB magnet powder mixed with epoxy resin using techniques such as cord rolling, injection molding, or extrusion. Bonded magnets have lower magnetic properties, but they can be formed in complex shapes with the best mechanical tolerances. In recent years, there have been great improvements in the cost and performance of bonded magnets. Injection molded isotropic bonded magnets range between 5.0 and 7.0 MGoe, and injection molded anisotropic magnets range between 8.0 and 12.0 MGoe and up to 15.0 MGoe with the application of hydrogenation-

disproportionation-desorption-recombination (HDDR) of the NdFeB powder processed route (Gasiorek 1999, Tupper 1999). High-temperature polyamide NdFeB injection molding material can withstand a long-term (3000 hours) high temperature of 150°C. Compression isotropic bonded magnet energy ranges between 8.0 and 11.0 MGOe and compression molded anisotropic bonded magnet energy ranges between 16.5 and 18.3 MGOe and up to 22.0 MGOe with the application of NdFeB HDDR powder. Bonded magnets satisfy requirements in some areas where sintered magnets are not feasible. Because of this as well as their low cost and unique features, they are finding more industrial applications. Their features include:

- Precise shape and tight dimensional tolerances
- Flexibility in a wide range of magnetic property requirements
- Wide variety of shapes and sizes
- Complex shape and thin wall
- Low number of surface imperfections, such as chips, cracks, porosity, voids, and roughness
- Minimum material waste during manufacturing process
- Possible use as structural components in highly integrated structures
- Multipole orientation in anisotropic materials for improved performance over traditional orientation
- Ideal choice for ease of assembly — molding onto the flux carrier and molding onto a shaft

Neodymium-iron-boron and samarium-cobalt magnets are known as rare-earth magnets because they are both composed of materials from the rare-earth group of elements. The general composition of neodymium-iron-boron is  $\text{Nd}_2\text{Fe}_{14}\text{B}$ . Often abbreviated to NdFeB, neodymium-iron-boron magnets are the most recent addition to the family of modern magnet materials developed simultaneously at the General Motors Research Labs and the Sumitomo Corporation in the 1980s (Croat 1985). At room temperature, NdFeB magnets feature the highest properties of all magnet materials. Samarium-cobalt magnets are manufactured in two compositions —  $\text{Sm}_1\text{Co}_5$  and  $\text{Sm}_2\text{Co}_{17}$ . The compositions are often referred to as the SmCo 1:5 and SmCo 2:17 types.  $\text{Sm}_2\text{Co}_{17}$  magnets, with higher  $H_{ci}$  values, offer greater inherent stability than the  $\text{Sm}_1\text{Co}_5$  magnets. The rare-earth magnet manufacturing process, based on a sintering operation for any magnet shape including ring magnets, is shown in Figure 1.3 (Daido 2003, Gieras and Wing 1994, Glinka et al. 2005, Hitachi 1999, Shimizu and Hirai 1990). Another technique that was applied to ring magnets is the extrusion process as shown in Figure 1.3 (Kasai 1992). Please note that the elongation of neodymium particles allows for magnetization in the direction perpendicular to elongation. Because this method provides an unutilized material at the bottom of an extrusion that has to be removed, it may be more costly in comparison with the sintered method.

This current evolution of technology in NdFeB magnets is coming from innovations in rapid solidification. New rapidly solidified alloys have been developed for sintered magnets. Because of these advancements, the existing NdFeB magnet composition is only several percent shy of its theoretical energy product limit of 64.0 MGOe. Sumitomo has reported new NdFeB magnets with an energy product record of 55.8 MGOe for Neomax 50 (Matsuura 1999).

However, some predictions indicate a magnet performance of 100.0 MGOe for composite alloys, consisting of a high magnetization component (e.g.,  $\text{Fe}_3\text{B}$  or  $\mu\text{Fe}$ ) and one having large anisotropy (e.g.,  $\text{Nd}_2\text{Fe}_{14}\text{B}$ ). The new rare-earth SmFeN magnets discovered in 1990

are now commercially available. They are suitable for anisotropic bonded magnets, particularly for applications requiring better temperature stability than NdFeB, and also have potential as a second source for the fast-growing isotropic bonded magnets industry. Hybrid grades of SmFeN in combination with ferrites offer an economical solution when the properties of bonded ferrites are not satisfactory. This material requires quite a different fabrication process than other rare-earth magnets with the essential step being a gas-solid reaction at about 400°C to produce the interstitially modified  $\text{Sm}_2\text{Fe}_{17}\text{N}_3$  intermetallic compound. Current value of  $(BH)_{max}$  for zinc-coated powder with 10% Co substitution is 46.0 MGOe; anisotropic polymer-bonded magnets offer 22.0 MGOe (Rashidi 1999).

Magnetic nanocomposites have shown very interesting novel magnetic properties such as giant magnetoresistive and exchange-spring magnet behavior. To achieve optimized unit magnetic properties with the later family of magnetic alloys, the control of structural parameters, such as grain size, distribution of precipitated crystal in alloys, and conditions for microalloying, are extremely important. Although the use of thin film deposition techniques (sputtering, laser ablation) are much better suited to achieving better results, standard bulk processing techniques normally used for the production of nanostructure material may not be sufficient to obtain satisfactory results. Improvement of thermal stability, reduction of material cost, advancements in injection molding technology, increasing bulk density of the material, and enhancing anisotropy of these materials are challenges that lie ahead for magnet researchers.

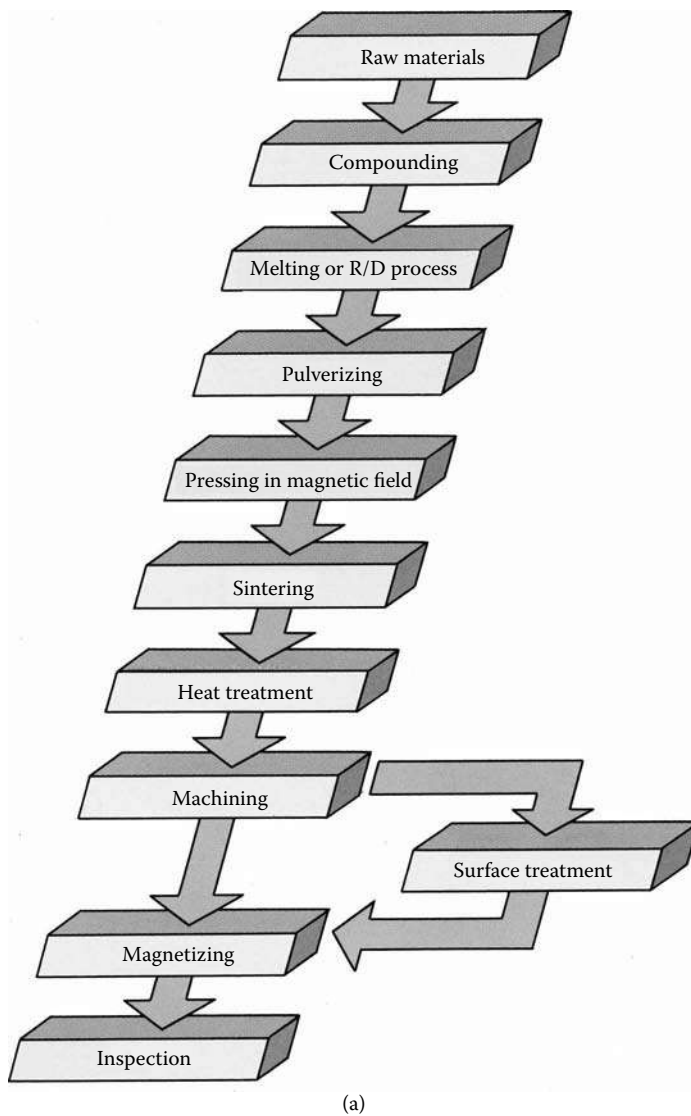
### 1.2.3 Coating Technologies

Corrosion continues to represent a challenging issue for magnet manufacturers because of the wide range of applications in severe environments (Mills 1999). Coating materials evolved by process improvements and are affected by the U.S. government's removal of certain chemical products from the market for environmental reasons. Coatings for sintered and bonded magnets include nickel plating organic electrocoating, spray coatings, and multiple layers of combination coatings for tough performance requirements.

Some companies developed an improved coating process where magnetic particles are encapsulated with organic coatings. Some companies developed an even more advanced coating process with precise functional characteristics by applying thin multiple coatings over individual powder particles. The layers are conformal, following the irregular contours of the magnetic powder particles. Each particle of the press-ready powder is 100% encapsulated. Benefits of this process include:

- Corrosion protection before, during, and after magnet manufacturing
- Extremely uniform metal distribution with reduced geometric or dimensional scattering
- Higher magnetic properties of the manufactured magnet
- Minimized magnetic temperature degradation associated with high-shear compounding of high-temperature injection molding operations
- Better flow characteristics — higher compaction, higher density / lower pressures, smaller cross sections, increased production rates

This coating process, therefore, allows for reducing magnet manufacturing costs by eliminating expensive compounding and blending costs, increasing production throughput, reducing rejects, and eliminating the need for secondary coatings in some applications.

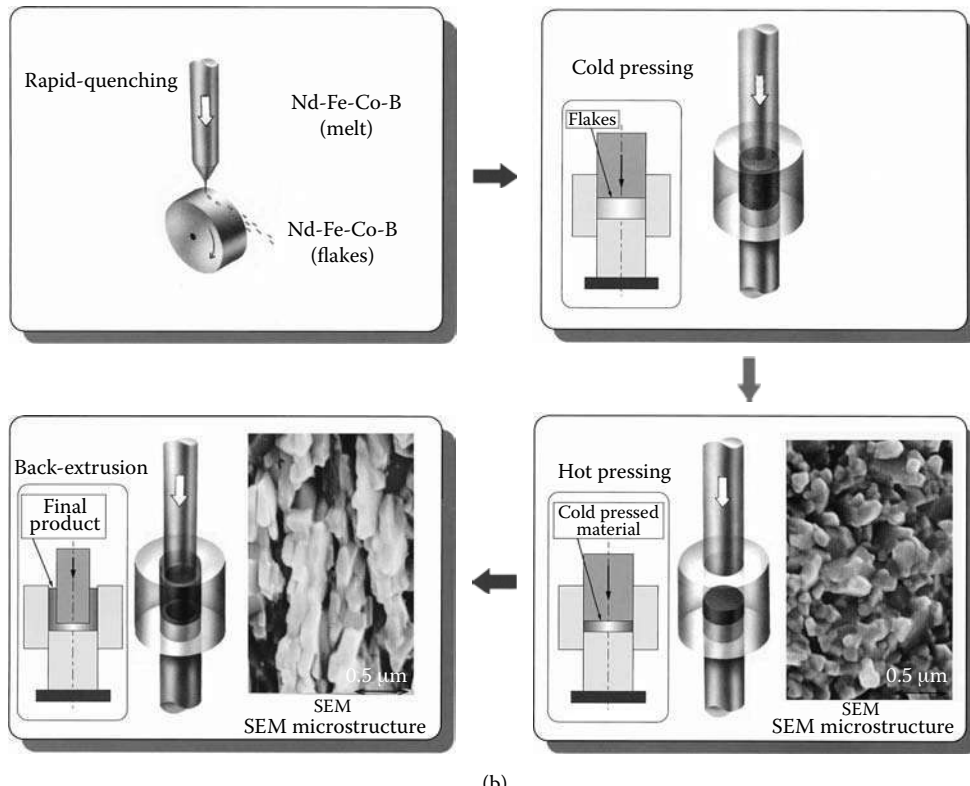
**FIGURE 1.3**

Rare-earth magnet manufacturing process: (a) sintered-based. (From Hitachi Metals Ltd., Hitachi Rare-Earth Magnets, 1999. With permission.)

#### 1.2.4 Magnetic Materials Market and Applications

Magnets serve as essential components in almost all domestic and industrial applications in the automotive, instrumentation, production machinery, aviation, marine, and space markets. Magnets are used in computers, electric motors, loudspeakers, smartcards, cell phones, tape recorders, cameras, camcorders, compact disk players, microwave ovens, kitchen robots, refrigerators, and washers and dryers, to name a few consumer products. Their contribution is often ignored because they are built into devices and are usually out of sight.

Magnets function as transducers and energy conversion devices, transforming energy from one form to another without any permanent loss of their energy. Energy conversion devices utilize PMs to convert mechanical-to-mechanical energy as attraction and repulsion

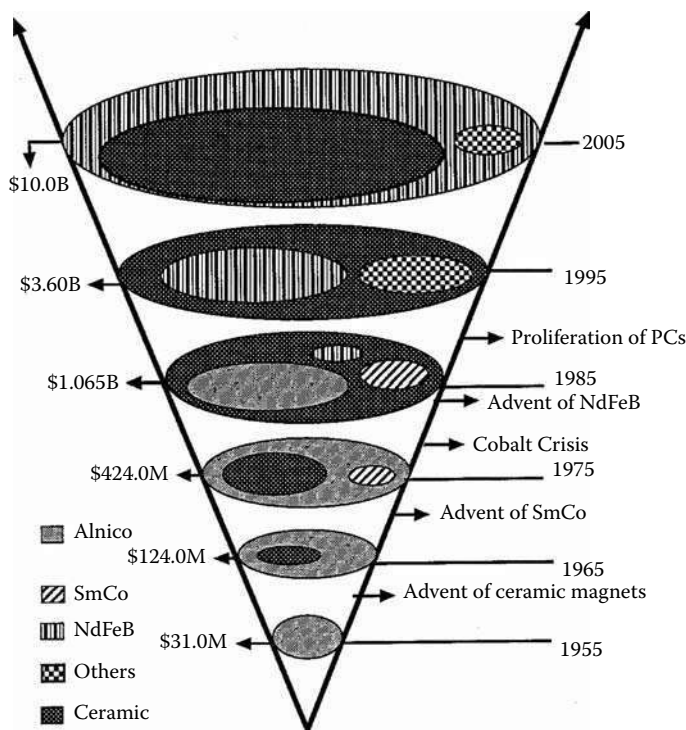
**FIGURE 1.3 (continued)**

Rare-earth magnet manufacturing process: (b) extrusion-based. (From Daido Electronics, Neoquench — DR, Radially Oriented Ring Magnets, 2003. With permission.)

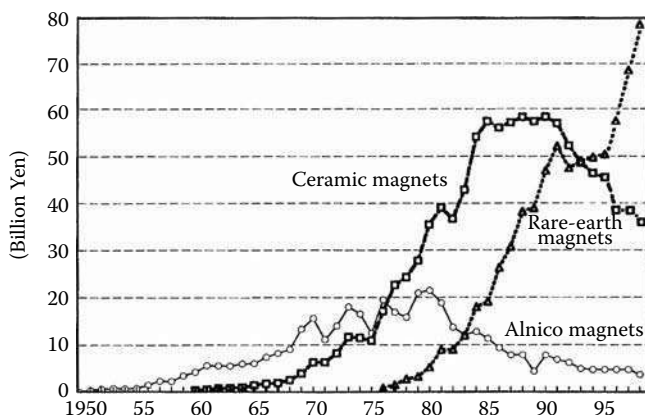
motion; mechanical-to-electrical energy as generators and microphones; electrical-to-mechanical energy as motors, loudspeakers, or charged particle deflection; mechanical energy to heat as eddy current and hysteresis torque devices and, as a special effect, devices for magnetic resonance. The development of hard magnetic materials has always advanced the development of novel electromagnetic devices (Macoit 1999, Pawlak 1995).

The PM business worldwide is now a \$10 billion industry, and it is predicted that this industry will grow at an annual average rate of 12% beyond the year 2005. Figure 1.4 shows the world PM usage coupled with milestones that changed the industry in the most profound ways and energy costs for all hard magnetic materials: ferrite ceramic magnets, alnico alloys, rare-earth samarium-cobalt and neodymium magnets and others, including the bonded magnet category (Rashidi 1999). The use of high-energy PMs made from alloys (neodymium, samarium, dysprosium, and terbium) and transition metals (cobalt and iron) have proliferated and replaced a large fraction of traditional families of PMs such as alnico and ferrites (Carsile 1986). This is because the use of rare-earth magnets in personal computers, mainframe computers, and other aspects of office automation, as well as penetration of smart devices into domestic goods, will continue at a much faster rate. It is also predicted that the second fastest growing sector of the rare-earth magnet market will be motors and actuators.

Japanese sales of PMs, as indicated in Figure 1.5, show strong rare-earth penetration in overall magnet production in Japan (Matsuura 1999). Both ceramic and alnico-based magnets show downturns but rare-earth magnets continue to show a strong increase in production, particularly in the last few years.

**FIGURE 1.4**

Growth of the PM market. (From Rashidi, S., NdFeB Opening Remarks, NdFeB '99 Conference, San Francisco, April 12–14, 1999, p. 3. With permission.)

**FIGURE 1.5**

Trend of PM production. (From Matsuura, Y., NEOMAX Update '99, NdFeB '99 Conference, San Francisco, April 12–14, 1999, p. 4. With permission.)

The overall manufacturing cost, the number of technical personnel who have been well trained and well educated at a low investment cost, and an abundance of rare-earth compounds have made China the largest manufacturer of PMs in terms of weight of production. China is known to have 60% of the world's reserve of rare-earth oxides and currently supplies about 85% of the world's rare-earth oxides' mining volume. It is

misleading to think that just the lower cost of labor has given China an edge in producing low-priced magnets. In actuality, it is a combination of low labor and overhead cost, therefore, low equipment cost as well as ready access to materials. Japan still has an edge on the total value of the magnets shipped globally. However, the Chinese cost of rare-earth powder metal used to produce equivalent quality magnets is less than half that of the Japanese.

Magnet manufacturers maintain that the following current trends in automotive system design should affect rare-earth magnet growth opportunities by increasing the penetration of electric motors in automobiles:

- Electronic control of motors — increase in integrated electronic controls for motors vs. centralized electronic control modules and growth of electronically controlled smart motors and smart systems
- Power-generation technologies — development of liquid-cooled alternators; fly-wheel-mounted, combined alternator and starter with active torque damping; and development of turbine alternator and generator strategy
- Motor technologies — development of powder-metal armature cores and hybrid PM or reluctance motors
- Minimizing parasitic engine losses — potential usage of electric-powered motors in place of hydraulics-driven and belt-driven systems, such as electric-powered oil and water pumps and electric-powered steering systems
- Worldwide supply considerations — greater market demand for “pancake” PM motors, miniaturized PM motors, and increased use of brushless PM motors
- Electrical system architecture — postponed, and perhaps still possible, introduction of 42/14 V dual system architecture, reduced cost of power electronics, growth of modularity and integrated subsystems
- Impact of modularity — modularity and large-scale system integration could result in pieces of motors assembled in modules for integrated functions

Cost, temperature, and manufacturing are the major barriers to the expanded use of neodymium magnets in automobiles:

- Cost barriers — neodymium not yet considered a ceramic replacement because of cost, system integration has potential in savings to offset system cost
- Thermal barriers — under-hood temperatures affected by engine compartment complexity, effect of operation and location of other heat-generating subsystems, component self-heating, and difficulties with predicting operating temperatures accurately
- Manufacturing barriers — feasibility of high volume production, fragile aspect of neodymium material, magnetizing and calibrating assembly, and difficulty of repair or rework



# 2

---

## *Magnetic Sensors*

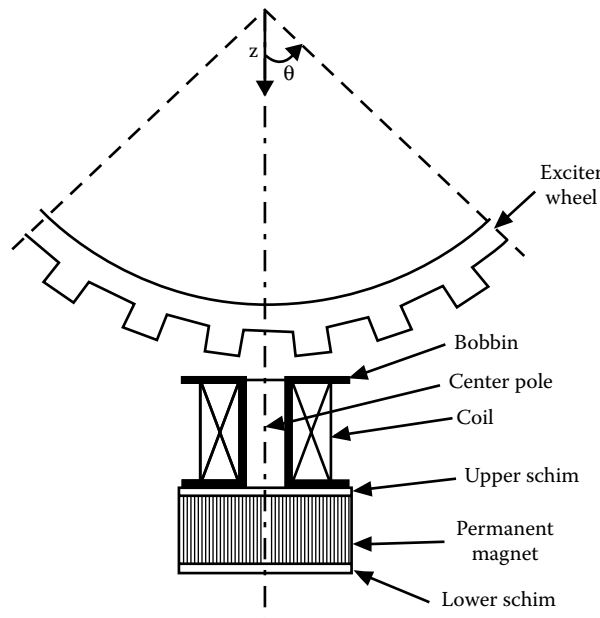
---

The market for magnetic velocity sensors is expanding rapidly, particularly in the automotive industry where they are used in a variety of mechatronic systems such as antiskid braking systems (ABS), traction control (TC), four-wheel drive systems, etc. However, as the number of applications grows, the specifications these sensors are expected to meet are becoming more and more demanding. Larger signals are required to improve signal-to-noise ratios and to relax manufacturing tolerances, thus lowering the cost. Despite the current interest in these sensors, the literature on the subject is insufficient and often limited to the description of a specific device (Foster 1988, Podeswa and Lachman 1989, Rowley and Stolfus 1990). Sometimes various technologies are compared (Ohshima and Akiyama 1989b), but because of the large number of possible approaches, the coverage of each concept remains overly general. In-depth analyses backed by theoretical frameworks are lacking, with some exceptions (Lequesne et al. 1996, Pawlak et al. 1991d, Ramsden 2001). Such analyses would allow us to understand and assess the relative importance of various design elements to the overall performance and provide the means for design optimization. They would not only be desirable, but also timely, because the emergence of new materials and manufacturing technologies holds the promise for improved configurations. This chapter attempts to fill this gap by providing both the theoretical background as well as practical optimization examples based on a number of novel sensor configurations.

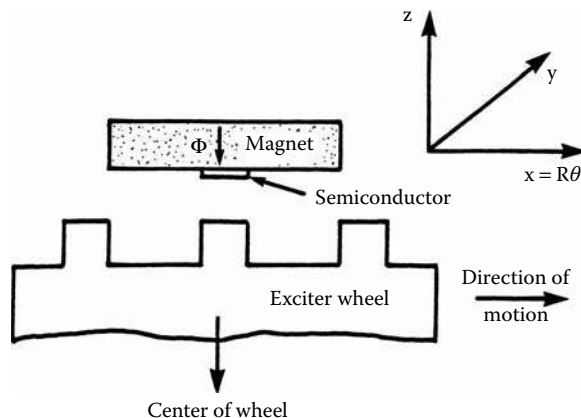
Two types of magnetic sensors based on these principles—VR sensors and galvanometric semiconductor (Hall-effect or MR) sensors—are described in this chapter. We show how recognizing this fundamental difference leads to markedly different sensor design approaches and describes modern configurations with improved performance. The analyses of magnetic sensors are based on a general theory specifically developed for these sensors. The magnetic computation uses two-dimensional (2D) and three-dimensional (3D) finite-element (FE) mathematical models, which are particularly well suited to problems involving complex magnetic configurations and the needs for the calculation of local flux densities and flux linkages. A variety of sensor examples are introduced to validate developed models and to confirm the efficiency improvements of the modern sensor structures.

The magnetic VR sensors feature a coil as a sensing device, a stationary PM operating in close vicinity of a rotary ferromagnetic wheel, sometimes called a target wheel or an exciter wheel. The outer surface of the wheel features a succession of teeth and slots which vary the magnetic permeance as the wheel rotates. This affects the magnetic flux pattern and the corresponding flux variations are sensed either by a pickup coil in the case of the VR sensor, shown conceptually in Figure 2.1, or by a galvanomagnetic semiconductor such as a Hall-effect or MR sensor, as presented in Figure 2.2. These two sensor types will be referred to as “VR sensor” and “solid-state sensor,” respectively.

PM wheels are also used instead of ferromagnetic wheels (Ohshima and Akiyama 1989a, Podeswa and Lachman 1989, Saito et al. 1988), with a solid-state device sensing the alternation of north and south poles on the magnet surface. However, these sensors can

**FIGURE 2.1**

VR sensor components. (From Lequesne, B. et al., *Transactions of IEEE/IAS*, 32(5), 1166–1175, 1996. With permission.)

**FIGURE 2.2**

Magnetic speed sensor with a semiconductor. (From Lequesne, B. et al., *Transactions of IEEE/IAS*, 32(5), 1166–1175, 1996. With permission.)

be used only in more protected environments and, because of magnet costs, the magnet wheel must be small. Their applications are, therefore, more limited and, for this reason, they were not included in this study. High-resolution sensors, such as resolvers (Ohshima and Akiyama 1989b, Podeswa and Lachman 1989) or “absolute” magnetic encoders, which rely on Permalloy-based magnetoresistors reading dense magnetic patterns (Miyashita et al. 1987, Pawlak et al. 1996, Schroeder et al. 1996), are much more expensive. They are designed differently and are beyond the scope of this chapter.

## 2.1 Theory of Magnetic Sensors

We first present a general theory of VR and solid-state sensors, which underscores both the similarities and differences between the two concepts. The theory is then applied to the specifics of each case. New configurations that make use of new materials and manufacturing technologies are presented. The analysis shows how the new designs can be optimized for given applications. Both the modeling approach and the superiority of the new designs are proven experimentally.

The magnetic sensors studied in this chapter depend on a stationary magnet as a source of magnetic flux and on the modulation of that flux by the movement of the exciter wheel. As the wheel rotates, the teeth, the slots, and the magnet assume various positions that can be characterized by the angular distance  $\theta$  between some arbitrary location on the wheel and some other arbitrary location on the stationary magnet. The wheel rotation results in magnetic permeance variations, which can be expressed as a function  $P(\theta)$ .

The permeance  $P(\theta)$ , shown in Figure 2.3, is a periodic function with a period  $T$  equal to the tooth pitch. Its maximum and minimum values,  $P_{\max}$  and  $P_{\min}$ , correspond to magnet locations across a wheel tooth or a wheel slot, respectively. The permeance variations affect the operating point of the PM and result in flux variations that are also periodic functions with a period  $T$ .

On the surface of the sensor facing the wheel, one can define an active area  $A$ , which corresponds to the cross section of the magnetic core in the VR-sensor case (the “center pole” in Figure 2.1) or to the area of the semiconductor in the solid-state sensor case (Figure 2.2). In principle, the flux density at any point  $\sigma$  on  $A$  is a function not only of the sensor position  $\theta$ , but also of the location of  $\sigma$  on  $A$ . However, variations over  $A$  are neglected in this section in order to obtain simplified formulae amenable to physical interpretation. Thus, a flux-density function  $B(\theta)$ , uniform over  $A$ , can be defined that corresponds to the permeance variations mentioned earlier.  $B(\theta)$ , like  $P(\theta)$ , is periodic with a period  $T$  equal to the tooth pitch and features maximum and minimum values,  $B_{\max}$  and  $B_{\min}$ , across the centers of the wheel teeth and slots, respectively.

The analysis is, therefore, based on the assumption of a uniform air gap flux-density function  $B(\theta)$  over the active area  $A$ , which is commonly done in electric machine theory. Usually, this assumption leads only to neglecting harmonics. VR sensors are different,

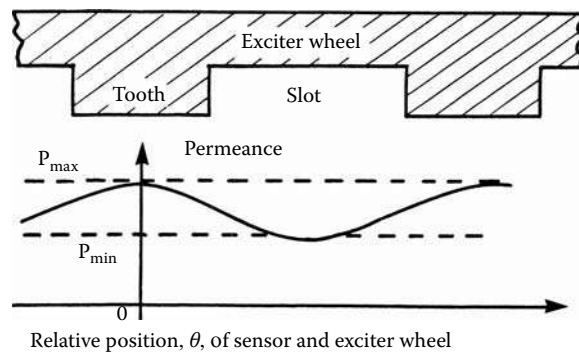


**FIGURE 2.3**

Exciter wheel permeance variation. (From Lequesne, B. et al., *Transactions of IEEE/IAS*, 32(5), 1166–1175, 1996. With permission.)

however, in that the useful part of their output signal is the peak-to-peak voltage and harmonics may contribute to it. More comprehensive formulae, presented in Section 2.2, are therefore needed to calculate the output signal of an actual VR sensor. They are based on flux-linkage variations for the two extreme sensor or target positions.

---

## 2.2 Magnetic Sensor Analysis

The analysis of VR and solid-state sensors presented in this chapter compares both the similarities and differences between the two concepts. For VR sensors, the sensor signal is the voltage  $e(t)$  generated in the coil by the time variation of the total flux linkage  $\psi$ , given by:

$$e(t) = -\frac{d\Psi}{dt} = -\frac{d}{dt} \left[ \sum_{i=1}^N \phi_i \right] \quad (2.1)$$

where  $e$  is the voltage generated in the coil,  $N$  is the number of turns of the coil,  $\psi$  is the total flux linkage, and  $\phi_i$  is the flux linkage in any of the  $N$  turns of the coil.

The flux linkages  $\phi_i$  are the sums of the flux crossing the air gap and linking to the coil. Because VR sensors are often designed with very large air gaps in order to lower construction costs, leakage may be very large. The leakage flux varies with wheel position; therefore, its time derivative is not zero and it contributes to the useful signal as presented in Equation 2.1. However, for simplicity, these variations are neglected in this section, but they will be included in the more comprehensive expressions given in Section 2.3. Neglecting the leakage allows us to equate each flux linkage  $\phi_i$  with a uniform flux  $\Phi$  in the magnetic core:

$$\phi_i = \Phi = \int_A B(\sigma) d\sigma \quad (2.2)$$

where  $B$  is the magnetic field density,  $\sigma$  is the location of any point on active sensor surface area,  $\Phi$  is uniform flux in the magnetic core, and  $A$  is the cross section of the active sensor surface core.

Assuming for simplicity a rectangular core of length  $L_y$  in the  $y$  direction (the  $y$  direction is defined in Figure 2.2),  $\Phi$  is:

$$\Phi = L_y \int_{\theta(t)}^{\theta(t)+\delta} B(\alpha) R_{ex} d\alpha \quad (2.3)$$

where  $\theta(t)$  is the location of the trailing edge of the core at time  $t$ , dimension  $\delta$  is the core width in the direction  $\theta$ , and  $R_{ex}$  is the exciter wheel radius.

Combining Equation 2.1 through Equation 2.3 yields:

$$e(t) = -NL_y R_{ex} \frac{d}{dt} \int_{\theta(t)}^{\theta(t)+\delta} B(\alpha) d\alpha = -NL_y R_{ex} \frac{d\theta}{dt} \frac{d}{d\theta} \int_{\theta(t)}^{\theta(t)+\delta} B(\alpha) d\alpha \quad (2.4)$$

During steady-state operation, the wheel turns at a constant velocity  $\omega$ . Therefore:

$$e(t) = -NL_y R_{ex} \omega \frac{d}{d\theta} \int_{\theta(t)}^{\theta(t)+\delta} B(\alpha) d\alpha = -NL_y R_{ex} \omega [B(\theta + \delta) - B(\theta)] \quad (2.5)$$

The maximum signal attainable with a VR sensor is:

$$E = NL_y R_{ex} \omega (B_{\max} - B_{\min}) \quad (2.6)$$

where  $E$  is the maximum sensor signal,  $L_y$  is the rectangular core of length in the  $y$  direction,  $\omega$  is an angular speed,  $B_{\max}$  is the maximum flux density, and  $B_{\min}$  is the minimum flux density.

The maximum sensor signal  $E$  is reached if the core width  $\delta$  is such that the positions of the core edges correspond to the locations of  $B_{\max}$  and  $B_{\min}$ . In most cases, the maximum value of  $B$  is in the middle of the tooth, the minimum value is in the middle of the slot, and the distance between these two points is one half of a tooth pitch. Therefore, a magnetic core size of one half of a tooth pitch is desirable. The optimum value may differ from this value, however, because Equation 2.6 is based on two simplifying assumptions: a single function  $B(\theta)$  is assumed over the sensor active area  $A$  and leakage variations are neglected. In practice, considerations other than output-signal magnitude, such as sensor volume and cost, are also taken into account. It can also be seen from Equation 2.6 that the output signal does not depend on the shape of the function  $B(\theta)$ , but on its maximum and minimum values. Equation 2.6 also shows that the output signal is proportional to the velocity  $\omega$ . The signal, therefore, disappears at low velocity and is crucial to maximize the term  $(B_{\max} - B_{\min})$  to ensure that, overall, the signal  $E$  is larger than the expected noise at the lowest specified speed. However, the signal is very large at high speeds and an over-voltage circuit protection must be included to protect the electronic circuitry.

The performance of a specific magnetic velocity sensor design requires the computation of flux densities or flux linkages. However, calculating these quantities with precision is challenging because of the complex geometry of the sensor, particularly the air gap. Therefore, conventional closed-form solutions based on reluctance paths (Roters 1967) are difficult to implement. The approach in this study was based on the more computer-intense, but more accurate, FE method.

The FE programs that are most readily available at the moment are limited to solving in two spatial dimensions. However, sensor geometries typically vary in all three dimensions. This particular issue was addressed in Sabonnadiere et al. (1989), where several methods to model a VR sensor, 3D, 2D, and tests were presented. The 2D results were processed by performing a weighted sum of results in the  $xz$  and  $yz$  planes, a technique inspired by Roters (1967). Such a summation is possible because the low level of magnetization of the ferromagnetic parts makes an assumption of linearity realistic. The results indicate that 2D results are reliable if used carefully and checked against experiments.

A 2D FE model was, therefore, selected. The test results shown in this chapter confirm that this approach is reliable qualitatively, even when computations are performed only in the  $xz$  plane without the summations proposed in Sabonnadiere et al. (1989). However, some of the experimental results given in this chapter also show that quantitative accuracy may suffer from neglecting the third dimension. Therefore, the approach presented in Rabinow (1951) remains relevant when quantitative accuracy is the prime objective. The magnetic flux density is calculated at each point of the  $\theta z$  plane (the  $\theta$  angle is linked to the  $x$  axis by  $X = R\theta$ ) by solving:

$$\nabla \times (\nu \nabla \times \bar{A}) = \bar{J}_s \quad (2.7)$$

where  $\nu$  is the material reluctivity,  $\bar{A}$  is the magnetic vector potential, and  $\bar{J}_s$  is the current density in the coil.

To take full account of both flux leakage and variations of the flux-density function on the sensor surface, the following formula, derived from Equation 2.1, was used for the VR sensors:

$$e(t) = -\omega \frac{d\Psi}{d\theta} \quad (2.8)$$

which requires the calculation of the flux linkage in the coil for various wheel positions, performed as follows. In the  $\theta z$  plane, the  $z$  axis cuts the coil into two separate areas, as presented in Figure 2.1, on either side of the magnetic core. These two coil areas are denoted by the superscripts ' and ". Each area is subdivided into  $m$  subsections and the flux linkage is obtained by performing the following summation:

$$\Psi = \frac{1}{m} \sum_{i=1}^m \left( A(\theta_i'', z_i'') - A(\theta_i', z_i') \right) \quad (2.9)$$

where  $A$  is the  $y$  component of the magnetic vector potential at the location  $(\theta_i', z_i')$  or  $(\theta_i'', z_i'')$  of the  $i$ th coil subsection and  $m$  is the number of subdivisions in the coil region.

In the  $xy$  plane, the  $y$  axis cuts the coil into two separate areas as presented in Figure 2.4, on the other side of the magnetic core. These two coil areas are denoted by the superscripts ' and ". Each area is subdivided into  $m$  subsections and the flux linkage is obtained by performing the following summation:

$$\Psi = \frac{N}{m} \sum_{k=1}^m \left( \Phi_k(x'', y'') - \Phi_k(x', y') \right) \quad (2.10)$$

where  $\psi$  is flux linkage,  $N$  is the number of turns of the coil,  $\Phi_k(x'', y'')$  is the  $k$ th magnetic vector potential of the one coil side, and  $\Phi_k(x', y')$  is the  $k$ th magnetic vector potential of the other coil side.  $L_1$  and  $L_2$  correspond to  $y'$  and  $y''$ , respectively, and  $K_1$  and  $K_2$  correspond to  $x'$  and  $x''$  at Equation 2.10 and Figure 2.4, respectively.

## 2.3 VR Sensors

VR sensors are well known for their low cost and reliability. These sensors are self-excited and, unlike solid-state sensors, they require no external voltage or current source. Conventional VR-sensor configurations, shown in Figure 2.1 and in Pawlak et al. (1991d), are, however, unable to develop high signal strength at low target-wheel speeds or with a large air gap between the sensor and the target wheel. They require a relatively large volume to accommodate a coil with a large number of turns and a large PM to develop

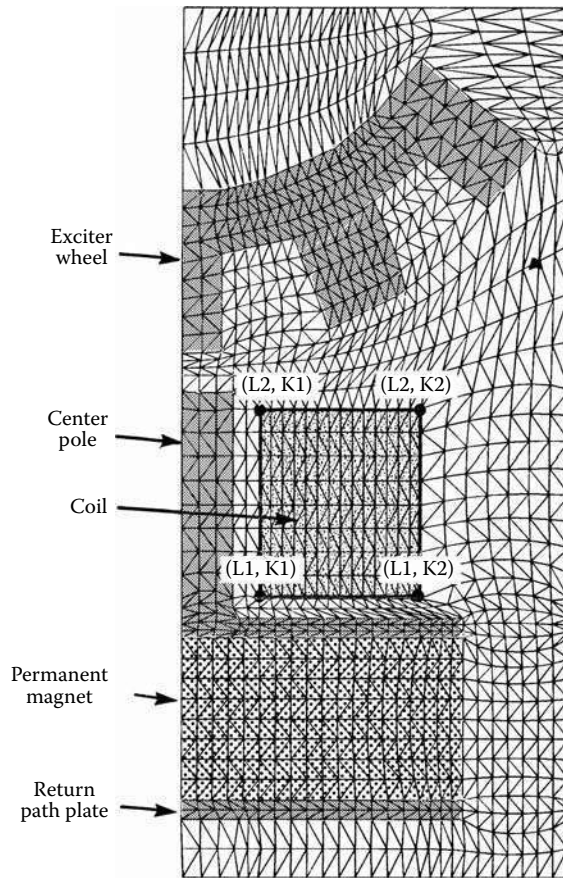


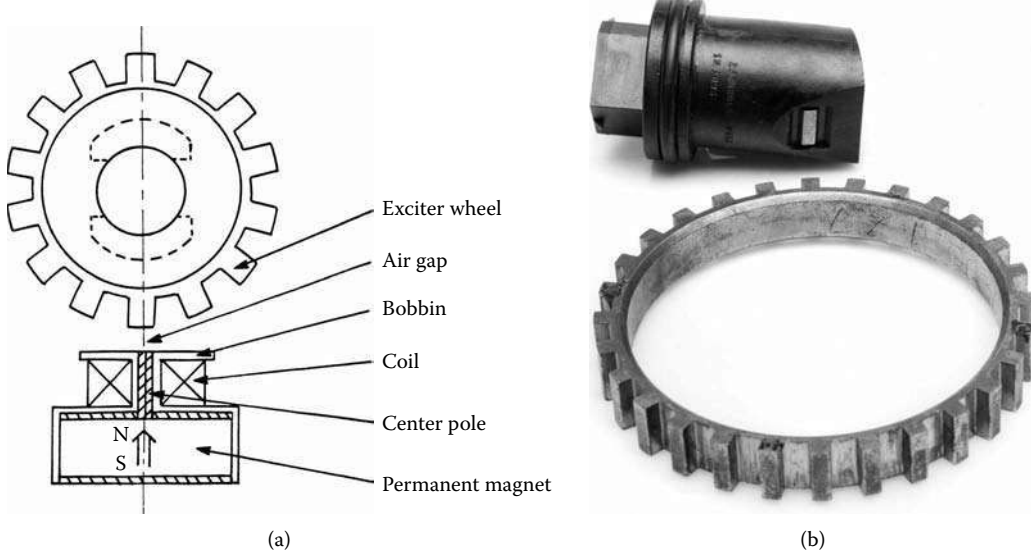
**FIGURE 2.4**  
Sensor geometry for the FE analysis. (Courtesy of Delphi Corp.)

the required signal strength. Because the coil is large, the magnet is usually located far from the target wheel and only a small percentage of the magnet flux, as low as 5%, contributes to the signal, resulting in low signal strength. Modern VR sensor configurations offer better utilization of the flux developed by the magnet; therefore, this chapter will focus on the ways of using VR sensor improvements to reduce their volume and improve their sensitivity. It is worthwhile to improve VR sensor deficiencies because of the advantages they offer. Because of their superior reliability, low cost, and simplicity, they will always find industrial applications, especially in harsh environments.

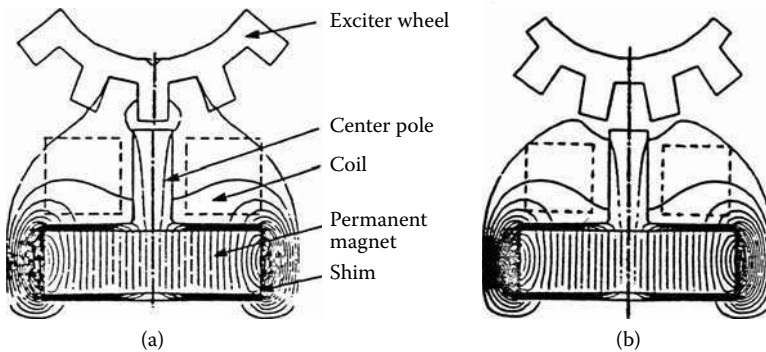
### 2.3.1 Conventional VR Sensors

A conventional VR speed sensor consists of a magnetic circuit, a coil, and a PM, which is located far from the exciter wheel, as shown in Figure 2.5. Conventional VR sensors feature no iron path, as shown in Figure 2.5(a). This is perceived to make the design simpler, more universal, and less expensive, but the flux is not properly guided because there is no main magnetic path. Generally, less than 5% of the magnetic flux contributes to the signal, which then relies almost entirely on the leakage flux.

Traditionally, these sensors have had a large volume to accommodate the large number of turns and a big PM necessary to develop the required signal strength. This is because

**FIGURE 2.5**

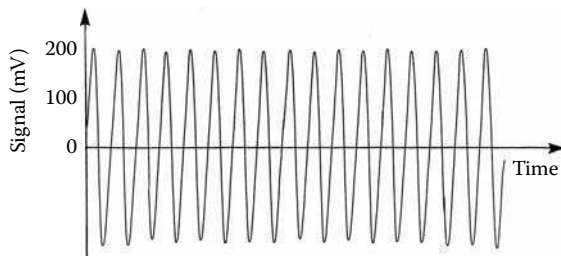
Conventional VR sensor configuration and manual transmission speed sensor example: (a) VR sensor components, (b) manual transmission speed sensor. ([a] From Pawlak, A.M. et al., *Novel Variable Reluctance Sensors*, Publ. No. 910902, Society of Automotive Engineers, Detroit, MI, 1991. With permission; [b] courtesy of Delphi Corp.)

**FIGURE 2.6**

Conventional VR sensor flux lines for two arrangements with exciter wheel for (a) maximum flux linkage and (b) minimum flux linkage. ([a] From Pawlak, A.M. et al., *Novel Variable Reluctance Sensors*, Publ. No. 910902, Society of Automotive Engineers, Detroit, MI, 1991. With permission; [b] from Lequesne, B. et al., *Transactions of IEEE/IAS*, 32(5), 1166–1175, 1996. With permission.)

of their low efficiency, since only a small percentage of the PM flux contributes to the signal development. A conventional sensor-wheel arrangement utilizes the modulation of magnetic flux by the movement of the exciter wheel, which occurs predominantly in the  $xy$  plane, as presented in Figure 2.6 for two different VR sensor arrangements with the exciter wheel. As the wheel rotates, the teeth, the slots, and the magnet assume various positions. The wheel rotation results in magnetic permeance variation, which is a periodic function with a period equal to the tooth pitch. Its maximum and minimum values correspond to maximum and minimum flux linkages in an  $xy$  plane, as presented in Figure 2.3.

By rotating an exciter wheel associated with the speed sensor, the permeance of the magnetic speed sensor changes, and this affects the magnetic flux linked to the coil. The

**FIGURE 2.7**

Sensor signal vs. time. (Courtesy of Delphi Corp.)

highest permeance occurs in the sensor-tooth position and the lowest permeance occurs in the sensor-slot position. The coil flux linkage changes due to permeance variation. The voltage signal induced by the coil (for speed or position sensor signal) is proportional to the number of coil turns, the rate of the flux-linkage change with respect to the time (Equation 2.8), as shown in Figure 2.7.

To evaluate the sensor structures, two figures of merit are defined. The first figure of merit is the sensor signal sensitivity  $s_v$  based on the signal  $v_s$  over volume  $V_s$  ratio indicating sensor electromagnetic efficiency of the investigated configuration:

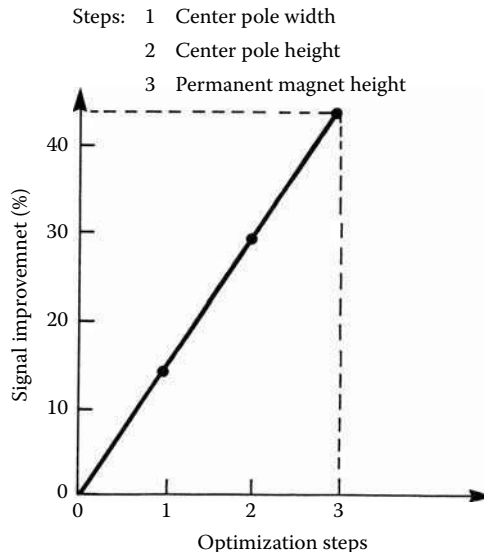
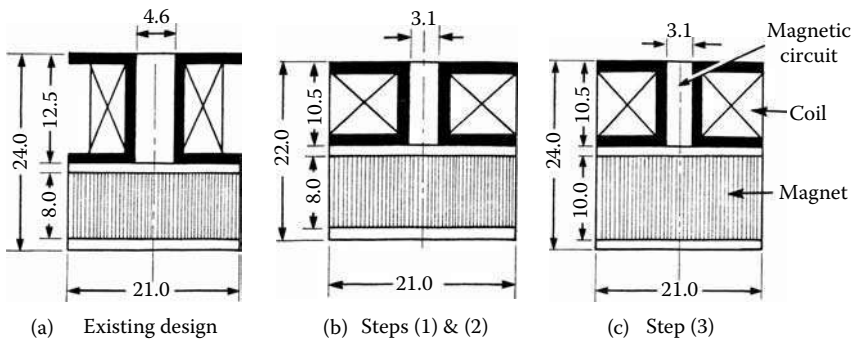
$$s_v = \frac{v_s}{V_s} \quad (2.11)$$

where  $s_v$  is the sensor signal sensitivity,  $v_s$  is the sensor signal, and  $V_s$  is the sensor volume. Sensor signal value is a measure of the sensor performance. If coupled with the sensor volume, it can be used as a figure of merit to evaluate and to compare sensor effectiveness. Quite often, requirements and, in particular, the available space envelope and exciter wheel geometry, lead to sensor configuration selection. The second figure of merit is the sensor flux sensitivity  $s_\phi$  indicating how much the total PM flux contributes to the signal generation:

$$s_\phi = \frac{\Delta\phi}{\phi_o} \quad (2.12)$$

where  $s_\phi$  is the sensor flux sensitivity,  $\Delta\phi = \phi_{\max} - \phi_{\min}$  is the flux-linkage change defined as the difference between the magnet flux linked to the coil for the maximum permeance position and the magnet flux linked to the coil at the minimum permeance position, and  $\phi_o$  is the total flux developed by the PM. The sensitivity  $s_\phi$  indicates the electromagnetic efficiency of the investigated sensor configuration and maximizing its value would help achieve a magnetically efficient and highly sensitive VR sensor design. For the best design, all parasitic air gaps in the magnetic circuit should be eliminated or minimized and all available coil envelopes should be used for the coil including full utilization of the magnetic flux developed by the PM.

Utilizing effectively FE math models and an iterative design approach, the conventional sensor structure can be optimized for the best signal volume. Optimization steps must be performed at two extreme sensor-wheel positions, as presented in Figure 2.6. Figure 2.8 shows three conventional sensor geometries side by side before and after optimization with 43% signal improvement, with 40% noise reduction and cost savings for this manual transmission speed sensor, as shown in Figure 2.5(b) and Table 2.1.

**FIGURE 2.8**

Conventional sensor signal improvement for three optimization steps: (a) original design, (b) intermediate improvement, (c) final design. (Courtesy of Delphi Corp.)

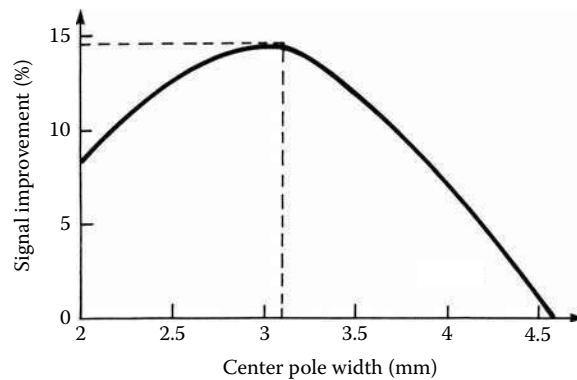
**TABLE 2.1**

Conventional VR Sensor Optimization Steps

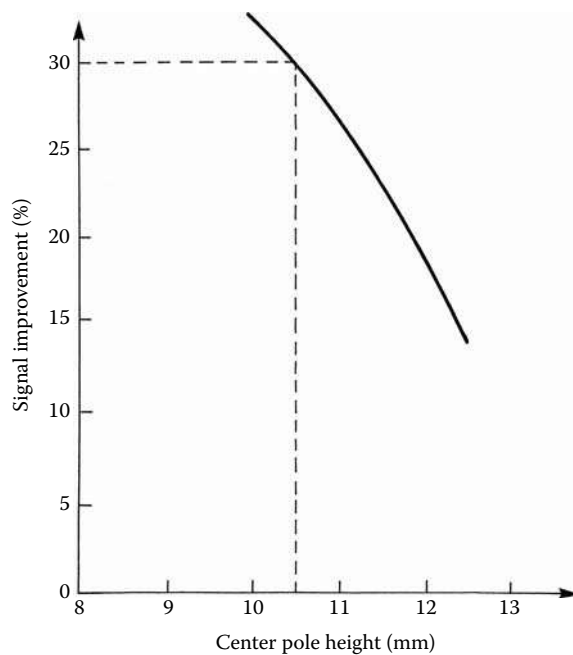
Sensor Geometry	Volume (cm <sup>3</sup> )	Signal (V)	Signal Sensitivity (V/cm <sup>3</sup> )
a — Original	3.96	0.364	0.092
b — Intermediate	3.63	0.473	0.13
c — Final	3.93	0.519	0.132

Source: Courtesy of Delphi Corp.

Intermediate sensor geometry includes both the center pole width and height optimization. The center pole width equal to the exciter wheel tooth width provides the highest signal value, as shown in Figure 2.5 and Figure 2.9, accounting for almost 15% of the sensor signal increase. Because space around the sensor coil was not fully utilized, the bobbin was shortened to accommodate the entire coil window with full utilization, and as a result, the sensor signal improved by another 15%, as shown in Figure 2.10.

**FIGURE 2.9**

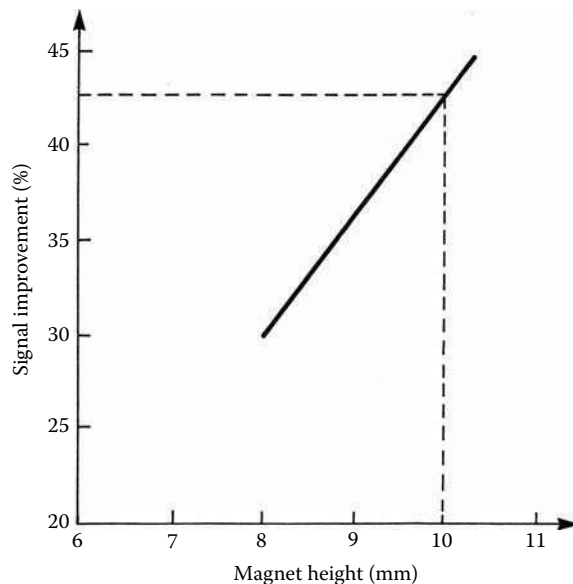
Signal vs. center pole width. (Courtesy of Delphi Corp.)

**FIGURE 2.10**

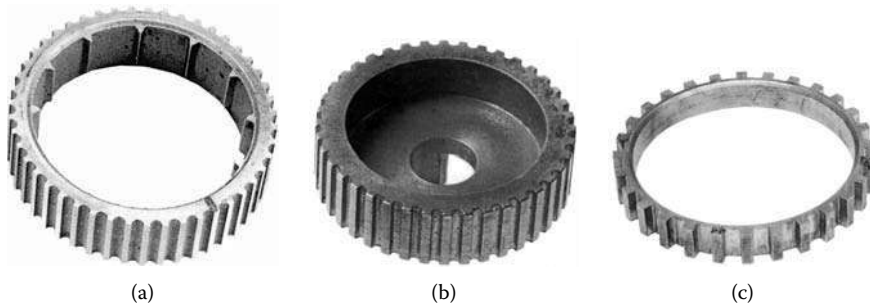
Signal vs. center pole height. (Courtesy of Delphi Corp.)

To fully utilize the sensor envelope, the sensor magnet was elongated to the original sensor height, which resulted in further signal improvement to about 10%, as shown in Figure 2.11. Combination of all improvement steps resulted in over a 40% signal gain.

Conventional VR sensors, which display low magnetic efficiency, are being replaced by much more efficient ones (Pawlak 1999b). Recent efforts are focused on new technical approaches at finding low-cost, magnetically efficient, sensitive VR structures that feature high signal strength for large air gaps with small PM volume and that address this technique for specific applications. Improved sensors have the ability to work with a variety of conventional and low-cost exciter wheels, e.g., stamped or embossed sheet metal, low- to high-density powder-metal, molded plastic with iron filler, and rolled teeth, as presented in Figure 2.12.

**FIGURE 2.11**

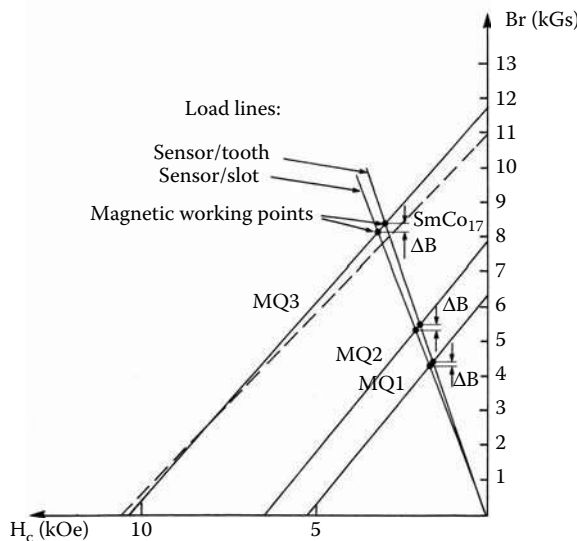
Signal vs. magnet height. (Courtesy of Delphi Corp.)

**FIGURE 2.12**

Exciter wheel configurations: (a) high-density powder, (b) low-density powder, (c) conventional machining. (Courtesy of Delphi Corp.)

### 2.3.2 High Performance VR Sensors

VR sensors whose configurations are different from those of conventional ones fall into the modern VR sensor category. In this category, both the distributed sensors and the stand-alone sensors are described. Recent developments in new magnetic materials and manufacturing technologies enabled the introduction of new sensor configurations and sensor wheel arrangements, which led to dramatic improvements in VR sensor performance. In particular, new PM materials with high-energy products, powder-metal manufacturing technology, bobbinless coil winding, and advanced plastic-molding technology can dramatically improve performance. Powder-metal technology allows for low-cost exciter wheels and unconventional shapes of magnetic circuit parts for the cost-efficient sensor. This technology was utilized for both the magnetic circuit and the exciter wheel for the dual-magnet sensor configuration described in Section 2.3.8.

**FIGURE 2.13**

PM working point for the extreme VR sensor positions. (From Pawlak, A.M. et al., *Novel Variable Reluctance Sensors*, Publ. No. 910902, Society of Automotive Engineers, Detroit, MI, 1991. With permission.)

Development of high-energy product PMs based on samarium-cobalt ( $\text{SmCo}_{17}$ ) and based on neodymium (such as Magnequench® MQ1, MQ2, and MQ3) allowed for sensor signal improvements. The location of the magnet working point on the  $BH$  characteristics of high-energy PMs enables the generation of larger change in the flux developed by the PM in comparison with the low-energy magnets, as shown in Figure 2.13.

The rotation of the excitation wheel changes the permeance value of the magnetic circuit surrounding the PM. The minimum and the maximum permeance values for two extreme sensor positions are indicated by load lines of characteristic positions, as indicated in Figure 2.13. The lower line corresponds to sensor-slot position with minimum permeance value and the higher line corresponds to sensor-tooth position with the maximum permeance value, as presented in Figure 2.13. During the exciter wheel rotation, the PM working point changes its position. For the low- and high-energy magnets, the flux variation with the load-line changes is different, larger for the magnets with high-energy product and smaller with the low-energy product magnets, as indicated by the  $\Delta B$  values in Figure 2.13. Therefore, the capability of generating not only higher flux, but also a larger difference in two extreme positions makes the high-energy magnet material more desirable for the sensor applications. Analysis and optimization studies should always start with the predetermination of the soft and hard magnetic materials used for the sensor structure. PM studies prove that the higher-energy magnets provide a higher sensor signal level. Signal level comparison for all four different magnet materials, as indicated in Figure 2.13 without additional changes, proves this point, as shown in Figure 2.14, where the highest signal level was achieved for the MQ3 material and the lowest for the MQ1 magnet material.

High-energy magnets allow for unconventional magnet geometries and locations, resulting in very large sensor signal improvements. Magnets with high-energy density permit the reduction of the magnet size, which provides greater design flexibility. In particular, the magnet can be located in the middle of the coil and in the proximity of the target wheel, instead of behind the coil as in conventional designs. That is, the magnet can be inserted in the area of the conventional center pole, such as the one shown in Figure 2.15(c). This new

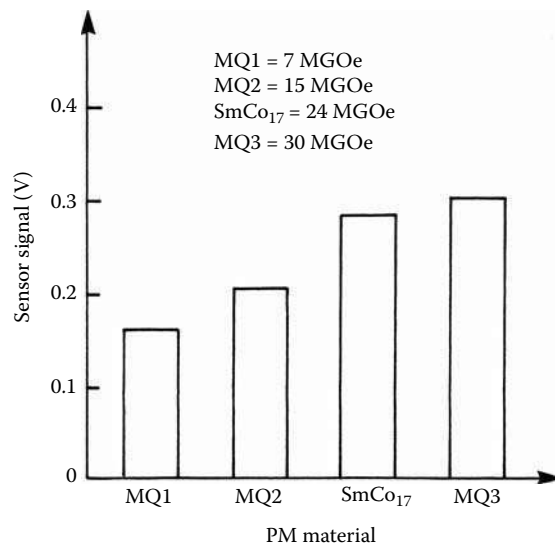


**FIGURE 2.14**  
Sensor signal for different magnet materials. (Courtesy of Delphi Corp.)

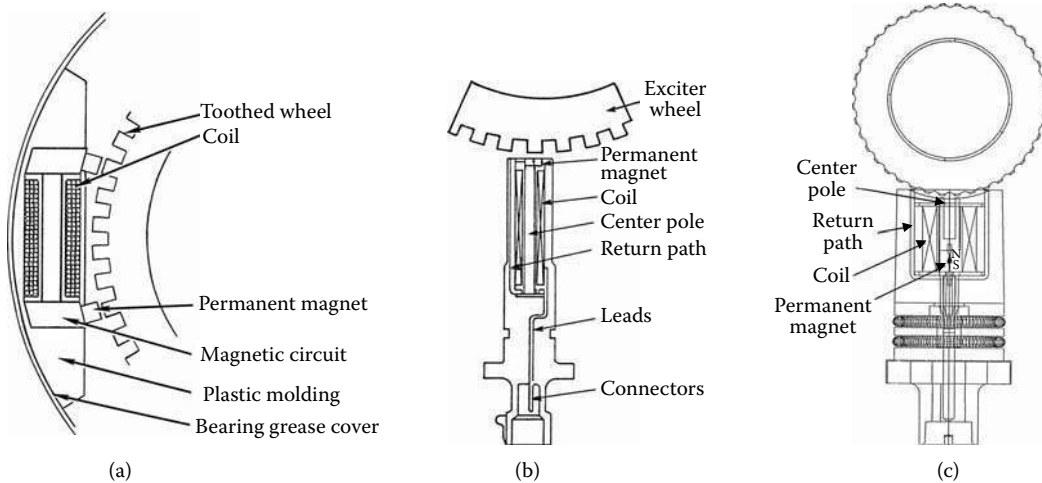


**FIGURE 2.15**  
Sensors with unconventional magnet location: (a) two-magnet sensor, (b) front-magnet sensor, and (c) inserted-magnet sensor. ([a] From Pawlak, A.M. et al., *Novel Variable Reluctance Sensors*, Publ. No. 910902, Society of Automotive Engineers, Detroit, MI, 1991. With permission; [b] from Pawlak, A.M., *Proceedings of the NdFeB '99 Conference*, San Francisco, April 12–14, 1999. With permission; [c] courtesy of Delphi Corp.)

structure will be referred to as the “inserted-magnet” configuration. A magnet that is located closer to the target wheel is favorable because the magnetic-circuit permeance is improved, and the source of the magnetic flux is embodied within a coil, and therefore, the flux distribution affects more directly the coil.

The structure with the magnet located in close proximity to the exciter wheel will be referred to as the “front-mounted-magnet” configuration, as presented in Figure 2.15(a,b). A magnet located closer to the target wheel is also favorable because the magnetic-circuit permeance is improved and the flux distribution affects the coil more directly. Effectiveness

of front magnet location was confirmed for an automotive application of this sensor where for the same signal level, the front-mounted-magnet design allowed the reduction of a sensor volume by a factor of 4 as compared to the conventional sensor design. As this shows, the performance improvement resulting from the new magnet location is such that in many applications, it should outweigh the higher magnet-material cost. The magnet design can be considered as 2D for both the magnet width and for its height, because the axial dimension is fixed to the thickness of the exciter wheel, which is also an optimum size.

Coil turns located in the proximity of the target wheel are more directly exposed to target-wheel permeance changes and embrace more flux lines. Therefore, short and wide coil geometries are preferable to long and narrow ones. In one particular case, the signal from a conventional design was improved by 30% by changing the coil-width/coil-height ratio from 0.41 to 1.00, the coil area being kept constant. Such coil geometries are easier to implement in the front-mounted-magnet case, which is another advantage of that configuration. Coil geometries that promote close coil locations to the exciter wheel are preferable. Precision coil winding with the bobbinless technology allows for better coil packaging, including unconventional coil winding directly on the magnetic circuit. Advanced plastic-molding technology makes feasible unusual sensor configurations where parts have to be kept together, fastened to the adjacent parts, and sealed at the connectors.

Four families of modern VR sensors are described and specific examples of automotive applications of these sensors are provided:

- Sensors with an inserted magnet having improved magnetic circuit and the inserted magnet as an automotive automatic transmission speed sensor
- Sensor with front-mounted magnet featuring significant performance improvement as an automotive crankshaft position sensor with U-shaped or with E-shaped magnetic circuit for the transmission speed sensor application
- Distributed sensor with two front-mounted PMs with limited angle of exciter wheel coverage for an automotive antiskid braking system (ABS)
- Distributed sensor with ring magnet having a multiplicity of PMs with unlimited angle of exciter wheel coverage for an automotive TC system

While both inserted-magnet and front-mounted-magnet sensors are having conventional arrangements with the exciter wheel, the distributed sensors are combined with the exciter wheel in a more complex manner. Sensors with two front-mounted magnets are arranged with the exciter wheel in one 2D plane, whereas the ring magnet distributed sensors are arranged with an exciter wheel three-dimensionally. These novel sensor-excitation wheel arrangements are additional opportunities to create modern high-efficiency VR sensors.

The conventional optimization technique is based on a parametric study of selected design variables with an iterative procedure. Therefore, the best design variables (dimensions, material properties, coil, etc.) found in the first parametric study are carried on to the second iterative procedure until all design variables are optimized. The process is repeated until consecutive iterations result in no further changes in the sensor design variables.

Electromagnetic circuits of all investigated sensors were optimized using described mathematical models supported by both 2D and 3D FE magnetic field solutions. The goal of the sensor design optimization is to maximize sensor signal strength. It includes optimization of the magnetic circuit and magnetic materials selection with the best available cost-effective qualities. The design variables for the magnetic material are selected on the basis of sensor configuration, magnetic material properties, and the coil parameters subject to given constraints. The design requirements for VR sensors include an available envelope

for the sensor, the signal strength at the required exciter wheel speed range, the exciter wheel geometry and material, and the size of the air gap between the sensor and the exciter wheel. The maximum coil resistance, the acceptable electromagnetic noise signal strength, and the sensor temperature range at which sensors operate are usually determined. Additionally, the wheel-sensor arrangements, the applied technology, and the type of material used for the exciter wheel can introduce extraordinary challenges for the sensor. Table 2.9 in Section 2.5 contains examples of such requirements, concerning all four investigated sensor types, the truck transmission sensor, the crankshaft position sensor, the integral bearing speed sensor, and the distributed sensor for the ABS/TC applications.

### 2.3.3 Sensors with Inserted Magnets

The inserted-magnet structure falls into the modern sensor category because the magnet location allows for its efficient utilization. Figure 2.16 presents a number of different VR sensor geometries with inserted magnets. Both the sensor and magnet geometry depend on selected structure and target-wheel geometry. For sensor 1 and sensor 2 structures, the magnet thickness is the same as the thickness of the magnetic circuit, whereas for the sensor 3 to sensor 6 structures with the U-shaped central pole, magnet thickness depends upon exciter wheel tooth pole-pitch geometry. The insert-magnet structure is more flexible and provides more geometry opportunities than conventional sensors.

The objective is to identify the least complex and the most efficient sensor configuration for the given application requirements: the sensor geometry that is simple for manufacturing

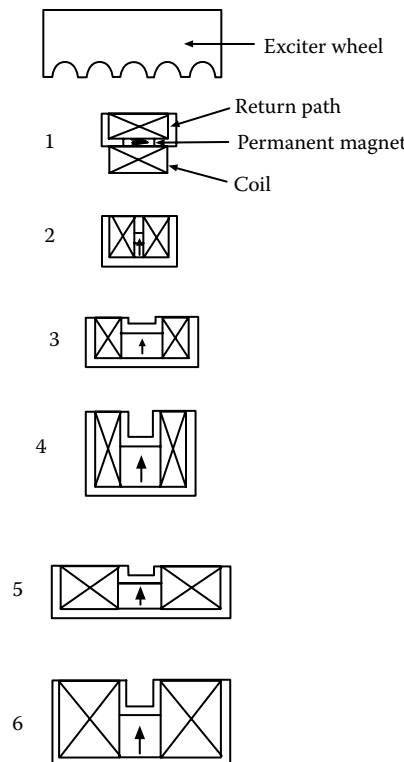


**FIGURE 2.16**

Inserted-magnet sensor configurations with exciter wheel segment: (1) magnet in the return path, (2) magnet in the single central pole, (3) through (6) magnet between return path and the split center pole. (Courtesy of Delphi Corp.)

**TABLE 2.2**  
Inserted-Magnet Sensor Performance Comparison

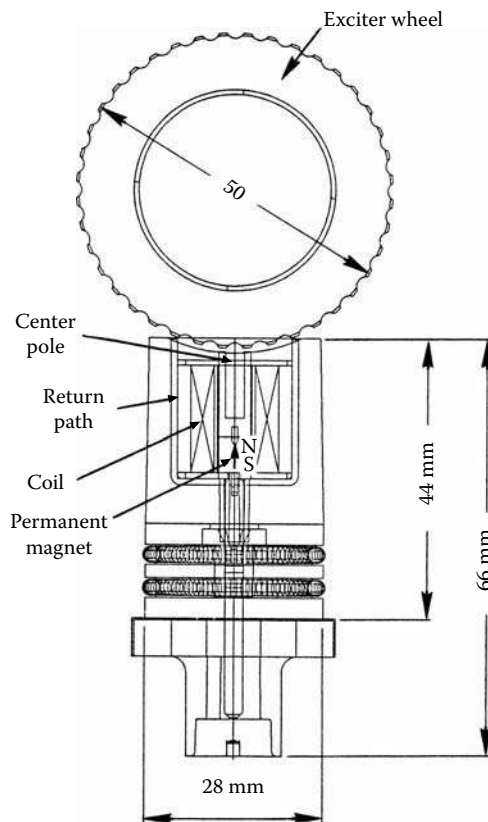
Sensor No.	Signal (V)	Volume (cm <sup>3</sup> )	Signal Sensitivity (V/cm <sup>3</sup> × 10)	Flux Sensitivity (%)
1	0.052	0.702	0.74	2.2
2	0.108	1.287	0.84	1.8
3	0.445	1.859	2.39	2.1
6	0.809	3.003	2.69	1.8
5	0.548	1.638	3.34	2.7
4	0.348	1.014	3.43	3.5

Source: Courtesy of Delphi Corp.

and cost-effective. Depending on the degree of complexity, the sensor geometry could have more elements that would improve its signal strength. The investigation was performed for all geometries presented in Figure 2.16. The search should begin at the simplest structures, sensor 1 and sensor 2, and because they cannot meet performance requirements, the search should continue to incorporate more complex structures, sensor 3 through sensor 6, or investigate a different sensor family. This is because more complex structures are more difficult for manufacturing and usually require more parts, resulting in sensor cost increase. Also, the sensor reliability degrades with increased complexity of its structure. Results of this investigation are summarized in Table 2.2, which shows the performance comparison of the described sensor structures.

Table 2.2 shows the inserted-magnet sensor configurations introduced in Figure 2.16 in increasing order of sensor signal sensitivity (signal/volume ratio) from 0.74 to 0.343, as shown in Equation 2.11. The results in this table indicate that the sensor 4 configuration is the most electromagnetically efficient, providing the highest signal sensitivity of 0.343 V/cm<sup>3</sup> and, at the same time, the best utilization of the magnet flux indicating flux sensitivity of 3.5%, as shown in Equation 2.12. The sensor flux sensitivity is quite low for all front-magnet sensor configurations, indicating that a very small part of flux developed by the magnet is utilized by the coil for signal generation. Signal strength is a function of flux-linkage variation as well as the number of coil turns (that depends on coil area), and therefore, it has the highest value for the sensor 6 configuration, which also has the highest sensor volume. The cost of the sensor is a function of sensor volume because this is an indication of the volume of magnetic and copper materials used; the sensor with the smaller volume is more cost-effective. From all these considerations the sensor 4 structure holds the best potential for further development to meet the required signal strength.

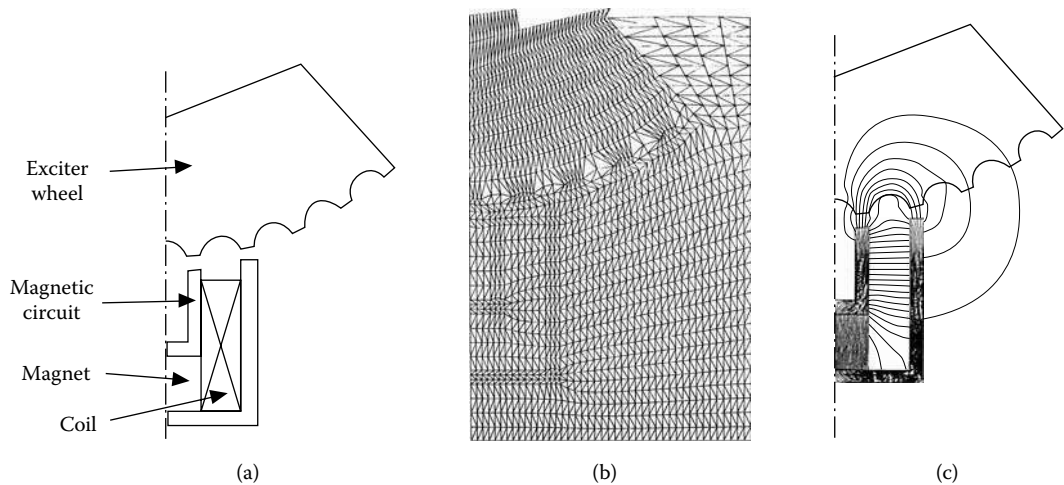
An exciter wheel for this configuration is manufactured using low-cost powder-metal technology. Because of this, the wheel has a much less distinctive tooth geometry in comparison with the conventional machining technology, and such a geometry features much less permeance variation in two extreme (poles vs. teeth and poles vs. slots) positions, as presented in Figure 2.12(b). A relatively large air gap, the teeth geometry, and low powder-metal density seriously degrade the signal; therefore, a highly sensitive sensor configuration is required for this application. Figure 2.17 shows a fully developed VR sensor based on the sensor 4 structure for an automotive truck transmission application that provides the signal output to the speedometer, cruise, and the truck transmission control system that met all signal requirements, as presented in Table 2.9. The large air gap between the sensor and the exciter wheel of  $1.2 \times 10^{-3}$  m is very beneficial for manufacturing because it allows the use of a wide range of mechanical tolerances that are associated with low manufacturing costs. It also drastically reduces the target-wheel vibration effect upon signal noise, improving the signal-to-noise ratio, as presented in Section 2.6.

**FIGURE 2.17**

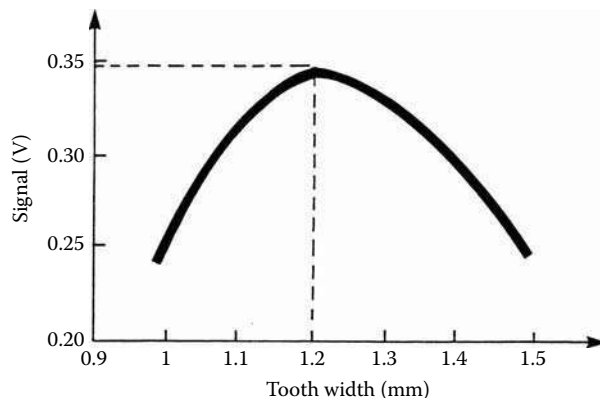
Inserted-magnet VR sensor for truck transmission application. (Courtesy of Delphi Corp.)

The sensor configuration selected for optimization consists of the two U-shaped magnetic parts providing a flux return path of a multipole sensor configuration. The internal center pole part is made of powder-metal technology because its thickness at the bottom of the U-shape is larger than the thickness of walls. Walls with different thicknesses can accommodate better magnetic flux distribution. An axially magnetized PM made out of high-energy product samarium-cobalt material, as presented in Figure 2.13 and Figure 2.14, is located inside a coil and thus is closer to the exciter wheel in comparison with the conventional sensor magnet location. The coil is located closer to the exciter wheel than conventional sensor coil, improving its sensitivity. The entire sensor structure is encapsulated using plastic-molding technology with sealed connectors to the sensor. This sensor features a very efficient use of electromagnetic components. Both the sensor and exciter wheel were optimized using the FE method. Because the sensor structure is symmetrical, only a half of the sensor structure needs to be analyzed. Figure 2.18 shows the sensor finite-element model, with configuration, FE grid structure, and flux lines.

Sensor optimization studies were initiated with a parametric study of the exciter wheel sensor teeth dimensions. The exciter wheel teeth width was investigated, as presented in Figure 2.19. For this sensor's magnetic core thickness of  $1.0 \times 10^{-3}$  m, the exciter teeth width of  $1.2 \times 10^{-3}$  m was found to be the best, as shown in Figure 2.19. The rectangular tooth shape was found to be the best; however, this was not acceptable because a die for an exciter wheel with powder-metal technology could not be made with sharp corners due to lifetime die limitations.



**FIGURE 2.18**  
Inserted-magnet VR sensor FE model: (a) configuration, (b) grid, (c) flux lines. (Courtesy of Delphi Corp.)

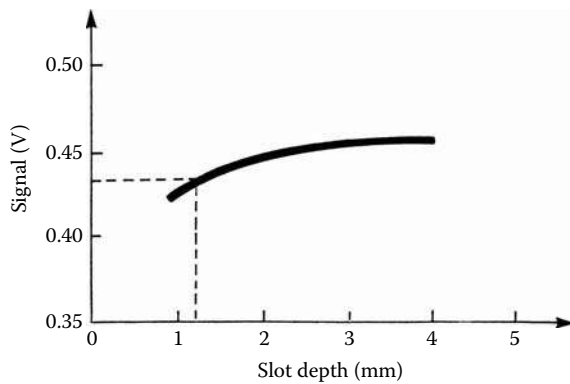


**FIGURE 2.19**  
Sensor signal vs. exciter wheel tooth width. (Courtesy of Delphi Corp.)

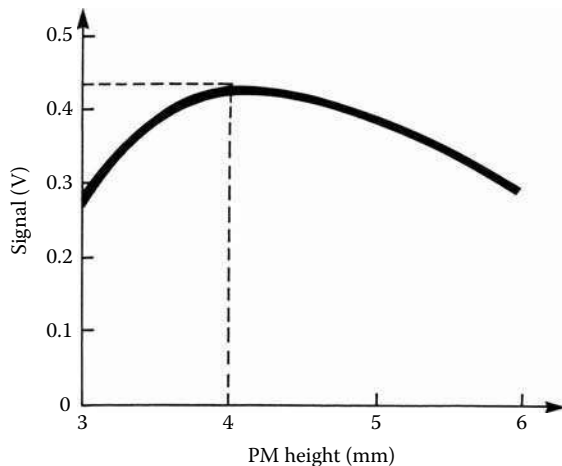
The next step was to optimize the exciter wheel. The slot depth was investigated and showed potential for further improvements for a deeper slot, as presented in Figure 2.20. Because the existing powder-metal technology limits the exciter wheel slot depth, it was not possible to utilize this approach; however, it might be possible in the future with advances in powder-metal technology.

Following this, the PM material was selected to generate high magnetic flux at given temperature requirements, as presented in Table 2.9. Implementing selected magnet material and optimizing magnet height to  $4.0 \times 10^{-3}$  m further increased the signal strength, as indicated in Figure 2.21. Please note that increasing magnet height and, therefore, the magnetomotive force (MMF) of a magnet or magnet strength beyond its optimum point causes signal deterioration. Therefore, there is a trade-off between magnet strength and its geometry, and hence these studies must be performed to devise proper magnet size and strength at the same time.

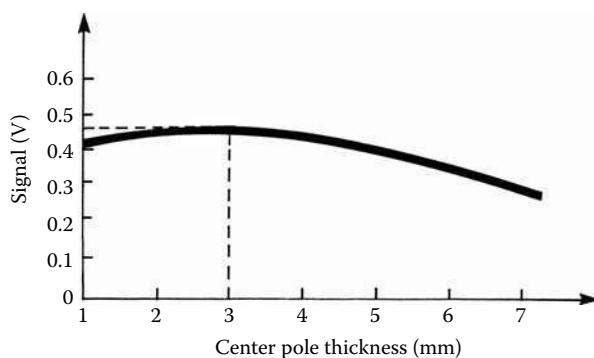
The center pole thickness parametric studies showed that  $3.0 \times 10^{-3}$  m thickness of the sensor center pole base further improved the signal strength, as presented in Figure 2.22.

**FIGURE 2.20**

Sensor signal vs. slot depth. (Courtesy of Delphi Corp.)

**FIGURE 2.21**

Sensor signal vs. magnet height. (Courtesy of Delphi Corp.)

**FIGURE 2.22**

Sensor signal vs. center pole base thickness. (Courtesy of Delphi Corp.)

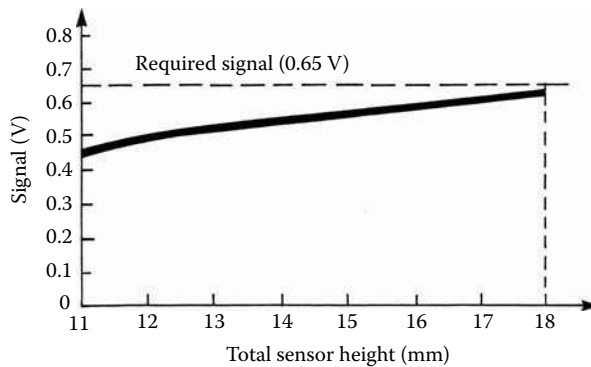


**FIGURE 2.23**  
Sensor signal vs. total sensor height. (Courtesy of Delphi Corp.)

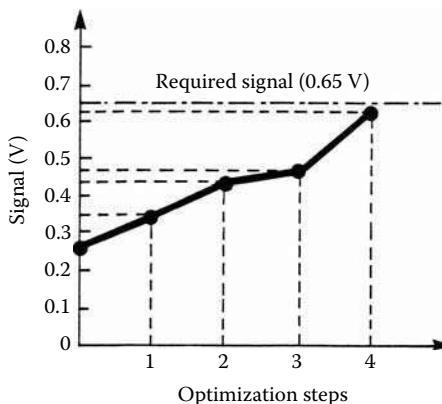


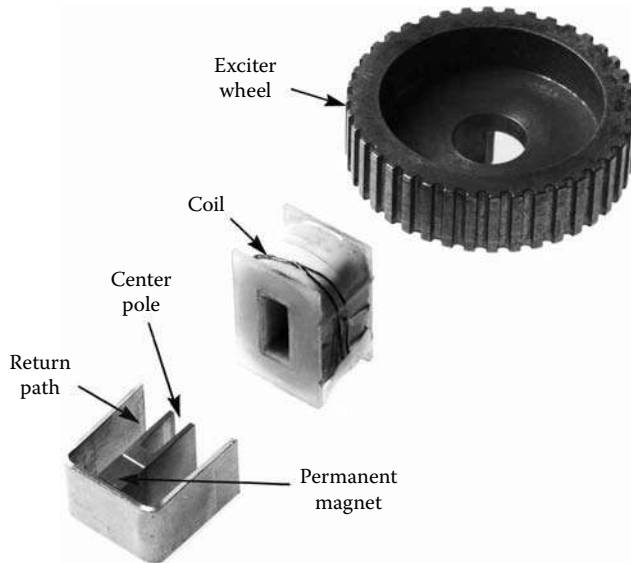
**FIGURE 2.24**  
Inserted-magnet sensor optimization steps: (1) tooth width, (2) magnet height, (3) center pole thickness, (4) total sensor height. (Courtesy of Delphi Corp.)

It is caused by concentration of the flux lines at the base of the center pole and, consequently, flux-density saturation of this magnetic part segment that limits proper flux distribution around a coil, as presented in Figure 2.18(c). Again, there is a trade-off between saturation and proper flux distribution around a coil and further increase of the center pole base thickness would change flux distribution around a coil, causing decreased signal performance.

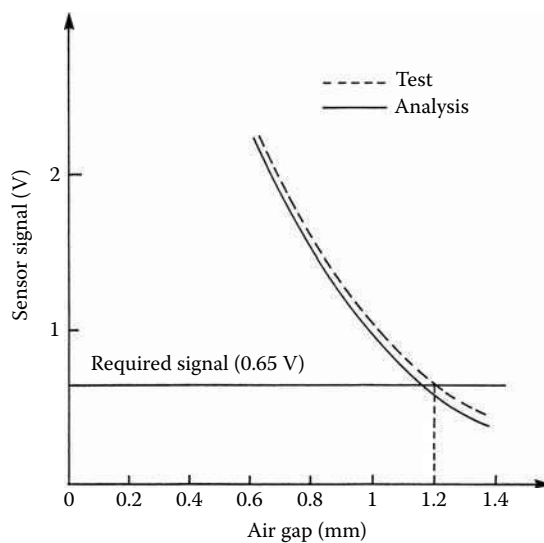
The total sensor height, including the magnet and center pole, was investigated. For the total unit height of  $18.0 \times 10^{-3}$  m the sensor signal increased to 0.63 V, which is about 97% of the required signal of 0.65 V at  $25.0^{\circ}\text{C}$  and 100 r/min, as indicated in Figure 2.23 and in Table 2.9. Sensor optimization studies were completed and, at this point, the final sensor design was good enough for the prototype design.

Figure 2.24 shows the inserted-magnet sensor optimization steps. With the consecutive iterative analysis and tests, the sensor met its signal requirements. Cost analysis showed that this sensor is cost competitive, and the sensor sensitivity is three times higher compared with the conventional sensor for this application.

Based on these optimization steps, the final dimensions of the sensor were established. Sensor components, as illustrated in Figure 2.25, were manufactured and assembled. The



**FIGURE 2.25**  
Inserted-magnet sensor prototype. (Courtesy of Delphi Corp.)



**FIGURE 2.26**  
Inserted-magnet sensor signal vs. air gap. (Courtesy of Delphi Corp.)

exciter wheel and center pole were manufactured using powder-metal technology. Magnetic-circuit elements were devised to maintain a fixed air gap between sensor poles and the exciter wheel, allowing for the exciter wheel radius curvature, as presented in Figure 2.17.

The test results, indicated in Figure 2.26, show a very close match with analytical predictions, within 5% for the wide range of air gaps, and prove that inserted-magnet structures could be viable and practical choices for manufacturing and industrial applications.

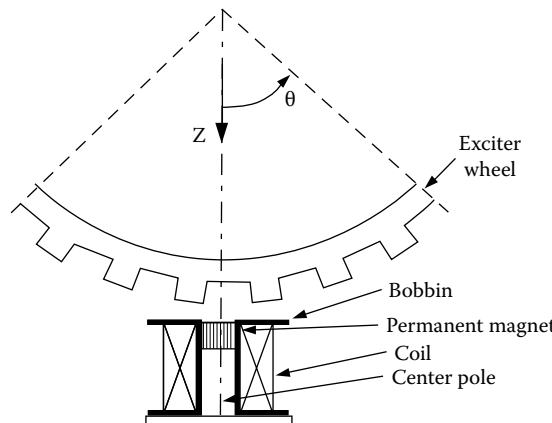


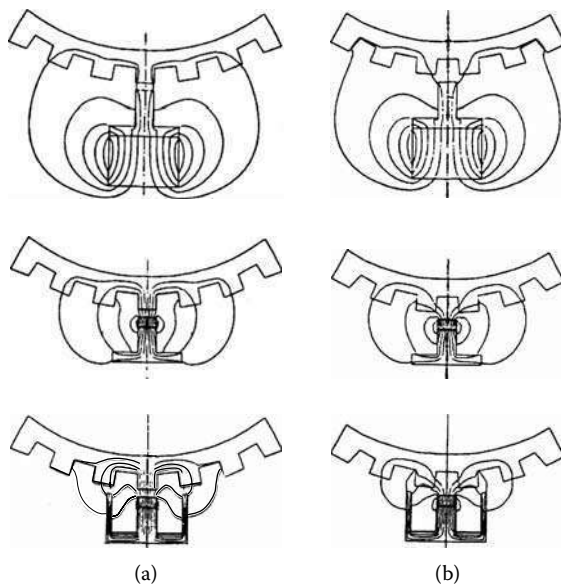
**FIGURE 2.27**  
Front-mounted-magnet sensor with the exciter wheel. (Courtesy of Delphi Corp.)

### 2.3.4 Front-Mounted-Magnet Sensors

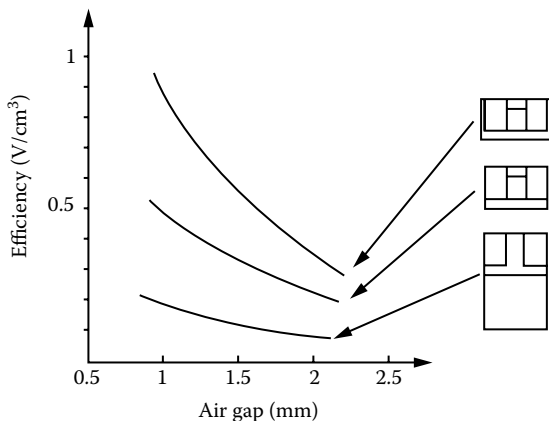
A VR sensor configuration with a PM located in the proximity of the exciter wheel is defined as a front-mounted-magnet sensor, as presented in Figure 2.27. This sensor configuration has a PM centrally located with a center pole and a back shim that construct only a partially magnetic flux return path. The magnetic circuit is partial because it does not provide the full path for the magnetic flux return path from the magnet to the center pole and further to the exciter wheel and back to the magnet. The portion from the magnetic shim to an exciter wheel is missing in the same way as it is for the conventional VR sensors, as demonstrated in Figure 2.28. The magnet location in the air gap is directly affected by the exciter wheel reluctance, which in turn affects the level of the magnetic flux developed by the magnet and its distribution. The front-mounted-magnet sensor signal performance is superior to the conventional sensor performance with the same volume because more flux lines generated by the PM contribute to the signal generation.

Figure 2.28 shows the magnetic flux distribution for the conventional sensor, the front-mounted-magnet sensor with a partial magnetic return path and the front-mounted-magnet sensor with an E-shaped magnetic return path with the same air gap for the two extreme positions with the maximum and minimum flux linkages. The E-shaped sensor structure provides the missing link by the addition of the magnetic return paths linking the back shim with an exciter wheel. Note the difference in the magnetic flux distribution around a coil window area. The coil of the front-mounted-magnet sensor with a partial magnetic return path is linked to the magnetic flux more effectively than the coil of the conventional structure, and almost all generated flux lines of the E-shaped structure with a fully developed magnetic return path are linked to a coil. Therefore, the signal of the front-mounted-magnet sensor with a partial magnetic return path is superior to the performance of conventional structures, and the signal of the front-mounted-magnet sensor with a full magnetic return path is superior to the performance of the front-mounted-magnet sensor with a partial magnetic return path. The signal-to-volume ratio for conventional and front-mounted-magnet sensors as a function of the air gap is shown in Figure 2.29.

Table 2.3 shows the performance comparison for the conventional, front-mounted-magnet sensor without a magnetic return path and a front-mounted-magnet sensor with an E-shaped magnetic return path at  $1.5 \times 10^{-3}$  m of air gap. The front-mounted-magnet sensor with a partial magnetic return path features more than twice the signal sensitivity with

**FIGURE 2.28**

Flux-lines distribution of the front-mounted-magnet sensors and conventional sensor for (a) maximum flux linkage and (b) minimum flux linkage. (From Pawlak, A.M., *Proceedings of the NdFeB '99 Conference*, San Francisco, April 12–14, 1999. With permission.)

**FIGURE 2.29**

The signal/volume ratio vs. air gap for front-mounted-magnet and conventional sensors. (Courtesy of Delphi Corp.)

over 50% better flux efficiency utilization than a conventional sensor having the same coil parameters, and a front-mounted-magnet sensor with an E-shaped magnetic return path features more than four times higher signal sensitivity with almost 90% better flux efficiency utilization, as presented in Table 2.3.

Because of this, for practical applications, however, the front-mounted-magnet sensor structure should always have a full return path for the magnetic flux. The return path enhances the flux level and guides the flux for better coupling with the coil turns. There are two basic shapes of the return magnetic path: an E-shaped structure that surrounds a

**TABLE 2.3**  
VR Sensor Comparison

Sensor Geometry and Performance	Volume (cm <sup>3</sup> )	Signal (V)	Signal Sensitivity (V/cm <sup>3</sup> × 10)	Flux Efficiency (%)
Conventional geometry	3.231	0.39	0.12	0.72
Front-mounted no-return path	1.385	0.44	0.32	1.1
Front-mounted E-shaped	1.385	0.74	0.54	1.35

Source: Courtesy of Delphi Corp.

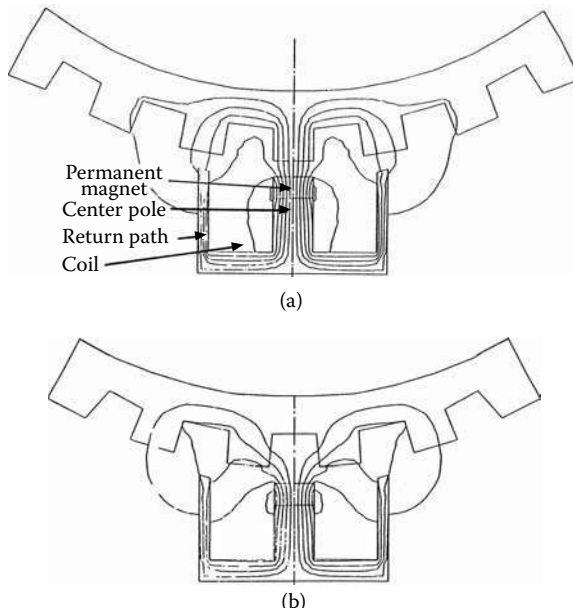


**FIGURE 2.30**

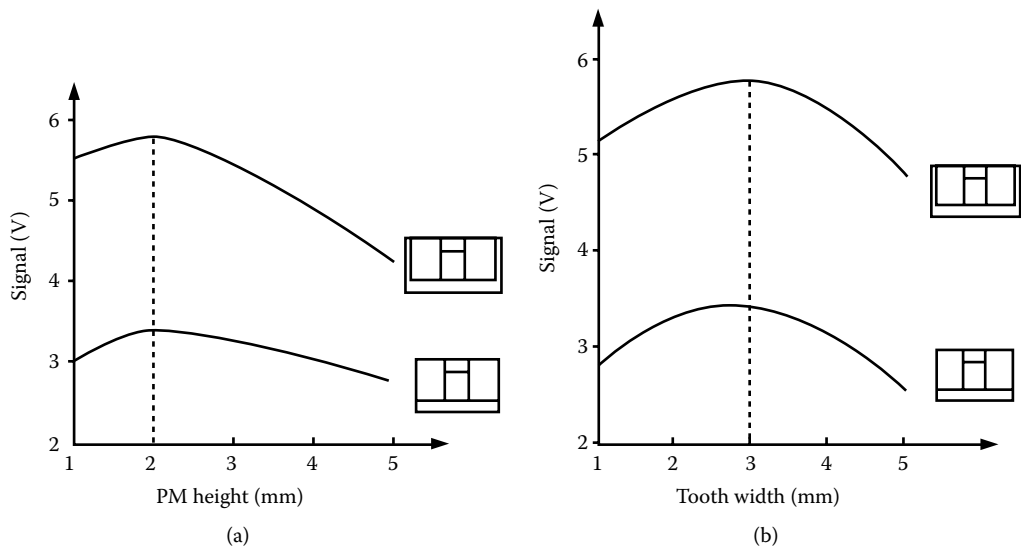
Magnetic flux distribution of the front-mounted-magnet sensor with E-shaped structure: (a) minimum flux linkages, (b) maximum flux linkages. (From Pawlak, A.M., *Proceedings of the NdFeB '99 Conference*, San Francisco, April 12–14, 1999. With permission.)

coil entirely, which has already been introduced, and a U-shaped structure that supports only one coil side with the magnetic return path, which will be discussed in Section 2.3.6.

### 2.3.5 Sensors with E-Shaped Magnetic Structure

In an application where there is sufficient space for a wide sensor with a relatively wide exciter wheel, the sensor with an E-shaped structure offers an efficient magnetic configuration. It extends between three (or more) exciter wheel teeth, where the exciter wheel geometry dictates the sensor width. Figure 2.30 shows the magnetic flux distribution of this structure for two extreme sensor-wheel positions. In contrast to a U-shaped front-mounted sensor, both sides of the coil of the E-shaped structure contribute equally to the signal generation because its structure is symmetrical.

The signal efficiency of the front-mounted-magnet sensor with an E-shaped magnetic structure is superior to the front-mounted-magnet sensor with a partial magnetic return path, as shown in Figure 2.29, for a sensor signal efficiency across any practical air gap size. For the E-shaped structure, the return path geometry is fixed by the exciter wheel

**FIGURE 2.31**

Magnet optimization for front-mounted-magnet sensors: (a) signal vs. PM height, (b) signal vs. tooth width. (Courtesy of Delphi Corp.)

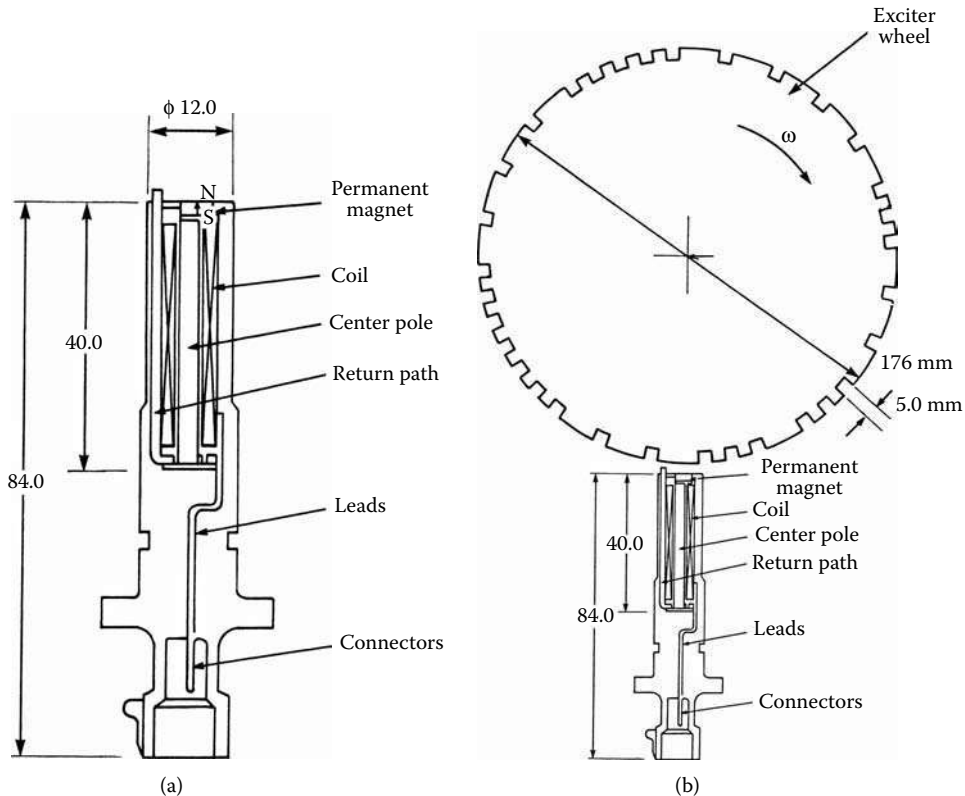
tooth pitch, where the center of the return path geometry meets the corresponding tooth center, as presented in Figure 2.30. Therefore, optimization of the E-type magnetic structure focuses on the geometry of the center pole and the magnet.

Figure 2.31(a) shows the magnet optimization for the E-shaped structure and, for comparison purposes, also for the front-mounted-magnet sensor with a partial magnetic return path. The optimum heights of both magnets are the same and equal to  $2.0 \times 10^{-3}$  m, but they provide different magnet utilization and signal sensitivity due to the difference in magnetic configuration, as presented in Table 2.3. The optimum magnet and center pole widths for the front-mounted-magnet sensor with a partial magnetic return path and front-mounted-magnet sensor with an E-shaped magnetic return path are the same and correspond in this case to the width of the exciter wheel tooth of  $3.0 \times 10^{-3}$  m, as presented in Figure 2.31(b).

Both analyses, one for the magnet height and the other for the center pole or magnet width, indicate that there is only one set of magnet width and height dimensions that would provide the best sensor signal performance for a given exciter wheel's tooth geometry across the entire air gap range. The magnet or center pole width must be equal to the exciter wheel's tooth width for the discussed sensor structures, and that is also true for other sensor structures.

### 2.3.6 Sensors with U-Shaped Magnetic Structure

U-shaped structure is defined as a VR configuration having a PM in proximity to the exciter wheel and a single return magnetic path also facing the exciter wheel, as presented in Figure 2.32. Such a sensor structure requires less space compared with the E-shaped structure because it extends between two teeth only and can be devised for very limited space requirements, such as for a crankshaft position application. However, unlike the U-shaped structures, where only one side of coil is affected by teeth permeance variations, the E-shaped configuration provides better utilization of magnetic structure, resulting in superior signal performance.

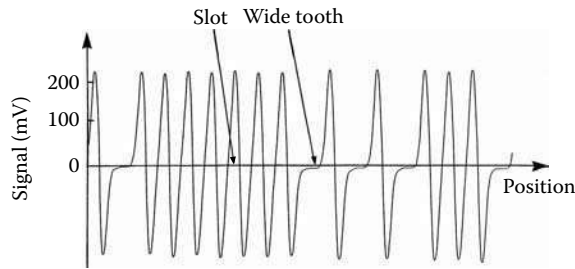
**FIGURE 2.32**

Front-mounted-magnet sensor with U-shaped magnetic structure: (a) sensor structure, (b) sensor-wheel arrangement. (Courtesy of Delphi Corp.)

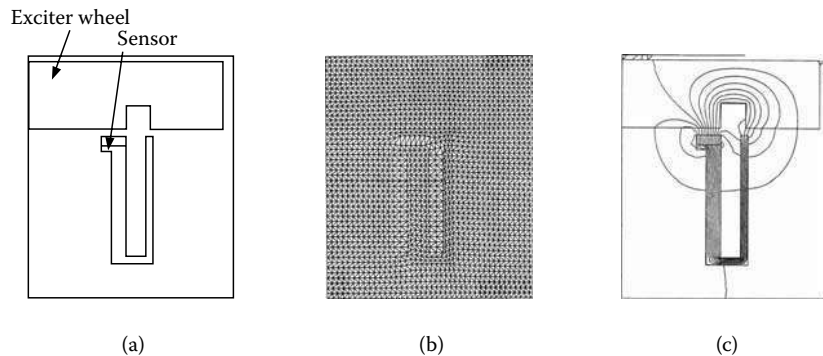
The VR front-mounted-magnet sensor consists of a PM, a U-shaped magnetic circuit, and a coil with a bobbin, as shown in Figure 2.32. The bobbin supports both the coil and the PM. Polarization of the magnet is perpendicular to the exciter wheel surface. The rectangular magnetic element under the PM collects the magnetic flux and through the magnetic center pole connected with the magnetic return path directs the flux back to the exciter wheel. The coil assembly has cylindrical symmetry, and the PM and the magnetic return path have rectangular geometry. The axis of symmetry and the center of the PM are offset in order to provide an optimum flux-linkage change at the extreme exciter wheel positions.

The sensor signal is presented in Figure 2.33. The maximum signal value of 224.0 mV was obtained at the exciter wheel speed of 30.0 r/min and an air gap of  $0.2 \times 10^{-3}$  m with no load. This signal is utilized as a position sensor where the real position of the exciter wheel is indicated by zero crossing of the signal at the narrow and wide teeth. Determining an optimum geometry for this nonsymmetrical structure is more complicated than for the symmetrical one. The entire sensor has to be modeled to obtain the magnetic field solution using the finite-element model, as shown in Figure 2.34, where the sensor configuration, meshing for the FE model, and the resultant flux lines are presented.

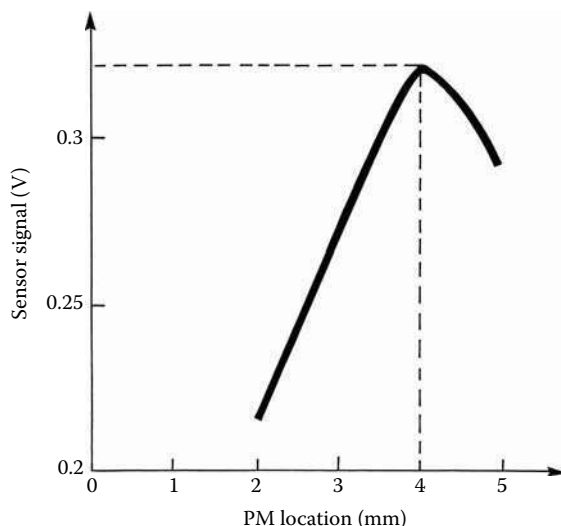
Parametric studies for this sensor configuration led to optimized position of the PM location in respect to the U-shaped magnetic circuit. Figure 2.35 identifies the distance of  $4.0 \times 10^{-3}$  m between the PM and the return path, which provides the maximum flux change linked to the coil in two extreme sensor-wheel positions for the exciter slot width of  $5.0 \times 10^{-3}$  m as

**FIGURE 2.33**

Front-mounted-magnet sensor with U-shaped magnetic structure. (Courtesy of Delphi Corp.)

**FIGURE 2.34**

Sensor FE model: (a) configuration, (b) grid, (c) flux lines. (Courtesy of Delphi Corp.)

**FIGURE 2.35**

Sensor signal vs. magnet location. (Courtesy of Delphi Corp.)

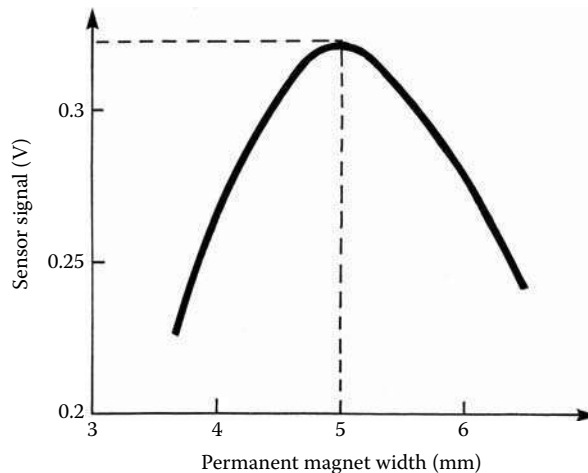


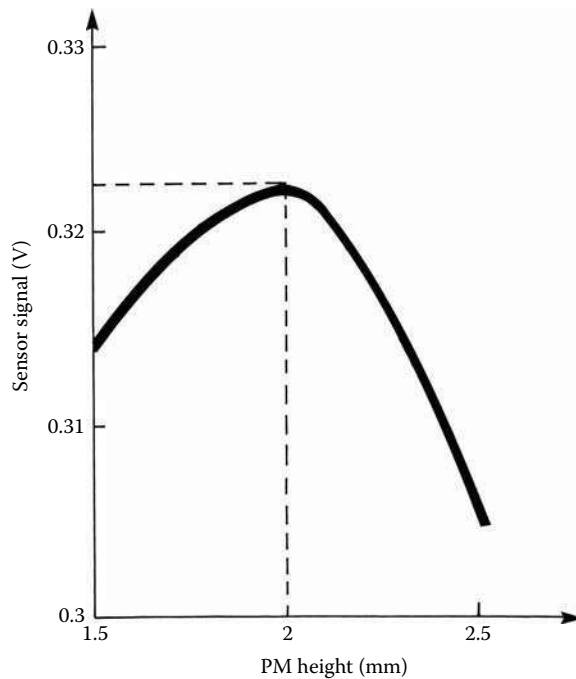
**FIGURE 2.36**  
Sensor signal vs. magnet width. (Courtesy of Delphi Corp.)

shown in Figure 2.32(b). Please note that the width of the exciter wheel's regular tooth is also  $5.0 \times 10^{-3}$  m. In order to utilize this geometry, the PM must be located asymmetrically to the coil, as shown in Figure 2.35.

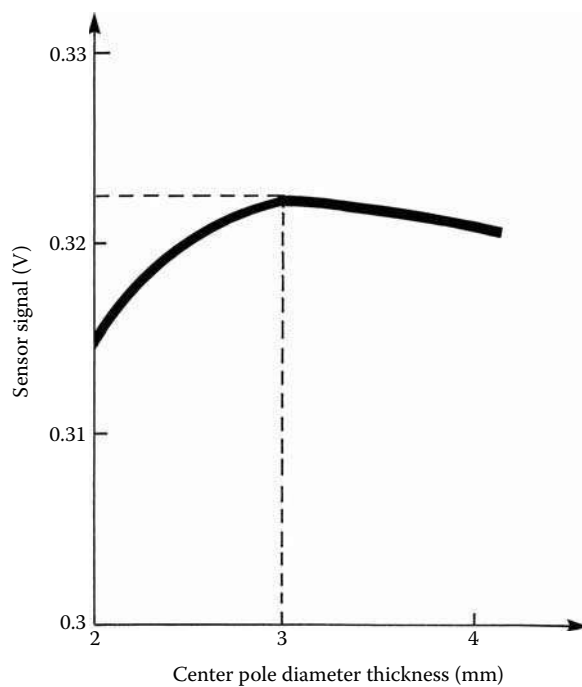
The PM location closer to the return path increases the amount of the magnetic flux linked to the coil, but reduces flux linkages in its two extreme positions, thus decreasing the sensor signal. On the other hand, the larger distance of the PM from the return magnetic circuit reduces the amount of the magnetic flux linked to the coil but enhances the change of the magnetic flux linkages in the extreme positions. Therefore, there is a trade-off location where flux reduction and increase of the flux-linkage change counterbalance. Because the location of the PM depends on its dimensions, the width of the PM also has to be optimized. The PM width affects the average value of the developed flux and, therefore, the flux linking to the coil. However, the flux distribution changes and this affects the flux linkages as well. For the PMs wider than the wheel slot opening, the level of the linkages increases, but the flux-linkage change for the two extreme positions decreases. Therefore, the sensor signal strength is reduced.

For the PMs narrower than the wheel slot opening, the level of the linkages reduces, but the flux-linkage change for the two extreme positions decreases even more. Therefore, the PM width equal to the slot opening is an optimum solution for this configuration. Figure 2.36 shows the results of this investigation. A PM width bigger as well as smaller than slot opening decreases the flux change and causes signal strength reduction. Therefore, a width opening of  $5.0 \times 10^{-3}$  m is an optimum dimension.

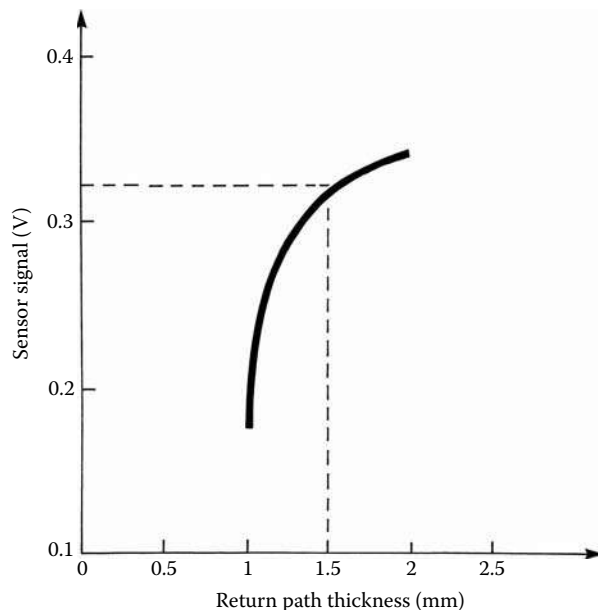
The PM is axially magnetized. Therefore, its height affects the total MMF of the PM. This affects the flux level and the flux linked to the coil. The height of the PM affects the coil location and its distance to the exciter wheel. For the long PM, the coil is further removed from the exciter wheel, while for the short one, the coil is closer to the exciter wheel. Therefore, the flux distribution is different in both cases. The coil location closer to the exciter wheel is preferable because in this position the coil is more sensitive to the flux, while the longer PM can generate more flux. Again, there is a trade-off for the length of the PM to produce the higher flux-linkage change for a given sensor geometry and magnet material. Figure 2.37 shows the optimum magnet height for this sensor geometry. A thickness of  $2.0 \times 10^{-3}$  m was selected because it provides the best signal generated for this geometry.



**FIGURE 2.37**  
Sensor signal vs. magnet height.



**FIGURE 2.38**  
Sensor signal vs. center pole thickness.

**FIGURE 2.39**

Sensor signal vs. return path thickness. (From Lequesne, B. et al., *Transactions of IEEE/IAS*, 32(5), 1166–1175, 1996. With permission.)

The magnetic-circuit thickness for the center pole and the return magnetic-circuit optimized values are presented in Figure 2.38. A round center pole geometry allows for the use of regular coil winding technology, whereas rectangular return magnetic-circuit geometry allows for the minimization of the sensor thickness while providing a sufficient cross-sectional area of the magnetic flux. Note, in Figure 2.39, that reduction of the return path thickness beyond  $1.0 \times 10^{-3}$  m results in rapid signal loss, and increase of the thickness beyond  $1.5 \times 10^{-3}$  m results in moderate signal improvement. The center pole with  $3.0 \times 10^{-3}$  m outside diameter (OD) and  $1.5 \times 10^{-3}$  m thickness of the return magnetic circuit were selected because they provide the highest signal level for the given geometry.

Implementation of the magnetic return path to the sensor structure significantly improves the sensor signal strength. With the higher magnetic-circuit permeability, the flux level increases. This is because of the flux leakage reduction and the higher magnet working point that effects the slope of the magnetic-circuit permeance. The magnetic return path also changes the flux distribution, especially in the area of the coil, which additionally improves the sensor signal strength. Conventional VR sensors feature no iron return path, as presented in Figure 2.1. This is perceived to make design simple, more universal, and less expensive, but the flux is not properly guided, with significant flux leakages, because there is no main magnetic circuit that would provide a magnetic path. Sensor structures that provide a return magnetic path feature minimum flux leakages. Finally, the total sensor height and the coil geometry were optimized to ensure the required signal, as presented in Figure 2.40.

For the  $25.0 \times 10^{-3}$  m total sensor height, the peak-positive signal reached a value of 0.325 V, which is about 103% of that required for this application. The optimization process requires iterations until there is no further improvement in signal performance. Consequently, models with the optimized structures were built and tested, as presented in Figure 2.41.

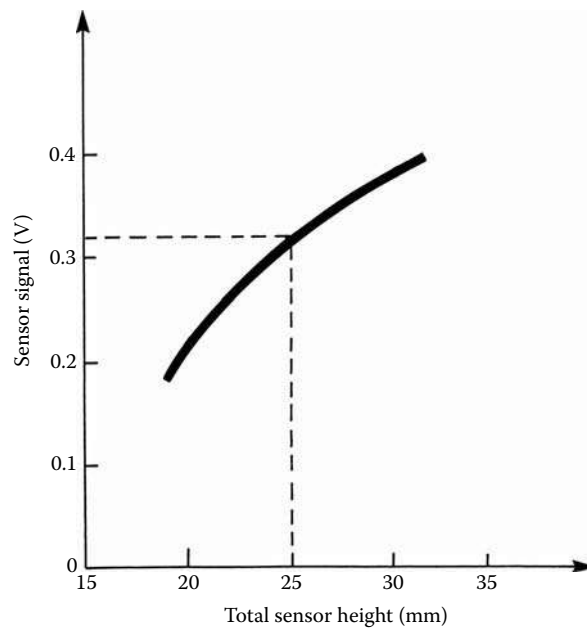


**FIGURE 2.40**  
Sensor signal vs. total sensor height.

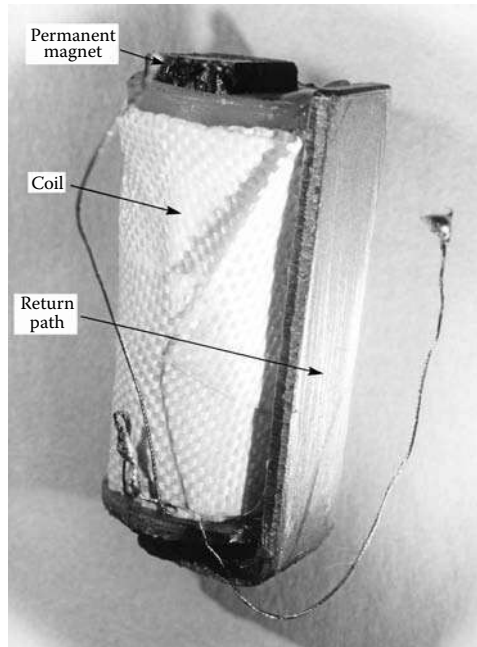


**FIGURE 2.41**  
The U-shaped sensor model.

Figure 2.42 shows the signal performance as a function of the air gap. It matches the investigation with a load of  $10\text{ k}\Omega$ , and the no-load performance is satisfactory and met requirements for the crankshaft position sensor application, as presented in Table 2.9. The no-load test results also show a close match with the analytical analysis.

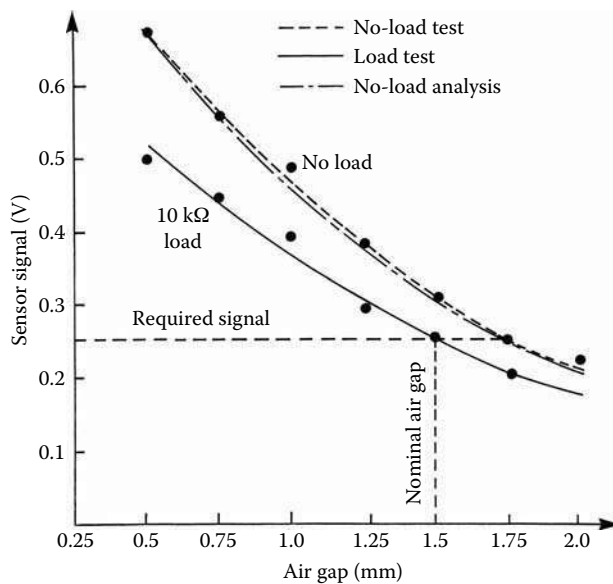


**FIGURE 2.44**  
Sensor signal vs. air gap test and analysis.

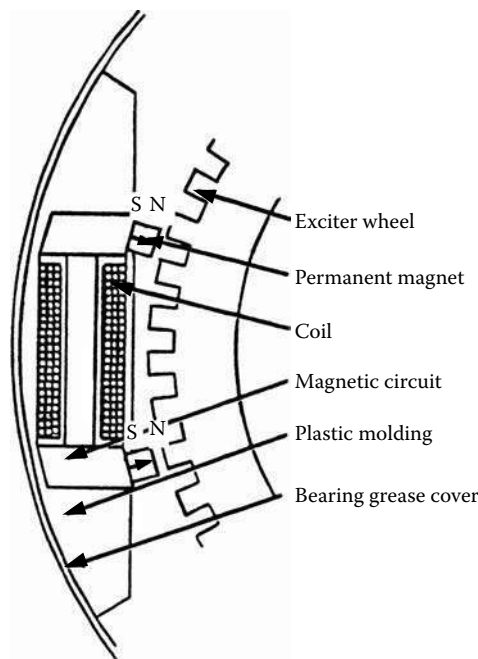
### 2.3.7 Multiple Magnets VR Sensors

A need to boost sensor performance that provides a high signal at a low speed of the exciter wheel led to the development of the VR sensor configuration with multiple magnets (Pawlak et al. 1991d, Pawlak and Shirai 1988, Pawlak et al. 1991a, Pawlak et al. 1991b, Shirai and Pawlak 1995a, Shirai and Pawlak 1995b). Such a requirement for a sensor performance came from an automotive application for the ABS. The particularly difficult sensor environment with high ambient temperature around the brakes led also to the selection of magnet material that is stable at elevated temperatures. Consequently, the two-magnet partially distributed sensor led to the magnetically distributed ring-shape sensor with a multipole magnet that would fit best and could be integrated within the bearing grease cover. This sensor is very desirable for manufacturing because only radial air gaps and radial tolerances are involved, unlike other sensors where an axial air gap is present. The sensor's magnetic distribution nature would also help compensate for the radial tolerances, as noted during the lumped element sensor's development, as presented in Section 2.3.9 and Section 2.6.

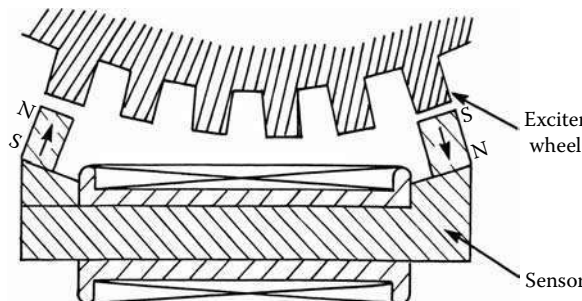
### 2.3.8 Dual-Magnet Sensors

The very tight envelope for a VR sensor structure within a grease cover of the wheel bearing led to the development of a magnetically partially distributed sensor structure with two magnets. Figure 2.43 shows a VR sensor structure with two magnets distributed along the teeth of the exciter wheel.

Magnets are mechanically attached to both ends of the magnetic circuit with one coil placed between magnets. Both magnets are in close proximity to the exciter wheel, which is right at the air gap, having in this design an unconventional sensor-wheel arrangement. Conventionally, all VR sensors are arranged in the same manner with respect to the exciter wheel, where the sensor pole is placed against the tooth of the exciter wheel for the

**FIGURE 2.43**

Two-magnet VR sensor with an exciter wheel.

**FIGURE 2.44**

Conventional sensor-wheel arrangement for two-magnet VR sensor with supportive magnetization. (From Lequesne, B. et al., *Transactions of IEEE/IAS*, 32(5), 1166–1175, 1996. With permission.)

maximum magnetic permeance. When the exciter wheel rotates one pole pitch, the pole is located against a slot for the maximum permeance. The sensors utilize the difference between the maximum and the minimum magnetic permeance positions to develop the signal. To utilize the conventional sensor-wheel arrangement for the sensor with more than one pole, all of them must be positioned against the teeth of the exciter wheel at the maximum sensor position; for the minimum permeance position, they must be positioned against the exciter wheel slots. These two positions provide the highest magnetic flux-linkage variation and the maximum sensor signal of the conventional sensor arrangement, which requires that PMs must be polarized in the supporting direction in order to develop the sensor signal, as presented in Figure 2.44.

Figure 2.44 shows the front-mounted-magnet sensor with two magnets. This sensor consists of a coil, a magnetic circuit, and two PMs located in proximity of the exciter wheel.

The magnetic core consists of three elements: a cylindrical central rod and two rectangular magnet supporters on both sides of the rod. For the sensor, which is designed without a bobbin, the magnetic core made out of soft iron must have at least two separate parts in order to assemble the coil. For the bobbinless coil design, where the coil is placed directly on the insulated (blue-coated) central rod, the magnetic core can be made out of one part using a powder-metal technology. The PM's shape is rectangular or trapezoidal depending on the method used for PM attachment to the magnetic core. The trapezoidal magnet is desirable, holding magnets attached to the magnetic core using a plastic-molding technology; although, a rectangular magnet shape can be used if magnets are glued to the magnetic core. For this configuration, high-energy magnets are desirable and, depending on the application and operating temperature, the magnet material can be neodymium or samarium-cobalt-based.

Analysis of the VR two-magnet sensor configuration requires the investigation of the signal generated in the coil. For analytical purposes only, it is assumed that the coil is split into two identical coils, each equal to one half of the original coil and both connected in a series to make a full coil. It is also assumed that both PMs assigned as PM 1 and PM 2 with identical geometry and material properties having the same distance to the exciter wheel's teeth are capable of generating identical flux  $\phi_1$  and  $\phi_2$ , respectively. In such a case, the total signal is a superposition of the signal components with appropriate phase and polarization as indicated below:

$$v = v_1 + v_2 \quad (2.13)$$

where  $v$ ,  $v_1$ , and  $v_2$  are the sensor signal, the signal component of coil 1, and the signal component of coil 2, respectively. With the assumption of the sinusoidal permeance variation, both signal components  $v_1$  and  $v_2$  can be expressed as:

$$v_1 = -\frac{d\phi_1}{dt} \times \sin \theta \quad (2.14)$$

$$v_2 = -\frac{d\phi_2}{dt} \times \sin \theta \quad (2.15)$$

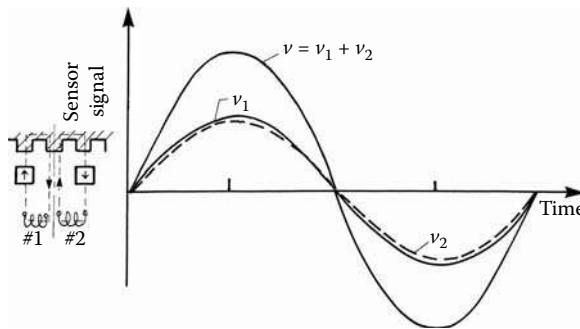
where  $\phi_1$  is a magnetic flux embraced by coil 1,  $\phi_2$  is a magnetic flux embraced by coil 2, and  $\theta$  is the sensor or rotor position. Combining Equation 2.13 with Equation 2.15, the total signal strength becomes:

$$v = -\left( \frac{d\phi_1}{dt} + \frac{d\phi_2}{dt} \right) \times \sin \theta \quad (2.16)$$

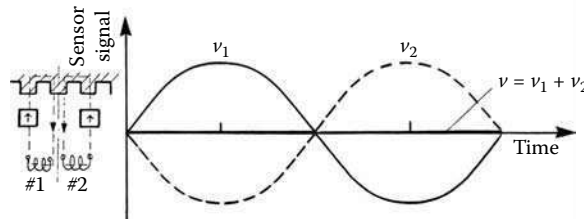
If  $\phi_1 = \phi_2$ , the total signal is:

$$v = -2 \frac{d\phi_1}{dt} \times \sin \theta \quad (2.17)$$

Figure 2.45 presents the sensor arrangement that corresponds to Equation 2.17 with the same flux sign for both PMs as they support each other. The signal components for magnets are arranged in the same manner with respect to the exciter wheel teeth. The total signal

**FIGURE 2.45**

Sensor signal for the conventional sensor-wheel arrangement for two-magnet VR sensor with supportive magnetization. (From Pawlak, A.M. et al., *Novel Variable Reluctance Sensors*, Publ. No. 910902, Society of Automotive Engineers, Detroit, MI, 1991. With permission.)

**FIGURE 2.46**

Sensor signal for the conventional sensor-wheel arrangement for two-magnet VR sensor with non-supportive magnetization. (From Pawlak, A.M. et al., *Novel Variable Reluctance Sensors*, Publ. No. 910902, Society of Automotive Engineers, Detroit, MI, 1991. With permission.)

reaches its maximum value in this arrangement. The use of a return path and a front-mounted-magnet approach led to a novel configuration, shown in Figure 2.45. It features two “supportive magnets” in a series in the magnetic circuit. This design provides a high output signal despite the relatively small sensor height required by this application.

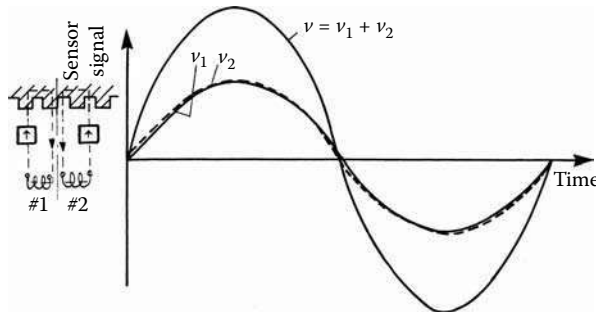
If the direction of magnetization of magnet 2 is reversed by  $180^\circ$ , then the magnetic flux  $\phi_2$  generated by this magnet is changing its sign. Therefore, the signal  $v_2$  component can be expressed as:

$$v_2 = \frac{d\phi_2}{dt} \times \sin \theta \quad (2.18)$$

Combining Equations 2.13, 2.14, and 2.18, the total signal strength becomes:

$$v = -\left( \frac{d\phi_1}{dt} - \frac{d\phi_2}{dt} \right) \times \sin \theta \quad (2.19)$$

Figure 2.46 presents the sensor arrangement that corresponds to Equation 2.19 with the opposite flux signs because the PMs do not support each other. The signal components for magnets are arranged in the same manner with respect to the exciter wheel teeth. The total signal reaches its maximum value in this arrangement. If  $\phi_1 = \phi_2$ , the total signal is zero, as presented in Figure 2.46.

**FIGURE 2.47**

Sensor signal for the nonconventional sensor-wheel arrangement for two-magnet VR sensor with nonsupportive magnetization. (From Pawlak, A.M. et al., *Novel Variable Reluctance Sensors*, Publ. No. 910902, Society of Automotive Engineers, Detroit, MI, 1991. With permission.)

Figure 2.47 shows a nonconventional sensor-wheel arrangement, where one of the magnets is facing a tooth and the other is facing a slot. For this arrangement, the sensor's PMs are assembled with opposite polarization and, therefore, facing the exciter wheel with the same polarities. If the magnetization of the PM 2 and its location change in comparison with the base design, as shown in Figure 2.47, then the signal sign and phase of coil 2 will change while the other components remain the same as the base design. Therefore, the signal  $v_2$  component can be expressed as:

$$v_2 = -\frac{d\phi_2}{dt} \times \sin(\theta + 180) \quad (2.20)$$

Combining Equations 2.13, 2.14, and 2.20, the total signal strength becomes:

$$v = -\left( \frac{d\phi_1}{dt} + \frac{d\phi_2}{dt} \right) \times \sin \theta \quad (2.21)$$

If  $\Phi_1 = \Phi_2$ , the total signal is:

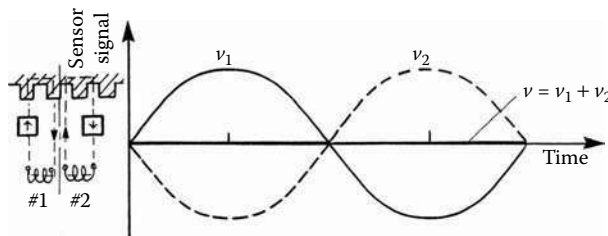
$$v = -2 \frac{d\phi_1}{dt} \times \sin \theta \quad (2.22)$$

If the direction of magnetization of magnet 2 is reversed by  $180^\circ$ , then the magnetic flux  $\phi_2$  generated by this magnet is changing its sign, as presented in Figure 2.48. Therefore, the signal  $v_2$  component can be expressed as:

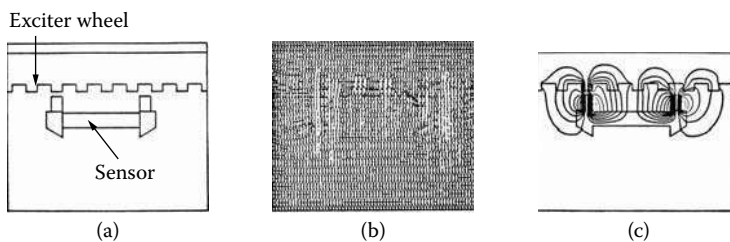
$$v_2 = -\frac{d\phi_2}{dt} \times \sin(\theta + 180) \quad (2.23)$$

Combining Equations 2.13, 2.14, and 2.23, the total signal strength becomes:

$$v = -\left( \frac{d\phi_1}{dt} - \frac{d\phi_2}{dt} \right) \times \sin \theta \quad (2.24)$$

**FIGURE 2.48**

Sensor signal for the nonconventional sensor-wheel arrangement for two-magnet VR sensor with supportive magnetization. (From Pawlak, A.M. et al., *Novel Variable Reluctance Sensors*, Publ. No. 910902, Society of Automotive Engineers, Detroit, MI, 1991. With permission.)

**FIGURE 2.49**

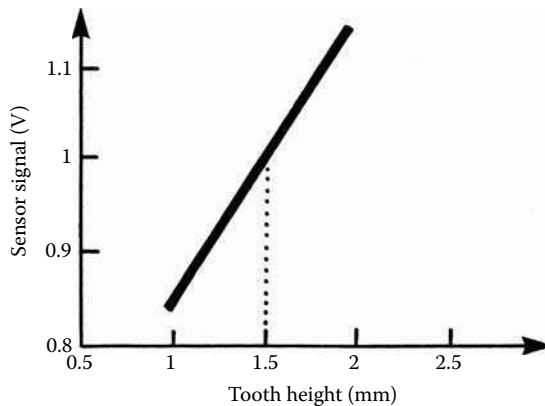
Two-magnet VR sensor FE model: (a) configuration, (b) grid, (c) flux lines. (From Pawlak, A.M. et al., *Novel Variable Reluctance Sensors*, Publ. No. 910902, Society of Automotive Engineers, Detroit, MI, 1991. With permission.)

Figure 2.48 presents the sensor arrangement that corresponds to Equation 2.24 with the opposite flux signs because these PMs do not support each other. The signal components for magnets are arranged in the same manner with respect to the exciter wheel teeth. The total signal reaches its minimum value in this arrangement. If  $\phi_1 = \phi_2$ , the total signal is zero.

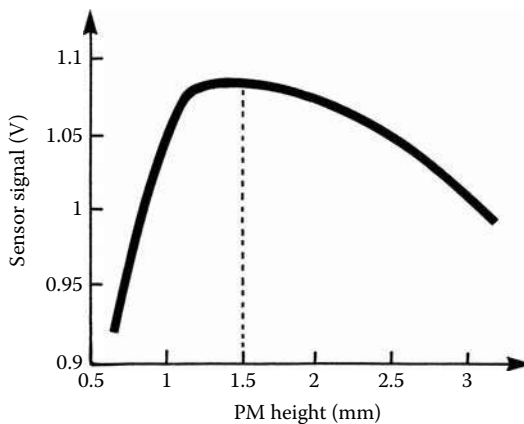
Thus, depending on the sensor-wheel arrangement, a sensor signal could be the maximum or zero. The signal developed by the sensor equals zero for both the conventional sensor-wheel arrangement with nonsupportive magnets and the sensor structure with supporting magnets and nonconventional sensor-wheel arrangement. Conversely, maximum signal strength can be obtained for both the conventional sensor-wheel arrangement and supportive magnets as well as the nonconventional sensor-wheel arrangement with nonsupportive magnets configuration. This structure was analyzed and designed using the FE technique. Assuming that the exciter radius is very large, Figure 2.49 shows the sensor configuration, mesh structure, and the flux lines.

Optimization of the exciter wheel and the sensor was conducted in the same manner as other sensor structures. This sensor configuration was optimized with the limitations that the total sensor height and width were restricted by the existing grease cover dimensions. First, the exciter wheel was optimized. Then the tooth height was investigated, indicating significant sensor improvement potential for higher teeth, as shown in Figure 2.50. Because powder-metal technology limits the exciter wheel slot depth, it was not possible to entirely utilize this gain. Again, it may be used in the future with further advances in powder-metal technology.

The PM height, which affects the total MMF developed and, consequently, the flux level and the signal strength, was also optimized. Implementing the selected magnetic material and optimizing PM height to  $1.5 \times 10^{-3}$  m, the signal strength improved about 8%, as shown in Figure 2.51.

**FIGURE 2.50**

Two-magnet VR sensor signal vs. exciter wheel tooth height. (From Pawlak, A.M. et al., *Novel Variable Reluctance Sensors*, Publ. No. 910902, Society of Automotive Engineers, Detroit, MI, 1991. With permission.)

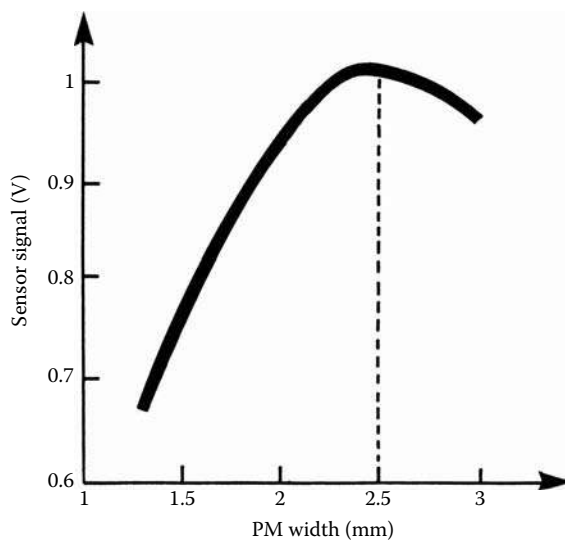
**FIGURE 2.51**

Two-magnet VR sensor signal vs. PM height. (From Pawlak, A.M. et al., *Novel Variable Reluctance Sensors*, Publ. No. 910902, Society of Automotive Engineers, Detroit, MI, 1991. With permission.)

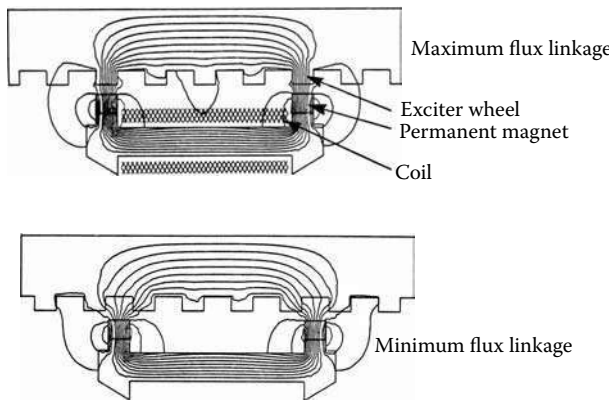
As proven previously for the front-mounted-magnet sensors, the width of the magnet has to be related to the exciter wheel tooth-slot width. Therefore, a PM width equal to the slot opening is the best dimension for this configuration. A PM width different from the exciter wheel tooth-slot width decreases the magnetic flux change, resulting in signal strength reduction, as presented in Figure 2.52. A variation of 40% of the magnet width can cause about 30% signal reduction.

For the conventional sensor-wheel arrangement and positive magnet polarization, the main magnetic path crosses both magnets, the central rod, and the exciter wheel. The entire magnetic flux links the coil, as presented in Figure 2.53. Only a small amount of the leakage flux is utilized for the signal generation.

For the nonconventional sensor-wheel arrangement, the sensor PMs are assembled with opposite polarization, facing the exciter wheel with the same polarities. The arrangement with opposite magnet polarization provides lower flux but much improved flux variations, thus enhancing the sensor signal strength. In this case, the magnets are offset by one half of a tooth pitch as compared to the design shown in Figure 2.55. Such an arrangement of

**FIGURE 2.52**

Two-magnet VR sensor signal vs. PM width. (From Pawlak, A.M. et al., *Novel Variable Reluctance Sensors*, Publ. No. 910902, Society of Automotive Engineers, Detroit, MI, 1991. With permission.)

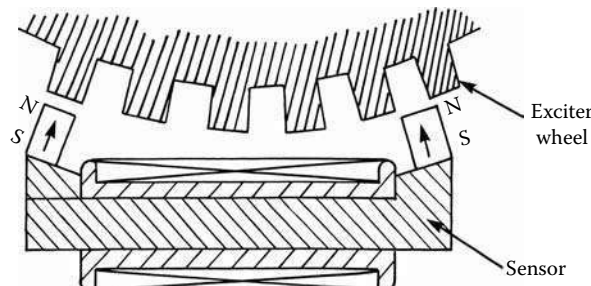
**FIGURE 2.53**

Flux lines of the two-magnet VR sensor with supportive magnetization and conventional sensor-wheel arrangement. (From Pawlak, A.M. et al., *Novel Variable Reluctance Sensors*, Publ. No. 910902, Society of Automotive Engineers, Detroit, MI, 1991. With permission.)

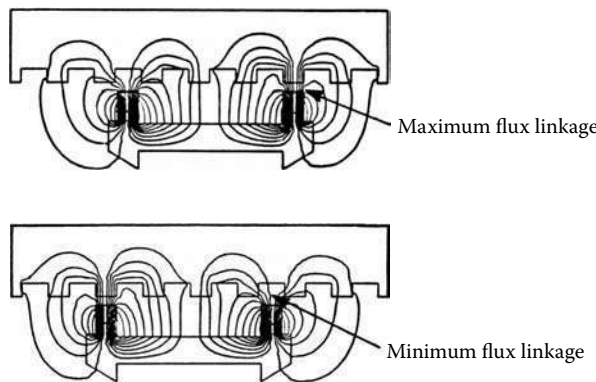
magnet polarization is nonsupporting for the magnetic flux; therefore, the magnetic flux links the coil from each magnet with different directions, as presented in Figure 2.53. The performance of the sensor was further improved, by a factor of 2.0, by assembling the magnets with opposite polarization, thus facing the target wheel with the same polarity but with a nonconventional sensor-wheel arrangement, as presented in Figure 2.54.

In this case, each of the magnets has its own magnetic path for the magnetic flux. A substantial amount of the magnetic flux is utilized for the signal generation.

There is significant difference in magnetic flux distributions for the supportive and nonsupportive magnet sensor arrangements. Because of the magnetic flux linking, the coil for the nonsupportive magnets is more sensitive for the exciter wheel position compared with the supportive magnet arrangement. Therefore, as shown in Figure 2.56, the sensor

**FIGURE 2.54**

Nonconventional sensor-wheel arrangement of the two-magnet VR sensor with nonsupportive magnetization. (From Lequesne, B. et al., *Transactions of IEEE/IAS*, 32(5), 1166–1175, 1996. With permission.)

**FIGURE 2.55**

Flux lines of the two-magnet VR sensor with nonsupportive magnetization and nonconventional sensor-wheel arrangement. (From Pawlak, A.M. et al., *Novel Variable Reluctance Sensors*, Publ. No. 910902, Society of Automotive Engineers, Detroit, MI, 1991. With permission.)

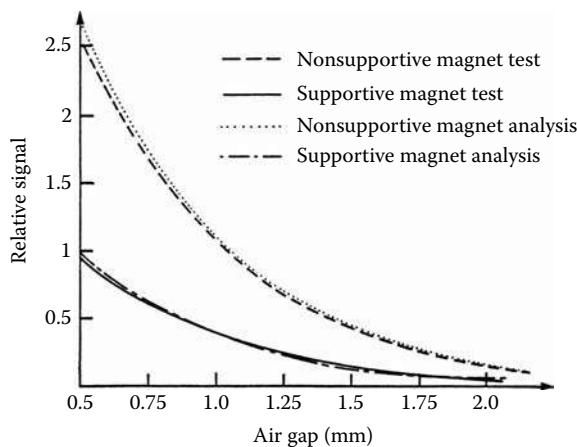
signal performance is superior to that of a sensor with the supportive magnets. The figure also shows an excellent correlation between the tests and the analysis based on an FE mathematical model.

Test results very closely match this analysis, within 5% for the wide range of air gaps, as shown in Figure 2.56. This also confirms that the signal sensor for nonconventional arrangements is superior to the conventional arrangement over the wide range of air gaps between the sensor and the exciter wheel. Vehicle performance evaluation tests, including temperature and noise tests, also indicated excellent sensor performance in automotive applications.

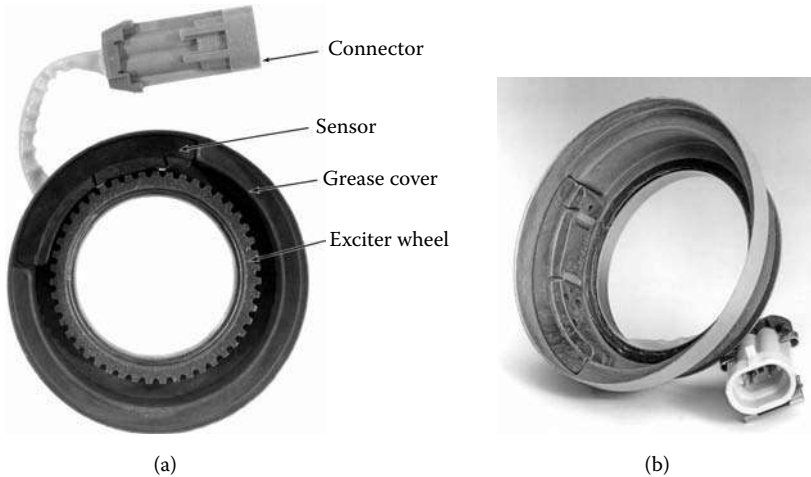
These sensors found an application in most of General Motors' passenger vehicles providing a wheel speed signal to the ABS system. Figure 2.57 shows two-magnet VR sensor components and assembly. Because this wheel sensor is located in close vicinity to the brake system where elevated temperature may be a typical sensor environment, this application requires 200°C temperature stability, and therefore, the samarium-cobalt magnet material SmCo17 was selected with 27.0 MGOe energy density.

### 2.3.9 Dual Sensor Arrangement

Two factors led to the development of the magnetically distributed sensor configuration. One is concerned with the shape of the wheel-bearing grease cover, where the sensor

**FIGURE 2.56**

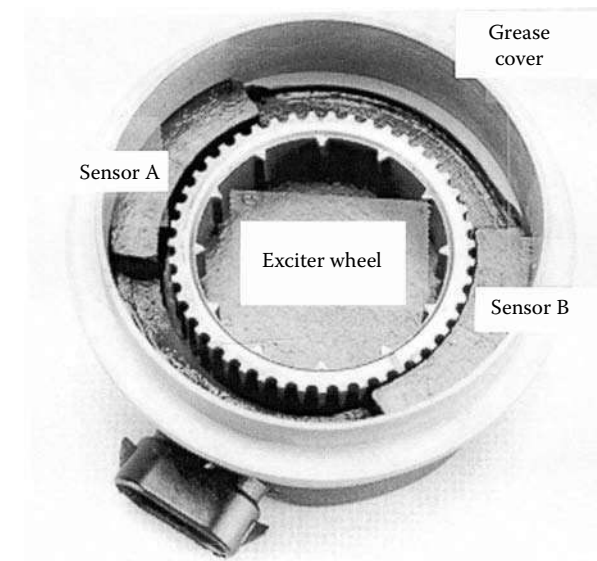
Analysis and test signal vs. air gap comparison for the nonconventional and conventional sensor-wheel arrangements of the two-magnet VR sensor. (From Lequesne, B. et al., *Transactions of IEEE/IAS*, 32(5), 1166–1175, 1996. With permission.)

**FIGURE 2.57**

Two-magnet sensor assembly: (a) sensor components, (b) sensor assembly. (Courtesy of Delphi Corp.)

would be integrated, and the second is concerned with the reduced sensitivity of the distributed sensor to the radial tolerances that offset the exciter wheel with respect to the sensor. A ring-shaped sensor would fit best and could be integrated within the bearing grease cover and its magnetic distribution nature would help compensate for the variation of radial tolerances, a deficiency that was noticed during the lumped element and partially distributed sensor's development.

In order to simulate a magnetically distributed sensor, two of the lumped element sensors (*A* and *B*) were assembled together and tested (Adams et al. 1991). Actually, the presented *A* and *B* sensors are partially distributed sensors described in Chapter 1. These sensors were assembled and electrically connected as a dual sensor arrangement 180° apart, as shown in Figure 2.58. The sensor's opposite location is selected to compensate for the offset due to tolerances of the shaft and exciter wheel. The sensor's signal vs. time

**FIGURE 2.58**

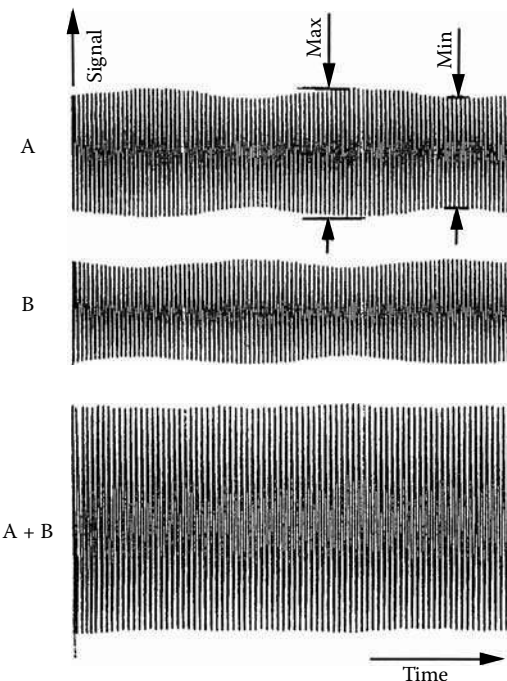
Two dual-magnet sensor arrangement. (Pawlak, A.M. et al., *Distributed Variable Reluctance Sensors*, Publ. No. 991039, Society of Automotive Engineers, Detroit, MI, 1999. With permission.)

characteristics are presented in Figure 2.59 for both the individual ( $A$  or  $B$ ) and combined ( $A+B$ ) sensor signals. Figure 2.59 also identifies both the local minimum and maximum signal values, which occur at local maximum and minimum air gaps, respectively, due to the exciter wheel offset. Table 2.4 presents the maximum and minimum signal values for both the individual ( $A$ ,  $B$ ) and combined ( $A+B$ ) sensor signals obtained from the test characteristics. The data were obtained for the concentric (no offset) sensor-wheel arrangement. The combined sensor signal ( $A+B$ ) shows only 3.1% tolerance sensitivity but individually each of the ( $A$ ,  $B$ ) sensors shows 14.3% and 13.5% signal variation, respectively, under the same conditions presented in Table 2.4 and Figure 2.58. The results proved the concept of the distributed sensor structure advantages. A clever solution to this problem is the distributed sensor described in Section 2.3.10.

### 2.3.10 Distributed VR Sensors

Distributed sensor configuration utilizes the entire exciter wheel all the time. Therefore, all tooth-pitch segments contribute to the sensor signal at any position. Conceptually, this requires the sensor to have multiple pole pairs that correspond to the exciter wheel tooth pitch. Each pole pair contributes to the signal independently under the condition that there is a common coil that collects all the signal components and the total sensor signal would be a sum of all signal vector components. Therefore, there is no signal cancellation at any time. The coil must be located in close vicinity of the flux-linkage changes and the magnetic circuit should guide the magnetic flux three-dimensionally to cross the coil. The distributed VR sensor concept presented in Figure 2.60 meets all these requirements (Pawlak 1999, Shirai and Pawlak 1993, Shirai and Pawlak 1996, Pawlak 1992a).

A distributed VR sensor features a ring structure, which consists of a coil and a multiplicity of evenly distributed magnets, as shown in Figure 2.60. In fact, the magnetically distributed sensor consists of a set of independent sensing devices, each having a PM, a section of the magnetic circuit, and a coil segment. Each of the independent sensor

**FIGURE 2.59**

Dual lumped element sensor signal vs. time: (a) sensor A, (b) sensor B, (c) sensors A and B. (Pawlak, A.M. et al., *Distributed Variable Reluctance Sensors*, Publ. No. 991039, Society of Automotive Engineers, Detroit, MI, 1999. With permission.)

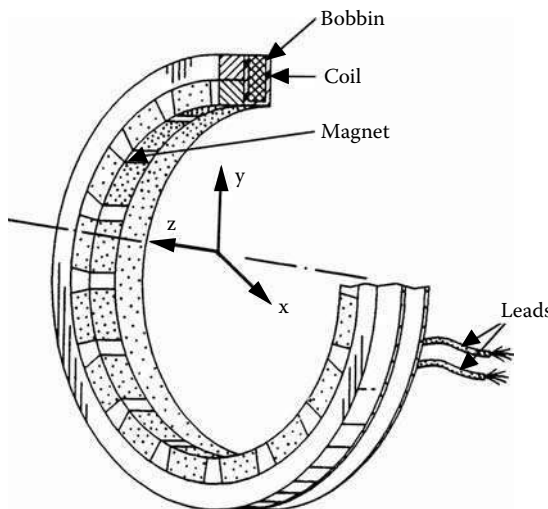
**TABLE 2.4**  
Distributed Sensor Comparison

Sensor or Signal	Maximum (V)	Minimum (V)	Location	Change (%)
Sensor A	1.26	1.09	Center	14.3
Sensor B	1.07	0.917	Center	13.5
Sensors A + B	2.15	2.22	Center	3.1

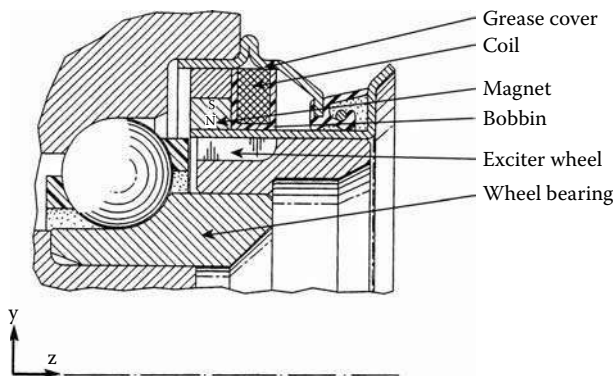
Source: Pawlak, A.M. et al., *Distributed Variable Reluctance Sensors*, Publ. No. 991039, Society of Automotive Engineers, Detroit, MI, 1999. With permission.

segments with a magnet contributes to the signal generation that enhances the total signal of the coil. The distributed sensor senses a toothed exciter wheel, which provides the VR effect on the magnetic field during rotation.

This sensor structure utilizes variation of the magnetic field three-dimensionally, rather than the conventional 2D sensor-excitator wheel arrangement, as presented in Figure 2.61 and Figure 2.62. Figure 2.61 shows the distributed sensor integrated with a wheel bearing, and Figure 2.62 identifies the magnetic flux path for this arrangement. In this structure, the flux lines are linked to the coil's turns and contribute to the signal generation along the axis of symmetry of the wheel bearing ( $y$ - $z$  plane) rather than in a perpendicular  $x$ - $y$  plane, which is utilized for conventionally arranged sensors. The ring-shaped distributed sensor also utilizes the modulation of that flux by the movement of the excitor wheel but in the  $y$ - $z$  plane. The distributed sensor consists of a series of independent sections, which generate signal components. Each section facing a tooth-slot segment (one pole pitch) of

**FIGURE 2.60**

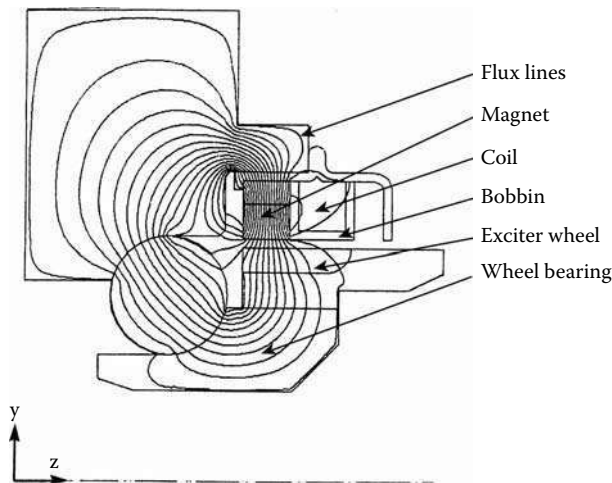
Magnetically distributed VR sensor configuration. (Pawlak, A.M. et al., *Distributed Variable Reluctance Sensors*, Publ. No. 991039, Society of Automotive Engineers, Detroit, MI, 1999. With permission.)

**FIGURE 2.61**

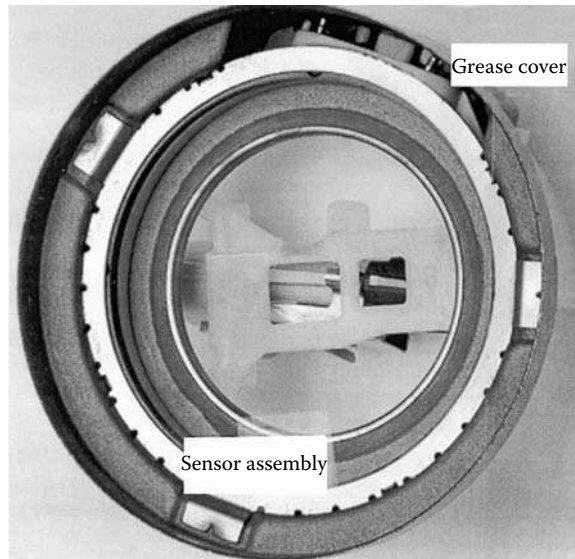
Distributed VR sensor-wheel assembly. (Pawlak, A.M. et al., *Distributed Variable Reluctance Sensors*, Publ. No. 991039, Society of Automotive Engineers, Detroit, MI, 1999. With permission.)

the exciter wheel makes a separate sensing device, and the continuous sensor coil is common for all of them and collects the individual sensor section's signal components in a combined total sensor signal. Therefore, such a sensor configuration allows for both the ring-shaped sensor to be integrated within the wheel bearing and to provide a magnetically distributed structure with low sensitivity to the variation of the radial tolerances. In its final design, the distributed sensor consists of two components only — a radially oriented multipole magnet and a coil. The coil's bobbin holds both the coil and the magnet. Figure 2.63 shows a picture of a distributed sensor assembled within a grease cover.

For mass production purposes, the magnet can be in the form of a multipole ring magnet molded with plastic or a multipole strip of a flexible resin-type material, which is bent to form a ring after it is magnetized. Figure 2.64 and Figure 2.65 show the sensor magnetized multipole magnet: one made using flexible magnet material, Figure 2.64, and the other with the plastic-molded multipole ring magnet, Figure 2.65. The flexible magnet, when assembled, will form a ring-shaped structure that is well integrated within the wheel

**FIGURE 2.62**

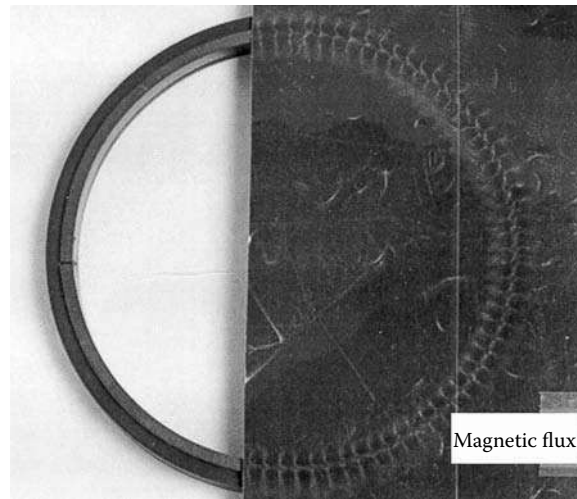
Flux lines of the distributed VR sensor. (Pawlak, A.M. et al., *Distributed Variable Reluctance Sensors*, Publ. No. 991039, Society of Automotive Engineers, Detroit, MI, 1999. With permission.)

**FIGURE 2.63**

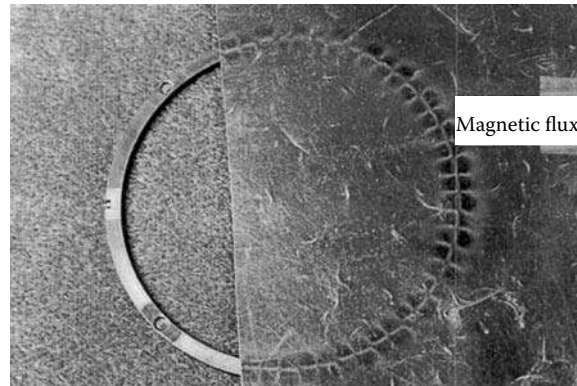
Distributed sensor assembly. (Pawlak, A.M. et al., *Distributed Variable Reluctance Sensors*, Publ. No. 991039, Society of Automotive Engineers, Detroit, MI, 1999. With permission.)

bearing grease cover. Magnetically sensitive film, which covers part of the magnet, indicates its magnetization. As shown, both the flexible and plastic-molded magnets are magnetized radially with multipole magnetization.

The flexible resin ring magnet, presented in Figure 2.64, is radially magnetized with 96 poles ( $p = 48$ ), and the plastic-molded ring magnet is magnetized radially with 58 poles ( $p = 29$ ), as presented in Figure 2.65. A large number of poles significantly enhances the sensor signal, which is proportional to the number of independent sections. It also helps

**FIGURE 2.64**

Flexible resin multipole ring magnet. (Pawlak, A.M. et al., *Distributed Variable Reluctance Sensors*, Publ. No. 991039, Society of Automotive Engineers, Detroit, MI, 1999. With permission.)

**FIGURE 2.65**

Plastic-molded multipole ring magnet. (Pawlak, A.M. et al., *Distributed Variable Reluctance Sensors*, Publ. No. 991039, Society of Automotive Engineers, Detroit, MI, 1999. With permission.)

reduce cost because it allows for a low-cost magnet material. In the case presented, the selected plastic-molded magnet-material energy density is less than 10.0 MGOe.

The signal of the VR sensor generated in the sensor coil is a time variation of the total flux linkage as shown in Equation 2.1, which is a function of time  $t$  and position  $\theta$ , given by:

$$\nu(t) = -N \frac{d\phi}{dt} = -N \frac{d\phi}{d\theta} \frac{d\theta}{dt} = -N\omega \frac{d\phi}{d\theta} \quad (2.25)$$

For the distributed sensor, the total sensor signal is the sum of the separate signal components that are generated by the individual sensor sections for each of the tooth-slot segments of the exciter wheel and the corresponding magnetic flux linkages for a single pole-pair section:

$$v_d(t) = \sum_{i=1}^p v_i \quad (2.26)$$

If the sensor-wheel arrangement is not concentric for every segment, the sensor air gaps are different and every section of the sensor generates a different signal level. In particular, sections with a small air gap between the sensor and the exciter wheel embrace high magnetic flux and generate a high signal, whereas sections exposed to large air gaps generate a low signal. Generally, the flux linked to the coil (with the same number of  $N$  turns for each section) for all the sections 1, 2, ...,  $p$  is different:

$$\phi_1 \neq \phi_2 \neq \dots \neq \phi_p \quad (2.27)$$

When Equations 2.25 through 2.27 are combined, the total distributed sensor signal can be expressed as:

$$v_d(t) = -N\omega \frac{d}{d\theta} \sum_{i=1}^p \phi_i \quad (2.28)$$

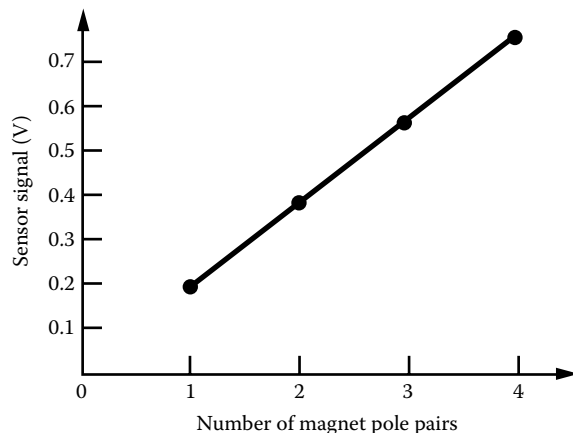
With the exciter wheel offset in the distributed sensor structure for each section, which generates a low signal, there is another section that generates a high signal. Because the total signal is the sum of all section signals and the number of sections contributing low signals is the same as the number of sections contributing high signals, the resultant total signal of the sensor is expected to be constant, as presented in Figure 2.59 ( $A + B$ ). For the concentric sensor-wheel arrangement, all air gaps are identical and the level of the magnetic flux for all the sections 1, 2, ...,  $p$  is also the same:

$$\phi_1 = \phi_2 = \dots = \phi_p = \phi_m \quad (2.29)$$

where  $v_d$  is the voltage generated in a coil of the distributed sensor,  $\phi_1$  is a magnetic flux embraced by the coil 1,  $\phi_2$  is a magnetic flux embraced by the coil 2,  $\phi_m$  is a median magnetic flux embraced by the coil for a single pole-pair section,  $\phi_p$  is a magnetic flux embraced by the  $p$  single pole-pair section,  $p$  is the number of magnet pole pairs or sensor sections,  $\omega$  is an angular speed, and  $\theta$  is the sensor or rotor position. When Equations 2.23, 2.24, and 2.27 are combined, the total sensor signal can be expressed as:

$$v_d(t) = -N\omega p \frac{d\phi_m}{d\theta} \quad (2.30)$$

Therefore, the signal of each section is the same and the total sensor signal is proportional to the number of  $p$  sections. The total signal of the distributed sensor signal is a function of the number of turns, angular speed of the target wheel, the number of pole pairs, and the variation of the median magnetic flux for the two extreme wheel positions. Unlike the lumped element sensor, the distributed sensor is a linear function of the number of magnets (pole pairs) (compare Equation 2.25 and Equation 2.30). Therefore, for a distributed sensor, it is advantageous to employ the maximum possible number of magnet pole pairs, which provides a magnetic gearing effect. The maximum signal value can be

**FIGURE 2.66**

Distributed sensor signal vs. number of pole pairs. (Pawlak, A.M. et al., *Distributed Variable Reluctance Sensors*, Publ. No. 991039, Society of Automotive Engineers, Detroit, MI, 1999. With permission.)

**TABLE 2.5**  
VR Sensor Signal Comparison

Sensor or Signal	Maximum (V)	Minimum (%)	Location	Change (%)
Lumped	1.88	1.26	Center	39.5
Lumped	1.6	1.01	Offset $x$	45.2
Lumped	1.94	0.98	Offset $y$	65.7
Distributed	1.67	1.5	Center	10.7
Distributed	1.39	1.39	Offset $x$	21.8
Distributed	1.46	1.46	Offset $y$	14

Source: Pawlak, A.M. et al., *Distributed Variable Reluctance Sensors*, Publ. No. 991039, Society of Automotive Engineers, Detroit, MI, 1999. With permission.

achieved for the multiplicity of magnets that are evenly distributed where one magnet pole faces a slot and another magnet with opposite magnetization faces a tooth and the number of magnets equals the number of teeth (slots) of the exciter wheel.

A number of distributed sensors were manufactured and tested. Today it is the most popular VR sensor design and has penetrated passenger vehicle markets in the millions every year. At first, all sensor magnets were assembled with segment magnets distributed symmetrically on the circumference of the sensor. All magnets with the same polarities are pointing toward the exciter wheel's teeth while the space between the magnets is facing the exciter wheel's slots. Therefore, one tooth pitch that is facing a magnet pole pitch is forming an independent sensor section. Figure 2.66 shows a sensor test that has various numbers of evenly distributed magnets. Because the characteristic presented is linear, it supports the developed mathematical model and proves that the distributed sensor signal is a function of the number of magnet pole pairs.

To verify the effect of concentricity between the sensor and the exciter wheel, as shown in Equation 2.26, both the distributed and lumped element sensors were tested. Table 2.5 shows the test results where the signal values were obtained at a constant speed of 200.0 r/min of the exciter wheel while introducing the concentric or  $x$  and  $y$  offsets of  $1.0 \times 10^{-3}$  m.

Results collected in Table 2.5 indicate that the percentage of the lumped element sensor signal variation is about four times that of the distributed sensor under the same sensor-wheel conditions. Therefore, one can conclude that the distributed sensor is superior to the lumped element sensor because the distributed sensor is less sensitive to the tolerance variations and provides a more stable signal in comparison to the lumped element sensor. Test results support the developed mathematical model and prove that, unlike the lumped element sensor, the distributed sensor signal is a function of a number of magnet pole pairs. The tests indicated that the percentage of the lumped element sensor signal variation is about four times of that variation for the distributed sensor under the same sensor-wheel conditions. A distributed sensor features structural simplicity and superior performance in comparison with the lumped element sensors.

---

## 2.4 Solid-State Sensors

The function of the solid-state sensors depends on the presence of the magnetic field; therefore, its effectiveness depends on the quality of the magnetic circuit. Both, the magnetoresistors and the Hall-effect generators fall into the category of the solid-state sensors (Ramsden 2001). Magnetoresistors are magnetically influenced resistors based on the InSb or NiSb material that acts on the Gaussian effect. The charge carriers that flow through the semiconductor material experience a sideways action in the presence of transverse magnetic field by Lorentzian forces. The Hall effect, named after its discoverer Edvin Hall, is the result of the Lorentzian force on electrons through the material when exposed to magnetic field  $B$ . The flow of the current without the presence of the magnetic field has a linear path and the equipotential electrical lines are perpendicular to the current flow path. In the presence of the magnetic field, the Lorentzian forces  $F$  that are affecting electrons are:

$$F = q/\sigma(j * B) \quad (2.31)$$

where  $F$  is the magnetic field of the Lorentzian forces,  $q$  is the electron charge,  $\sigma$  is the material conductivity,  $j$  is the current density, and  $B$  is the magnetic field density.

The cross product indicates that the force is in the direction perpendicular to the current flow and the magnetic field. The angle through the current flow is changed by the presence of the magnetic field  $B$  and is called the Hall angle  $\theta_H$ . The material specifically determined by the electron mobility  $\mu$  determines the Hall coefficient  $R_H$ . With the presence of the magnetic field, the equipotential lines are skewed and this generates the Hall voltage  $V_H$  across the material. The angle between the original current and that to which it charges on the introduction of the magnetic field is known as the Hall angle  $\delta$ . It depends on the electron mobility  $\mu$  and the magnetic field density  $B$ .

$$\tan \delta = \mu * B \quad (2.32)$$

where  $\mu$  is the electron mobility and  $B$  is the magnetic field density.

For the InSb material, the exceptionally high electron mobility of  $7.0 \text{ m}^2/\text{Vs}$  results in a Hall angle of  $\delta = 80^\circ$  with  $B = 1.0 \text{ T}$ . As opposed to Hall generators, the InSb crystal has, irrespective of the low-resistive NiSb that it has alloyed into, maintained an equal distribution of the charge carriers throughout its cross section. The lengthening of the paths of

the charge carriers with increasing magnetic field results in an increase of the resistance of the magnetoresistor that is dependent on the magnetic field polarity.

Although present in all materials, the Hall effect is practical in only a few materials, where the electron mobility is high, such as gallium arsenite, indium antimonite, and with amplification done on a chip it is usable also in silicon and germanium. The result of the simultaneous action of these parameters is the generation of the voltage  $V_H$  across the chip:

$$V_H = R_H * I_1 * B/d \quad (2.33)$$

Providing the supplied current  $I_1$  is constant and  $R_H$  is the Hall constant of the material, the resultant voltage  $V_H$  is a function of the magnetic field density  $B$ . This allows the Hall generator to be used as a sensing device commonly known as a Hall sensor or an MR sensor.

#### 2.4.1 Solid-State Sensor Analysis

The electric characteristics of some semiconductors depends on the magnetic field to which they are exposed. In Hall-effect devices, a voltage can be measured, and in magnetoresistors, a resistance variation is observed. If such a semiconductor is located on a stationary magnet across from a moving wheel, as shown in Figure 2.2, an electric signal  $v(t)$  is obtained, which reflects the permeance changes due to the wheel motion. If the size of the semiconductor were infinitely small, the signal  $v(t)$  at time  $t$  would be (Lequesne et al. 1996):

$$v(t) = f[B(\theta(t))] \quad (2.34)$$

where  $f(B)$  is the characteristic of the semiconductor and  $\theta(t)$  is the position of the semiconductor at time  $t$ .

The semiconductor, however, encompasses some width  $\delta$  and some averaging occurs over its area. The mathematics of averaging depends on the semiconductor nature and design but, in general, such averaging reduces the magnitude of the sensor's output signal. Therefore, it is preferable to have the width  $\delta$  as small as is practically possible. Because it is feasible with current technology to have the width  $\delta$  small compared to the wheel features, Equation 2.32 holds approximately and the sensor output can be characterized by the maximum and minimum of Equation 2.32:

$$v_{\max} = f(B_{\max}) \text{ and } v_{\min} = f(B_{\min}) \quad (2.35)$$

where  $v_{\max}$  is the sensor signal characterized by the maximum flux density  $B_{\max}$ ,  $B_{\max}$  is the maximum flux density,  $v_{\min}$  is the sensor signal characterized by the minimum flux density  $B_{\min}$ , and  $B_{\min}$  is the minimum flux density.

We conclude, therefore, that the output of a solid-state sensor depends also on the maximum and minimum values of flux density and is independent of the shape of the function  $B(\theta)$ . This establishes a common ground between VR and solid-state sensor designs. The other conclusion, however, is that the best sensor output is obtained from the smallest value of width  $\delta$ , a conclusion that makes the design of solid-state sensors differ sharply from that of VR sensors.

Note also that the output of VR sensors (Equation 2.6) is proportional to the wheel speed  $\omega$ , whereas the output from solid-state sensors (Equation 2.35) is independent of speed.

This known difference (Ohshima and Akiyama 1989a, Rowley and Stolfus 1990) has important practical implications for choosing one type of sensor over the other for a particular application, but as underscored by the mathematical expressions, Equation 2.6 and Equation 2.35, it does not affect the magnetic design. In the solid-state sensor case, the flux density in the location of the semiconductor is provided by the FE software. The output from the sensor depends on the characteristic of the solid-state device. To assess performance in as general a way as possible, a figure of merit, the device sensitivity  $S$ , in percent, was defined that prorates the difference between the maximum and minimum to their mean value, as follows:

$$S = \frac{B_{\max} - B_{\min}}{B_{\text{mean}}} \quad (2.36)$$

$$B_{\text{mean}} = \frac{B_{\max} + B_{\min}}{2}$$

where  $S$  is the device sensitivity and  $B_{\text{mean}}$  is the mean value of the flux density.

#### 2.4.2 Solid-State Sensor Design

Solid-state sensors require an external source of voltage or current, but they have the significant advantage over VR sensors in that their output signal is independent of the target-wheel speed. Also, the absence of a coil makes them more compact. Their success in the end, however, may hinge on the ability to manufacture them as inexpensively as VR sensors and, in that respect, improvements in magnetic-circuit design and sensitivity are critical for overall cost reduction. Their disadvantages include complexity, four leads, the presence of constant current source, fragility, and temperature dependence that requires stability provisions.

Unlike the VR-sensor case, the magnet size must be chosen in the solid-state sensor case to enhance the flux-density variations in one precise location, i.e., that of the semiconductor. This difference is well illustrated by studying the impact of the magnet width on sensor sensitivity, as defined in Equation 2.34, and as presented in Figure 2.67.

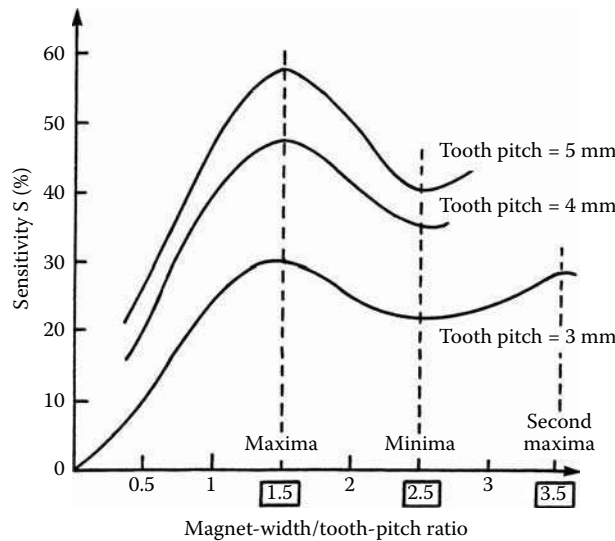
A first observation is that contrary to VR sensors, magnet widths much larger than a tooth pitch yield the best sensitivities. Another observation is the existence of sensitivity peaks that do not depend separately on magnet width and tooth pitch, but rather on their ratio. A general formula for the ratio  $R_{\text{peak}}$  yielding such a peak is:

$$R_{\text{peak}} = (1.5 + 2i) \frac{W}{T} \quad (2.37)$$

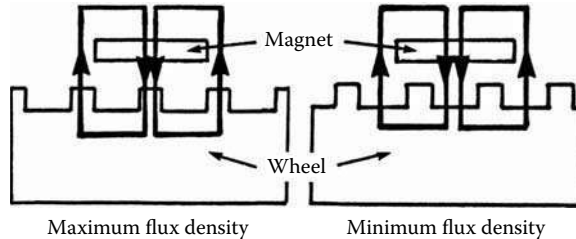
where  $R_{\text{peak}}$  is the magnet-width/tooth-pitch ratio,  $i$  is an integer,  $W$  is the magnet width, and  $T$  is the tooth pitch.

The respective locations of the magnet edge and of the wheel teeth explain the presence of sensitivity peaks and valleys. Consider the flux return paths sketched in Figure 2.68 for the case  $W/T = 1.5$ . The plot shows that in the maximum flux-density position, the signal is enhanced by the presence of teeth in the flux return path, and in the minimum flux-density position, it is reduced by the presence of slots near the magnet edges where the flux returns. The converse (not shown) is true for sensitivity valleys.

As shown in Figure 2.69, the concentration of magnet flux toward the teeth occurs primarily in the air gap. Figure 2.69 shows flux plots drawn from the FE calculation. The

**FIGURE 2.67**

Sensor sensitivity vs. magnet-width/tooth-pitch ratio. (From Lequesne, B. et al., *Transactions of IEEE/IAS*, 32(5), 1166–1175, 1996. With permission.)

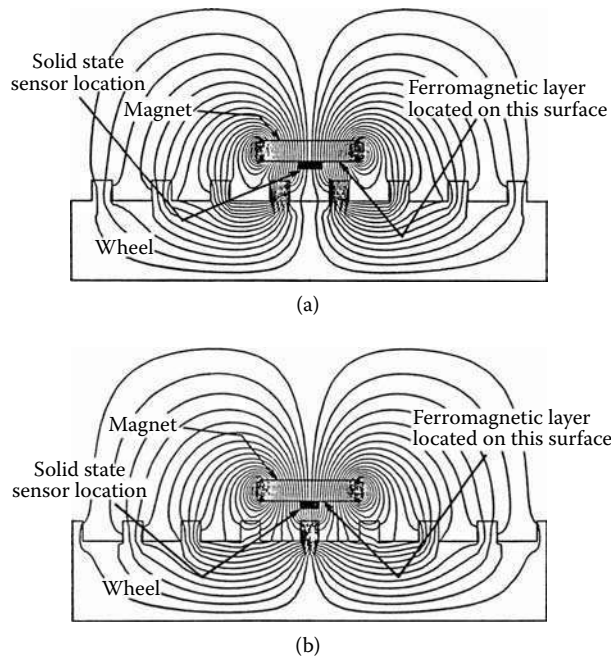
**FIGURE 2.68**

Sketch of flux paths for  $W = 1.5$  T. (From Lequesne, B. et al., *Transactions of IEEE/IAS*, 32(5), 1166–1175, 1996. With permission.)

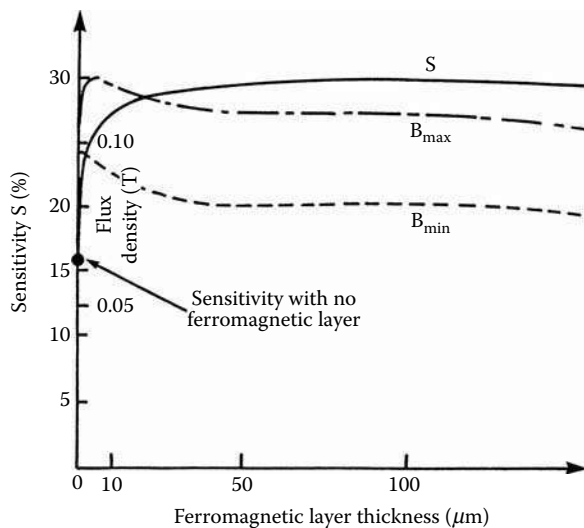
semiconductor, however, must be located close to the magnet surface to facilitate construction. Therefore, much of the flux variation bypasses the sensor and does not contribute to the signal. In order to direct more of the flux variation toward the sensing element, a thin ferromagnetic layer was added on the magnet surface (Schroeder et al. 1996). The high permeability of this layer allows for a larger flux concentration to take place between the magnet and the sensor and, therefore, enhances the signal.

Figure 2.70 plots sensitivity vs. the thickness of the ferromagnetic layer. It shows that even a very thin layer can be highly effective, almost doubling the sensitivity as compared to a similar sensor with no ferromagnetic layer. Thanks to its extreme thinness, the high permeability layer does not cause excessive leakage on the magnet edges.

In some designs, an iron member is added as a return path to the back of the PM to reduce the overall reluctance and increase the mean flux density in the sensor. However, it is interesting to note that its presence does not affect sensitivity. The same is true when the magnet thickness is increased or as the magnet material is changed from a weaker magnet material to a stronger one. These results are illustrated in Table 2.6, which shows that different designs may feature different mean flux densities  $B_{\text{mean}}$  (from 1.0 per unit

**FIGURE 2.69**

Flux plots for solid-state sensor: (a) minimum flux-density position, (b) maximum flux-density position. (From Lequesne, B. et al., *Transactions of IEEE/IAS*, 32(5), 1166–1175, 1996. With permission.)

**FIGURE 2.70**

Influence of ferromagnetic layer thickness on sensitivity. (From Lequesne, B. et al., *Transactions of IEEE/IAS*, 32(5), 1166–1175, 1996. With permission.)

[pu] to 3.1 pu) yet similar sensitivities  $S$ . This functional equivalence between iron flux guide, magnet thickness, and material strength (see, for instance, the similar values of  $B_{\text{mean}}$  and  $S$  for design 2 and design 3) is an important design tool because it allows the comparison of various options for a given application.

**TABLE 2.6**  
Comparison of Various Designs

Design No.	Magnet Design		Output		
	Iron Flux Guide	Magnet Thickness	Magnet Strength (kJ/m <sup>3</sup> )	B <sub>mean</sub> (pu)	Sensitivity
1	No	Base	100	1	1
2	Yes	Base	100	2.1	0.96
3	No	2.5 × Base	100	2.1	0.91
4	No	Base	300	1.6	0.98
5	No	2.5 × Base	300	3.1	0.94

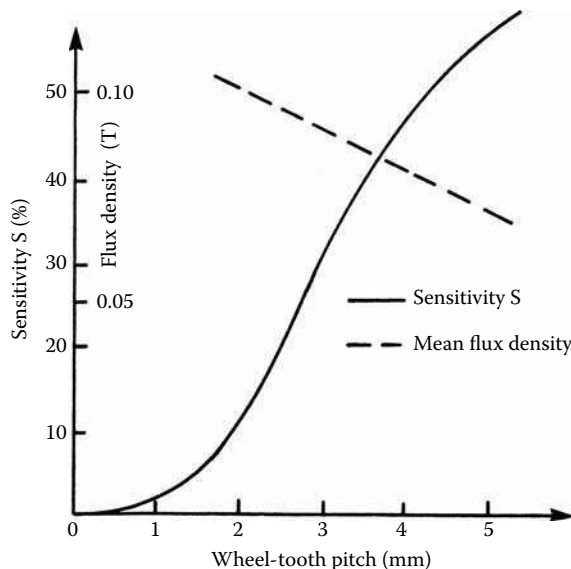


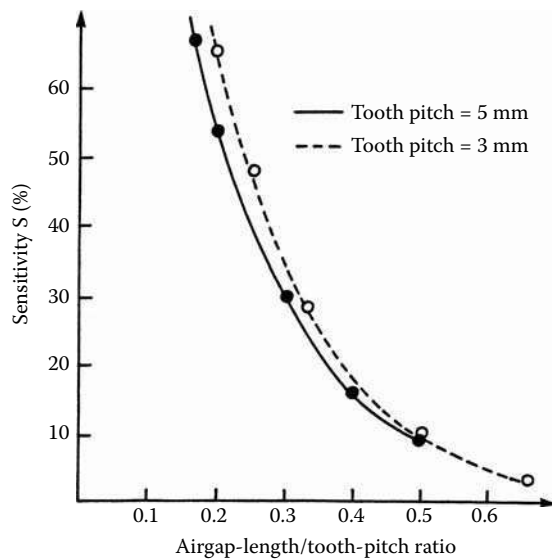
**FIGURE 2.71**  
Influence of wheel tooth pitch on sensitivity. (From Lequesne, B. et al., *Transactions of IEEE/IAS*, 32(5), 1166–1175, 1996. With permission.)

The sensitivity of the sensor depends on the wheel-tooth pitch. If the tooth pitch is large, teeth are far from one another and the flux concentrates significantly toward any tooth located across the magnet. If the tooth pitch is small, the flux leaks toward the neighboring teeth and flux concentration occurs only to a smaller degree. Therefore, the sensitivity is higher with larger tooth pitches, as presented in Figure 2.71 (for each point in Figure 2.71, the magnet width was chosen according to Equation 2.37). The mean flux density, also shown in the figure, drops slightly as the tooth pitch increases.

Longer air gaps obviously yield smaller mean flux densities. The sensitivity also decreases with longer air gaps. The physical reasons for this are similar to those given above to relate sensitivity to tooth pitch. In fact, it can be shown that the sensitivity does not depend separately on air gap length and tooth pitch, but rather on their ratio, as presented in Figure 2.72.

#### 2.4.3 Solid-State Sensor Test Results

Two sensors were built to check the validity of the model and the conclusions derived from it. The same magnet was equipped, in one case, with a  $51 \times 10^{-6}$  m thick steel layer

**FIGURE 2.72**

Correspondence between air gap and tooth pitch. (From Lequesne, B. et al., *Transactions of IEEE/IAS*, 32(5), 1166–1175, 1996. With permission.)

**TABLE 2.7**

## Comparison Test Calculations

Sensor Design	Unit	Ferromagnetic Layer			No Ferromagnetic Layer		
		Test	Model	Difference (%)	Test	Model	Difference (%)
Maximum flux density	T	0.206	0.2028	1.6	0.207	0.2054	0.8
Minimum flux density	T	0.168	0.1693	0.8	0.183	0.1896	3.6
Sensitivity	%	20.3	18.0	11.3	12.3	8.1	34.1

Source: Lequesne, B. et al., *Transactions of IEEE/IAS*, 32(5), 1166–1175, 1996. With permission.

and none in the other case. The results are shown in Table 2.7. The computed and measured flux densities match within 4%.

The wheel in the experimental set-up was fairly deep ( $13 \times 10^{-3}$  m) compared to the semiconductor size (less than  $1 \times 10^{-3}$  m deep). Therefore, the 2D approximation was a good representation of the wheel. The magnet, however, is usually small ( $2$  or  $3 \times 10^{-3}$  m deep) because of its cost. A 2D model, which results in neglecting the end effects around the magnet edges in the direction perpendicular to the wheel rotation, tends, therefore, to be somewhat inaccurate. In order to assess the impact of this simplification on performance predictions, two sensors were tested which differed only by the magnet depth in the third direction. In one case, the magnet depth was  $9.5 \times 10^{-3}$  m, and in the other case, it was only  $3.2 \times 10^{-3}$  m, the deeper magnet being closest to the 2D simplification. The test data are shown in Table 2.8, along with the results of the 2D model in this case. Because the end effects constitute a reluctance path parallel with the main flux path, the consequence of their presence, as seen in Table 2.8, is to increase the mean flux density and to reduce the sensitivity, by 32% in the case studied. The impact of the end effects on the results, however, is mainly quantitative as the reluctance load that the end effects constitute for the magnet is relatively constant, regardless of the design. A 2D model, therefore, is appropriate for qualitative comparison and design selection, but not for precise quantitative prediction.

**TABLE 2.8**

Influence of the End Effects

Performance or Sensor Design	Shallower Magnet	Deeper Magnet	2D Model
Maximum flux density (T)	0.216	0.206	0.2028
Minimum flux density (T)	0.188	0.168	0.1693
Mean flux density (T)	0.202	0.187	0.186
Sensitivity (%)	13.9	20.3	18.0

Source: Lequesne, B. et al., *Transactions of IEEE/IAS*, 32(5), 1166–1175, 1996. With permission.

**TABLE 2.9**

Requirements for Sensors in Automotive Applications

Performance or Sensor Type	Inserted-Magnet Sensor Transmission Speed	Front-Magnet Sensor Crankshaft Position	Multimagnet Sensor ABS Application
<b>Signal (p-p) V</b>			
at 25°C	>0.65 at 100 r/min at 1.2 mm gap		
at 150°C	>0.55 at 100 r/min at 1.2 mm gap	>0.5 at 30 r/min at 1.5 mm gap >0.65 at 100 r/min	3.75, 5.5, 7.0 mV/Hz at $1.0 \times 10^{-3}$ m gap
<b>Geometry</b>			
Diameter ( $m \times 10^{-3}$ )	27.0	12.0, 15.0	
Height ( $m \times 10^{-3}$ )	57.5	30.0, 35.0	10.0
Width ( $m \times 10^{-3}$ )			13.0
Length ( $m \times 10^{-3}$ )			25.0
Volume ( $m^3 \times 10^{-6}$ )	32.9	9.6	3.25
<b>Temperature (°C)</b>	-40 to +150	-40 to +150	-40 to +200
<b>Speed range (r/min)</b>	100 to 6250 <0.15 at 5000 r/min	30 to 7000 NS	42 to 5000 NS
<b>Noise signal (V)</b>	engine speed		
<b>Load (kΩ)</b>	NS	10	NS

NS = not specified.

Source: Courtesy of Delphi Corp.

## 2.5 Magnetic Sensor Applications

The applications of magnetic velocity sensors are increasing rapidly, particularly in the automotive industry, where they are used for ABS, TC, four-wheel drive, steering wheel and cam shaft position, etc. VR speed and position sensors are widely used in industry and, in particular, the automotive industry because of their low cost and high reliability. To date, many types of lumped element VR sensors have been utilized, but more and more modern VR sensors are used in a variety of applications.

### 2.5.1 Magnetic Speed Sensor Requirements

Typical VR sensor requirements for automotive applications pertain to the sensor signal, usually defined as the peak-to-peak value, its geometry, speed range, temperature range, and the acceptable noise level. Sometimes load is also specified. Requirements for four families of novel sensors utilized in automotive applications are shown in Table 2.9.

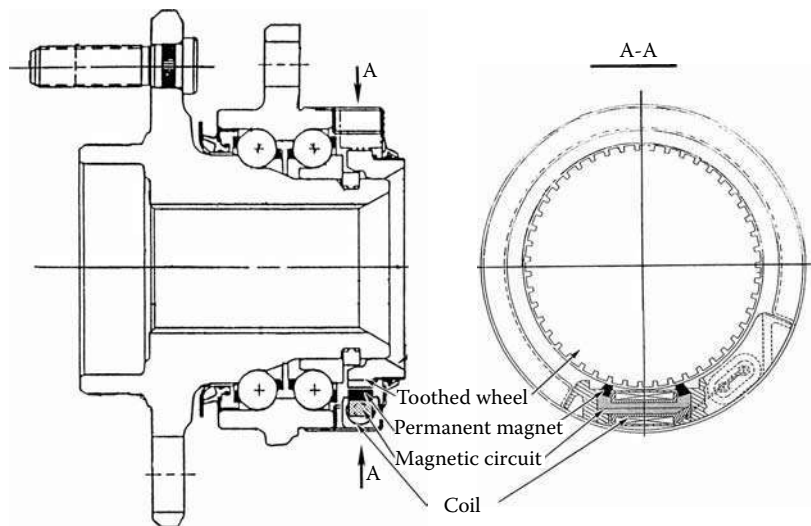


**FIGURE 2.73**  
Two-magnet sensor integrated with the wheel bearing for ABS.

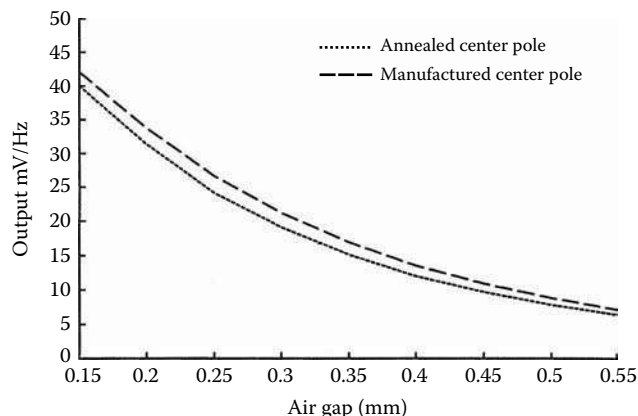
### 2.5.2 Magnetic Speed Sensor Applications

A need to boost sensor performance that provides high signal at a low speed of the exciter wheel led to the development of the VR sensor configuration with multiple magnets. Such a requirement for sensor performance came from an automotive application for ABS, as presented in Table 2.9. Figure 2.73 shows a two-magnet sensor applied to the wheel speed sensing application for the ABS system. The sensor fits under the grease cover that is a part of the wheel bearing and provides a signal to the ABS system. The particularly difficult sensor environment with high ambient temperature around the brakes led also to the selection of a magnet material that is stable at elevated temperatures. Consequently, the two-magnet partially distributed sensor led to the development of the magnetically distributed ring-shape sensor with multipole magnet that fits best and could be integrated within the bearing grease cover, and its magnetic distribution nature would help compensate for the radial tolerances. This enables this sensor to provide signals for both the ABS and TC system with a much more difficult requirement to meet. The magnetically distributed sensor, shown in Figure 2.74, can provide a full signal of 1.0 V at the wheel speed of 0.25 mph; however, the two-magnet sensor capability at full signal is limited to 0.9 mph vehicle speed, which is sufficient for ABS but not satisfactory for the TC.

Typical ABS system requirements vary from system to system: Bosch = 7.0 mV/Hz, GM6 = 5.5 mV/Hz, and Teves = 3.75 mV/Hz, as presented in Table 2.9. During the development of the two-magnet sensor integrated with the wheel bearing for the ABS, meeting all requirements was quite a challenge. For this modern sensor structure, shown in Figure 2.73, additional improvement was introduced by heat treatment of the magnetic parts. One should always remember to reduce mechanical stresses exerted to the magnetic parts by the manufacturing process in the form of machining or stamping operations. Proper annealing, usually guided by the material manufacturer, is a necessary element in releasing and eliminating stresses in the magnetic circuit. In this particular case, annealing of a central rod has provided performance improvement over 12% in the achieved signal value, as demonstrated in Figure 2.75, especially because cost increase per sensor is less than a penny.



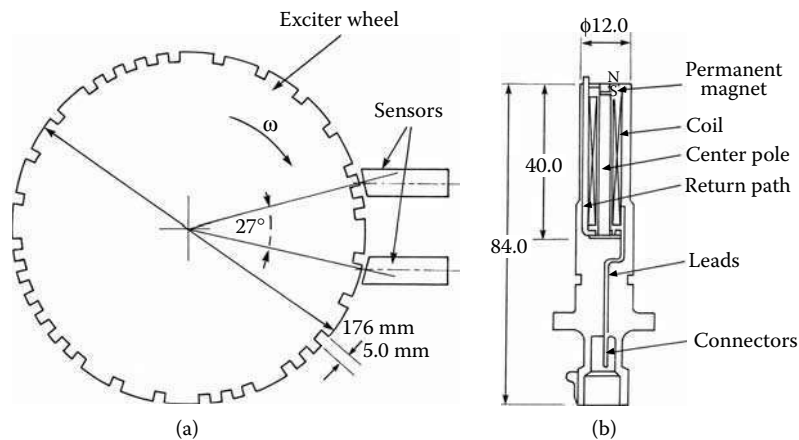
**FIGURE 2.74**  
Magnetically distributed sensor integrated with wheel bearing.



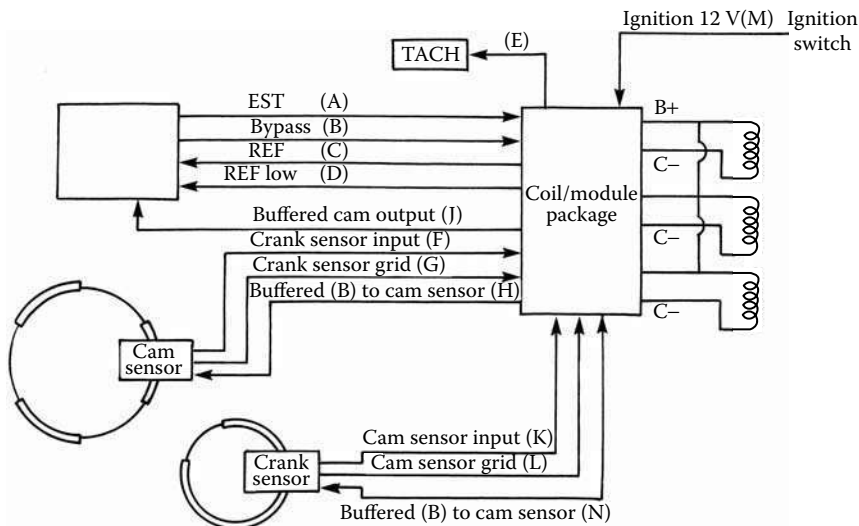
**FIGURE 2.75**  
Output signal vs. air gap performance for the annealed center pole vs. the original manufactured center pole of the two-magnet VR sensor structure.

### 2.5.3 Magnetic Position Sensor Applications

The front-mounted-magnet sensor in Figure 2.76 is presented with an exciter wheel that has a particular tooth and slot pattern that would provide accurate crankshaft position. There are two such sensors adopted for this application to provide additional information on the direction of rotation. The sensor signal is presented in Figure 2.33. This signal is utilized as a position sensor where the real position of the exciter wheel is indicated by zero crossing of the signal at the narrow and wide tooth. The rotation of the wheel creates a change in magnetic flux linkage in the sensor, which generates a voltage signal based upon the flux rate change.

**FIGURE 2.76**

Front-mounted position sensor: (a) sensor-wheel arrangement, (b) front-mounted sensor.

**FIGURE 2.77**

Crankshaft position sensor. (From Pawlak, A.M., *Proceedings of the NdFeB '99 Conference*, San Francisco, April 12–14, 1999. With permission.)

The electronic module, shown in Figure 2.77, processes the signal from the sensor to determine a crankshaft position and engine speed. It responds to voltage transmissions generated in the sensor by the slotted wheel passing by. This voltage must rise above a certain positive threshold and then move through zero volts on negative transition. The positive threshold varies from 250 mV at minimum cranking speed of 40% of the previous positive peak. The latter is to safeguard against recognition of noise at higher speeds. The module triggers off of the zero crossing of the waveform. The positive threshold is used only as an arming mechanism to filter out noise. The module counts the time between zero-crossing events of the sensor to determine the engine speed and the crankshaft position. The special slot distribution of the wheel allows recognition of the crankshaft position at its half revolution.

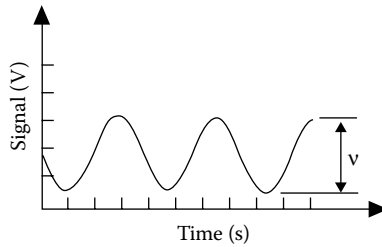


**FIGURE 2.78**  
Sensor signal vs. time.

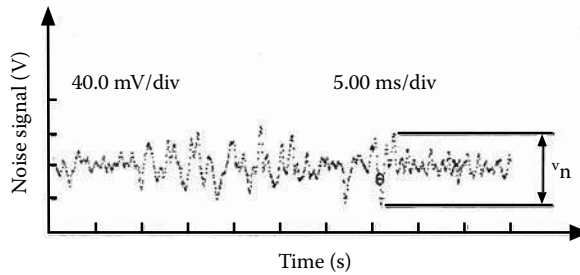


**FIGURE 2.79**  
Noise signal vs. time.

## 2.6 VR Sensor Noise

In automotive applications, a VR sinusoidal sensor signal, as presented in Figure 2.78, is filtered and squared by a remote buffer circuit, whose output can be used by the speedometer, cruise control, TC, and other systems. Because it is not possible to determine the level of noise signal before the sensor is built and applied, usually it is a matter of sensor modifications after the sensor is designed and tested. Sometimes the same sensor applied to one environment's noise level is acceptable, yet in a new arrangement may not be acceptable. Noise should be measured at the worst conditions: highest temperature, highest engine rotation, and for sensor position when the flux linkages are at their maximum values (wheel tooth vs. pole tip). Under extreme conditions, the noise signal vs. time characteristic should be determined for the original sensor.

A typical example of the noise vs. time characteristic is presented in Figure 2.79. In this example, the transmission speed sensor noise signal was recorded at 5000 rpm of engine speed at transmission gear in neutral or park position. Because the vehicle is not moving, the sensor signal should be zero as well as the speedometer reading. Because the sensor indicates the noise signal, the threshold is set up for 0.15 V signal value (peak-to-peak) and no speed reading is displayed as a false speed if the noise signal is below this level.

### 2.6.1 Math Model and Noise Analysis

Equation 2.1 for induced signal  $v_s$  in the sensor coil can be expressed as a function of time and angular position as:

$$v_s = -N \frac{d\phi}{d\theta} \times \frac{d\theta}{dt} \quad (2.38)$$

where  $v_s$  is the induced signal in the sensor coil,  $N$  is the number of turns of the coil,  $\theta$  is the angular position, and  $t$  is the time.

Substituting for  $dv_s/dt = \omega$ , one can see that the induced signal depends on the wheel angular speed, the number of turns  $N$ , and flux changes for different wheel positions, of which the latter is the most difficult to determine. A similar equation that describes the noise signal as a function of the relative sensor-wheel position  $A$  and time  $t$  can be expressed as follows:

$$v_n = -N \frac{d\phi}{dA} \times \frac{dA}{dt} \quad (2.39)$$

A vibration mode relative to sensor-wheel movement has three degrees of mechanical freedom, resulting in position term  $A$ , which can vary in all three coordinates:

$$A = A(x, y, z) \quad (2.40)$$

Because of the complex 3D nature of sensor-wheel interaction and geometry, an FE numerical solution of the magnetic field is necessary. Evaluation of the noise signal change has to be based on the noise-signal-to-sensor-signal ratio  $v_n/v_s$  and that sensor signal level  $v_s$  is satisfactory.

### 2.6.2 Noise Problem Solutions

The investigated sensor was applied to two different automotive power train transmissions, as presented in Figure 2.80. Because the axial length of the exciter wheel is different,

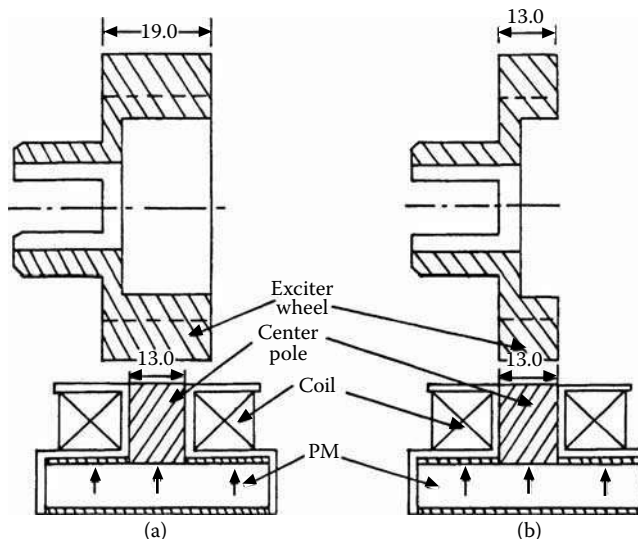


**FIGURE 2.80**

Sensor-wheel arrangements for two different power train transmissions: (a) wide exciter wheel, (b) narrow exciter wheel.

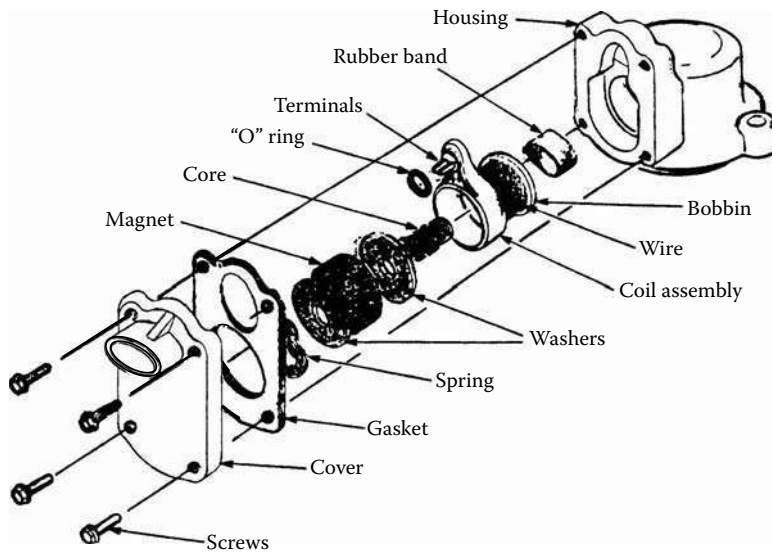


**FIGURE 2.81**  
Transmission speed sensor components.

the transmission with the shorter exciter wheel is more sensitive to axial vibrations. Therefore, a vehicle equipped with this exciter wheel was found to have the most severe noise signal problem and was selected for experimental noise evaluation of sensor prototypes.

The voltage signal can only be generated in the coil as a result of a change in the flux linked with the coil. If the analyzed sensor is installed on a vehicle and the vehicle is stationary, this change in flux linkages can result from engine vibration, causing a relative motion between the sensor coil and the transmission speed sensor components of the sensor assembly: magnet, washers, coil and center pole, as shown in Figure 2.81, or externally between the sensor assembly and the exciter toothed wheel. Therefore, it is necessary to determine the noise contribution in each case to find the appropriate remedies. The first step is to mechanically couple, by cementing all internal sensor components, and measure noise signal on a relatively large number of sensors (50). A large number of speed sensors should be tested because of unrepeatable test conditions. In the examined case, cementing internal parts resulted in 30% of noise reduction. It was assumed that the remaining 70% of their noise is due to vibration of the exciter wheel with respect to the speed sensor assembly, as presented in Figure 2.81, which can be reduced by using tighter exciter wheel tolerances. However, cementing components and tightening the tolerances are both costly alternatives, so we started looking for other solutions.

Three areas of the sensor geometry were considered — geometry of the center pole, coil design, and air gap length. Unfortunately, any changes in the pole design that were considered show no measurable improvements in the  $v_n/v$  signal ratio. The coil design study was conducted for full available coil space (window) utilization with different coil wire sizes [American wire gauge (AWG)]. The results of these considerations are presented in Figure 2.82. The noise-to-signal ratio  $v_n/v$  is reduced for thicker wire.

The influence of the length of the air gap between the sensor and the sensor assembly was investigated. Figure 2.83 presents the results of this study. It was found that the noise decreases three times faster than the signal as the air gap increases. Therefore, this can be considered a very effective way to reduce noise. As shown in Figure 2.84, increasing the air gap from  $0.9 \times 10^{-3}$  m to  $1.2 \times 10^{-3}$  m reduces the noise from 0.5 V to the specified 0.15 V.

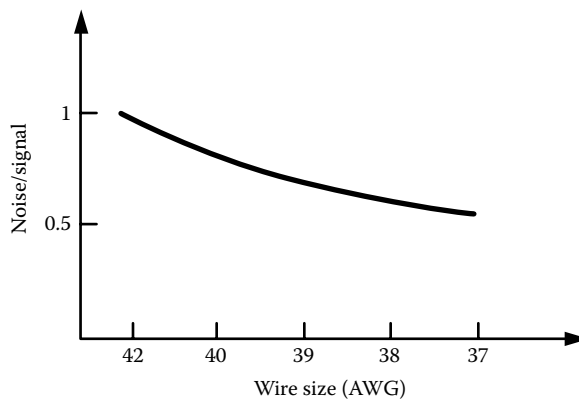


**FIGURE 2.82**  
Noise/signal ratio vs. wire size.

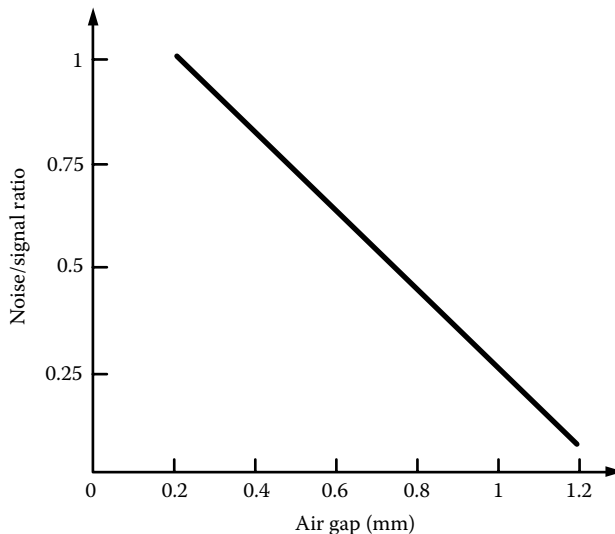


**FIGURE 2.83**  
Noise/signal ratio vs. air gap length.

For the same change in the air gap, the signal is decreased from 0.87 V to 0.68 V, as shown in Figure 2.85.

Comparing the slopes of this characteristic indicates that the signal is less dependent on air gap changes. This can be explained by the different nature of generating signal and noise, as shown in Equation 2.37 and Equation 2.38. Even though the sensor signal level is determined by the geometry of the wheel, its angular speed, and the length of the gap, the noise is generated due to vibrations that cause variations of magnetic permeance that are independent of the wheel geometry and depend mainly on the air gap length and its variation with respect to the time. Therefore, the noise is more sensitive to air gap variation than the sensor signal.

On the basis of these results, a new air gap of  $1.2 \times 10^{-3}$  m was proposed to replace the existing  $0.9 \times 10^{-3}$  m gap. It provides a signal of 0.68 V and a reduced noise level of 0.15 V. Implementing this change does not affect the production cost and the manufacturing procedures of the device in any adversarial way. On the contrary, because of the resulting

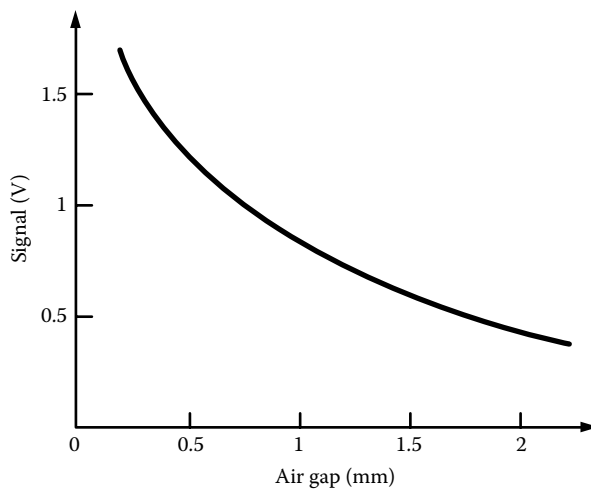


**FIGURE 2.84**  
Noise vs. air gap length.

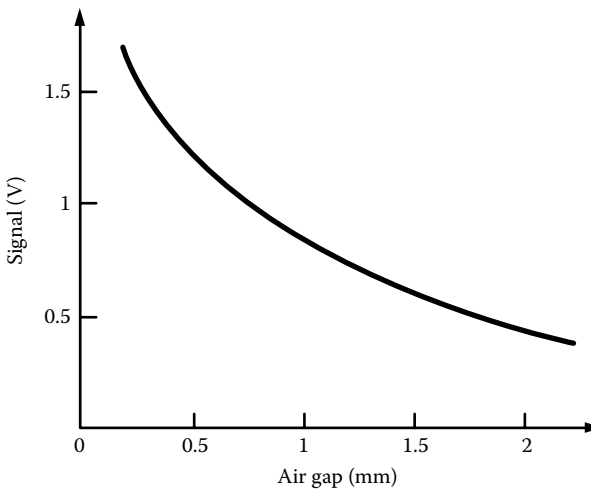


**FIGURE 2.85**  
Sensor signal vs. air gap length.

low sensitivity to noise, the manufacturer may relax some tolerance requirements for the sensor parts and the wheel, which may lead to lower costs.

---

### Example 2.1

Estimate the sensor signal and flux utilization of the front-magnet sensor with no changes in the coil and magnet for an E-shaped structure if the sensor with partial magnetic structure (having a central pole and shim) indicated a signal value of 0.44 V at  $1.2 \times 10^{-3}$  m air gap and 51 r/min exciter wheel speed.

### **Step 1. Calculate Signal Performance**

The solution is based on Table 2.3. The signal sensitivity ratio of the E-shaped sensor to a sensor with partial magnetic structure having center pole and shim is:

$$\frac{S_{vE}}{S_{vp}} = \frac{0.54}{0.32} = 1.69$$

Because the volume of both sensors is the same, from Equation 2.11 we have:

$$\frac{S_{vp}}{S_{vE}} = \frac{V_{sp}}{V_s} \frac{V_s}{V_{sE}} = \frac{V_{sp}}{V_{sE}}$$

Substituting for the signal value, the sensor model signal of  $v_{sp} = 0.44$  V and combining the calculated ratio, we have the E-shaped sensor signal estimated performance:

$$S_{vE} = \frac{0.54}{0.32} v_{sp} = \frac{0.54}{0.32} \times 0.44 = 0.743 \text{ V}$$

Verify this value for the E-shaped sensor in Table 2.3.

### **Step 2. Calculate Flux Efficiency**

From Equation 2.12, we can estimate flux utilization:

$$s_{\phi p} = \frac{\Delta\phi_p}{\phi_o} \quad \text{and} \quad s_{\phi E} = \frac{\Delta\phi_E}{\phi_o}$$

Assuming the same magnet generates the same flux  $\phi_o$ , we can calculate the flux efficiency improvement based on the ratio from Table 2.3:

$$\frac{s_{\phi E}}{s_{\phi p}} = \frac{\Delta\phi_E}{\Delta\phi_p} \times \frac{\phi_o}{\phi_o} = \frac{1.35}{1.10} = 1.23$$

The flux utilization of the E-shaped sensor is 23% better than the sensor model and it would provide a signal of 0.743 V. This concludes the solution for Example 2.1.

### **Example 2.2**

Calculate the two-magnet VR sensor signal for ABS and verify which of the ABS system requirements can be satisfied: Bosch = 7 mV/Hz, GM6 = 5.5 mV/Hz, or Teves = 3.75

mV/Hz. The sensor test was performed at the required air gap of  $1.0 \times 10^{-3}$  m with a speed of 127 r/min. The signal level, provided from Figure 2.56, is based on test results and sensor analysis. The signal of 1.1 V for nonconventional (nonsupportive magnets) and 0.4 V for conventional sensor-wheel arrangements (supportive magnets) is provided by Figure 2.56.

### Step 1. Signal Calculations of Two-Magnet VR Sensor Nonsupportive Magnet Configuration

The electrical frequency of the sensor signal is:

$$f_{el} = f_{mech} \times N_t = \frac{127}{60} \times 47 = 99.48 \text{ Hz}$$

where  $N_t = 47$  is the number of exciter wheel teeth. The sensor signal value of 1.1 V can be obtained from Figure 2.56 for nonsupportive magnets at the required air gap of  $1.0 \times 10^{-3}$  m and it corresponds to an already calculated frequency of operation:

$$1100 \text{ mV} \equiv 99.48 \text{ Hz}$$

Therefore, the signal achieved by the nonsupportive sensor at 1 Hz is:

$$v_1 = \frac{1100}{99.48} \left[ \frac{\text{mV}}{\text{Hz}} \right] = 11.06 \left[ \frac{\text{mV}}{\text{Hz}} \right]$$

Signal  $v_1$  achieved by the nonsupportive sensor structure meets all requirements. This sensor has satisfied all (Bosch = 7 mV/Hz, GM6 = 5.5 mV/Hz, and Teves = 3.75 mV/Hz) system requirements.

### Step 2. Signal Calculations of Two-Magnet VR Sensor Supportive Magnet Configuration

The electrical frequency of the sensor signal is:

$$f_{el} = f_{mech} \times N_t = \frac{127}{60} \times 47 = 99.48 \text{ Hz}$$

As Figure 2.56 shows, at an air gap of  $1.0 \times 10^{-3}$  m the signal value for supportive magnets equals 0.4 V and that corresponds to the value of frequency of operation.

Because  $0.4 \text{ V} \equiv 99.48 \text{ Hz}$ , the signal achieved by the nonsupportive sensor at 1 Hz is:

$$v_2 = \frac{400}{99.48} \left[ \frac{\text{mV}}{\text{Hz}} \right] = 4.02 \left[ \frac{\text{mV}}{\text{Hz}} \right]$$

Signal  $v_2$  achieved by the supportive sensor structure meets only Teves = 3.75 mV/Hz system requirements. This sensor did not satisfy Bosch = 7 mV/Hz and GM6 = 5.5 mV/Hz requirements. This concludes the solution for Example 2.2.

---

### **Example 2.3**

Calculate the signal value generated by the rectangular VR sensor 3 structure with inserted magnet, as presented in Figure 2.16. The FE software simulations, as presented in Figure 2.18, have provided the maximum flux-linkage value (corresponding to a tooth with maximum permeance value) of  $2089 \times 10^8$  Wb/cm and the minimum flux value (corresponding to a slot with minimum permeance value) of  $2029.5 \times 10^8$  Wb/cm. The sensor thickness is 1.3 cm with 4000 turns and is based on the MQ2 magnet. Assume 100 r/min speed rotation of the exciter wheel having 40 teeth.

The mechanical frequency of rotation is calculated as:

$$\omega = 2\pi f_{mech} = 2\pi \frac{100}{60} = 10.47 \text{ rad/s}$$

and the mechanical angular displacement is calculated as:

$$\Delta\theta = \frac{2\pi}{2 \times N_t} = \frac{2\pi}{2 \times 40} = 0.0785 \text{ rad}$$

The signal value can be calculated from Equation 2.25:

$$v(t) = -N\omega \frac{\Delta\phi \times 1.3}{\Delta\theta} = 4000 \times 10.47 \frac{(2089 \times 10^{-8} - 2029.5 \times 10^{-8}) \times 1.3}{0.0785} = 0.4127 \text{ V}$$

Because the flux-linkage values were provided in Wb/cm due to the FE software limitation, we need to multiply that value by the real thickness of the sensor of 1.3 cm. The calculated value of the sensor signal corresponds to the measured value of the sensor 3 structure from Table 2.2. This concludes the solution for Example 2.3.

# 3

---

## *Linear Actuators*

---

Fast-acting solenoids are finding increasingly more new industrial applications and the demand for electronically controlled magnetic linear actuators is expanding rapidly, particularly in the automotive industry. These solenoids are found in a variety of sizes, configurations, and load requirements as the use of electronics increases to replace conventional hydraulics and mechanical systems with modern mechatronics. They are utilized as fuel injectors, exhaust gas recirculation (EGR) and transmission control solenoids, fuel pumps, compressor solenoids, speed-sensitive steering system solenoids, active suspension systems, air bag deployment, etc. From the armature design point of view, linear solenoids are divided into four families of solenoid actuator geometries — solenoids with disk, plunger, conical, and ball armatures — as shown in Figure 3.1.

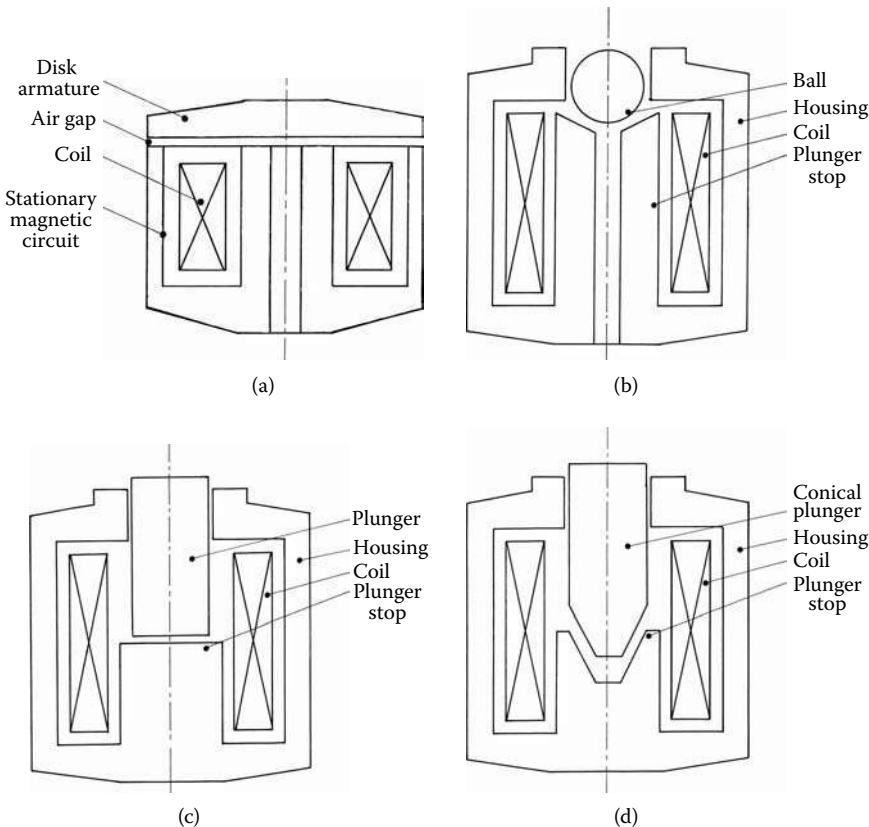
A variety of geometries have mixed configurations taking advantage of armature geometry features. Each of these basic geometries is discussed separately because of their different advantages, helping to serve different purposes. The selection of geometry is the first and most important step in the design application; therefore, thoroughly understanding the pros and cons of each solenoid type is critical. A conventional linear actuator consists of an armature, magnetic-circuit housing with a central rod serving as an armature stop, a return spring, and a coil.

Typically, solenoids are PWM driven and the variation of the duty cycle of the voltage applied to the solenoid results in a smooth operation. In order to obtain a wide range of duty cycle operations at a given frequency, the response time of the actuator should be minimized. It should be a design target stressed through the actuator dynamic analysis. The variables of the optimization study are the solenoid geometry, magnetic material properties, and electromagnetic circuit including coil parameters. Utilized mathematical models would couple the electrical, mechanical, hydraulic, and magnetic systems of these devices by taking into account the nonlinearity of the magnetic materials, eddy currents, and motion (Boldea 2001).

---

### **3.1 Mathematical Model for Linear Actuators**

A transient 2D FE model for fast-acting PWM solenoid actuators is presented in this chapter. The unique feature of this model is the coupling of the electrical, mechanical, and magnetic systems of solenoid actuators. Transient calculations based upon 2D FE magnetic field solutions, including nonlinearity of magnetic materials, eddy currents, and motion, are compared with test results for a ball-type solenoid. Flexibility of the software allows one to apply it to any type of PWM solenoid actuator with any desired excitation profile.

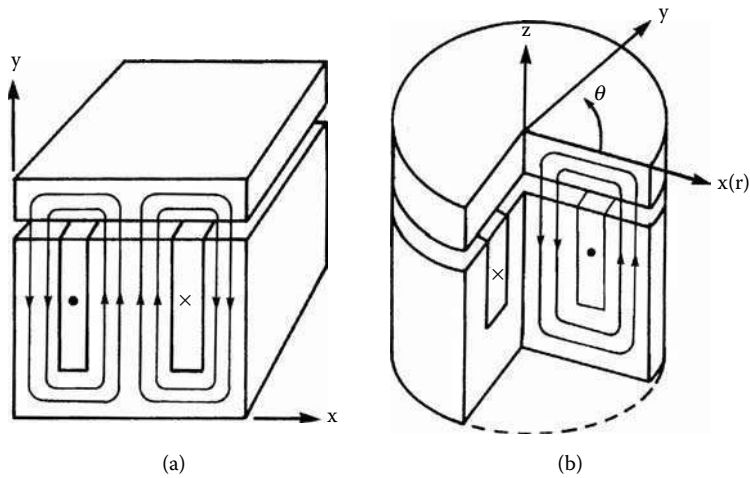
**FIGURE 3.1**

Linear solenoid actuators with different armatures: (a) disk, (b) plunger, (c) conical, (d) ball. (Courtesy of Delphi Corp.)

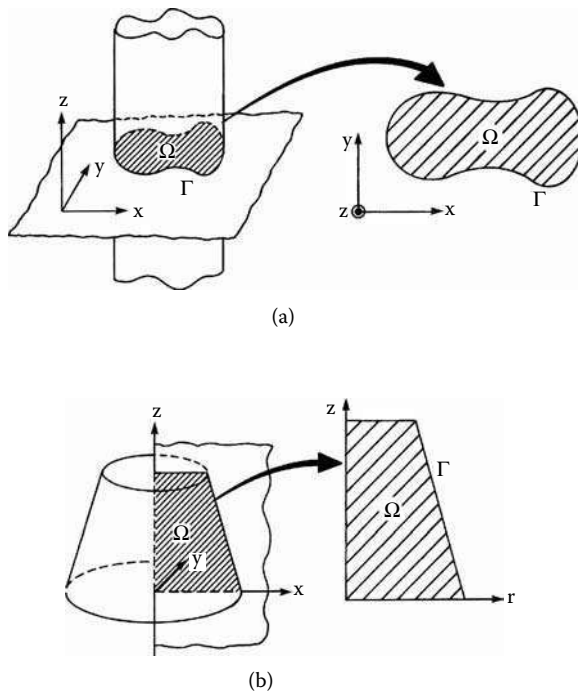
### 3.1.1 Symmetrical Analysis of Electromagnetic Devices

Many typical electromagnetic devices can be analyzed based on a 2D FE software system for magnetic field analysis in rectangular and cylindrical coordinates, as presented in Figure 3.2 (Nehl et al. 1988, Hammond 1978). With the assumption that end effects are negligible, it can solve field equations of both the rectangular coordinates for most of the conventional solenoids and a variety of inductors and transformers, as well as conventional rotary machines. In these devices, the high permeabilities of the magnetic cores force a majority of the magnetic flux into the  $x$ - $y$  plane, perpendicular to the direction of excitation. For these problems it is sufficient to analyze a slice of unit thickness parallel to the  $x$ - $y$  plane. Furthermore, if motion is restricted to the vertical ( $x$ ) axis, the current densities and the vector potential are both  $z$  directed, while the magnetic flux and the flux densities lie in the  $x$ - $y$  plane.

The majority of solenoids and injectors, as well as a large number of small inductors and transformers for power processing applications, are axisymmetric about one axis, as shown in Figure 3.2(b). In these cases, the excitation and the vector potential are cylindrical with respect to the axis of symmetry and the resulting flux and flux density exists in planes radial to the axis of symmetry. Note that fields are independent of the angle  $\theta$ . Consequently, one can restrict the analysis to a pie-shaped slice of the device of unit angle in the  $\theta$  direction.

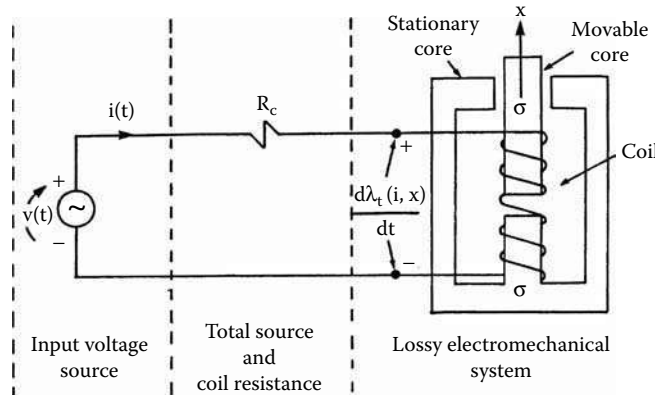
**FIGURE 3.2**

Symmetrical analysis of electromagnetic devices: (a) rectangular coordinates, (b) cylindrical coordinates. (Courtesy of Delphi Corp.)

**FIGURE 3.3**

Field regions for (a) rectangular and (b) cylindrical coordinates. (Courtesy of Delphi Corp.)

Neglecting the end effect for long devices or using axisymmetry in cylindrical devices allows us to reduce a 3D geometry into a 2D region  $\Omega$  with the boundary  $\Gamma$ , as shown in Figure 3.3. The governing field equation must be satisfied everywhere in the region  $\Omega$ . In order to complete the specification for the field problem that would allow reduction of a 3D geometry into a 2D region, one must confirm that boundary conditions are specified

**FIGURE 3.4**

Lumped model parameter of a mechatronic system. (Courtesy of Delphi Corp.)

properly for zero-flux crossing (homogeneous Dirichlet), flux crossing (homogeneous Neumann), and periodicity.

### 3.1.2 Electrical Network Equations

In the majority of applications, the voltage applied to the terminal of a device as a function of time is specified rather than the transient current. In such cases, the field solution must be coupled to the external electrical network that provides the excitation. Problems involving mechanical motion add another source of coupling, which must be accounted for. This chapter provides equations describing the dynamics of the electrical network. This is followed by equations of motion and finally the coupling between the field equations, the electrical network, and the mechanical network, which are presented in terms of the system power balance.

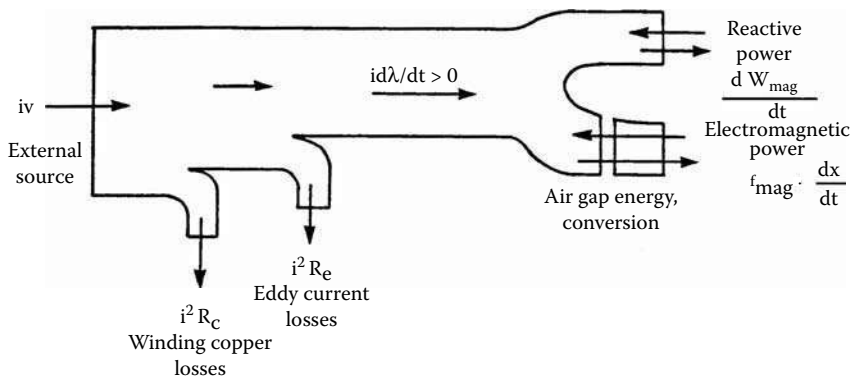
The lumped-parameter electrical network model of a single winding mechatronic (electromechanical or electromagnetic) device is shown in Figure 3.4. The model consists of three components; an ideal voltage source, a resistor, and a lossy electromechanical system. The voltage source is assumed to be a known function of time and, therefore, independent of the state of the system. The resistor accounts for the ohmic losses in the source and the winding of the device. The state of the system is governed by the differential equation that couples electric and magnetic models through the voltage equation:

$$v = iR_c + \frac{d\lambda_t}{dt} \quad (3.1)$$

where  $v$  is the specified voltage source,  $i$  is the winding current,  $R_c$  is the total ohmic resistance, and  $\lambda_t$  is the total flux linkage of the winding.

The time derivative of the total flux system flux linkage, given in this equation, is the total induced voltage of the device. This voltage includes components due to induced eddy currents, time variations in the applied source voltage, and motion. The total induced voltage can, therefore, be split into two components:

$$\frac{d\lambda_t}{dt} = iR_e + \frac{d\lambda}{dt} \quad (3.2)$$

**FIGURE 3.5**

Power flow diagram of an electromechanical system. (Courtesy of Delphi Corp.)

where  $R_e$  is the reflected resistance due to induced eddy currents and  $\lambda(i,x)$  is an equivalent flux linkage of the winding assuming a lossless magnetic circuit.

Note that this flux linkage is a function of winding current  $i(t)$  and of the position  $x(t)$  of the moving part in the case of the motion problem. Substituting this expression into Equation 3.1 and multiplying both sides by the winding current  $i$  yields the instantaneous power balance of the electromechanical system as follows:

$$iv = i^2 R_c + i^2 R_e + i \frac{d\lambda}{dt} \quad (3.3)$$

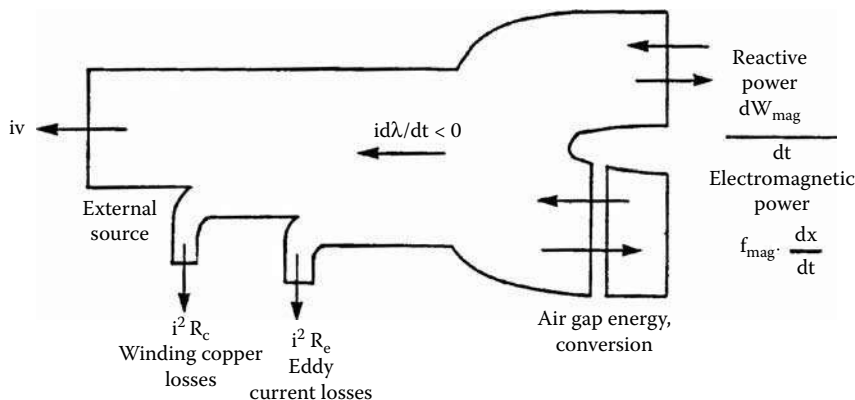
This power balance can also be expressed in terms of the rate of change of stored magnetic energy and the mechanical power (White and Woodson 1959) as:

$$iv = i^2 R_c + i^2 R_e + \frac{dW_{mag}}{dt} + F_{mag} \frac{dx}{dt} \quad (3.4)$$

where  $W_{mag}$  is the total stored magnetic energy and  $F_{mag}$  is the magnetic force on the moving part.

The interpretation of the various terms in these power balance equations is given in the two power flow diagrams of Figure 3.5 and Figure 3.6. Figure 3.5 illustrates the power flow when power is consumed by the coil. In this case, the power supplied by the external source enters on the left. The amount of input power is first reduced by ohmic or copper losses of the coil winding. Next, the total reflected eddy current losses are subtracted from this amount. The remaining power,  $id\lambda/dt$ , is available for conversion to mechanical output (the electromechanical power) or to produce a net rate of change in stored magnetic energy (reactive power). This situation is reversed when the power flow changes direction, that is, when the coil supplies the power to the external source, as shown in Figure 3.6. In this case, the sum of the reactive and electromagnetic powers,  $id\lambda/dt$ , is negative. This indicates that the coil is supplying power to the external source. Consequently, the power available at the coil terminals must be less than  $id\lambda/dt$ .

The relationship between the derivative terms of Equation 3.3 and Equation 3.4 can be deduced by applying the chain rule to both equations and comparing terms. This yields the following:

**FIGURE 3.6**

Power flow diagram of an electromechanical system. (Courtesy of Delphi Corp.)

$$i \frac{\partial \lambda}{\partial i} \frac{di}{dt} = \frac{\partial W_{mag}}{\partial i} \frac{di}{dt} \quad (3.5)$$

and

$$i \frac{\partial \lambda}{\partial x} \frac{dx}{dt} = \left( \frac{\partial W_{mag}}{\partial x} + F_{mag} \right) \frac{dx}{dt} \quad (3.6)$$

Inspection of these two equations reveals that the first represents the rate of change of the stored magnetic energy due to changes in the winding current, and the second accounts for both the energy conversion and the rate of change in the stored magnetic energy due to motion. To simplify the notation, the five power terms appearing in the system power balance, Equation 3.4, will be identified as follows:

$$P_s = P_c + P_e + P_r + P_{em} \quad (3.7)$$

where  $P_s$  is the source power,  $P_c$  is the power loss due to winding resistance,  $P_e$  is the eddy current loss,  $P_r$  is the rate of change in the stored magnetic energy (reactive power), and  $P_{em}$  is the rate of energy conversion (electromagnetic power).

### 3.1.3 Mechanical Equations

Problems involving mechanical motion require additional state equations to describe the dynamics of the moving masses. The motion is usually restricted to one axis and is used in the dynamic analysis of solenoids, injectors, and linear actuators. The assumed positive references for distance, velocity, and force are provided in Figure 3.7. Note that the positive direction for the position, velocity, and acceleration is in the negative  $x$  direction. It is assumed that the initial position of the moving region (plunger) is the point at which the distance  $s$  is equal to zero. The sum of all forces acting on a body along the unconstrained portion of the  $x$  axis yields the accelerating force on the body. In this region, the net

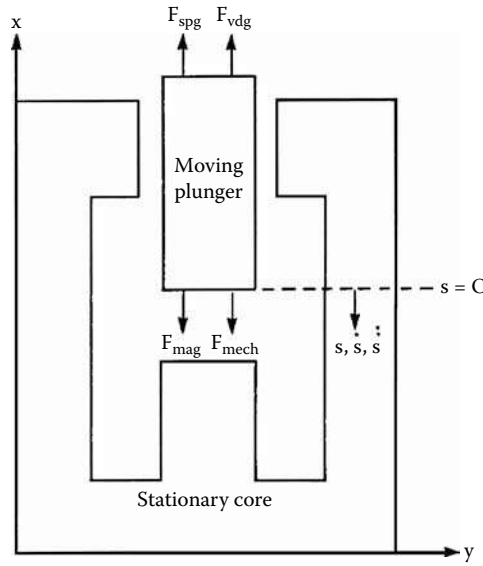


**FIGURE 3.7**  
Force references for motion problems. (Courtesy of Delphi Corp.)

mechanical accelerating force is the result of the magnetic, spring, and viscous forces acting on the moving body as follows:

$$F_{mech} = F_{mag} - F_{spg} - F_{vdg} \quad (3.8)$$

where  $F_{mech}$  is the net mechanical accelerating force,  $F_{mag}$  is the magnetic force,  $F_s$  is the total spring force, and  $F_{vdg}$  is the viscous damping force.

The spring force acting on the moving part consists of two components. The first is a specified preload force, and the second is the normal spring force given by the product of the spring constant  $k$  and the deflection  $s$ . It is assumed that the deflection of the spring and the position of the moving part are identical and defined by the variable  $s$ , as presented in Figure 3.7. The magnetic force acting on the movable body can be determined by using air gap flux density or by integrating the Maxwell stress tensor over the surface of the body. Each of these methods will be discussed in Chapter 4. The calculated magnetic force  $F_{mag}$  is one component in the equation of motion that takes into account the moving mass, the spring forces, and viscous damping, as presented in Equation 3.8:

$$F_{mag} = m \frac{d^2s}{dt^2} + c \frac{ds}{dt} + ks + F_{pl} \quad (3.9)$$

where  $s$  is the position of the moving armature,  $m$  is the total mass of all moving parts including at least half of the spring mass,  $k$  is the spring constant,  $c$  is the viscous damping coefficient, and  $F_{pl}$  is the spring preload.

The instantaneous powers associated with the mechanical subsystem can be now calculated by multiplying the forces acting on the moving body by the velocity of this body. Solving Equation 3.8 and multiplying it by the velocity  $\dot{s}$  yields the power balance for the mechanical subsystem:

$$P_{em} = P_{mech} + P_{spg} + P_{vdg} \quad (3.10)$$

where  $P_{em}$  is the electromagnetic power,  $P_{mech}$  is net mechanical power,  $P_{spg}$  is the spring power, and  $P_{vdg}$  is the viscous damping power.

Comparison of the power balance for the electromagnetic and mechanical subsystems, Equation 3.7 and Equation 3.10, respectively, reveals the coupling of these systems via the electromagnetic power. This term represents the rate of energy conversion between the two systems due to the electromagnetic coupling between the stationary and moving parts of the magnetic circuit. Combining Equation 3.7 and Equation 3.10 yields the overall system power balance:

$$P_s = P_c + P_e + P_r + P_{mech} + P_{spg} + P_{vdg} \quad (3.11)$$

Note that ohmic, eddy current, and viscous damping terms must always be positive because they represent the dissipative mechanisms (sinks) of the system. The reactive, spring, and net mechanical powers, however, may be positive or negative (sinks or sources) depending on the state of the system. Conversely, the input or source power is positive when the source delivers power to the system and negative when the system delivers power to the source.

### 3.1.4 Magnetic Forces

The coupling between the electromagnetic and mechanical components of an electromechanical device manifests itself in the form of magnetic forces exerted on the various parts of the magnetic circuit. The dynamic simulation of such a device, therefore, requires accurate methods for calculating the magnetic force. The conventional method for calculating the force limits its range of applications and its accuracy. In this approach, it is assumed that the faces of the stationary and moving parts are parallel and that the length of the air gap (distance between the faces) is small. Under this assumption, the fields are perpendicular to the face of the moving part and the amount of fringing flux is small. Figure 3.8(a) shows a solenoid device, which satisfies these simplifying assumptions. In such cases, the magnetic force is proportional to the square of the flux density multiplied by the area of the air gap, as follows:

$$F_{mag} = \frac{B_g^2 A_g}{2\mu_0} \quad (3.12)$$

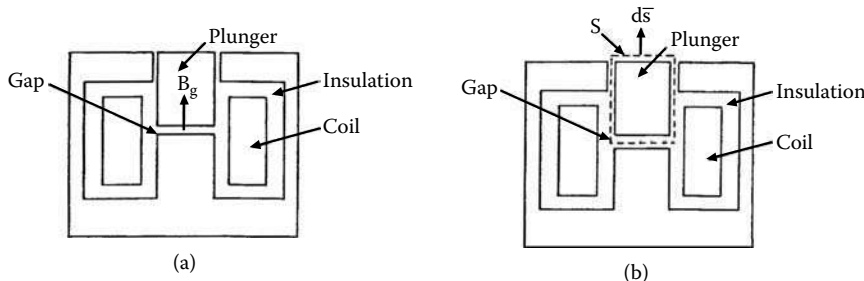


**FIGURE 3.8**

Comparison of methods for force calculations: (a) conventional method, (b) accurate method. (Courtesy of Delphi Corp.)

where  $F_{mag}$  is the magnetic force,  $B_g$  is the flux density in the air gap,  $A_g$  is the area of the air gap, and  $\mu_0 = 4\pi \times 10^{-7} \text{ H/m}$  is the permeability of the free space (air).

Note that in this method only the main air gap field of the plunger face in Figure 3.8(a) is considered. Therefore, the influence of leakage field and “pull-back” phenomena created by the field in parasitic air gap of the plunger is ignored. This method may be used in a simple calculation based on the lumped-parameter model. The analysis of solenoids with tapered or ball-shaped plungers, for example, requires a more accurate method for force calculation, one that will take into account the total field distribution over the surface of the moving part. The magnetic force calculations are based on the Maxwell stress tensor over the surface of the plunger and along the dashed line in Figure 3.8(b), defined by:

$$F_T = \left[ \iint_S \bar{T} \cdot d\bar{s} \right] \cdot [-\bar{a}_x] \quad (3.13)$$

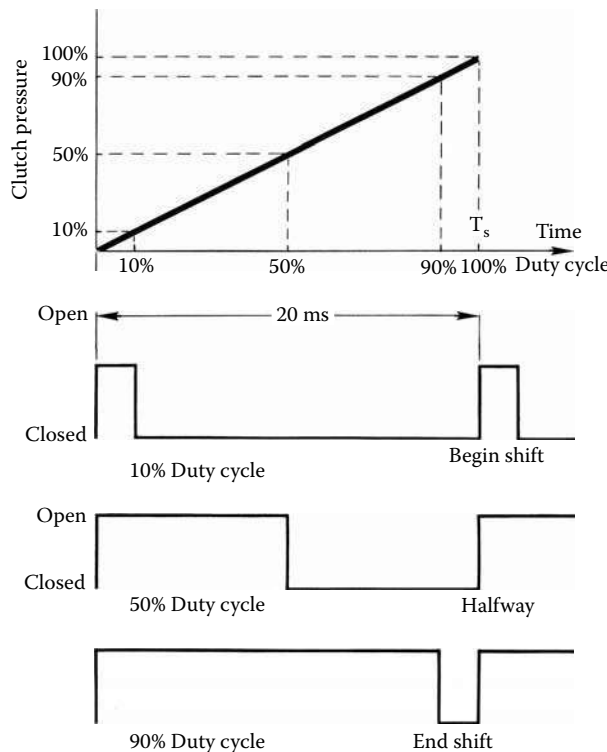
where  $F_T$  is the magnetic force,  $\bar{T}$  is the Maxwell stress tensor in dyadic form,  $\bar{a}_x$  is a unit vector in the vertical ( $x$ ) direction, and  $S$  is the surface of integration.

The integral expression appearing in Equation 3.13 yields the total magnetic force exerted on the body contained within the surface of integration  $S$ . Because motion is constrained to the vertical or  $x$  axis, only the vertical component of this total force is of interest. This component of force is obtained by the dot product of the total force with the vertical unit vector, as given in Equation 3.13. The negative sign appearing in this equation is due to the assumed positive reference for the magnetic component of force, as presented in Figure 3.7. The surface of integration  $S$  completely encloses the moving part, as shown by the dashed line in Figure 3.8(b). The exact path of this integration is not important as long as the moving part is completely enclosed and the path encloses no other magnetizable regions. Therefore, the magnetic force calculated this way includes the influence of all fields impinging on the moving part.

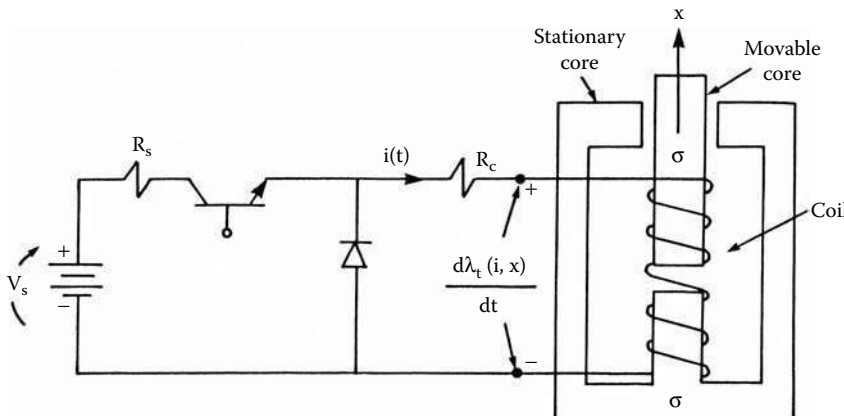
### 3.1.5 PWM Analysis

A PWM voltage source is required for the fast-acting solenoids to achieve smooth operation. This is particularly important to control the average value of the applied voltage and the variation of the duty cycle of the voltage applied to the solenoid. The result is smooth control of the fluid pressure. Figure 3.9 shows the variation of the fluid pressure as a function of the duty cycle and sequence of pulses applied to the solenoid with a frequency of 50.0 Hz (20.0 ms). To obtain a wide range of duty cycle operations (10–90%) at this frequency, as presented in Figure 3.9, the response time of the actuator should be less than 2.0 ms. The current level in the solenoid is controlled by superposing pulses to the applied voltage pulse having a subfrequency in the range of 500.0 Hz. These phenomena are also included in our analytical model.

The analysis of the fast-operating solenoid from the PWM voltage sources requires a mathematical model, which simulates power electronics, as well as the mechanical and magnetic systems (Demenko and Pietrowski 2004, Demenko and Sykulski 2002, Marinova et al. 2000, Nowak and Demenko 2000, Pawlak et al. 1988, Roel Ortiz et al. 2001, Nowak 1989). The 2D FE model solves the magnetic field problem by taking into account the moving armature, eddy currents, currents due to motion, and nonlinearity of the magnetic circuit. The mechanical system of the model includes the moving masses, the spring characteristics, viscous damping, and rebound decay constants. A schematic of a typical solenoid operated from a PWM controlled voltage source is shown in Figure 3.10.

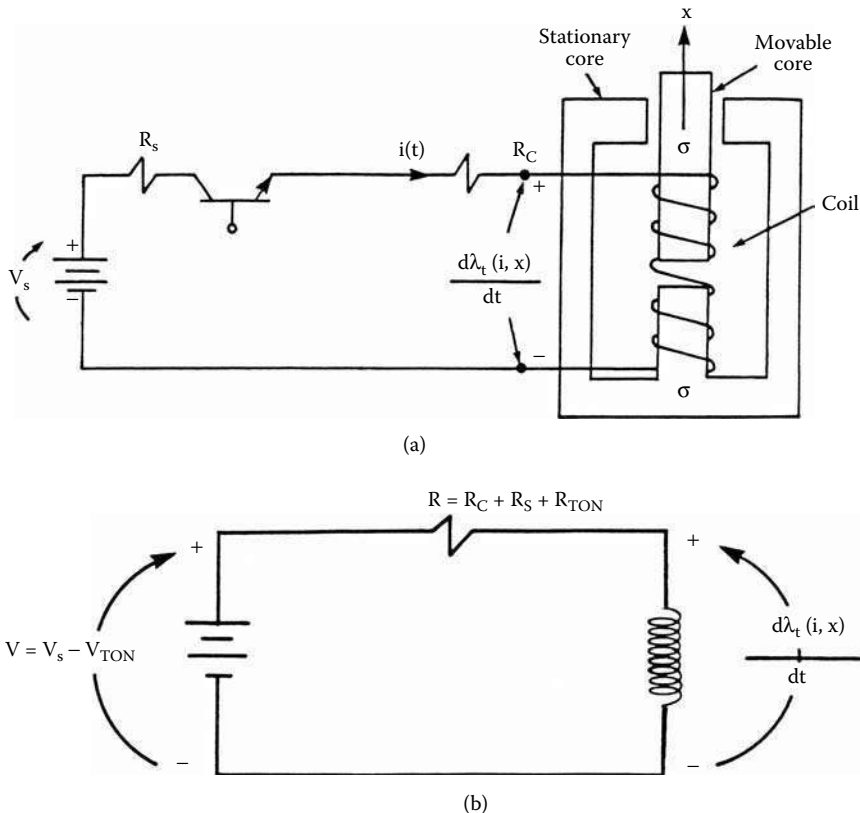
**FIGURE 3.9**

PWM to control fluid pressure. (From Pawlak, A.M. et al., *IEEE Transactions on Magnetics*, 24(1), 270–274, 1988. With permission.)

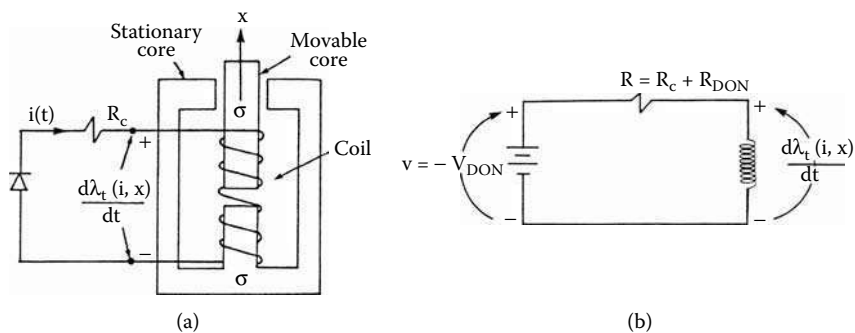
**FIGURE 3.10**

PWM voltage source operated solenoid. (From Pawlak, A.M. et al., *IEEE Transactions on Magnetics*, 24(1), 270–274, 1988. With permission.)

In automotive applications, the source is the car battery and the PWM is usually performed by a transistorized DC chopper. The power circuit switches between two states depending upon status (ON or OFF) of the chopper transistor. When the transistor is conducting (ON), the diode is reverse biased (OFF), as shown in Figure 3.11(a). In this

**FIGURE 3.11**

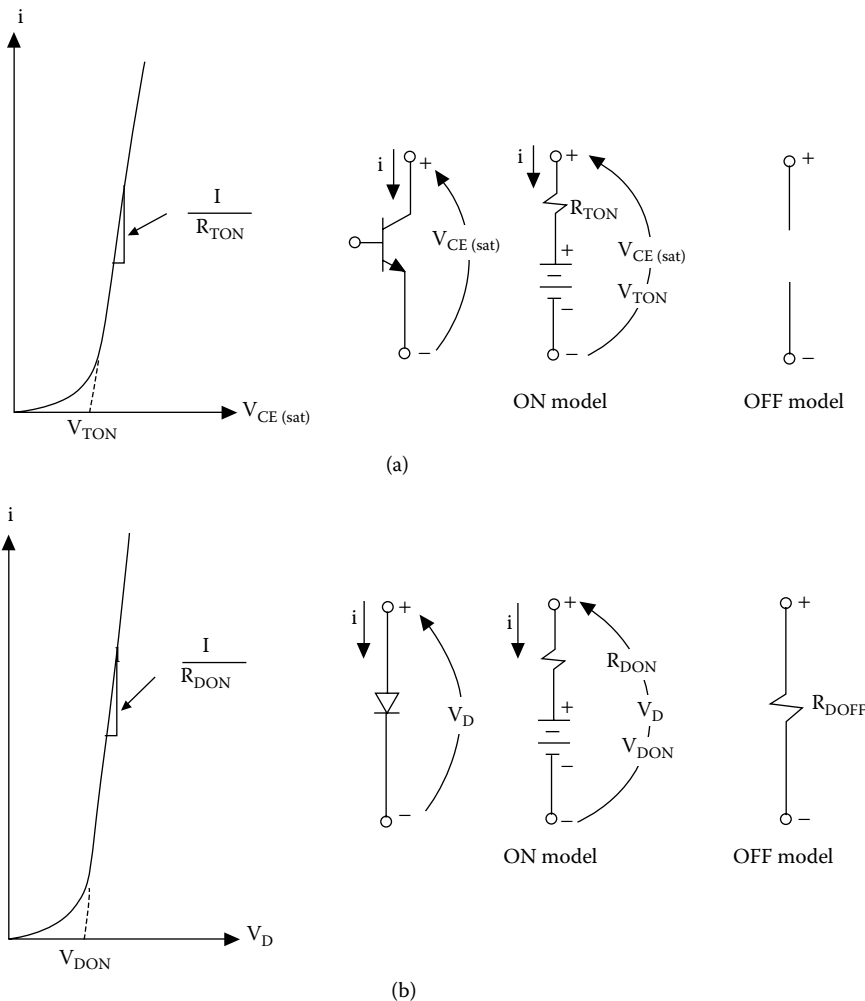
Solenoid operated from a PWM voltage source (ON state): (a) lumped-parameter model, (b) equivalent electrical network model. (From Pawlak, A.M. et al., *IEEE Transactions on Magnetics*, 24(1), 270–274, 1988. With permission.)

**FIGURE 3.12**

Solenoid operated from a PWM voltage source (ON state): (a) lumped-parameter model, (b) equivalent electrical network model. (From Pawlak, A.M. et al., *IEEE Transactions on Magnetics*, 24(1), 270–274, 1988. With permission.)

case, the DC voltage source is connected to the solenoid and the current in the coil increases provided that the source voltage is greater than the voltage induced in the coil.

The diode is forward biased (ON) whenever the transistor turns off. During this state, the source is disconnected from the solenoid, as shown in Figure 3.12(a), causing the current to decrease.

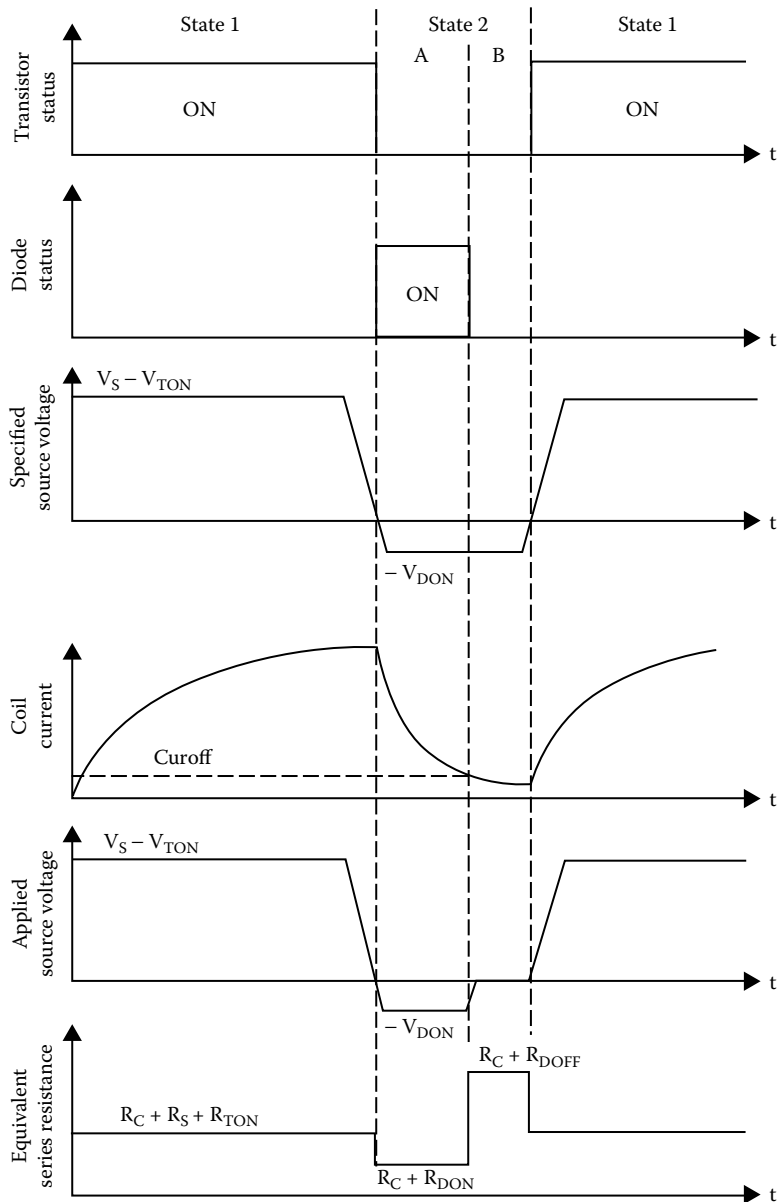
**FIGURE 3.13**

Transistor and diode models for PWM voltage source: (a) transistor model, (b) diode model. (From Pawlak, A.M. et al., *IEEE Transactions on Magnetics*, 24(1), 270–274, 1988. With permission.)

The transistors and diode models used to represent this switching action are shown in Figure 3.13(a) and Figure 3.13(b), respectively.

During the ON state, both devices are represented by a series of connected resistance and voltage source. During the OFF state, the transistor is replaced by an “open circuit,” as shown in Figure 3.13(a), thereby disconnecting the solenoid from the voltage source. The OFF state of the diode is represented by an open circuit whenever the transistor is OFF, as shown in Figure 3.13(b). The finite diode resistance is required during the OFF state of the transistor to avoid singularities with the voltage source option in the FE model.

With these simple switching models, one can replace the two states of this system, shown schematically in Figure 3.11(a) and Figure 3.12(a), with the equivalent network models of Figure 3.11(b) and Figure 3.12(b), respectively. The topologies of these network models are identical, consisting of a series of connected resistances, a voltage source, and a coil. The difference between the two models is in the values assigned to the equivalent voltage

**FIGURE 3.14**

Timing diagram for the PMW voltage source. (From Pawlak, A.M. et al., *IEEE Transactions on Magnetics*, 24(1), 270–274, 1988. With permission.)

source and resistance. The relationship between the states of the network and the equivalent voltages, resistance, and current are given in the timing diagram, Figure 3.14.

Note that the OFF state of the transistor is divided into two substates (A and B). This is necessary because a forward biased diode turns off when the current passes through zero. To simulate the behavior, the equivalent series resistance is set to a specified OFF value when the diode current drops below a specified current level CUROFF, as shown in Figure 3.14. When the diode current drops below this value, the ON diode model is replaced by the OFF diode model and the applied source voltage is set to zero.

### 3.1.6 Solenoid Analysis and Simulations

The typical 2D FE software system for magnetic field analysis solves Poisson's equation for the magnetic vector potential as introduced in Equation 2.7 and described in more detail in Ando et al. (2001), Ansoft (1991), Box et al. (1969), Brauer (1988), Brauer et al. (2000), Dąbrowski (1971), Demenko (1994), McBain (1981), Melgoza and Rodger (2002), Nehl et al. (1988), Silvester and Ferrari (1990), and Sykulski et al. (1995):

$$\nabla \times (v \nabla \times \bar{A}) = \bar{J}_s + \bar{J}_{pm} - \sigma \frac{\partial \bar{A}}{\partial t} + \sigma \bar{V} \times \nabla \times \bar{A} \quad (3.14)$$

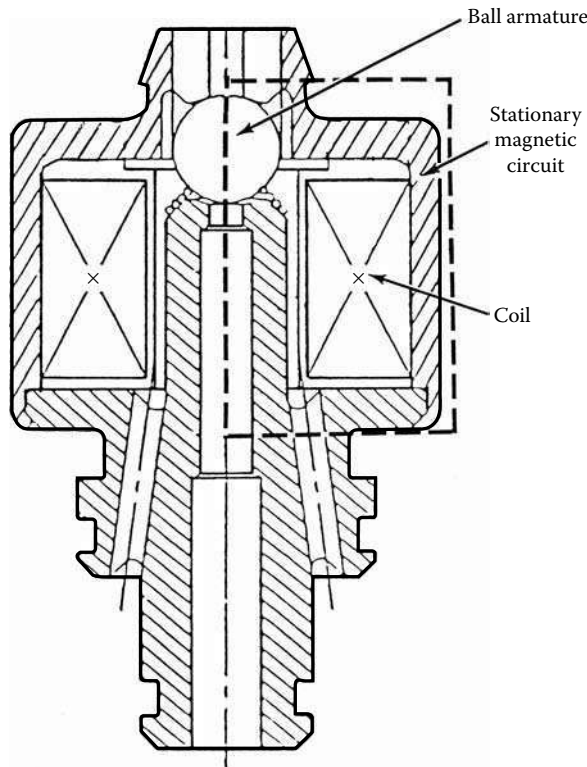
where  $v$  is the material reluctivity,  $\bar{A}$  is the magnetic vector potential,  $\sigma$  is the material conductivity,  $\bar{J}_s$  is the external source current density,  $\bar{J}_{pm}$  is the equivalent PM current density, and  $\bar{V}$  is the velocity of the field point.

The first term on the right-hand side of this equation is the current density due to a specified source. This includes windings excited by voltage or current source. The second term is the current density due to PMs. The third term accounts for induced currents due to possible motion of the field point with respect to the fixed coordinate reference frame.

Problems with a specified voltage source excitation require a solution of both the field problem, Equation 3.14, and the electrical network problem, Equation 3.1. This is accomplished using an iterative procedure. First, a guess at the winding current  $i$  is made based upon the value at the previous time step by means of the predictor step. Using this guess at the winding current, the field equation is solved for the vector potentials. The vector potentials are then used to calculate the total flux linkage of the winding. Using the flux linkage from the previous time step, the time derivative of the flux linkage is approximated. This information is then used to calculate the voltage  $v$  in Equation 3.1. If this voltage differs from the specified value by more than a given percentage, the winding current is recalculated using a corrector step. The iterative process is repeated until this difference meets the specified voltage tolerance. Equations 3.1, 3.9, 3.13, and 3.14 constitute a set and are solved simultaneously to obtain solutions of the dynamic behavior of the solenoid actuators.

Ball-type solenoid actuators are suitable for fluid control due to their good sealing capabilities. The solenoid, shown in Figure 3.15, has a cylindrical symmetry and consists of a ball armature, a stationary magnetic circuit, a stationary coil, and a return spring. Because of the cylindrical symmetry, only the section of the device enclosed by the dotted line in this figure needs to be modeled. The distribution of the magnetic circuit at different points in time is shown in Figure 3.16. The diffusion (penetration) of the flux into the magnetic core is clearly illustrated for these successive points in time. Actually, the ball motion does not begin until the flux penetrates the ball and the resulting force overcomes the spring preload (Bottauscio et al. 2003).

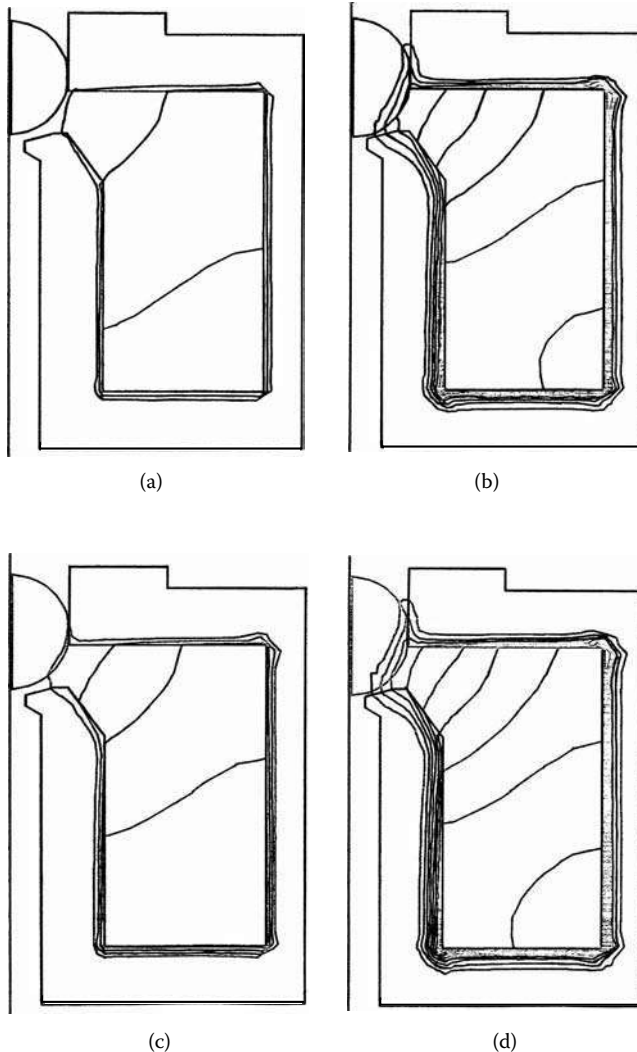
Figure 3.17 displays eight sample waveforms obtained using a software postprocessor. Included in these figures is Figure 3.17(a), which presents a specified voltage with a frequency of 50 Hz having a high subfrequency of 500 Hz imposed on a regular frequency

**FIGURE 3.15**

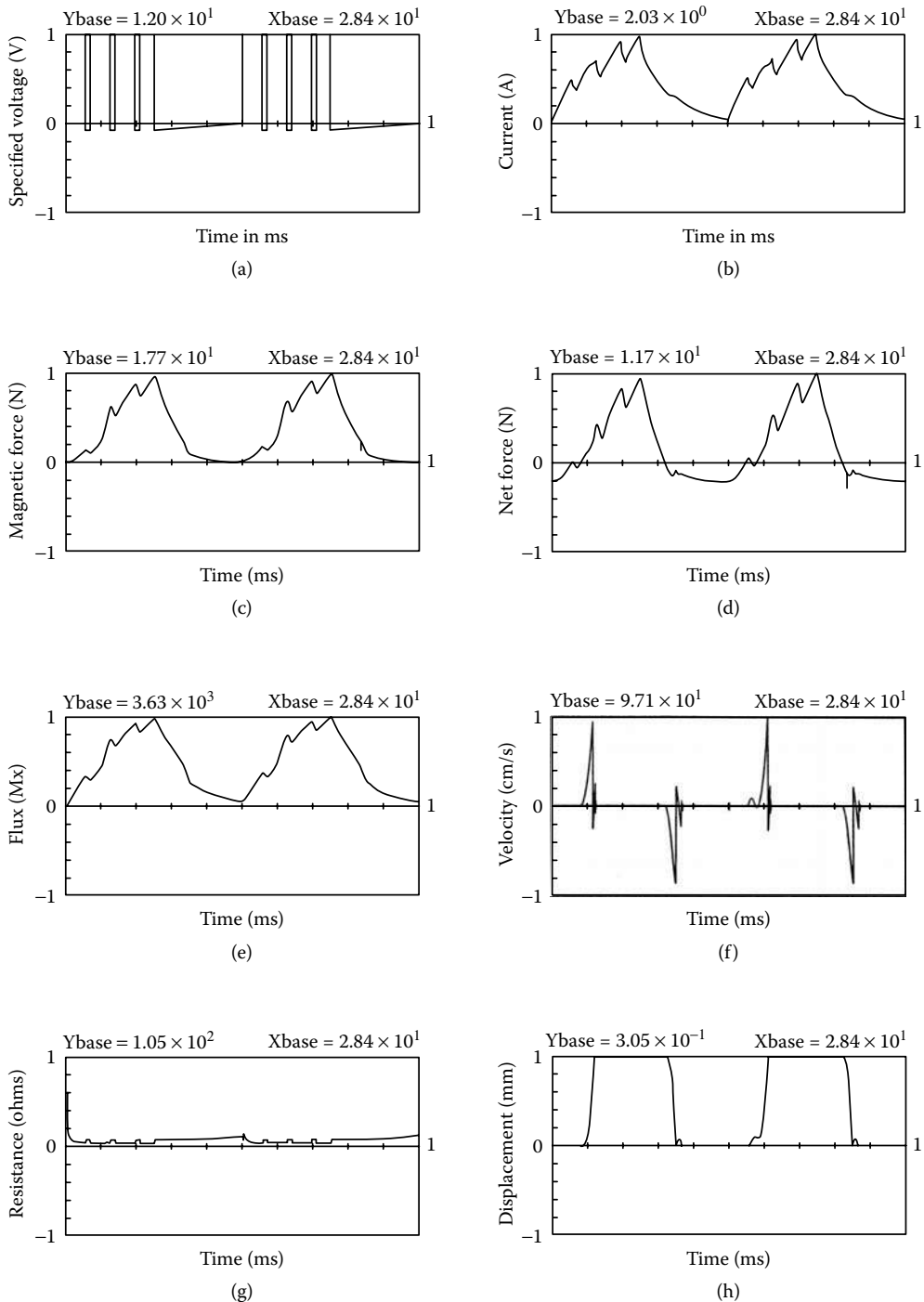
Ball-type solenoid actuator. (From Pawlak, A.M. et al., *IEEE Transactions on Magnetics*, 24(1), 270–274, 1988. With permission.)

to control the current level. Figure 3.17(b) illustrates the calculated current that shows a saw-type characteristic that limits the final current level. Both the flux crossing the main air gap and the total magnetic force on the ball shown in Figure 3.17(e) and Figure 3.17(c), respectively, have similar characteristics to the source current. The net force on the ball shown in Figure 3.17(d) is the result of the spring forces and the total magnetic forces indicating the net forces exerted on the ball with a ball velocity shown in Figure 3.17(f). The resistance vs. time and velocity vs. time are shown in Figure 3.17(g) and 3.17(h), respectively. Zero crossing of the net force identifies points where the net force changes its direction and also identifies the beginning and the end of the motion displacement, as shown in Figure 3.17(h) (Nehl et al. 1988, Pawlak 1989, Piron et al. 1999).

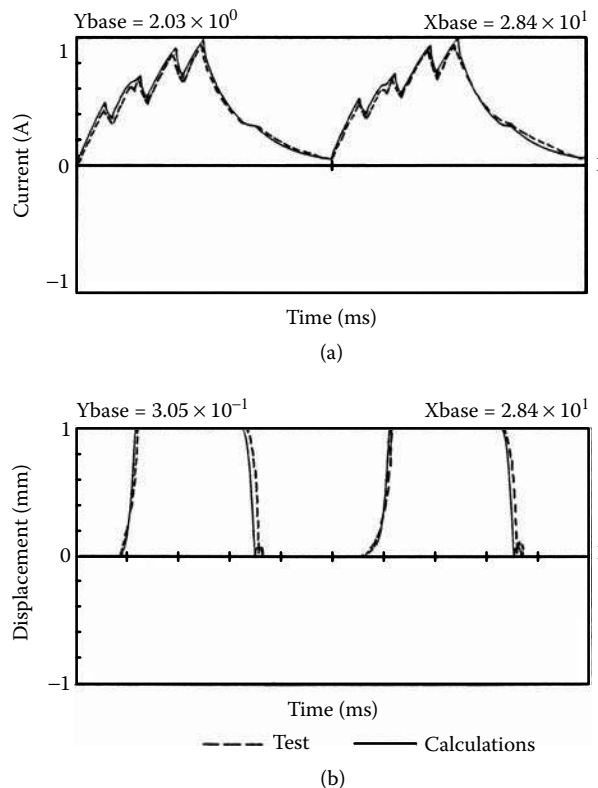
The ball-type solenoid was tested in dry conditions. With the specified voltage applied, the coil current and the armature displacement were measured using a calibrated current probe and the armature displacement was measured using a commercial proximity transducer. The test results for the current and displacement vs. time are compared with the corresponding calculated data in Figure 3.18, showing good agreement (Nehl et al. 1988).

**FIGURE 3.16**

Flux distribution of ball-type solenoid: (a) time 1.0 ms, (b) time 2.0 ms, (c) time 3.0 ms, (d) time 4.0 ms. (From Pawlak, A.M. et al., *IEEE Transactions on Magnetics*, 24(1), 270–274, 1988. With permission.)

**FIGURE 3.17**

Sample waveforms for ball-type solenoid dynamics: (a) specified voltage vs. time, (b) current vs. time, (c) magnetic force vs. time, (d) net force vs. time, (e) flux vs. time, (f) velocity vs. time, (g) resistance vs. time, (h) displacement vs. time. (From Pawlak, A.M. et al., *IEEE Transactions on Magnetics*, 24(1), 270–274, 1988. With permission.)

**FIGURE 3.18**

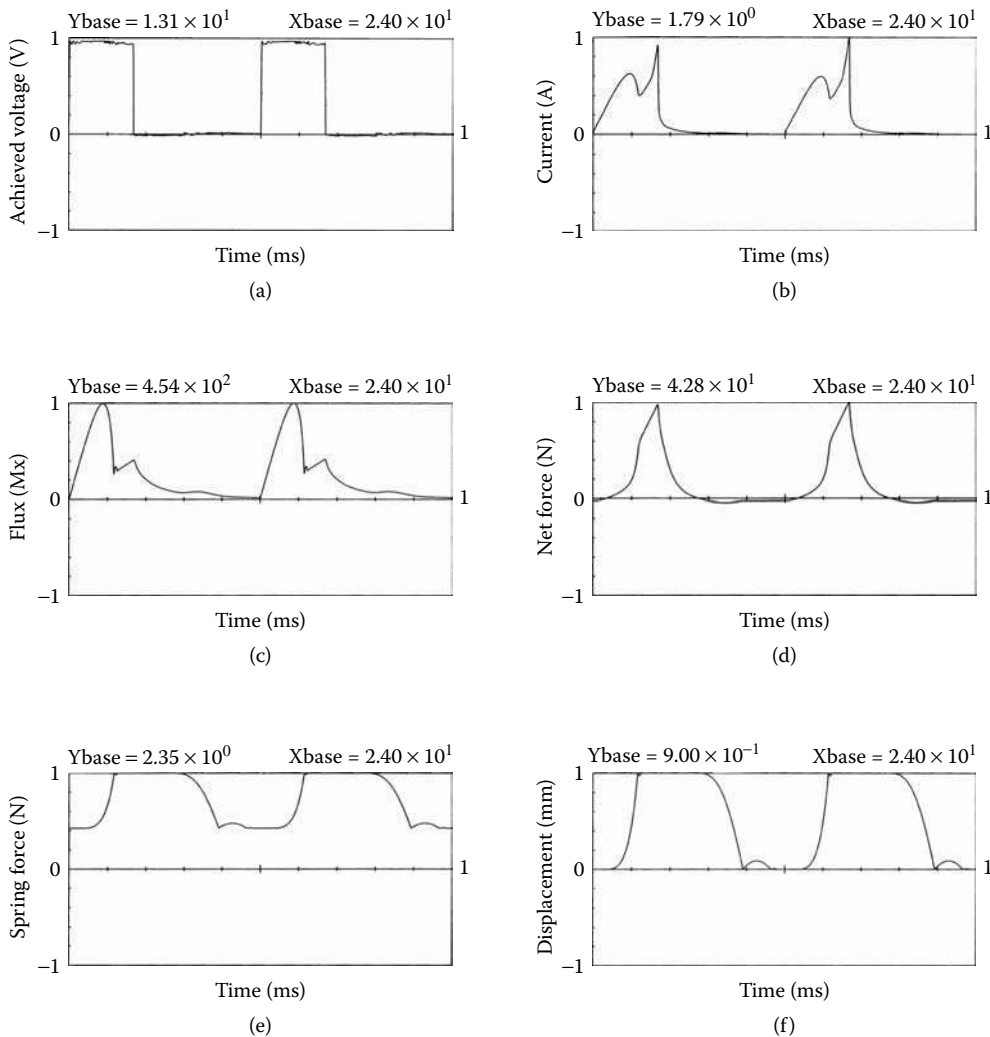
Current and displacement of ball-type solenoid analysis and test comparison: (a) current vs. time, (b) displacement vs. time. (From Pawlak, A.M. et al., *IEEE Transactions on Magnetics*, 24(1), 270–274, 1988. With permission.)

### 3.2 Fast-Acting Actuators

Four basic solenoid configurations with disk, plunger, conical, and ball armatures are the subjects of analysis in this chapter. Each of these configurations has unique features that predetermine applications. Pros and cons of these structures are discussed in detail. For comparison purposes, cylindrical symmetry is assigned to all the solenoid types. For the FE analysis, each solenoid is divided into a number of regions that describe the universe (air), the stationary magnetic circuit, the coil with the current source, and magnetic armature. Additionally, the main air gap region can be specified separately to maintain a linear displacement of the armature and prevent shrinking the air gap to zero, which may cause converging problems.

#### 3.2.1 Disk Solenoids

Unlike other solenoid types, the disk solenoid configuration has double the main air gap for flux to cross, as shown in Figure 3.1(a). At the same time, it has two relatively large surfaces of inner pole and outer magnetic circuit around a coil where flux is perpendicular to its surface — at least at the small air gaps. This promotes applications with small travel

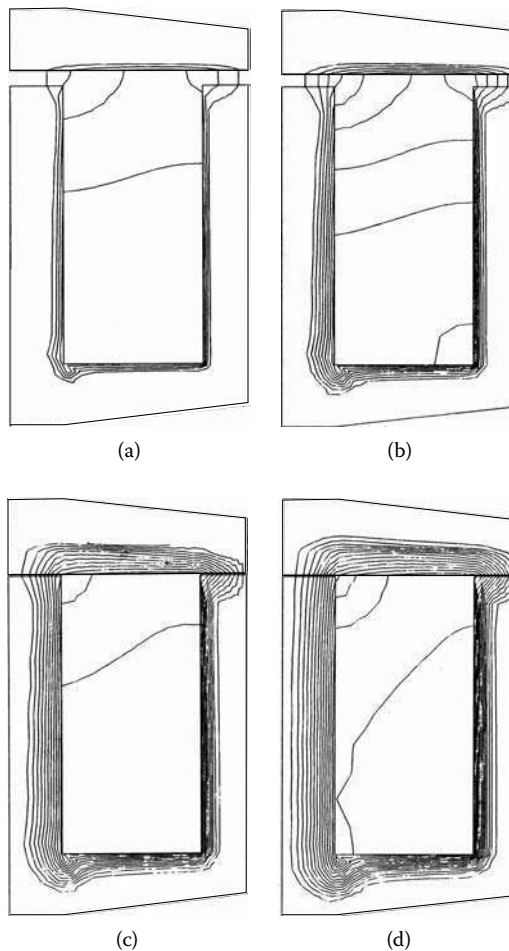
**FIGURE 3.19**

Disk solenoid magnetic flux vs. time: (a) achieved voltage vs. time, (b) current vs. time, (c) flux vs. time, (d) net force vs. time, (e) spring force vs. time, (f) displacement vs. time. (Courtesy of Delphi Corp.)

and fast action. A small travel would secure high solenoid electromagnetic efficiency, where large forces would help complete the travel distance in a relatively short period of time. Therefore, disk solenoids may find applications as injectors where all these attributes can be utilized.

The dynamic characteristics of the disk solenoid are presented in Figure 3.19(a) through Figure 3.19(f) for the input voltage, corresponding coil current, magnetic flux developed in the armature, the net force of the disk armature, the spring force, and the displacement of the armature.

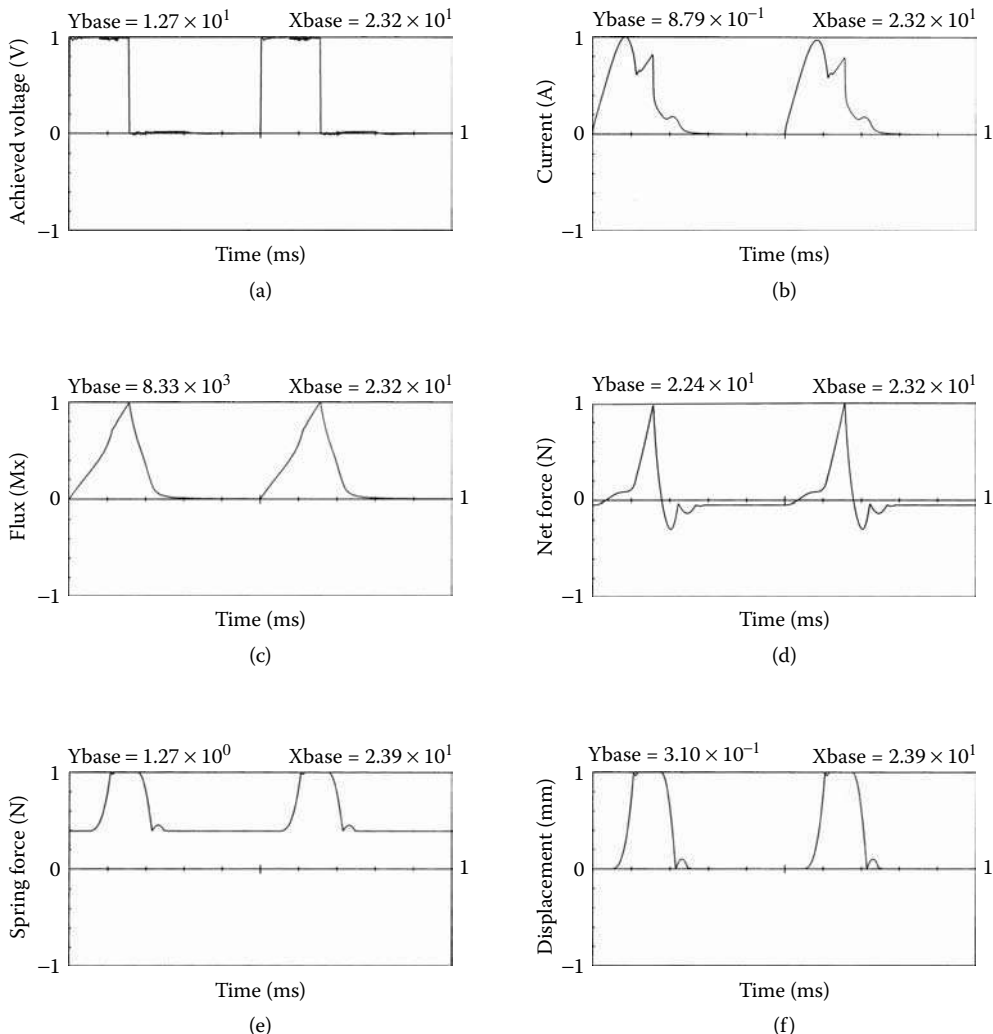
Figure 3.20 shows the magnetic flux distribution for the disk solenoid at different time intervals. Note that at the beginning of the cycle, the armature is in the upper position with low penetration of the magnetic flux within the magnetic circuit, but at the end of the cycle, the armature rests against the lower magnetic circuit with zero air gap and deep penetration of the magnetic flux within the magnetic circuit.

**FIGURE 3.20**

Dynamic characteristics of the disk solenoid: (a) flux at 1.0 ms, (b) flux at 2.0 ms, (c) flux at 4.0 ms, (d) flux at 6.0 ms. (Courtesy of Delphi Corp.)

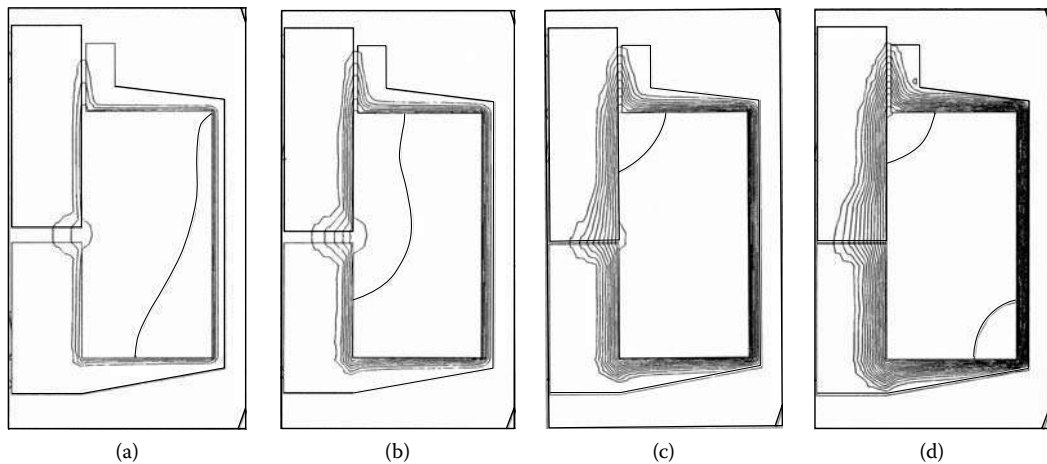
### 3.2.2 Plunger Solenoids

Plunger solenoid types are the most popular solenoid configuration with a variety of applications. This is because the plunger solenoid configuration has a single main air gap for flux to cross and one parasitic air gap that is usually perpendicular to the main one. The inner pole surface of the main air gap carries the flux that is perpendicular to its surface, especially at the small air gaps where the flux crossing a parasitic air gap does not contribute to the axial forces, and in most of the cases, when the parasitic air gap is even around the axis of symmetry, these forces cancel out. This promotes applications with small travel and fast action such as injectors and other fast-acting solenoids. The plunger solenoid electromagnetic efficiency may be secured with small plunger travel and small parasitic air gap with provisions to reduce flux density in this region by elongating the parasitic gap axially.

**FIGURE 3.21**

Dynamic characteristics of the plunger solenoid: (a) achieved voltage vs. time, (b) current vs. time, (c) flux vs. time, (d) net force vs. time, (e) spring force vs. time, (f) displacement vs. time. (Courtesy of Delphi Corp.)

The dynamic characteristics of the plunger solenoid are presented in Figure 3.21(a) through Figure 3.21(f) for the input voltage, corresponding coil current, magnetic flux developed in the armature, the net force of the disk armature, the spring force, and the displacement of the armature. Figure 3.22 shows the magnetic flux distribution for the plunger solenoid at different time intervals. Note that at the beginning of the cycle, the armature is in the upper position with low penetration of the magnetic flux within the magnetic circuit. At the end of the cycle, the armature rests against the lower magnetic circuit with zero air gap and deeper penetration of the magnetic flux within the magnetic circuit, yet not as deep as in the disk solenoid case.

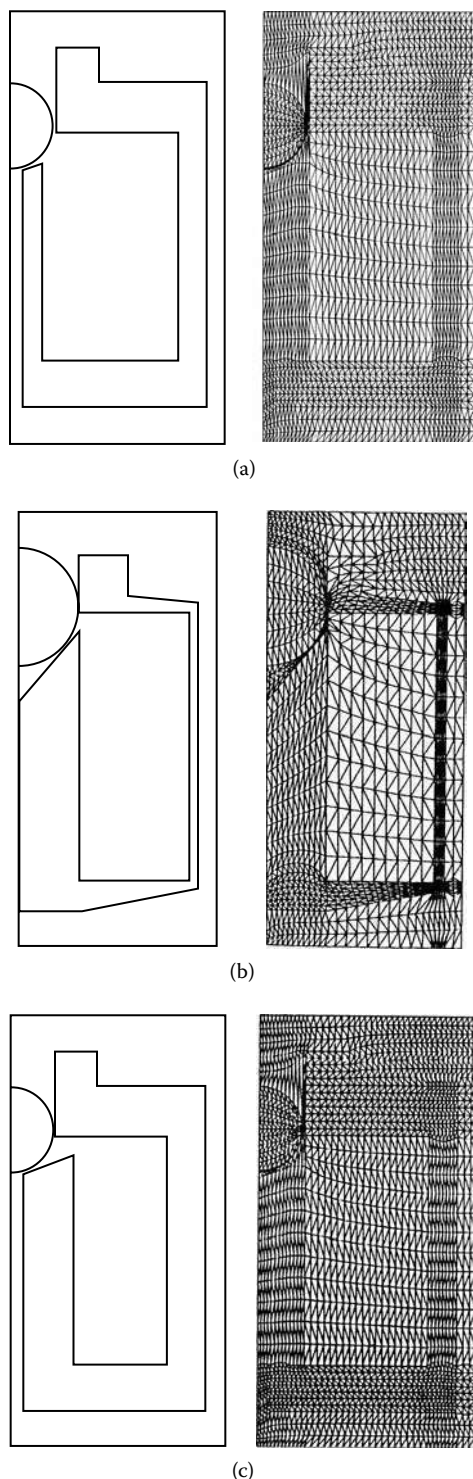


**FIGURE 3.22**  
Plunger solenoid magnetic flux vs. time: (a) flux at 1.0 ms, (b) flux at 2.0 ms, (c) flux at 3.0 ms, (d) flux at 4.0 ms. (Courtesy of Delphi Corp.)

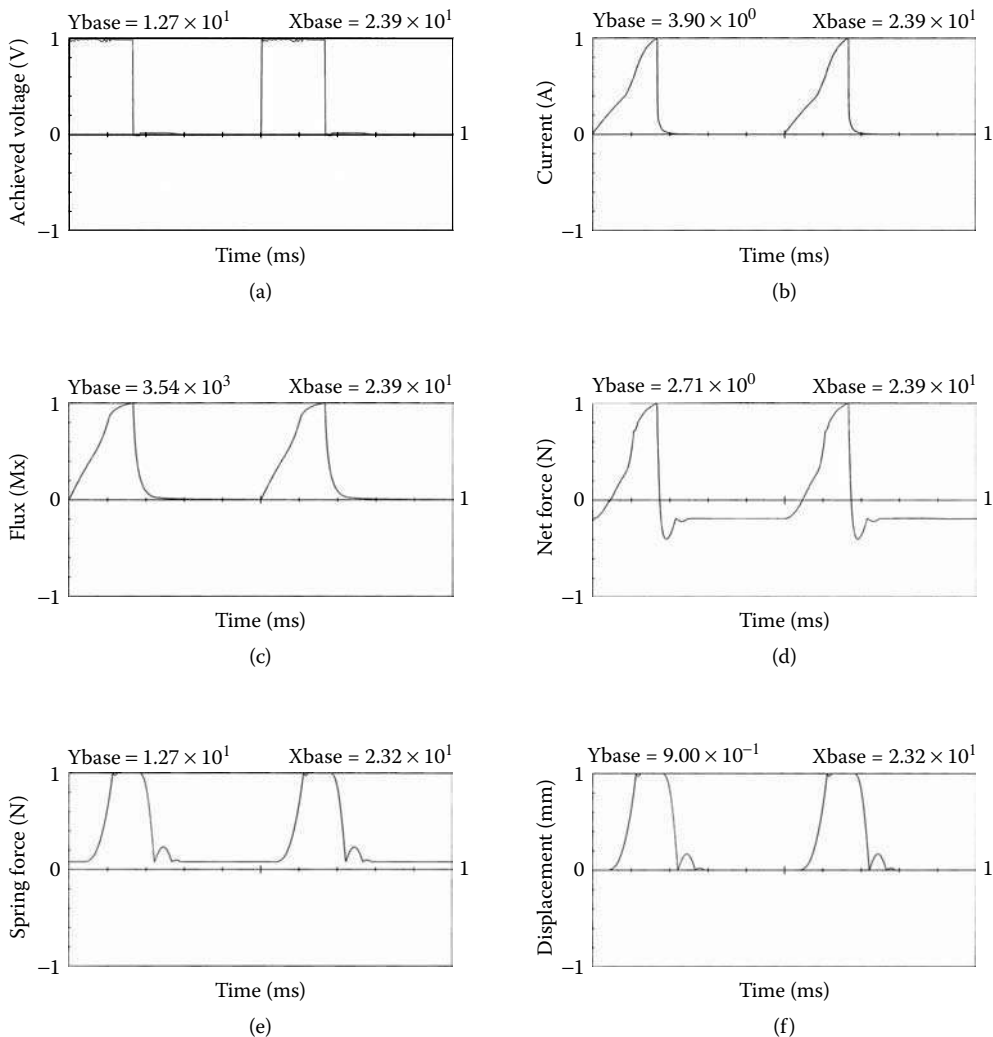
### 3.2.3 Ball Solenoids

Ball-type solenoid actuators can be applied in fluid control applications, such as automatic transmissions, due to their good sealing capabilities and response time. They are also used in applications where the ball armature, due to its inertia in a car crash, is separated from a PM ball stop and may be, therefore, used as an air bag deployment mechanism. The ball solenoid configuration has limited applications that are also more difficult to analyze because of the shape of the armature. This is a result of its uneven main air gap for flux to cross and uneven parasitic air gap, which is usually perpendicular to the main one. The inner pole surface of the main air gap carries the flux that is not perpendicular to its surface; therefore, a portion of the entire flux crosses the main air gap contributing to the axial forces. In addition, the flux crossing the parasitic air gap may not be even around the axis of symmetry, and these forces may not cancel out. This promotes only applications where the geometry of a ball can be applied in fluid dynamics. The ball solenoid electromagnetic efficiency is not very effective because its total average air gap is larger than a mechanical air gap for the axial motion. Depending on requirements and applications, three inner stop OD versions are considered, as shown in Figure 3.23.

The dynamic characteristics of the ball solenoid are presented in Figure 3.24(a) through Figure 3.24(f) for the input voltage, corresponding coil current, magnetic flux developed in the armature, the net force of the disk armature, the spring force, and the displacement of the armature. Figure 3.25 presents the magnetic flux distribution for the ball solenoid at different time intervals. Note that at the beginning of the cycle, the armature is in the upper position with low penetration of the magnetic flux within the magnetic circuit. During the consecutive steps of the cycle, flux shows deeper penetration within the magnetic circuit, and the ball armature is attracted to the inner stop.

**FIGURE 3.23**

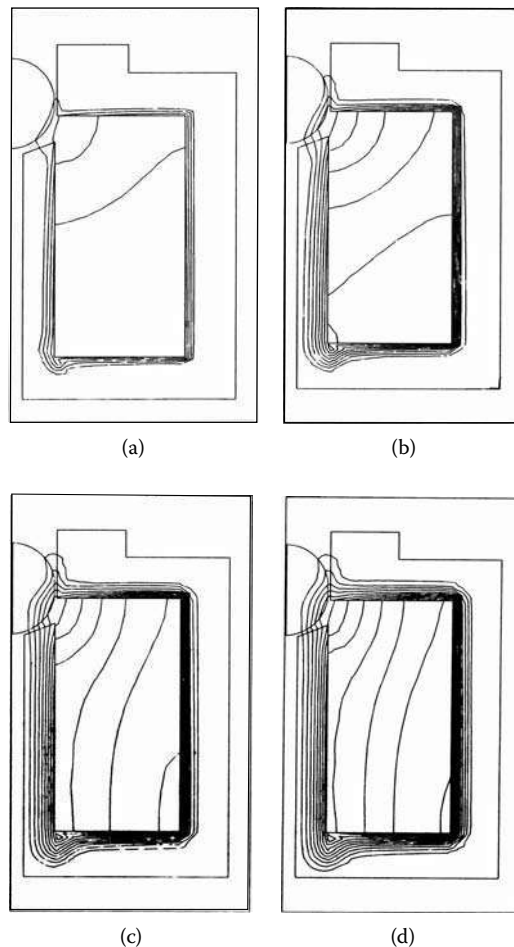
Ball solenoid with different inner stop OD versions: (a) OD ball > OD stop, (b) OD ball = OD stop, (c) OD ball < OD stop. (Courtesy of Delphi Corp.)

**FIGURE 3.24**

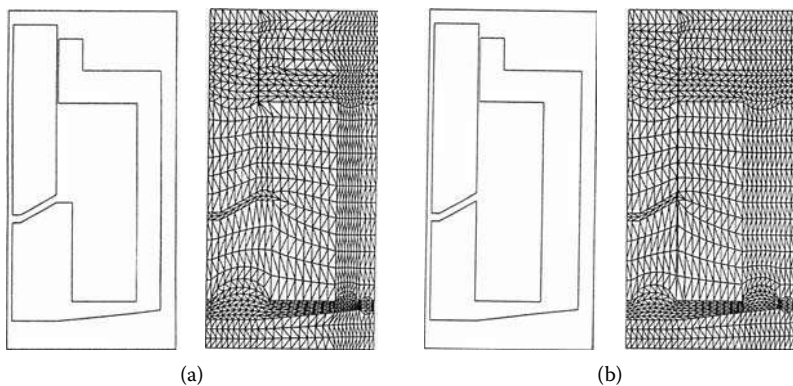
Dynamic characteristics of the ball-type solenoid: (a) achieved voltage vs. time, (b) current vs. time, (c) flux vs. time, (d) net force vs. time, (e) spring force vs. time, (f) displacement vs. time. (Courtesy of Delphi Corp.)

### 3.2.4 Conical Solenoids

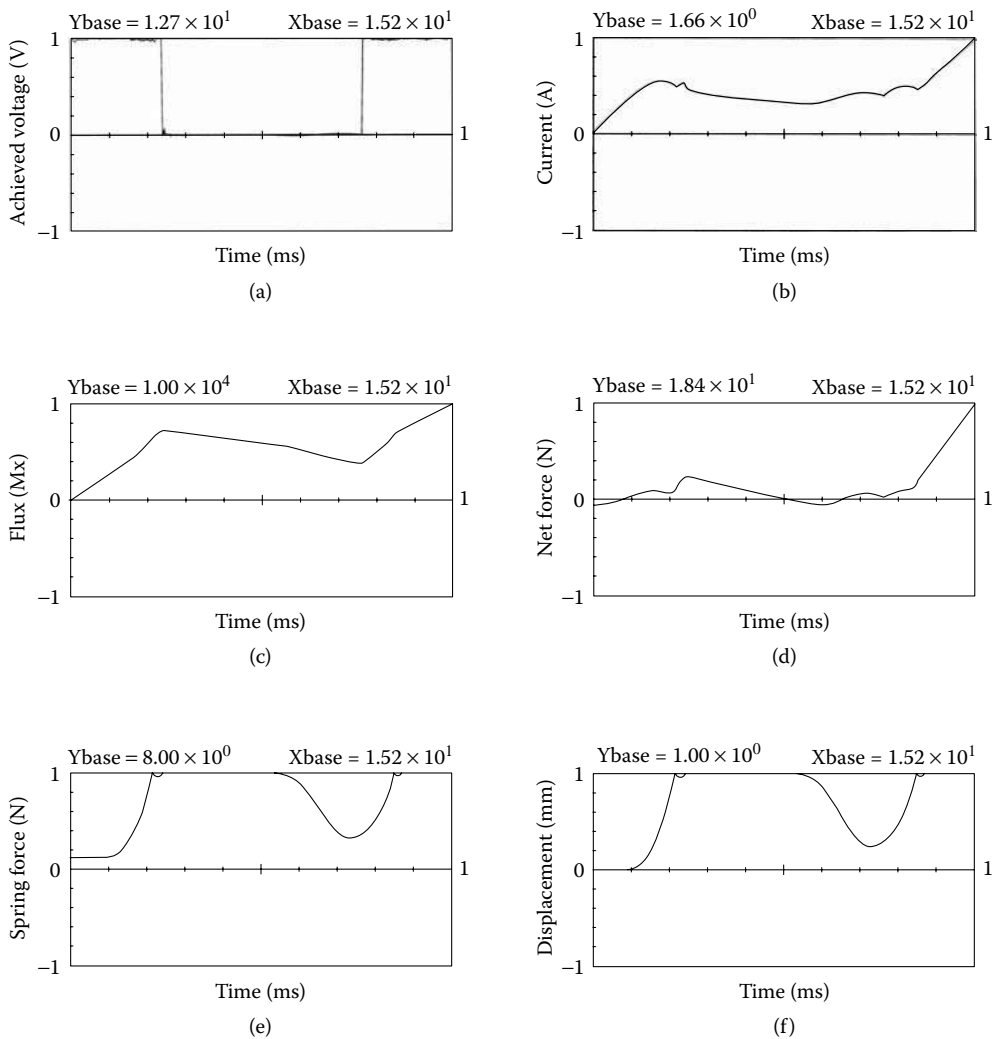
Conical solenoid actuators can be used in long stroke applications, such as in automotive door locks, due to their high force over long stroke capabilities. They can also be applied in situations where the armature can develop a relatively large force due to a smaller magnetic air gap than axial stroke. The conical solenoid configuration has limited applications in long stroke travel without fast response time. This is because the conical solenoid configuration has a single main air gap for flux to cross that is always smaller than mechanical travel distance and one parasitic air gap that is usually perpendicular to the direction of motion. The inner pole surface of the main air gap carries the flux that is perpendicular to its surface but not perpendicular to the axial motion. The flux crossing a parasitic air gap does not contribute to the axial forces, and in most cases, when the parasitic air gap is even around the axis of symmetry these forces cancel out. Depending on requirements and applications, the inner stop OD versions are considered, as shown in Figure 3.26.

**FIGURE 3.25**

Ball solenoid magnetic flux vs. time: (a) flux at 1.0 ms, (b) flux at 2.0 ms, (c) flux at 3.0 ms, (d) flux at 4.0 ms.  
(Courtesy of Delphi Corp.)

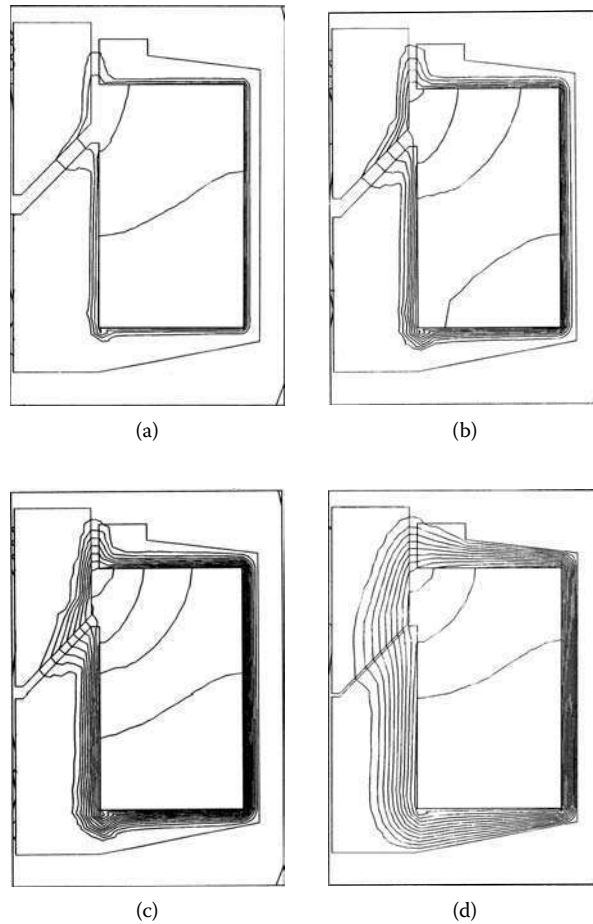
**FIGURE 3.26**

Conical solenoid with different inner stop OD versions: (a) OD conical arm < OD stop, (b) OD conical arm > OD stop. (Courtesy of Delphi Corp.)

**FIGURE 3.27**

Dynamic characteristics of the conical solenoid: (a) achieved voltage vs. time, (b) current vs. time, (c) flux vs. time, (d) net force vs. time, (e) spring force vs. time, (f) displacement vs. time. (Courtesy of Delphi Corp.)

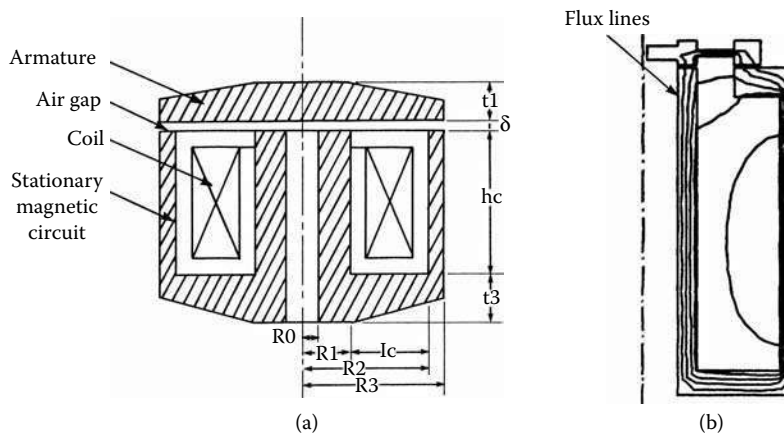
The dynamic characteristics of the conical solenoid are shown in Figure 3.27(a) through Figure 3.27(f) for the input voltage, corresponding coil current, magnetic flux developed in the armature, the net force of the disk armature, the spring force, and the displacement of the armature. As shown, the conical solenoid requires a longer period of voltage pulse than other types of solenoids to bring the armature to the rest position against the plunger stop. Figure 3.28 presents the magnetic flux distribution for the conical solenoid at different time intervals. Note that at the beginning of the cycle, the armature is in the upper position with low penetration of the magnetic flux within the magnetic circuit, although in all of the following steps of the cycle, flux shows deeper penetration within the magnetic circuit. The flux leaving the conical armature is perpendicular to the surface of the armature stop.

**FIGURE 3.28**

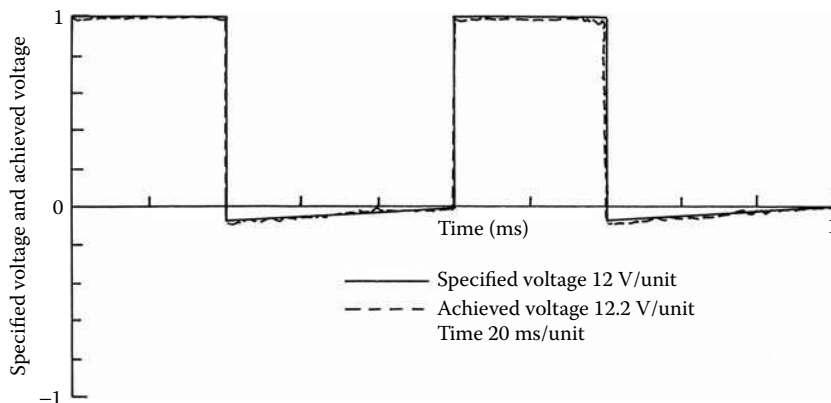
Conical solenoid magnetic flux vs. time: (a) flux at 1.0 ms, (b) flux at 2.0 ms, (c) flux at 3.0 ms, (d) flux at 4.0 ms.  
(Courtesy of Delphi Corp.)

### 3.2.5 Optimization of Fast-Acting Actuators

Optimization of an electromagnetic device is an art (Matsumoto et al. 2004, Pawlak 1989, Yoon et al. 1999). The challenge is in devising the best structure to meet all the requirements. Traditionally, optimization has been limited to a parametric study where only one parameter varies at a time, and this book is a good example of it. Optimization, however, suggests searching for a goal function, whereby all variables change and lead to achieving a goal solution. Therefore, one has to first determine a goal function and second to select all variables that can affect the selected goal function. The next step is to reduce the number of variables by subtracting from them all the requirements. Examples of such requirements may be an envelope, travel, voltage and current limitations, etc. Suppose that the subject of our optimization is a disk solenoid with the minimum mass as determined by the goal function and three variables that are not limited by any of the requirements and constraints. These variables are the thickness of the disk armature  $t_1$ , the thickness of the bottom of the stationary magnetic circuit  $t_3$ , and the coil window ratio defined as the coil height to its thickness  $h_c/l_c$  that affects the geometry of the stationary magnetic circuit, as presented in Figure 3.29.

**FIGURE 3.29**

Geometry and flux lines of the optimized disk solenoid: (a) geometry, (b) flux lines. (Courtesy of Delphi Corp.)

**FIGURE 3.30**

Specified and achieved voltage vs. time. (Courtesy of Delphi Corp.)

The FE analysis that is utilized for the magnetic field solutions identifies the flux path in a symmetrical portion of the disk solenoid's magnetic structure. Consequently, the voltage source is applied with the required duty cycle and one has to verify that, indeed, the achieved voltage matches the specified voltage within a reasonable error. This is shown in Figure 3.30, whereby the voltage was converging within 2% of error.

Applied voltage induces the current that in turn generates a magnetic flux in the disk armature. The current limitation affects the flux and has to be cut so as not to exceed 2.0 A. One has to make sure that the current, and consequently the flux, is not discontinued before an armature accomplishes its motion, as presented in Figure 3.31. A small dip in the current characteristic identifies the armature motion. In our case, it is visible in the second wave because both the current and flux started with higher values due to energy stored in the magnetic circuit.

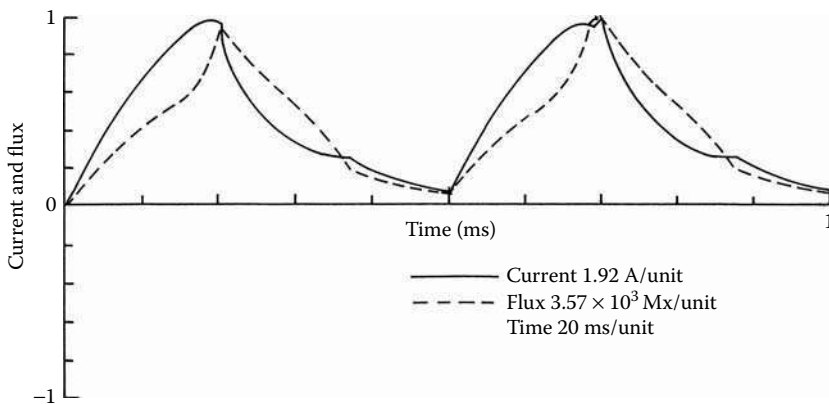


**FIGURE 3.31**  
Current and flux vs. time. (Courtesy of Delphi Corp.)

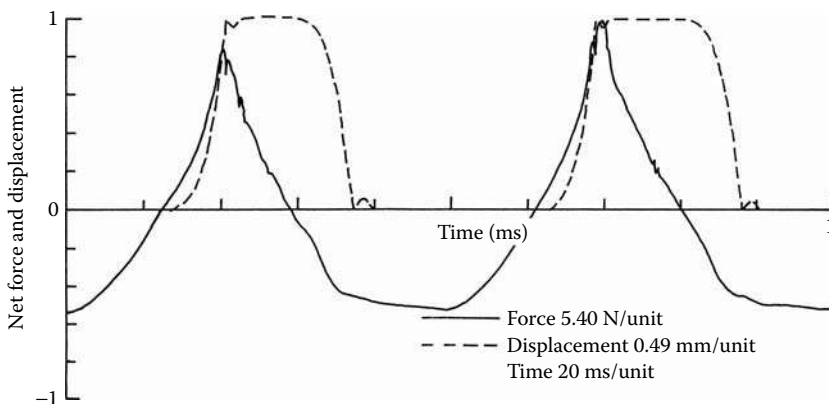


**FIGURE 3.32**  
Magnetic force and displacement vs. time. (Courtesy of Delphi Corp.)

Flux, in turn, develops a magnetic force in the armature sufficient to move it toward to the stationary magnetic circuit. The armature movement further compresses a spring and closes the air gap to  $0.49 \times 10^{-3}$  m (almost to zero as the specified gap is  $0.5 \times 10^{-3}$  m), as presented in Figure 3.32.

With all dynamics of the disk actuator under control, one can start an optimization procedure that is continuously iterative. Such a process typically requires about 700 iterations for a simple structure. An optimization subroutine, therefore, has to be employed to do this job (Kuester et al. 1973). Results of such an optimization are presented separately for one variable, two variables, and finally for all three variables in Figure 3.33. Avoid local minima that may cause misleading results (Coulomb and Meunier 1983, Fletcher 1987, Matsumoto et al. 2004, Navarra 1990).

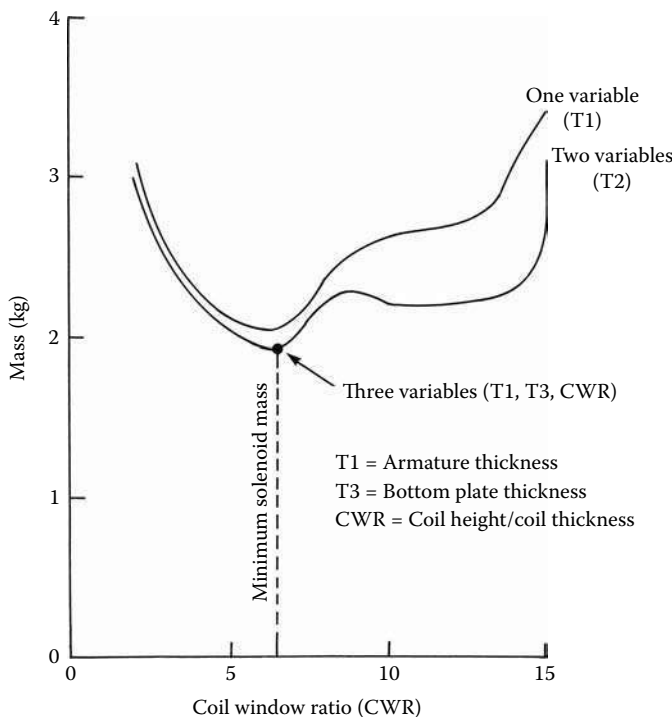


**FIGURE 3.33**  
Disk solenoid mass optimization for three variables. (Courtesy of Delphi Corp.)

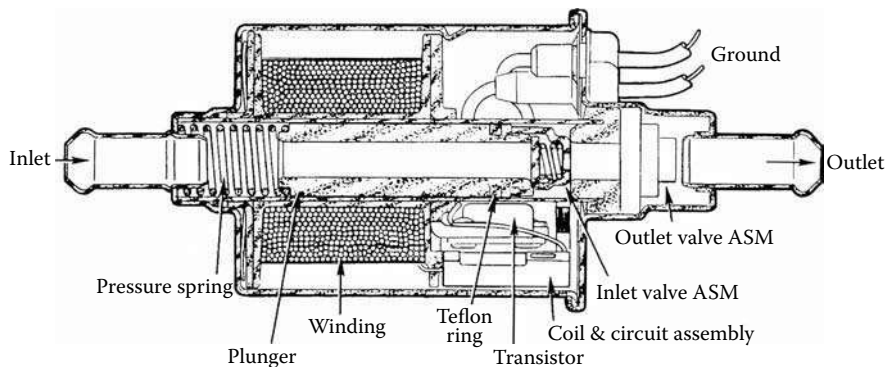
### 3.3 Applications of Solenoid Actuators

Solenoid actuators are the most commonly applied electromagnetic devices in the automotive industry. They are used for fast-acting operations with a short stroke, such as gasoline, natural gas, and diesel fuel injectors or compressors, fuel pumps, and transmission solenoid valves. For long stroke operations, solenoid actuators are used in solenoid fuel pumps or door locks.

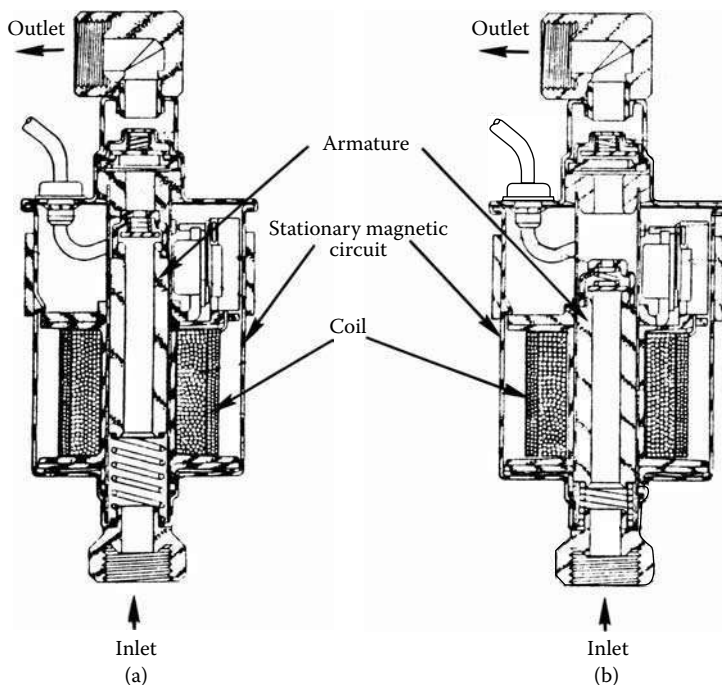
#### 3.3.1 Long Stroke Solenoid Fuel Pump

Solenoid strokes with total travel of more than several millimeters fall into the long stroke solenoid category. Most of them are conical where the total travel distance is larger than the magnetic air gap for the magnetic flux crossing. An example of this is a door lock solenoid. All other long stroke solenoids are plunger types with coil-plunger asymmetry and spring offset. A good example of this configuration is a solenoid fuel pump.

A common application of electronic fuel pumps is an automotive diesel engine. The pump has very good priming capabilities and its proximity to the engine does not obstruct the pump from drawing fuel from the tank at the rear of the vehicle and delivering it to the engine. It has few moving parts and no points exposed to wear. It provides a quiet operation with proven durability. Figure 3.34 shows a cross section of the fuel pump with no current excitation, and Figure 3.35 shows the fuel pump in two extreme positions.

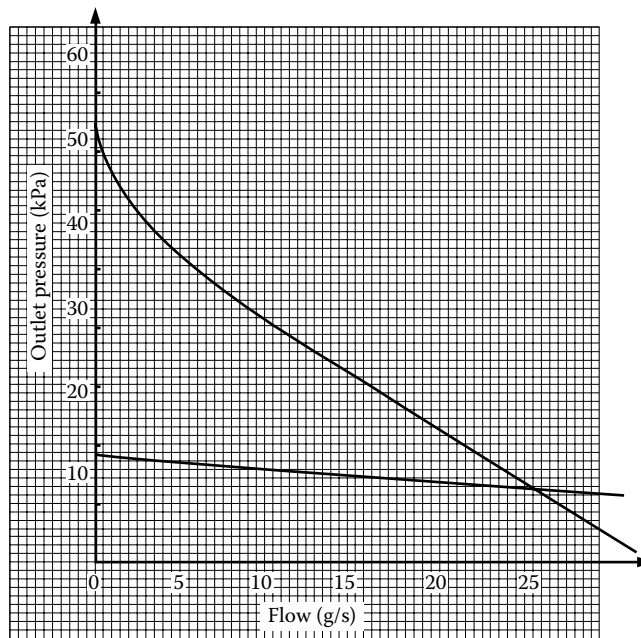


**FIGURE 3.34**  
Solenoid fuel pump. (Courtesy of Delphi Corp.)



**FIGURE 3.35**  
Solenoid fuel pump in two extreme positions: (a) current OFF and spring released, (b) current ON and spring compressed. (Courtesy of Delphi Corp.)

The pump action of the fuel pump is created by the movement of the plunger inside the cylinder, which is completely sealed against the leakage. When electrical power is applied, the resulting magnetic force pulls the plunger piston down against the pressure spring, as presented in Figure 3.35(a). The reason for this is the initial movable plunger location vs. the stationary coil that is not symmetrical to the coil and magnetic circuit. When the magnetic field is applied, it pulls the movable magnetic plunger to its center, trying to achieve the maximum magnetic permeance (and minimum magnetic reluctance) for the magnetic flux. As the plunger piston moves toward the spring, the outlet valve

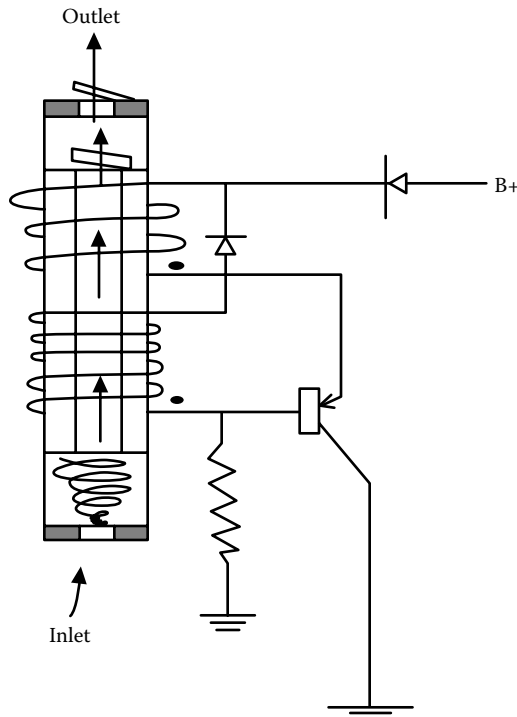
**FIGURE 3.36**

Outlet pressure vs. flow. (Courtesy of Delphi Corp.)

closes and the inlet valve opens. Fuel then enters the pumping chamber through the center of the piston. As the downward motion is completed, the magnetic field is turned off and the pressure spring forces the piston in the reverse position, as presented in Figure 3.35(b). At this time, the inlet valve closes, the outlet valve opens, and the fuel is released. This sequence occurs many times per second. As the pumping action continues, pressure on the outlet increases.

As this pressure increases, the piston stroke decreases, as presented in Figure 3.36, and only the required amount of fuel is pumped to the engine. Fuel is confined to the pump cylinder and does not enter sections of the pump that contain the coil assembly and electronics. The electronic circuit shown in Figure 3.37 indicates that the solenoid coil consists of two coils: the upper primary coil with 325 turns and wire size 12 AWG having  $1.2 \Omega$ , and the lower secondary coil with 164 turns and wire size 37 AWG having  $300 \Omega$ .

The purpose of the solenoid pump improvements is to increase its pressure, flow, or both. Two factors can contribute to this goal. One is to reduce the eddy currents in the movable piston and the other is to reduce the plunger inertia. The magnetic-circuit improvement can be accomplished by examining magnetic-circuit materials and, in particular, the plunger material. By replacing the low-carbon steel plunger to 2% silicon steel (Carpenter) more force can be produced by reducing eddy currents (Carpenter 1989). As changing the entire circuit would be too costly, only the plunger material should be changed. The test results of the improved device indicated improved flow by 12.8% from 15 g/s to 19.2 g/s at a pressure of 35 kPa, as presented in Figure 3.36. In addition, it required only 1.65 A of current compared with 1.85 A for the original pump, a 10.8% reduction. By changing the stroke and by raising the current to its original level, the redesigned pump has the potential for total flow improvement of 25%. In examining the coil winding, a low coil window fill factor of about 35% was identified. Increasing the coil fill factor to 50% allows shortening of the coil by  $8.25 \times 10^{-3}$  m. At the same time, the plunger axial size can be reduced to result in total mass reduction of 21%. With the lower

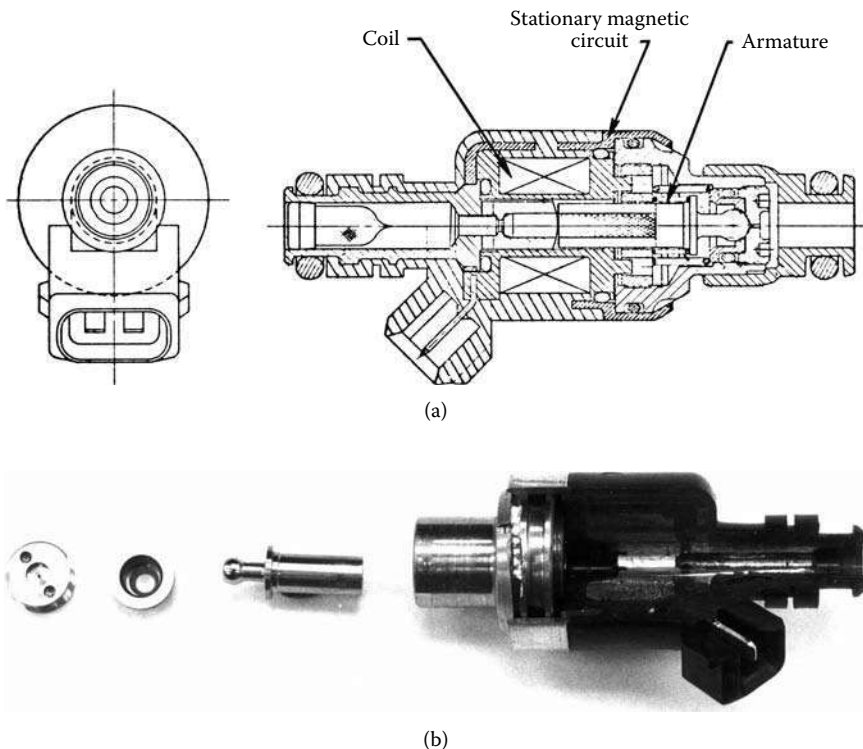
**FIGURE 3.37**

Solenoid pump drive circuit. (Courtesy of Delphi Corp.)

mass plunger, a weaker spring can be used, reducing the travel time significantly and, thus, increasing the frequency of the operation and fuel flow. These changes are well recognized and viewed as standard because they do not affect a device's size or the manufacturing process. As a result, they can be easily adopted in industry. Engineers should focus on these factors because they can bring significant improvement without any significant change to design or process.

### 3.3.2 Gasoline Injectors

With hundreds of millions in use annually, fast-acting solenoid actuators are by far the most popular electromechanical devices in production. They are most commonly used as natural gas, diesel fuel, and gasoline injectors. Another common use is as solenoid valves, with the most popular application in automotive transmissions. Fuel injection performs better, provides crisper throttle response, improves fuel economy, allows much easier starts especially during cold weather, and produces much lower emissions than carburetors. These advantages led to the introduction of computer-controlled engine management systems with electronic fuel injection. Gasoline-powered engines with fuel injection do not use direct injection systems, but rather indirect systems that spray fuel into either the intake manifold or head ports. The first systems introduced in the early 1980s were throttle body injection systems. The injectors spray fuel into the intake manifold, where it mixes with air and is carried through the intake runners and ports to the engine's cylinders. Nowadays, the multiport fuel injector or port fuel-injection systems are used, where a separate fuel injector is provided for each of the engine's cylinders. The injectors are mounted in the intake manifold and spray fuel into the cylinder head intake ports. In

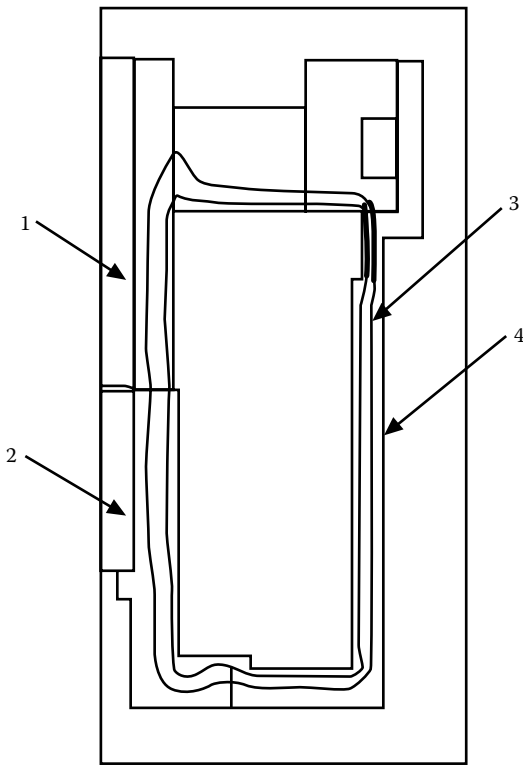
**FIGURE 3.38**

Multec port fuel injector: (a) Multec injector design components, (b) Multec distributed view components. (Courtesy of Delphi Corp.)

some injection systems, all the injectors squirt simultaneously once every engine revolution. In other systems, each injector is triggered individually as its cylinder begins the intake stroke and the intake valve opens. Sequential systems are better because they can react more quickly to changing operating conditions. For better air/gasoline control more complex air atomizer injectors are proposed (DeNagel et al. 1994).

All advanced injection systems require better dynamic injector response—the opening and closing travel time. To provide such devices, one has to use an FE tool to optimize injector dynamics. The world's first FE dynamic optimization of the fast-acting solenoid with a moving part (plunger) was applied to the Multec injector, as illustrated in Figure 3.38 (Nehl et al. 1988). Pioneer dynamic optimization of the dynamic analysis of the Multec design was performed using FE techniques including eddy currents, nonlinear magnetic materials, and motion. Proposed magnetic modifications resulted in significant improvements in performance, making Multec an extremely competitive product that for more than two decades has been manufactured with a peak volume of 50 million units annually. This dynamic optimization technique has been successfully applied to many fast-acting, solenoid-based products to improve existing and help create new designs (Matsumoto et al. 2004, Pawlak 1989, Rischmuller et al. 2000, Yoon et al. 1999).

Figure 3.39 indicates the FE analysis results for the magnetic flux distribution passing the plunger, main air gap, the plunger stop, parasitic air gaps, and the rest of the magnetic circuit. Note an additional air gap of the inside plunger insert that caused the uneven main air gap for the FE analysis.

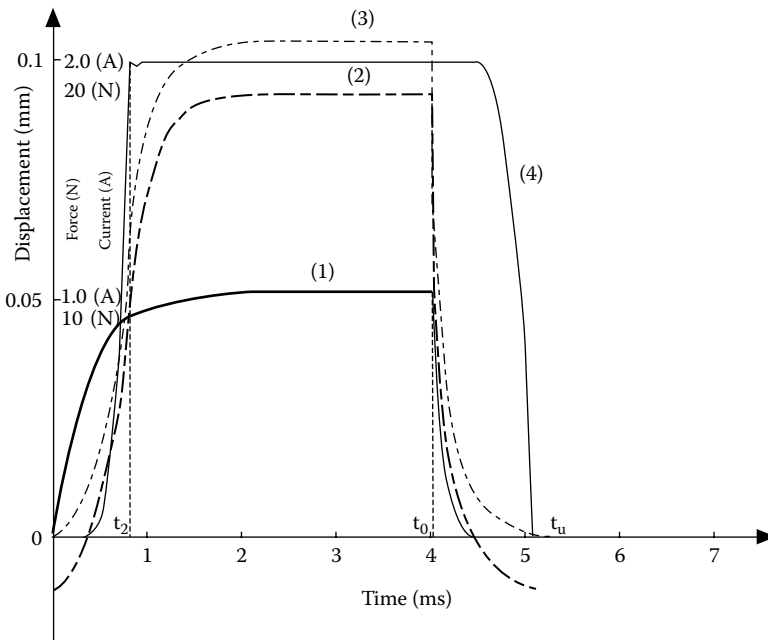
**FIGURE 3.39**

Magnetic flux lines for the Multec injector: (1) plunger, (2) plunger stop, (3) magnetic flux lines, (4) housing. (Courtesy of Delphi Corp.)

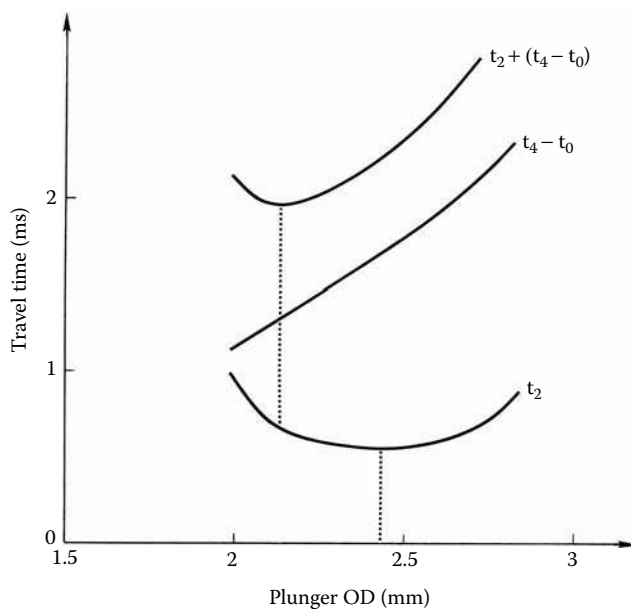
Dynamic performance of the Multec injector is illustrated in Figure 3.40. The current in the Multec coil reaches its saturation and, with constant voltage applied, it drops as soon as the voltage is discontinued. Both the magnetic and net forces resemble the current shape. As soon as the net force changes its sign from negative (due to the spring preload) to positive, the plunger starts moving until it reaches the plunger stop. When the voltage is discontinued, the net force drops, its sign changes again, and the armature then starts moving back and returns to its previous position, as shown in Figure 3.40.

The design optimization process includes changes in injector geometry and configurations to reduce magnetic saturation and flux leakage. Implementing magnetic material with higher electrical resistivity reduces eddy current effects. Incorporating the changes in the final product design significantly improved injector performance. In a Multec optimization process, several parametric studies were iteratively performed to determine the desired position of the main air gap and plunger geometry, as well as application of a high resistivity material to critical parts of the magnetic circuit.

Figure 3.41 shows the effect of changing the outside plunger diameter upon the plunger opening and closing times and on the total travel time. Table 3.1 indicates the results of this optimization. If we use optimized materials and dimensions and assume the sum of opening and closing times as a figure of merit, total travel time can be reduced by 35%.

**FIGURE 3.40**

Dynamic performance of the Multec injector: (1) current, (2) net force, (3) total magnetic force, (4) displacement. (Courtesy of Delphi Corp.)

**FIGURE 3.41**

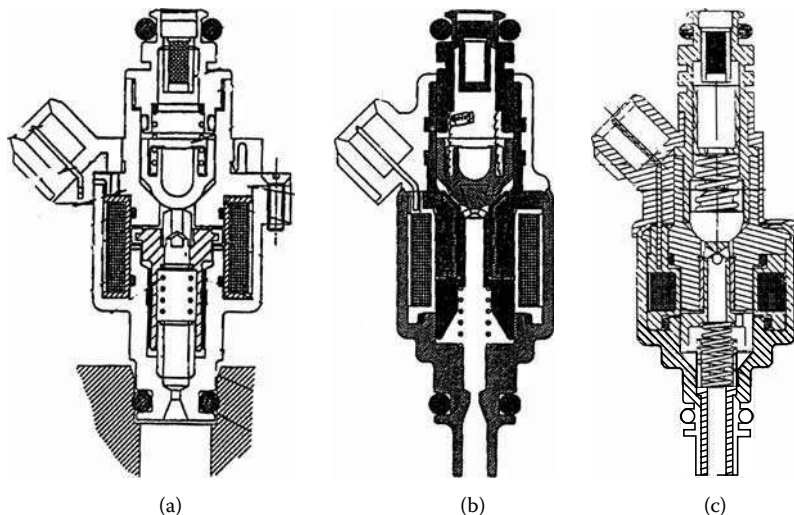
Travel time vs. plunger OD:  $t_2 + (t_4 - t_0)$  = total travel time,  $t_2$  = opening time,  $(t_4 - t_0)$  = closing time. (Courtesy of Delphi Corp.)

**TABLE 3.1**

Multec Injector Optimization Results

Design and Performance	Opening Time (ms)	Opening Time (%)	Closing Time (ms)	Closing Time (%)	Total Travel Time (ms)	Total Travel Time (%)
Original design	1.65	0.0	1.42	0.0	3.07	0.0
New materials	1.4	15.0	1.13	20.0	2.53	18.0
New materials and dimensions	1.33	19.0	0.65	54.0	1.98	35.0
Requirements	1.5	9.0	0.9	37.0	2.4	22.0

Source: Courtesy of Delphi Corp.

**FIGURE 3.42**

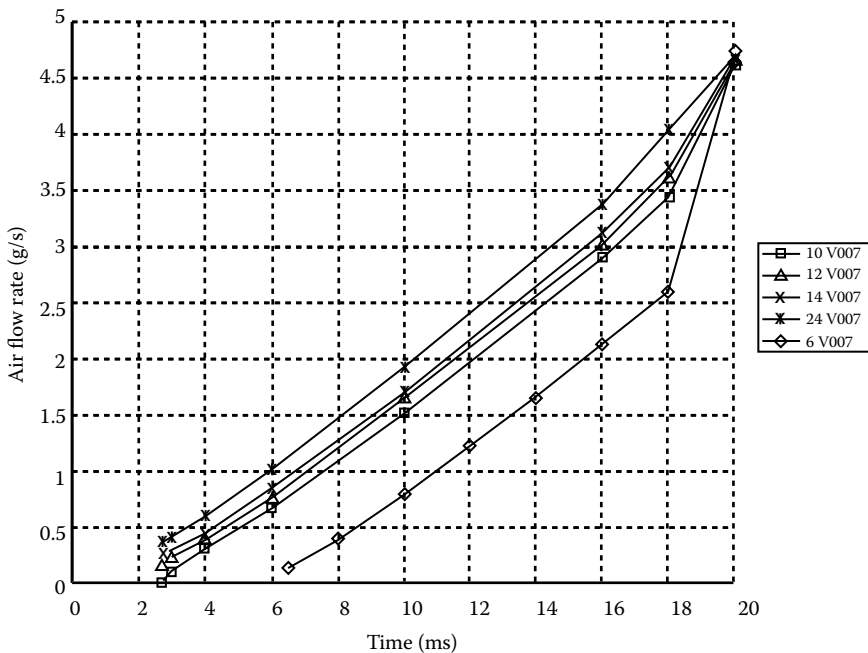
Natural gas injector designs: (a) conventional gas injector, (b) improved gas injector, (c) optimized gas injector. (Courtesy of Delphi Corp.)

### 3.3.3 Natural Gas Injectors

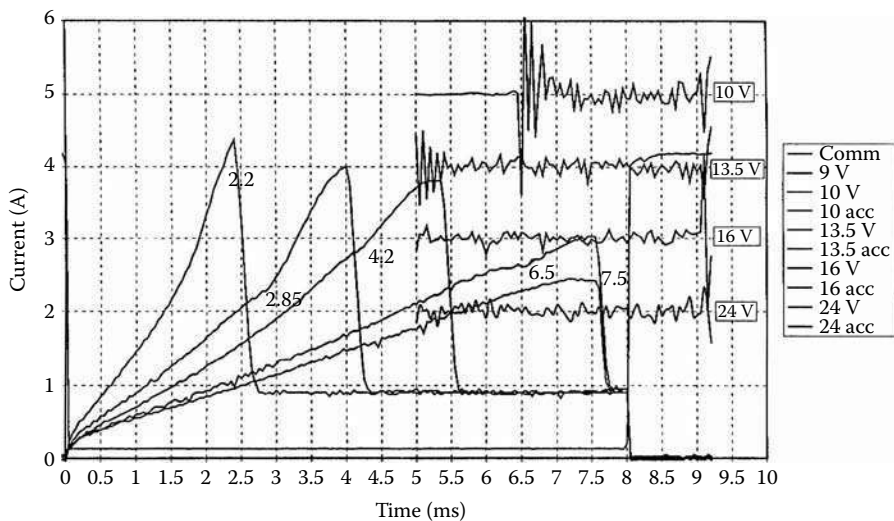
The increasing cost of gasoline is driving interest in natural gas as a less expensive energy option for automotive use. As a result, natural gas injectors are finding more and more applications in the automotive industry. Figure 3.42(a) shows a cross section of a typical natural gas injector that closely resembles a gasoline injector with its connector, coil, movable plunger, magnetic circuit, and return spring components.

Natural gas injectors have to meet natural gas requirements for automotive applications ranging from small passenger car 1.6 l engines to large truck 6.0 l engines. They have to provide the required flow rate of natural gas media under temperature and pressure requirements varied by a PWM cycle rate within a required voltage range. Figure 3.43 shows a family of natural gas flow rate characteristics ranging from 0 up to 5.0 g/s vs. PWM ranging from 2.0 to 20.0 ms for a voltage applied to a controller ranging from 6.0 to 24.0 V. The injector must perform under an ambient temperature of 21.0°C and a natural gas pressure of 414.0 kPa.

The most difficult requirement is meeting the low voltage requirement of 6.0 V because an injector has to develop sufficient force to operate under the required pressure. Figure 3.44 shows the current vs. time performance characteristic for the conventional injector

**FIGURE 3.43**

Natural gas injector flow rate vs. pulse-width performance. (Courtesy of Delphi Corp.)

**FIGURE 3.44**

Current vs. pulse-width performance of conventional natural gas injector at different voltages: 10.0 V, 13.5 V, 16.0 V, and 24.0 V. (Courtesy of Delphi Corp.)

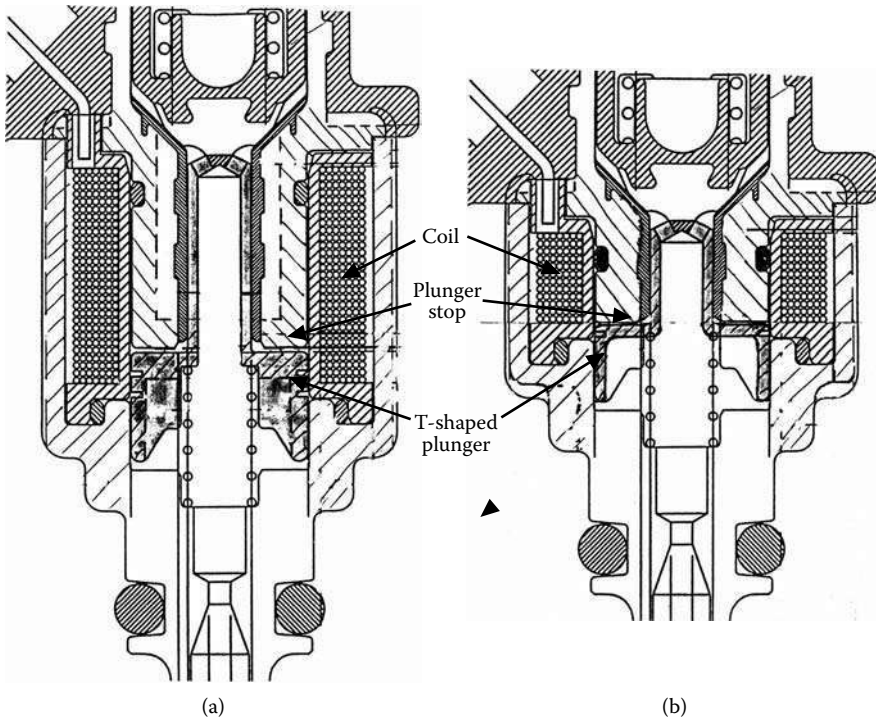
presented in Figure 3.42(a). The figure shows that the conventional injector design did not meet this critical requirement and, in fact, stopped its operation at a voltage of 9.0 V, as presented in Table 3.2.

Because of this, a T-shaped plunger configuration was adopted, as shown in Figure 3.42(b) and Figure 3.45. For this design, almost the entire original structure of a typical

**TABLE 3.2**  
Performance Comparison

Design	Performance Voltage (V)				
	6	10	13.5	16	24
Plunger armature opening time (ms)	none	7.5	6.5	2.85	2.2
T-shaped armature opening time (ms)	6.45	3.2	2.3	1.95	1.4

Source: Courtesy of Delphi Corp.

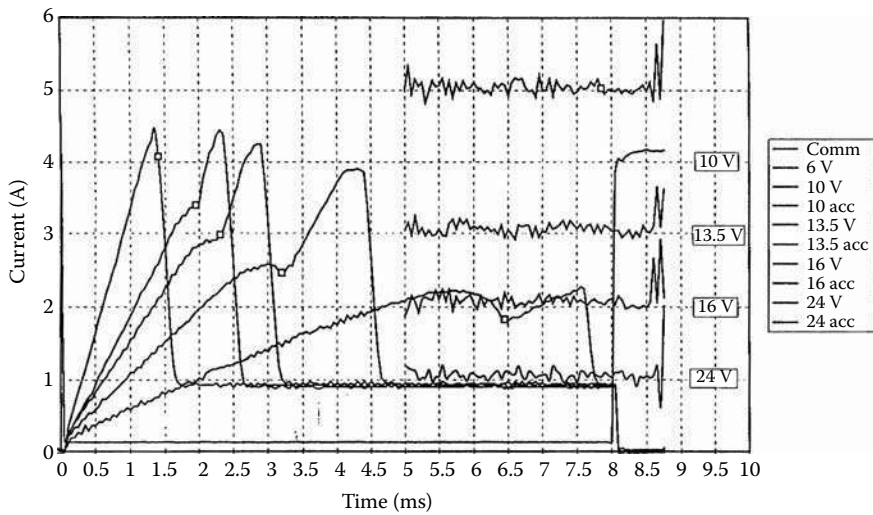


**FIGURE 3.45**

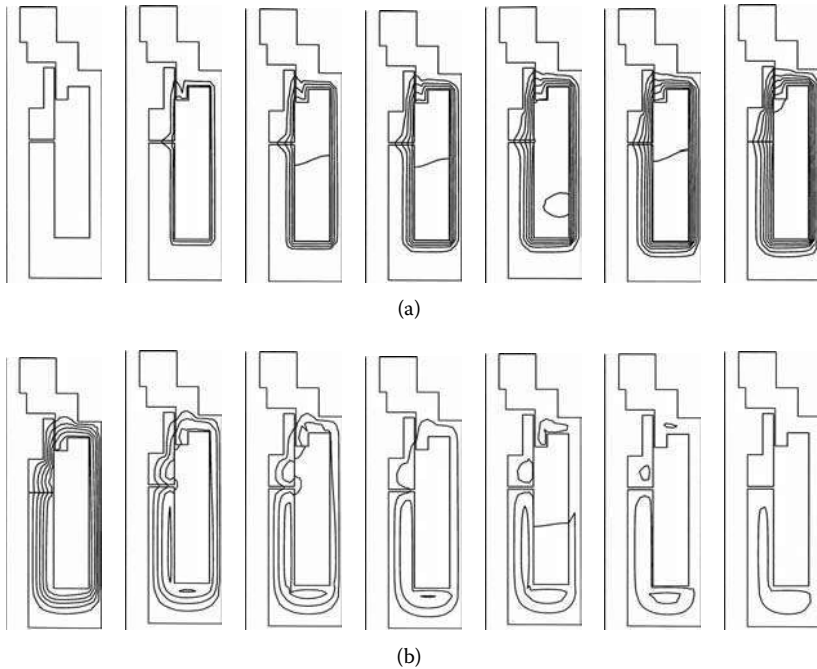
Natural gas injector with T-shaped plunger: (a) adopted T-shaped plunger, (b) optimized T-shaped plunger. (Courtesy of Delphi Corp.)

injector was preserved, except in the area of the plunger stop and the T-shaped plunger, as presented in Figure 3.45(a). The T-shaped plunger has a number of advantages over a hollow plunger armature, as presented in Figure 3.45(a). It has a relatively large active area in the vicinity of the main air gap that develops high magnetic forces and its thin walls allow for significant mass reduction and ease of manufacturing relative to the original plunger. Test results of this improved configuration are given in Figure 3.46.

The improved natural gas injector with a T-shaped armature has satisfied the low voltage requirement of 6.0 V with a response time of 6.45 ms under the required pressure of 414.0 kPa, as presented in Figure 3.46 and Table 3.2. Figure 3.46 shows the current vs. time performance characteristic for the improved injector for the entire voltage range from 6.0 to 24.0 V. Table 3.2 shows the opening time comparison for the conventional and improved solenoid configuration. At the typical automotive voltage of 13.5 V, the natural gas injector configuration with T-shaped armature has three times faster dynamic response time in comparison with the conventional hollow plunger injector design. This shows the dynamic potential of the T-shaped armatures.

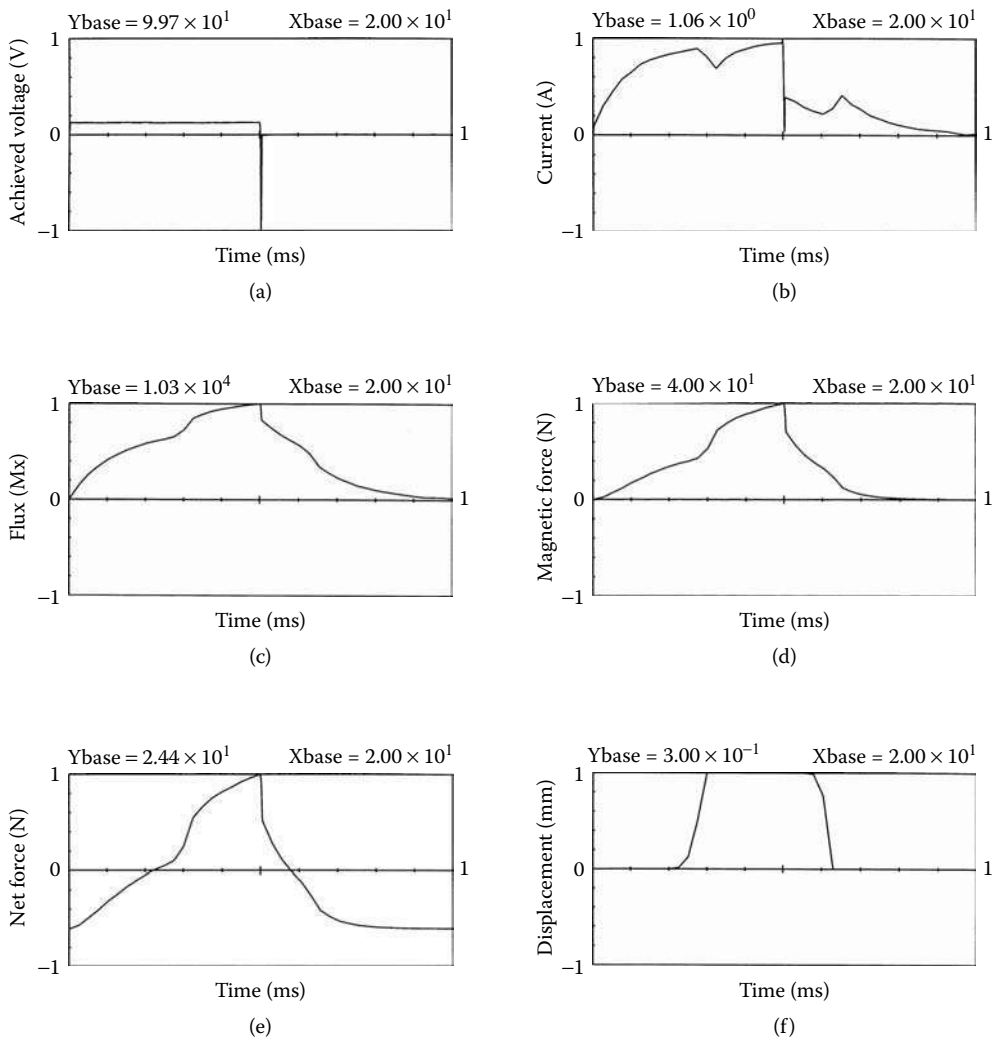
**FIGURE 3.46**

Current vs. pulse-width performance of improved natural gas injector at different voltages: 10.0 V, 13.5 V, 16.0 V, and 24.0 V. (Courtesy of Delphi Corp.)

**FIGURE 3.47**

Flux distribution of T-shaped plunger solenoid: (a) penetration of the magnetic field, (b) decay of the magnetic field. (Courtesy of Delphi Corp.)

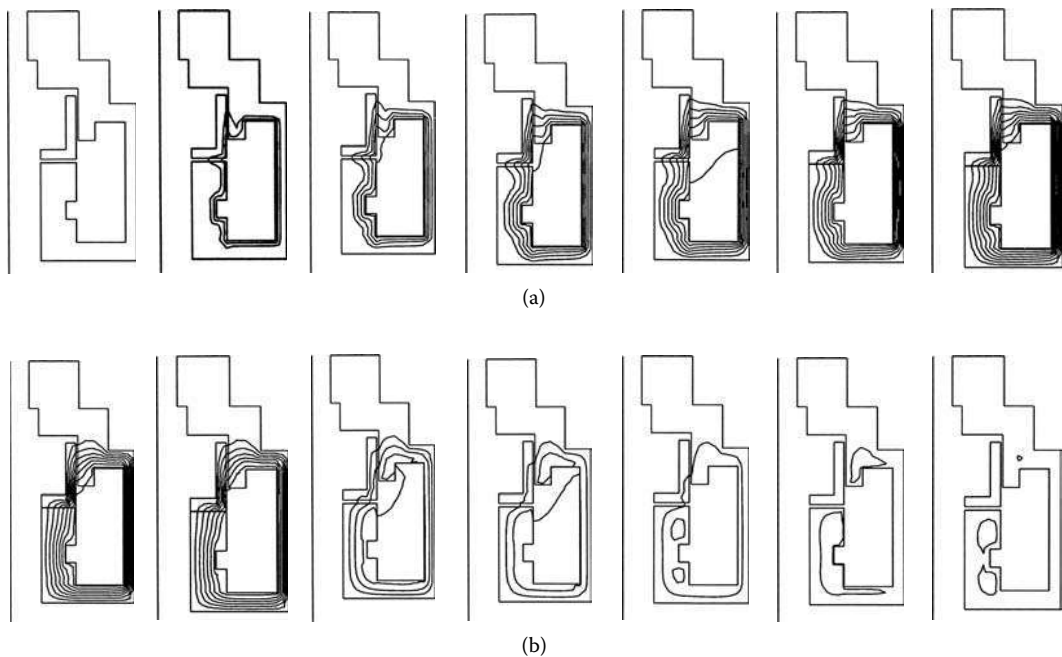
Because of the cylindrical symmetry, only one side of the device needs to be modeled. The distribution of the magnetic circuit at different points of time is shown in Figure 3.47. The diffusion (penetration) of the flux into the magnetic core is clearly illustrated at these

**FIGURE 3.48**

Dynamics of the T-shaped plunger solenoid: (a) achieved voltage vs. time, (b) current vs. time, (c) flux vs. time, (d) net force vs. time, (e) spring force vs. time, (f) displacement vs. time. (Courtesy of Delphi Corp.)

successive points of time. Actually, the armature motion does not begin until the flux penetrates the entire plunger surface at the main air gap and the resulting force overcomes the spring preload, as shown in Figure 3.47(a). Due to negative voltage spike at the end of the travel, the current is suppressed and the magnetic field is decaying faster, allowing the armature to return to its previous position, as presented in Figure 3.47(b).

Figure 3.48 displays dynamic characteristics of the T-shaped plunger solenoid. Figure 3.48(a) presents a specified voltage with a frequency of 50 Hz (20.0 ms pulse width), where the high negative voltage spike suppresses the current level. Figure 3.48(b) illustrates the calculated current that shows the effect of the negative spike that limits the decreasing current level. Both the flux crossing the main air gap and the total magnetic force on the T-shaped armature, shown in Figure 3.48(c) and Figure 3.48(d), respectively, have characteristics similar to the source current. The net force on the T-shaped armature shown in Figure 3.48(e) is the result of the spring forces and the total magnetic forces and identifies the beginning and the end of the motion displacement, as shown in Figure 3.48(f).

**FIGURE 3.49**

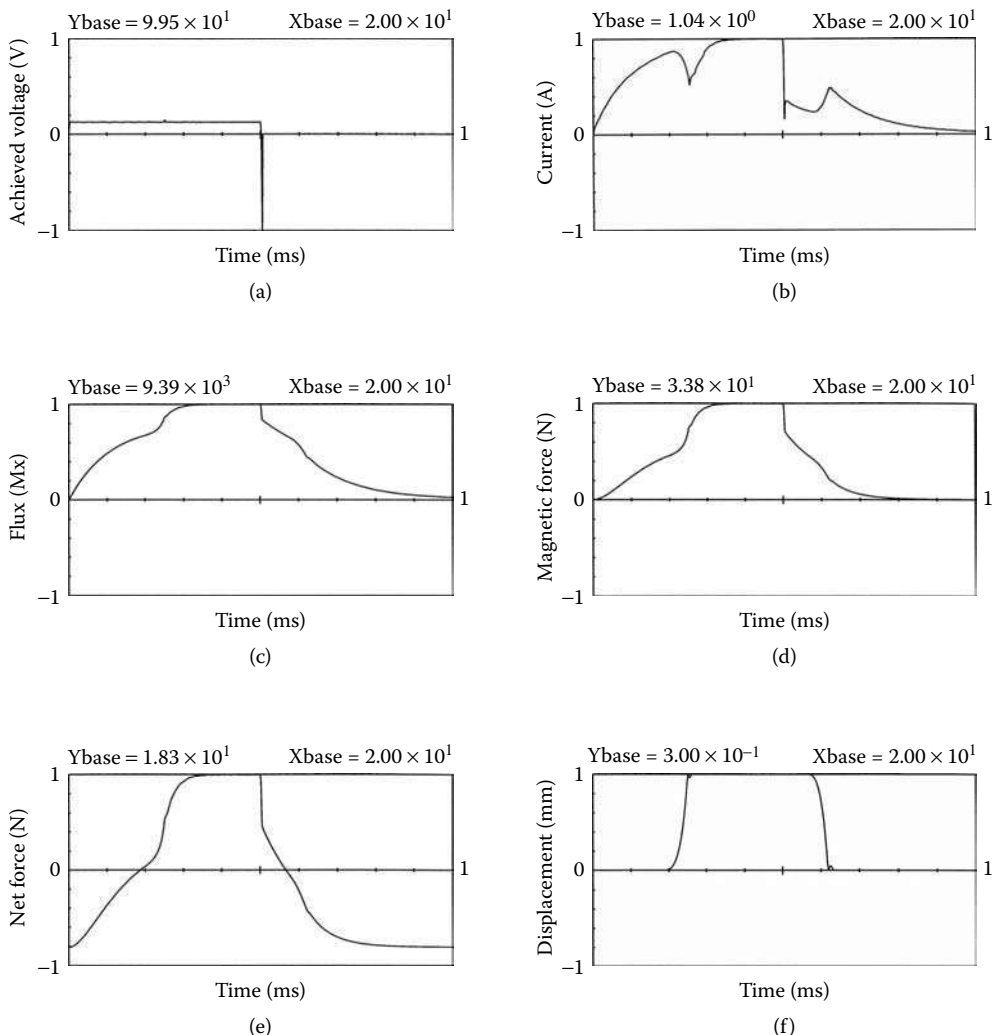
Flux distribution of optimized solenoid structure: (a) penetration of the magnetic field, (b) decay of the magnetic field. (Courtesy of Delphi Corp.)

Because the flux for the optimized injector reaches its maximum value much faster than in its previous configuration, it is possible to apply a peak and hold controller that reduces a holding current and saves energy. This is described in detail in Section 3.3.6.

Although the improved natural gas injector with a T-shaped armature has satisfied the low voltage requirement of 6.0 V, the entire magnetic circuit of the solenoid should be optimized to involve both the stationary and movable magnetic circuit as well as the coil in the optimization process. Figure 3.42(c) and Figure 3.45(b) show the optimized natural gas configuration. Both the coil and the magnetic circuit were optimized, resulting in the substantial reduction of total injector length from its original  $26.7 \times 10^{-3}$  m to  $15.32 \times 10^{-3}$  m, or 42.6%, and with a small reduction of the total OD from  $25.0 \times 10^{-3}$  m to  $24.4 \times 10^{-3}$  m. Altogether, the total solenoid volume has been reduced by 45.3%, driving its mass cost of material down substantially while improving its dynamic performance.

Again, because of the cylindrical symmetry, only one half of the device needs to be analyzed. The flux distribution of the magnetic circuit at different points in time is shown in Figure 3.49. The diffusion (penetration) of the flux into the magnetic core is clearly illustrated at these successive points in time. Actually, the armature motion does not begin until the flux penetrates the entire plunger surface at the main air gap and the resulting force overcomes the spring preload; see Figure 3.49(a). Due to negative voltage spike at the end of the travel, the current is suppressed and the magnetic field decays faster, allowing the armature to return to its previous position, as presented in Figure 3.49(b).

Figure 3.50 displays the dynamic characteristics of the optimized plunger solenoid. Included in this figure is Figure 3.50(a), presenting a specified voltage with a frequency of 50 Hz (20.0 ms pulse width) having a high negative voltage spike to suppress the current level, as shown in Figure 3.50(b). Both the flux at the main air gap and the total magnetic force on the T-shaped plunger shown in Figure 3.50(c) and Figure 3.50(d), respectively, have characteristics similar to the source current. The net force on the T-shaped armature

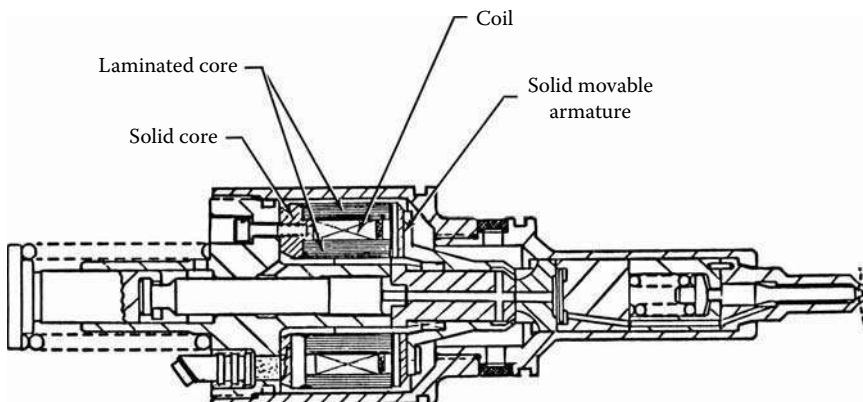
**FIGURE 3.50**

Dynamics of the T-shaped plunger solenoid: (a) achieved voltage vs. time, (b) current vs. time, (c) flux vs. time, (d) net force vs. time, (e) spring force vs. time, (f) displacement vs. time. (Courtesy of Delphi Corp.)

shown in Figure 3.50(e) is the result of the spring forces and the total magnetic forces and identifies the beginning and the end of the motion displacement shown in Figure 3.50(f). This dynamic performance also allows for the pick-and-hold driver that is described in detail in Section 3.3.6.

### 3.3.4 Diesel Fuel Injectors

The diesel fuel injector is a pressure valve with the capability of dispersing diesel fuel in required specific patterns, depending on the design of the valve nozzle. The diesel fuel injector distributes a pressurized fuel within the combustion chamber. The injector has to be able to withstand the temperature and pressure inside the cylinder and still deliver the fuel in a fine mist. Diesel engines are compression ignition engines that have no spark plugs and the diesel fuel is ignited by extreme heat and pressure. This requires a very high compression ratio (16 to 1 or higher) in the cylinders, much higher injector operating pressures (10,340 to 17,240 kPa) to overcome compression pressures in the cylinders, and

**FIGURE 3.51**

Electronic diesel injector. (Courtesy of Delphi Corp.)

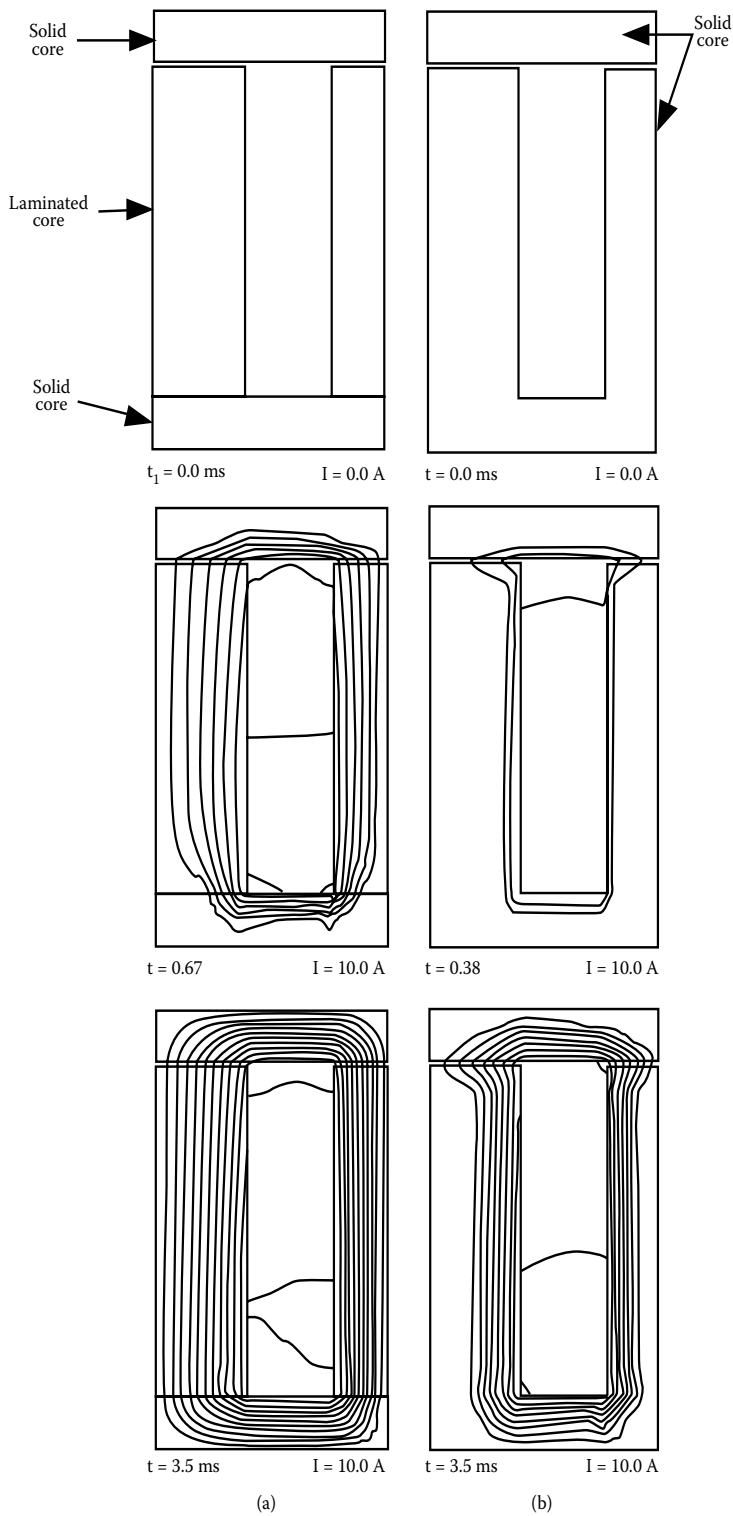
precise injector timing because diesel engine speed and power are controlled by the amount of fuel injected into the engine rather than airflow. Figure 3.51 shows a cross section of a diesel electronic injector. The actuator consists of a coil, an armature, and a magnetic circuit. The magnetic core has both laminated and solid core parts. Laminated parts are introduced in the form of a wound core to suppress eddy currents and to allow for fast penetration of the magnetic field.

Figure 3.52 shows a comparison of the penetration of the magnetic field within a laminated and solid core at the same MMF level with a current of 10.0 A. Clearly, the magnetic field penetrates much deeper into the laminated core despite the fact that both the bottom and the top (armature) parts are solid. Figure 3.53 shows the performance comparison of dynamics between the diesel injectors having partially laminated and solid magnetic cores. Figure 3.53(a) shows that the slope of the partially laminated core injector is steeper than the current slope of the injector having a solid core circuit. Because of this, the magnetic force developed by the injector with the partially laminated core is established much faster than the magnetic force of the injector having a solid core circuit; see Figure 3.53(b). Finally, the displacement performance of the armature for the injector with the partially laminated core is superior in comparison with the magnetic force of the injector having the solid core circuit, as presented in Figure 3.53(c).

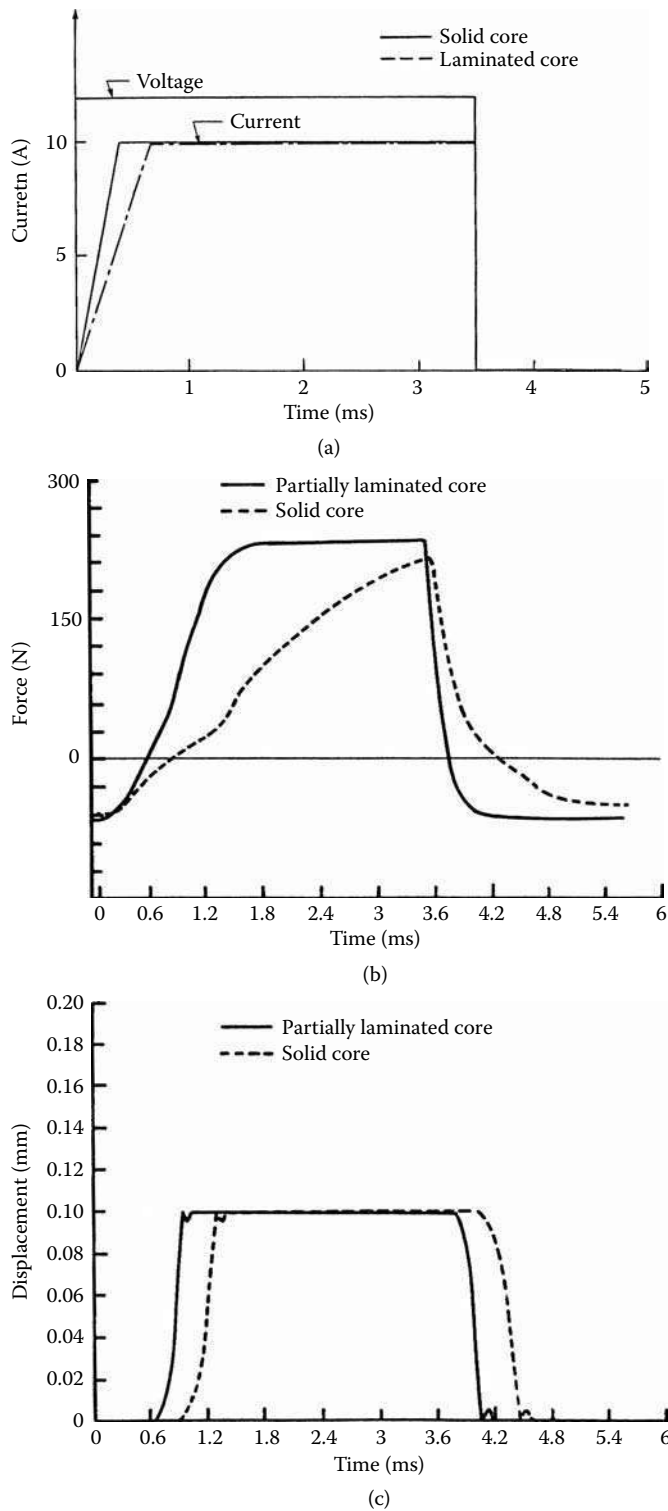
Diesel injector optimization was performed for the injector geometry introduced in Figure 3.51 for two different air gaps — a small gap of  $0.11 \times 10^{-3}$  m and a big gap of  $0.2 \times 10^{-3}$  m — and a specified plunger displacement of  $0.06 \times 10^{-3}$  m and  $0.11 \times 10^{-3}$  m, respectively. For a diesel injector, it is critical that a high armature force is established very quickly to withstand the engine's high pressure. The time to achieve the required injector force of 200.0 N in a function of coil parameters (number of turns) is analyzed. First, the current vs. time characteristics are established for both air gaps, as presented in Figure 3.54.

Dynamic response of the diesel injector for both air gaps is presented in Figure 3.55. The start time is  $t_1$ , the opening time is  $t_2$ , the return time is  $t_4 - t_0$ , the time to reach required magnetic force of 200.0 N (or 45 lb) is  $t_{45}$ , and the total travel time is  $t_2 + (t_4 - t_0)$ . The injector performance and details of the selected coil (gauge and turns) are presented in Table 3.3 and are also shown in Figure 3.55(a) and Figure 3.55(b).

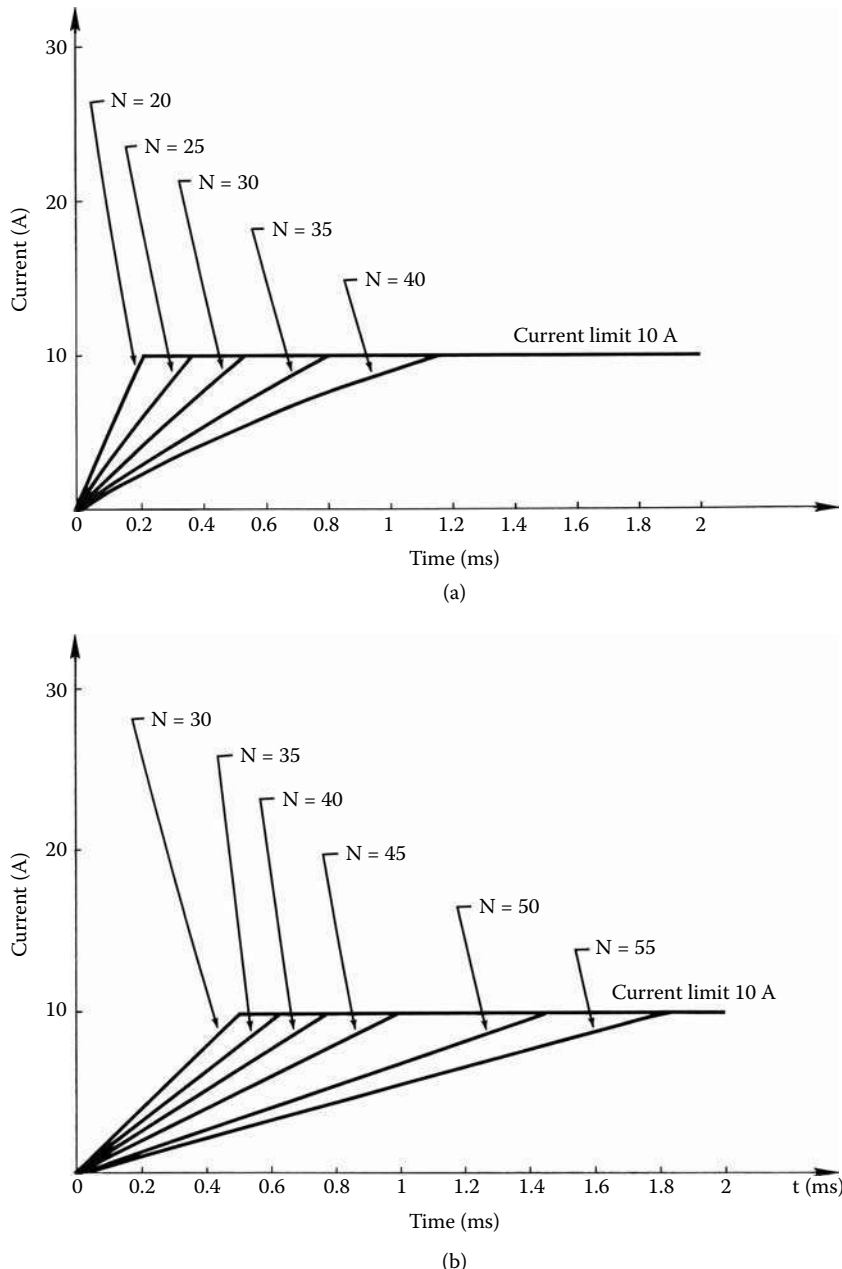
The comparison of the critical  $t_{45}$  characteristics for both air gaps is presented in Figure 3.56. By establishing different air gap openings and, therefore, different displacement distances (that provide information about an amount of fuel delivered for a given pulse width), one can determine the coil parameters, provided the other magnetic-circuit dimensions already have been optimized.

**FIGURE 3.52**

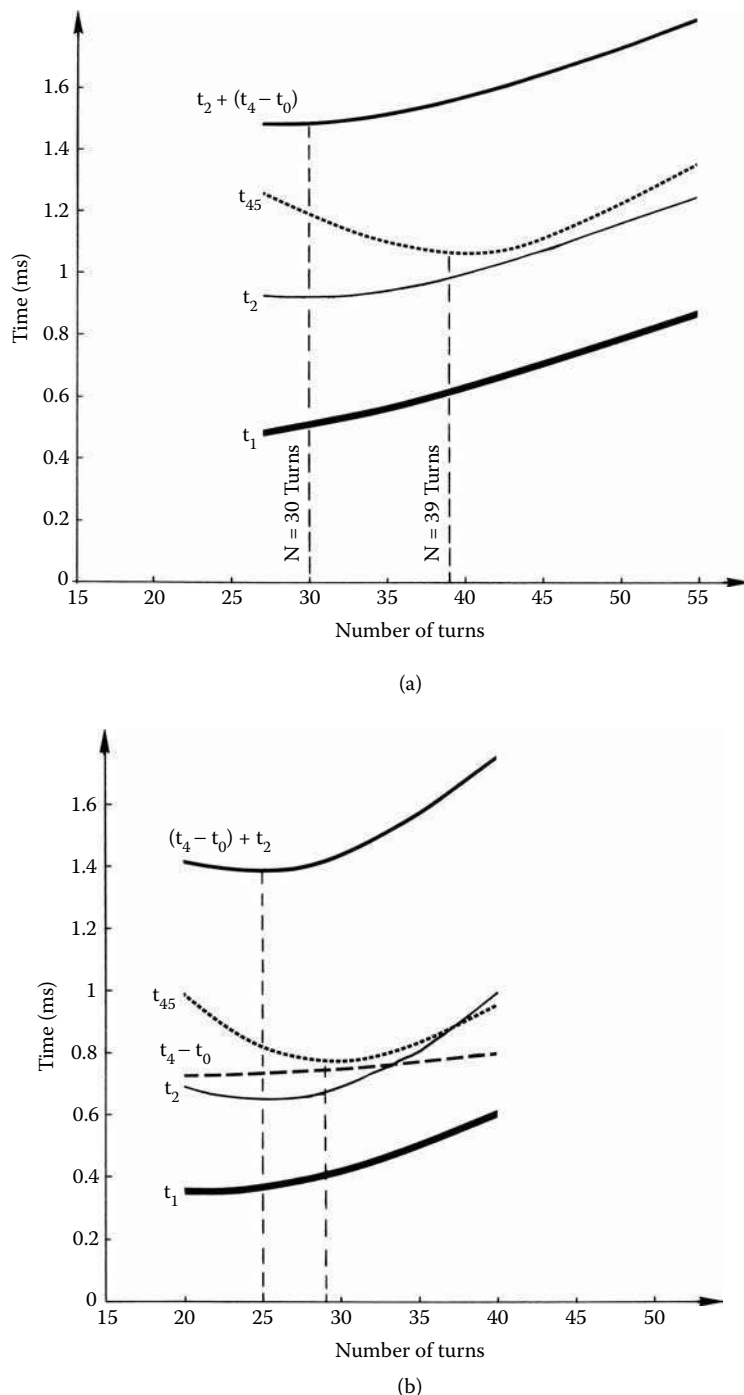
Flux lines penetration into magnetic core comparison: (a) partially laminated core, (b) solid core. (Courtesy of Delphi Corp.)

**FIGURE 3.53**

Dynamics of the diesel injector: (a) current vs. time for voltage source comparison, (b) force vs. time comparison, (c) current vs. time comparison. (Courtesy of Delphi Corp.)

**FIGURE 3.54**

Current vs. time characteristics: (a) small air gap of  $0.11 \times 10^{-3}$  m, (b) big air gap of  $0.2 \times 10^{-3}$  m. (Courtesy of Delphi Corp.)

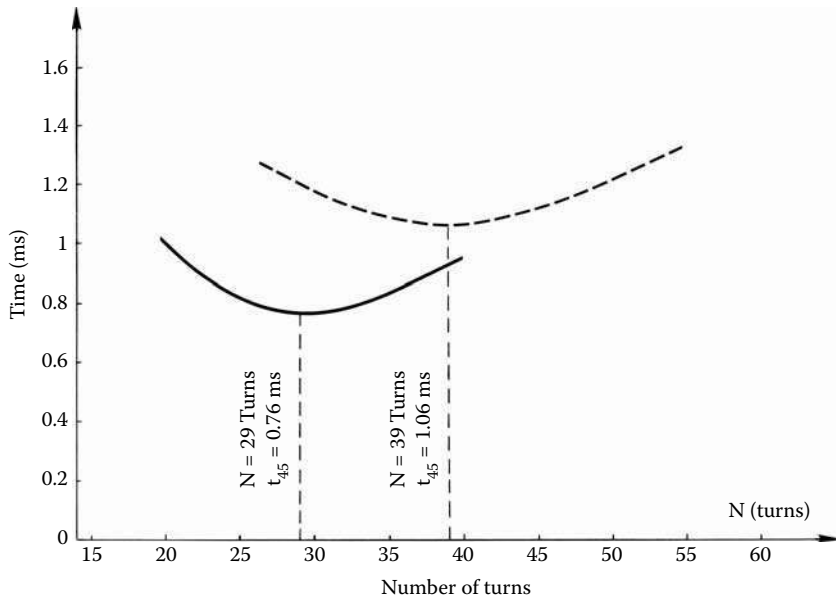
**FIGURE 3.55**

Displacement time vs. coil turns characteristics: (a) small air gap of  $0.11 \times 10^{-3}$  m, (b) big air gap of  $0.2 \times 10^{-3}$  m.  
(Courtesy of Delphi Corp.)

**TABLE 3.3**  
Performance Comparison

Air Gap ( $\times 10^{-3}$ m)	Displacement ( $\times 10^{-3}$ m)	Coil		Time of Response (ms)				
		N (turns)	AWG (gauge)	$t_1$	$t_2$	$t_3$	$t_4$	$t_{45}$
0.2	0.1	39	21	0.53	0.94	3.75	4.06	1.19
0.11	0.06	29	19	0.43	0.69	3.95	4.26	0.76

Source: Courtesy of Delphi Corp.

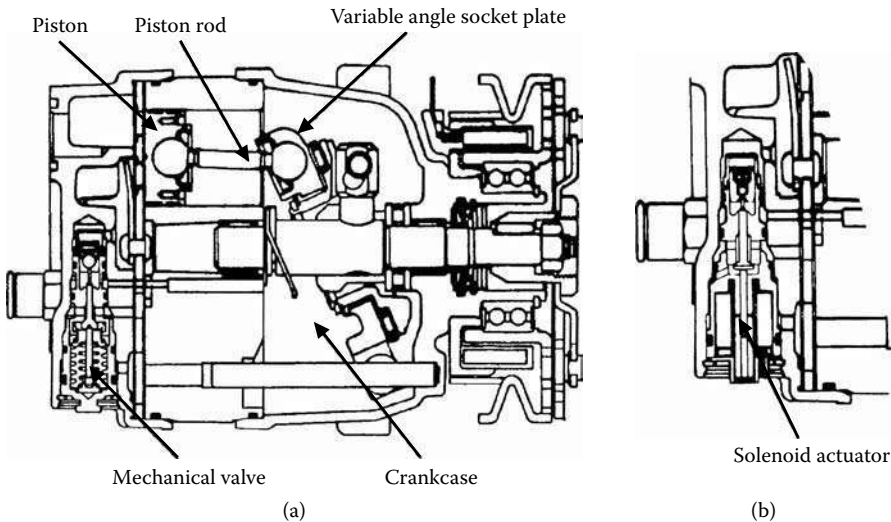


**FIGURE 3.56**  
Time vs. coil turns for the required force of 200.0 N. (Courtesy of Delphi Corp.)

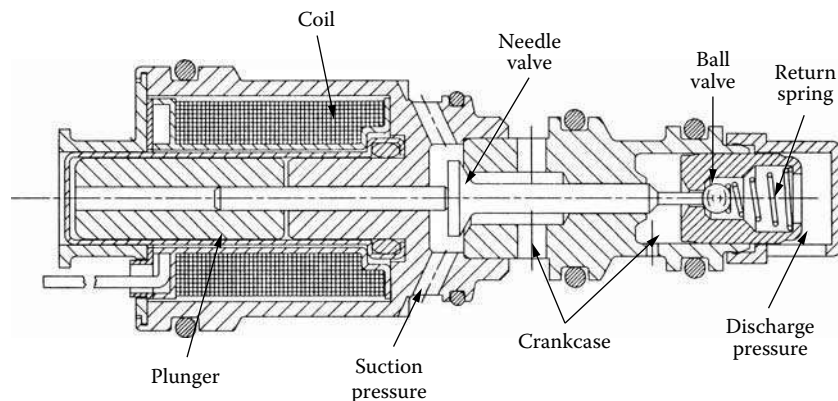
### 3.3.5 Compressor Solenoid Valves

Another application of the solenoid valve is an air-conditioning compressor with variable displacement. A unique feature of this compressor is that the displacement can vary depending on the cooling needs by varying the piston stroke. Changing the pressure in the crankcase of the compressor modulates the displacement. A mechanical valve senses evaporator pressure and bleeds a controlled amount of high-pressure gas into the crankcase. The amount of bleed determines the crankcase pressure and the compressor displacement, as presented in Figure 3.57(a).

A solenoid valve replaces the mechanical valve with a plunger-type solenoid actuator, as presented in Figure 3.57(b). This permits microprocessor control, resulting in greater flexibility and improved passenger comfort. By operating in pulse-width operating mode, the solenoid actuator controls the crankcase pressure between the low-pressure suction gas and high-discharge gas pressure. The pressure differential between the top and the bottom of the pistons creates a net force coupled with changes of angle of the socket plate, as presented in Figure 3.57(a). This varies the piston stroke and, thus, the displacement of the compressor.

**FIGURE 3.57**

Cross section of the variable displacement compressor: (a) mechanical pressure control, (b) solenoid pressure control. (Courtesy of Delphi Corp.)

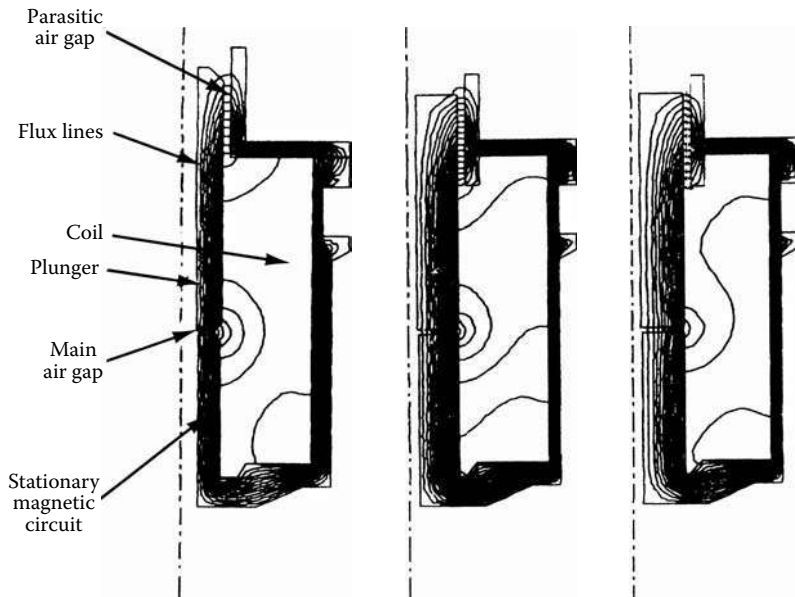
**FIGURE 3.58**

Solenoid valve actuator. (Courtesy of Delphi Corp.)

This section describes the results of optimization of the solenoid design. In fact, two solenoid designs are obtained: one with maximum plunger force and another with the minimum current draw. Maximizing the force at the nominal current should improve valve stability and make performance less sensitive to manufacturing tolerances. However, minimizing the current draw at the nominal plunger force should simplify the driver unit and reduce its cost.

The original design of the solenoid actuator for the compressor is shown in Figure 3.58. When the coil is energized, the needle valve closes and a ball valve opens. This exposes the crankcase to a high-pressure discharge gas, which increases the crankcase pressure. When the coil is not energized, the needle valve opens by the return spring, which vents the compressor crankcase to low-pressure suction gas.

The solenoid operates at a relatively low frequency of 8.0 Hz or 125.0 ms time period. Dynamic operation of the original solenoid takes 6% of the time period and because this

**FIGURE 3.59**

Flux lines for three solenoid designs: (a) original design, (b) maximum force design, (c) minimum current design. (Courtesy of Delphi Corp.)

is relatively slow, it is acceptable to optimize the static performance of the solenoid. The static performance should be optimized at worst-case operating conditions, a minimum voltage of 9.5 V and an elevated coil temperature of 120.0°C.

Before the optimization procedure, it is recommended to simulate both static and dynamic behavior of the solenoid valve, as presented in Equations 3.1, 3.9, and 3.12–3.14. The results of these simulations are helpful in the optimization steps. Because the first objective is to maximize the force of the plunger, any changes should increase the solenoid's working air gap flux density and enlarge the plunger active area according to Equation 3.12. It is best to increase flux density by reducing the flux leakage and by increasing the effective flux, eliminating flux local saturation bottlenecks. To do this, both the magnetic circuit and the coil should be considered. The optimum position of the main air gap helps achieve flux leakage reduction. Substituting the sharp corners at the plunger and the plunger stop in place of rounded corners and increasing the plunger and plunger stop ODs also help increase the total surface area. Enlarging the active surface area of the parasitic air gap by lowering the position of the magnetic flange reduces the MMF drop in this area by avoiding local saturation. Generally, all dimensions can be changed, as presented in Figure 3.59, except the outside envelope because that is usually prohibited.

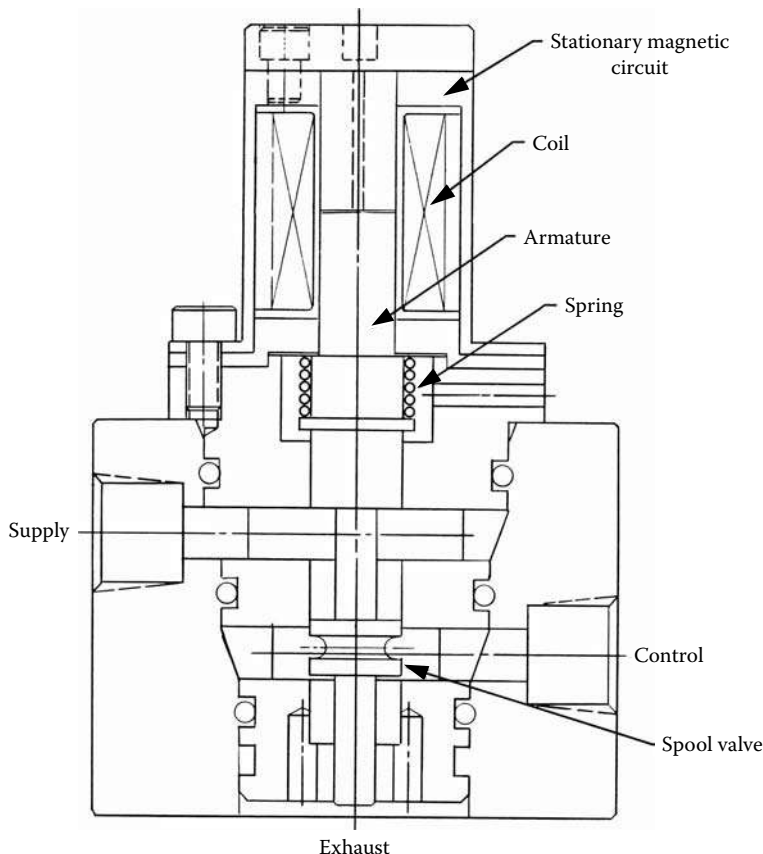
For the coil optimization, the available coil space can be redesigned, as well as the wire diameter and the number of turns. The objective is to utilize fully the available coil window area. Table 3.4 combines the effect of all these steps for the solenoid valve. It compares the flux density at the three magnetic-circuit locations and certain solenoid parameters. The flux densities in the optimized designs are more uniform, which indicates better magnetic-circuit utilization by avoiding local saturations. The achieved results indicate that the maximum force design has 91% greater force than the original design with 6% less current. Minimum current versions have 56% lower current with the same force. Note that a small design difference in current (0.69 A vs. 0.65 A) is the result of designing with discrete wire gauge sizes.

**TABLE 3.4**

Solenoid Performance Comparison

Design	Coil Parameters		Plunger Force (N)	Flux Density			Response Time (ms)
	Current (A)	MMF (At)		Air Gap (T)	Plunger (T)	Housing (T)	
Original	0.69	572	9.81	1.3	1.8	0.4	7.7
Maximum force	0.65	532	18.7	1.4	1.6	1.1	7
Minimum current	0.31	355	9.81	1	1.1	0.9	13.5

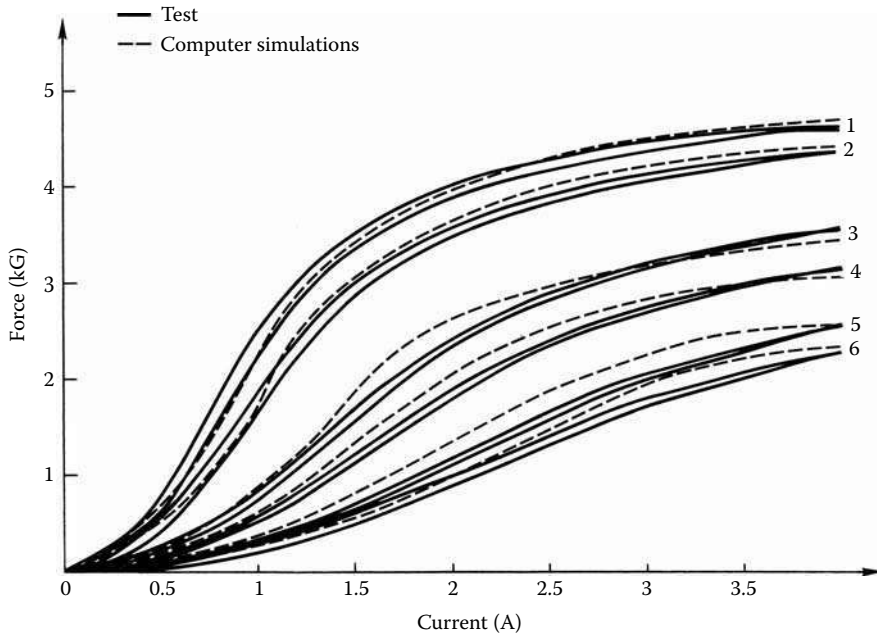
Source: Courtesy of Delphi Corp.



**FIGURE 3.60**  
Transmission spool valve solenoid. (Courtesy of Delphi Corp.)

### 3.3.6 Transmission Solenoids

A conventional hydraulic valve body for a hydraulic transmission that used to be specially adapted for each vehicle has been replaced with a microprocessor-based solenoid valve with a controller that permits easier calibration and more precise control of shift. In addition, electronic control permits the integration of the engine and transmission computers to optimize powertrain control. An important item in developing the electronically controlled transmission is a fast-acting solenoid, as presented in Figure 3.60, to control

**FIGURE 3.61**

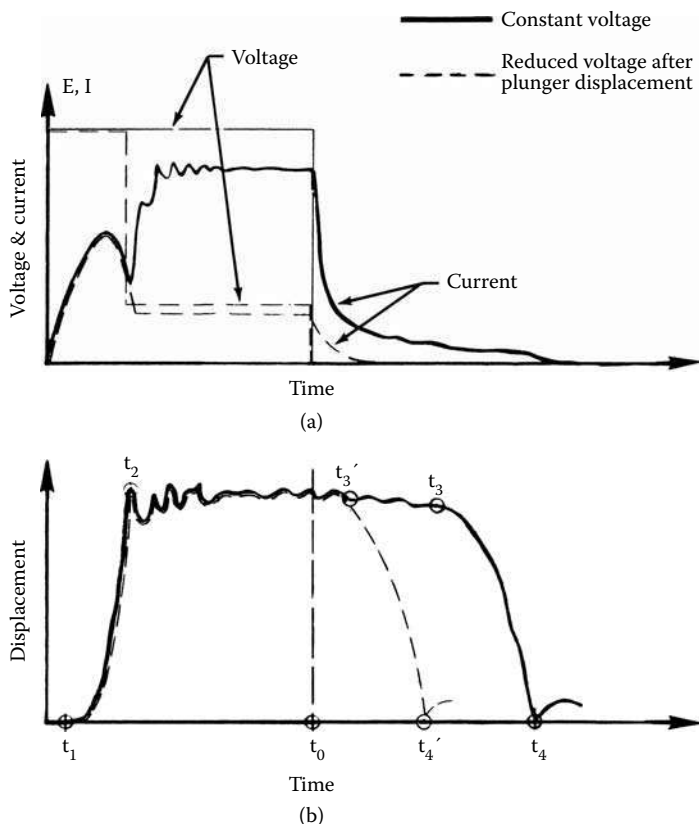
Static force vs. current for different air gaps: (1)  $0.0125 \times 10^{-3}$  m, (2)  $0.0196 \times 10^{-3}$  m, (3)  $0.0367 \times 10^{-3}$  m, (4)  $0.049 \times 10^{-3}$  m, (5)  $0.0735 \times 10^{-3}$  m, (6)  $0.088 \times 10^{-3}$  m. (Courtesy of Delphi Corp.)

clutch pressure by PWM operating a spool valve between a supply and exhaust pressures during shifting with a low current drain from the battery. Because there are as many as seven solenoids in a passenger car transmission, three of which are typically on at any one time, even a 1.0 to 2.0 A current drain has a significant impact on fuel economy, alternator size, etc.

Design and optimization of the transmission solenoid can be done using the mathematical model introduced in Section 3.1. Static analysis of the solenoid has to be performed by evaluating the plunger force at the different discrete plunger positions. The force acting on the plunger is a function of the current level and of the plunger position vs. plunger stop (value of the working air gap). Solenoid total air gap value of  $0.082 \times 10^{-3}$  m and maximum current value of 4.0 A can be used as maximum values for the gap position and current level, respectively. Because at least five testing points are needed to draw a characteristic, it is advisable to use six different positions from  $0.0125 \times 10^{-3}$  m to  $0.082 \times 10^{-3}$  m and six different current values from 0.0 to 4.0 A for static simulations.

Figure 3.61 shows the results of the analysis where all the characteristics were recorded for the increasing current, the lower part of hysteresis, and for the decreasing current, the upper part of hysteresis. In experiments, the test fixture should provide the same exact air gaps of the load cell to record a force at the desired current level. Because of the different current excitation, a family of the force curves is obtained as a function of current characteristics, as shown in Figure 3.61. A comparison of the test results and calculations shows good agreement. The dynamic behavior of the actuator is described in the mechanical Equation 3.9, and the electromagnetic force expressed in Equation 3.12 depends generally on all four current components, as presented in Equation 3.14.

There are two ways to operate such a solenoid actuator in the dynamic mode, as presented in Figure 3.62:

**FIGURE 3.62**

The voltage and current (a) and displacement (b) vs. time:  $t_1$  start time,  $t_2$  travel time up,  $t_4 - t_0$  travel time down. (From Pawlak, A.M., *Proceedings of COMPEUMAG, Conference on the Computation of Electromagnetic Fields*, No. AP33, Tokyo, September 3–7, 1989. With permission.)

**TABLE 3.5**  
Transmission Solenoid Requirements

Parameter	Unit	Requirement
Preload of the spring	N	1.785
Spring constant	$\times 10^3$ N/m	5.465
Spring mass	$\times 10^{-3}$ kg	0.75
Maximum travel	$\times 10^{-3}$ m	0.9
Holding current at full voltage pulse	A	4
Peak current at full voltage pulse	A	4
Holding current at full voltage pulse	A	1.5
Peak current at reduced voltage pulse	A	2.5

Source: Courtesy of Delphi Corp.

1. The applied voltage pulse does not change its value.
2. The applied voltage pulse has its value reduced after a certain time, generally when the plunger reaches end of the travel.

**TABLE 3.6**  
Test and Analysis Comparison

Results	Start Time $t_1$ (ms)	Travel Time $t_2$ (ms)	Requirements $t_2$ (ms)
Analysis	0.99	2.98	2.0
Test	1.01	3.07	2.0

Source: Courtesy of Delphi Corp.

In the first case, the applied voltage pulse stays unchanged beyond the  $t_2$  time, where the current reaches its maximum value, which depends only upon applied voltage and resistance of the coil. The current beyond the  $t_2$  time is called the holding current because it works against the compressed spring and holds the plunger in the closed position. The holding current for the reduced voltage case has the lower value, and therefore, time of operation is more appropriate in any application because less energy is consumed. Moreover, because less energy is stored in the magnetic circuit, the open  $t_3$  time and  $t_4$  are much faster in the second mode of operation. This also permits the use of a high current to get the plunger moving and then a low current to keep the average consumption low.

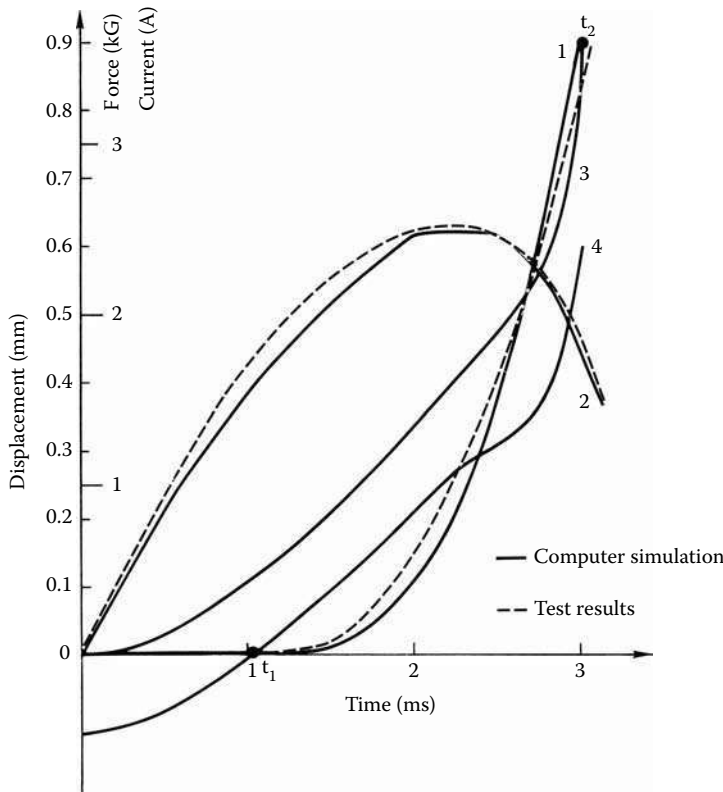
Because the voltage pulse is applied with  $t_0$  width, the current increases and the plunger starts moving in  $t_1$  time. The travel of the plunger is accomplished in  $t_2$  time. The current does not rise monotonically because of the change of inductance due to the shrinking air gap. Typical requirements for the transmission solenoids are presented in Table 3.5, which also includes the maximum values for the peak current and the holding current for both modes of operation.

With the proper specification and input data, one can obtain good agreement between dynamic FE simulations and test results for dry operation with 2.0% difference for the  $t_1$  start time and  $t_2$  travel up, as presented in Table 3.6.

For the dynamic simulations, the reduced voltage mode was used to verify dynamic performance with requirements for this mode as shown in Table 3.5. Because good agreement was obtained for the static and dynamic cases, it also proves that using proper mathematical models, dynamic behavior of the transmission solenoid can be predicted within good engineering accuracy. Figure 3.63 shows the comparison of the computer simulations and test results of the transmission solenoid.

One can optimize fast-acting solenoids through changes in the magnetic circuit and in the coil design or both. Because the magnetic circuit of the solenoid is a solid core, selecting good material with high electrical resistivity (to suppress eddy currents) and good magnetic properties (to increase magnetic flux) is recommended. A good candidate is silicon steel. In our case, Carpenter silicon steel-type "B-FM" was selected (Carpenter 1989). Optimization is an iterative process and for the magnetic circuit the first step is to consider the plunger stop position and the plunger OD. Considering these variables in the computer simulations, the appropriate plunger mass (inertia) should be taken into account. In the existing design, introduced in Figure 3.60, the plunger with a spool valve (total moving mass) weighs  $11.78 \text{ g}$  and the plunger stop is located in the center of the coil,  $17.0 \times 10^{-3} \text{ m}$  from the plunger base. The computer simulations provide a response time  $t_2$  of  $2.98 \text{ ms}$ . Figure 3.64 shows the dynamic response of the plunger for start time and the total travel time vs. plunger OD and the corresponding plunger weight.

From these results, the best OD obtained from the plunger is  $11.2 \times 10^{-3} \text{ m}$ . Because a bigger OD of the plunger reduces the available space for coil (as outside solenoid diameters must remain the same), a plunger OD of  $10.36 \times 10^{-3} \text{ m}$  was selected because the total travel time is almost the same ( $2.20 \text{ ms}$  instead of  $2.18 \text{ ms}$ ). For the new diameter, its best

**FIGURE 3.63**

Dynamic simulations and test results of the transmission solenoid: (1) displacement, (2) current, (3) magnetic force, (4) plunger force. (Courtesy of Delphi Corp.)

position was optimized and compared with its previous location with the original plunger diameter, as presented in Figure 3.65.

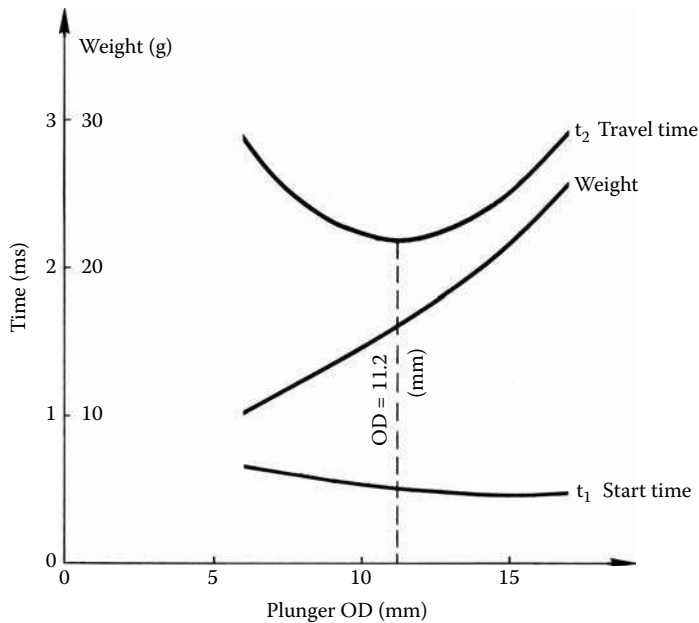
This analysis led to the conclusion that the best plunger location and diameter are a trade-off between the weight of the plunger and a magnetic flux buildup in the plunger for a given current source. Also, the best magnetic flux utilization with minimum flux leakage exists when the plunger is located in the center of the coil. By minimizing the total moving mass of the plunger, the total travel time can be reduced. One way to do this is to provide a hole in the plunger. The hole, however, affects flux distribution and decreases the active plunger surface, although the plunger weight also decreases. The hole was investigated and the results presented in Figure 3.66 show that any hole in an active plunger would increase total travel time. Therefore, this direction is not recommended.

After the best magnetic circuit is established, the coil can be optimized to increase the rate of rise of the current vs. time and reduce peak holding current, improving response time, and reducing the current drain from the battery, respectively. Based on two well-known equations that describe the slope of the current, neglecting coil resistance:

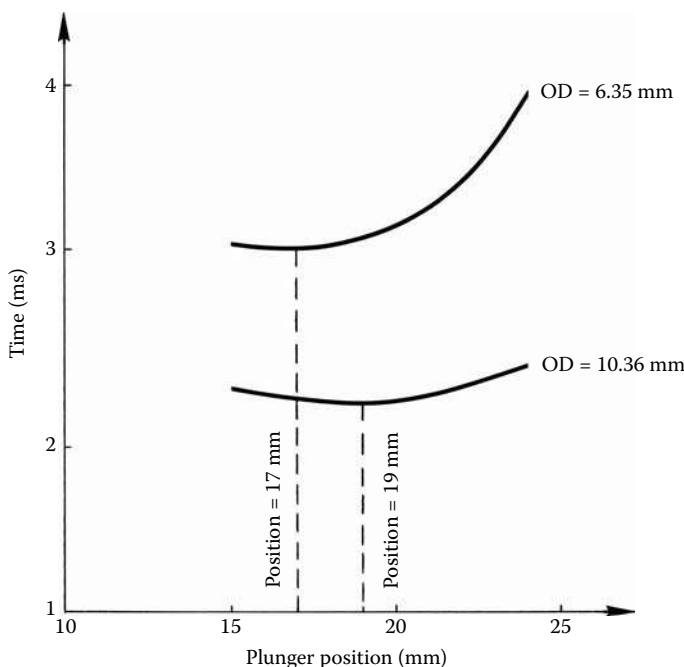
$$\frac{di_s}{dt} = \frac{e_s}{L} \quad (3.15)$$

and

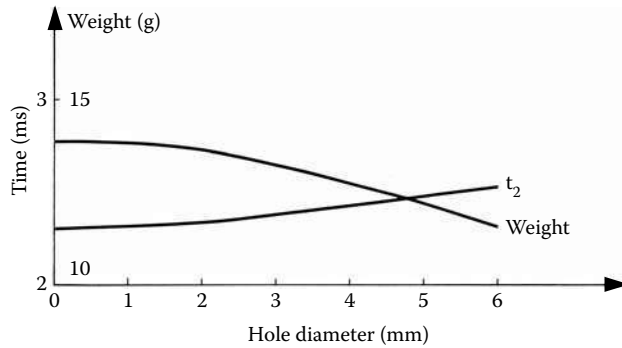
$$L = \frac{N\phi}{i_s} \text{ or } L = N^2 P \quad (3.16)$$

**FIGURE 3.64**

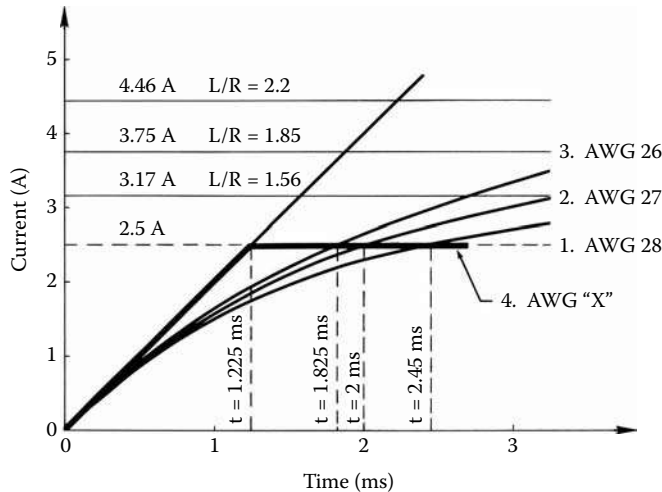
Plunger response and mass vs. OD. (From Pawlak, A.M., *Proceedings of COMPLUMAG, Conference on the Computation of Electromagnetic Fields*, No. AP33, Tokyo, September 3–7, 1989. With permission.)

**FIGURE 3.65**

Total travel time vs. plunger position for different ODs. (Courtesy of Delphi Corp.)

**FIGURE 3.66**

Total travel time and plunger mass vs. plunger hole diameter. (Courtesy of Delphi Corp.)

**FIGURE 3.67**

The current vs. time. (Courtesy of Delphi Corp.)

where  $i_s$  is a current in the coil,  $e_s$  is applied voltage,  $L$  is inductance,  $N$  is number of turns,  $\phi$  is magnetic flux, and  $P$  is the permeance of the magnetic circuit. Taking into account the constraints, Equation 3.15, and Equation 3.16, the slope of the current can be increased if the voltage input is increased or the inductance is reduced. Increasing the voltage is not possible because of the automotive system battery voltage limitation, but one can try to reduce inductance by reducing the number of turns or changing the permeance of the magnetic circuit. The inductance of the coil may not be decreased by reducing the number of turns because this may reduce the holding force requiring an increase in holding current,

**TABLE 3.7**

Solenoid Performance for Different Coil Parameters

Coil and Performance (AWG)	Turns (No.)	Resistance (Ω)	Diameter ( $\times 10^{-3}$ m)	Opening Time (ms)	Total Time (ms)	Time at 2.5 A (ms)
28	400	3.79	20.0	0.71	2.46	2.45
27	400	3.2	21.6	0.68	2.33	2.00
26	400	2.69	23.5	0.66	2.2	1.825
"X"	400	TBD	TBD	0.59	2.08	1.225

Source: Courtesy of Delphi Corp.

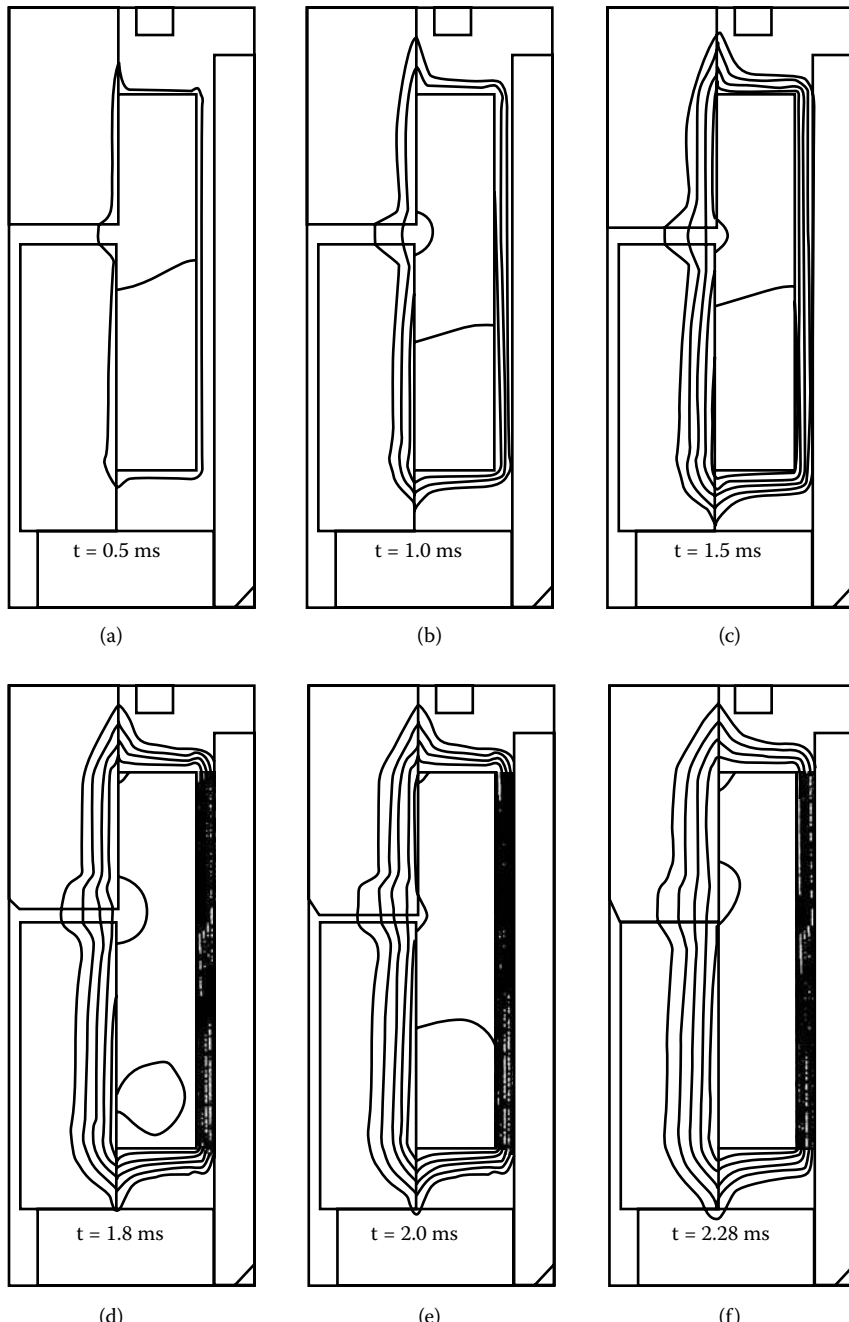
which is not possible because of the requirements presented in Table 3.5. Because of the fixed geometry, the permeance is also fixed, so changing permeance cannot change the inductance. Even so, one should not be interested in reducing permeance because it would reduce flux density and force. Therefore, the only way to change the slope of the current is to change its resistance with the same number of turns by fully utilizing available space. This can be done by changing the wire diameter and resistance at the same time. Figure 3.67 and Table 3.7 show how the diameter of wire (resistance) affected the current vs. time shape and the time when the current reaches the peak current limit of 2.5 A for the reduced voltage source. The current shapes vs. time were calculated on the basis of the inductances and resistances neglecting the eddy current effect. Therefore, these current shapes are more optimistic and reach the peak current limit faster than in the real case, as shown by the equation:

$$i_s(t) = \frac{e_s}{R} \left( 1 - e^{-\frac{R}{L}t} \right) \quad (3.17)$$

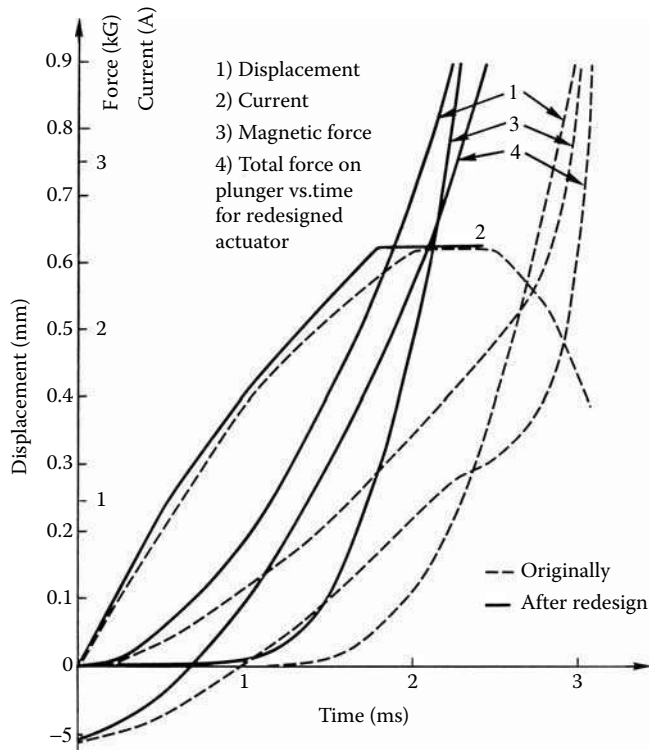
where  $i$  is the winding current and  $R$  is the coil resistance. The total travel time of 2.98 ms with the same original coil was reduced to 2.46 ms after the magnetic circuit was changed with the same coil parameters (AWG size 28 and number of turns = 400). As a result of these changes, the OD increased from  $20.0 \times 10^{-3}$  m to  $23.5 \times 10^{-3}$  m and the total travel time was further reduced to 2.20 ms, which is 26% faster than the original design. Theoretically, even by increasing wire diameter to the point where resistance is neglected (see "X" wire diameter) the current shape will change the total travel time of 2.08 ms achieved, which is still not satisfactory according to solenoid requirements, as presented in Table 3.5 and Table 3.7.

The flux lines and the displacement of the optimized solenoid are shown in Figure 3.68, where one can notice an increased number of flux lines and movement of the armature.

Figure 3.69 shows the displacement, the forces, and the current vs. time for the actuator before and after the magnetic circuit and coil optimization. The optimized actuator showed a big improvement in the dynamic response but it still does not satisfy requirements as presented in Table 3.5. Therefore, a bistable latching solenoid having a PM that provides a latching force without current application may be an option for these applications; see Chapter 4.

**FIGURE 3.68**

Flux lines vs. time with different plunger positions at dynamic operation: (a) flux at 0.5 ms, (b) flux at 1.0 ms, (c) flux at 1.5 ms, (d) flux at 1.8 ms, (e) flux at 2.0 ms, (f) flux at 2.28 ms. (From Pawlak, A.M., *Proceedings of COMPUMAG, Conference on the Computation of Electromagnetic Fields*, No. AP33, Tokyo, September 3–7, 1989. With permission.)

**FIGURE 3.69**

Dynamic analysis for the original and optimized solenoid valve: (1) magnetic force, (2) current, (3) displacement, (4) net force. (Courtesy of Delphi Corp.)

### Example 3.1

Calculate magnetic flux, core and air energy, inductance, and force of the disk solenoid with simple rectangular *E-I* core based on a lumped-parameter model. *BH* characteristic is assumed linear for simplicity. Solenoid drawing, dimensions, and other solenoid parameters are provided in Figure 3.70:

Number of turns: 100

Nominal current 10 A

Permeability of air =  $0.1256 \times 10^{-5}$  H/m

Permeability of iron =  $0.1256 \times 10^{-2}$  H/m

Where the dimensions are:

$$D_1 = 20 \times 10^{-3} \text{ m} \quad H = 10 \times 10^{-3} \text{ m}$$

$$D_2 = 10 \times 10^{-3} \text{ m} \quad L = 10 \times 10^{-3} \text{ m}$$

$$D_3 = 10 \times 10^{-3} \text{ m} \quad W_1 = 10 \times 10^{-3} \text{ m}$$

$$G = 0.25 \times 10^{-3} \text{ m} \quad W_2 = 20 \times 10^{-3} \text{ m}$$

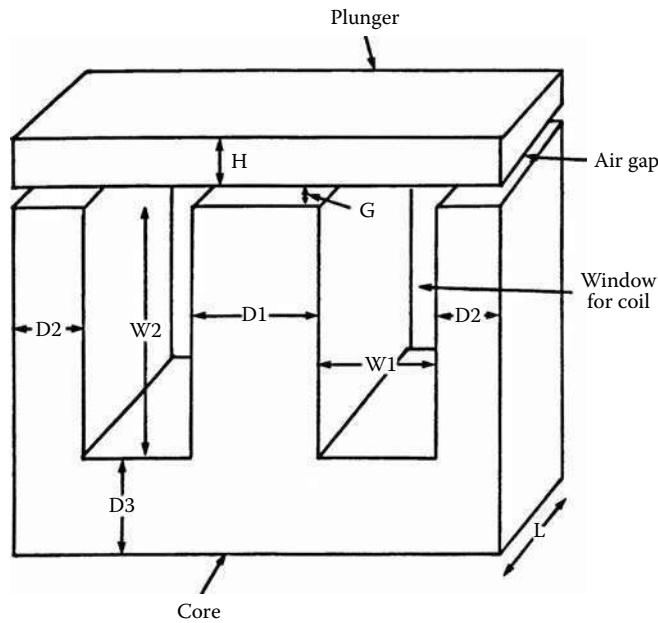


**FIGURE 3.70**  
E-I core disk solenoid geometry. (Courtesy of Delphi Corp.)

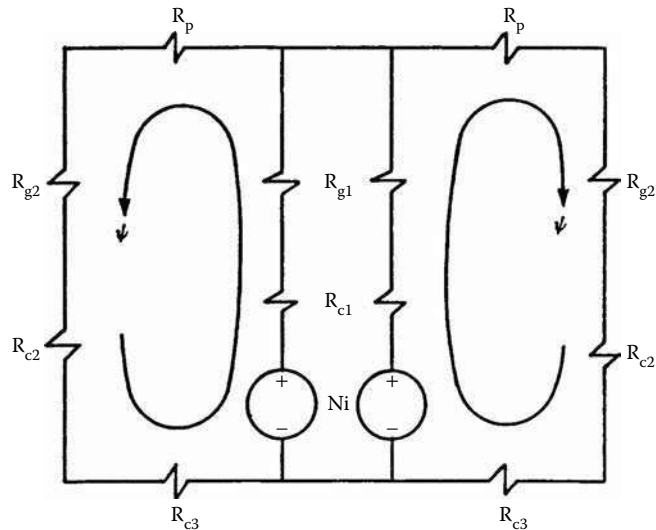


**FIGURE 3.71**  
E-I core solenoid lumped-parameter model. (Courtesy of Delphi Corp.)

### Step 1. Sketch Lumped-Parameter Model for E-I Core Solenoid, Figure 3.71

Here  $\phi$  is the magnetic flux,  $Ni$  is the MMF,  $R_p$  is the reluctance of the plunger,  $R_{g1}, R_{g2}$  are air gap reluctances,  $R_{c1}, R_{c2}, R_{c3}$  are core reluctances.

## Step 2. Calculations of the Lumped-Parameter Model; Model Description

Magnetic-circuit reluctance:  $R = R_p + R_{c1} + R_{c2} + R_{c3} + R_{g1} + R_{g2} = 4.785 \times 10^6 \text{ A/Wb}$

Total reluctance:  $R_T = R/2 = 2.392 \times 10^6 \text{ A/Wb}$

Magnetic flux:  $\phi = \frac{Ni}{R} = \frac{1000}{4.785 \times 10^6} = 0.000209 \text{ Wb}$

Inductance:  $L = \frac{N^2}{R_T} = \frac{100^2}{2.392 \times 10^6} = 4.19 \times 10^{-3} \text{ H}$

Total energy:  $Energy = \frac{R_T \phi_T^2}{2} = \frac{2.392 \times 10^6 \times (2 \times 2.09 \times 10^{-4})^2}{2} = 0.209 \text{ J}$

Force:  $F = \frac{B^2 A}{2 \times \mu_0} = \frac{1.324^2 \times 1 \times 10^{-4}}{2 \times 4\pi \times 10^{-8}} = 698.0 \text{ N}$

This concludes Example 3.1.

## Example 3.2

Run FE analysis for the  $E-I$  core rectangular solenoid presented in Example 3.1. Plot flux lines and flux distribution. Calculate flux, total air and core energy, inductance, and force of the disk solenoid, and compare with the lumped-parameter model.

## Step 1. Make Assumptions and Prepare Input Data for FE Model

- The solenoid is assumed to be infinitely long (in the  $z$  direction), which means that end effects can be neglected. Consequently, the magnetic field exists in the  $x-y$  plane and is independent of position along the  $z$  axis. For these reasons, the analysis can be restricted to a slice in the  $z$  direction of per unit length.
- Because the device and its excitation are symmetric about the centerline, the magnetic field, therefore, must also be symmetric around the same axis. Consequently, only one half of the device needs to be modeled, as presented in Figure 3.70.
- Assume physical and logical coordinates and mark on Figure 3.72 along with assumed relative permeabilities of the various regions.

## Step 2. FE Simulations of the Solenoid's Static Parameters at MMF = 1000 At and Plot Flux Lines and Flux Distribution; Compare Data with Lumped-Parameter Calculations

Plot magnetic flux lines, Figure 3.73, and flux vs. position, Figure 3.74:

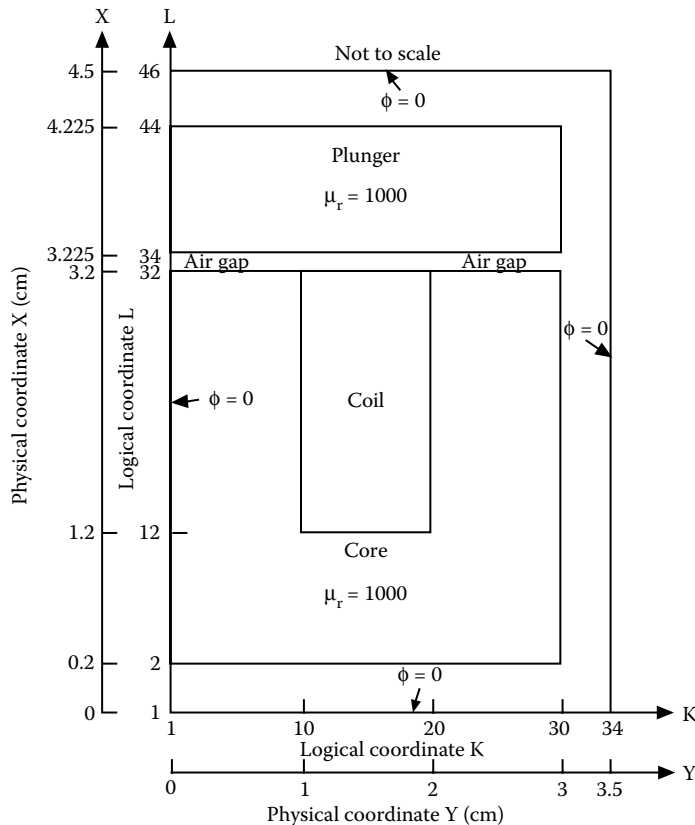


**FIGURE 3.72**  
E-I core solenoid region to be modeled. (Courtesy of Delphi Corp.)

FE simulations results:

Flux: 0.000227 Wb

Total energy: 0.2225 J

Force: 705.4 N

Inductance: 4.45 mH

FE simulation comparison with lumped-parameter calculations:

Flux:  $\Delta\phi = 7.9\%$

Total energy:  $\Delta E = 6.1\%$

Force:  $\Delta F = 1.0\%$

Inductance:  $\Delta L = 5.8\%$

Comparison of the two sets of results reveals excellent agreement. One of the reasons is because the magnetic circuit is not saturated. This concludes Example 3.2.

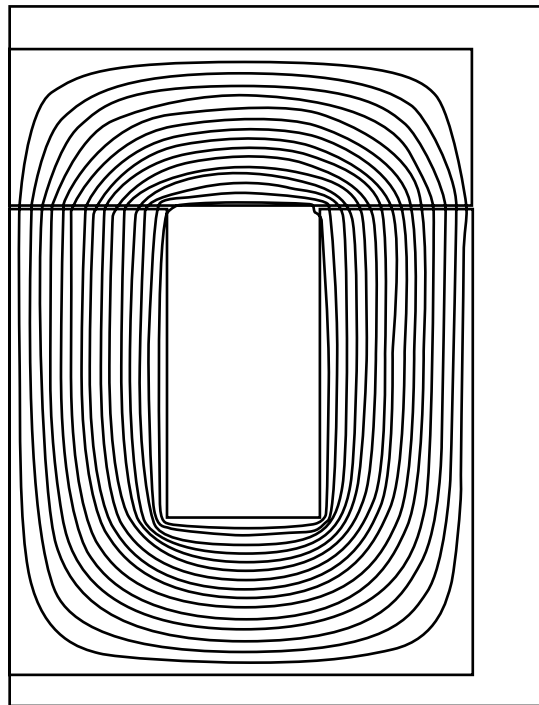


**FIGURE 3.73**  
*E-I* core solenoid flux lines. (Courtesy of Delphi Corp.)

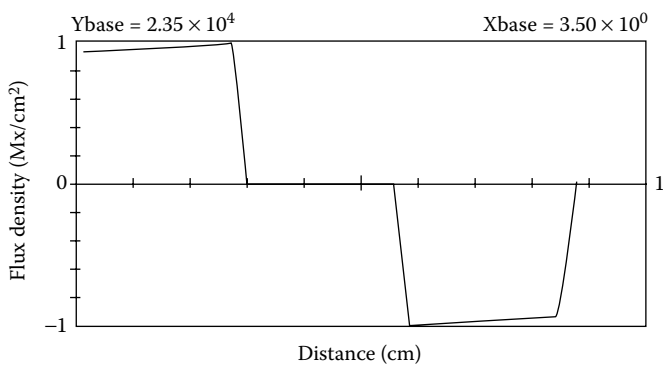


**FIGURE 3.74**  
*E-I* core solenoid flux density distribution. (Courtesy of Delphi Corp.)



# 4

---

## *Latching Linear Actuators*

---

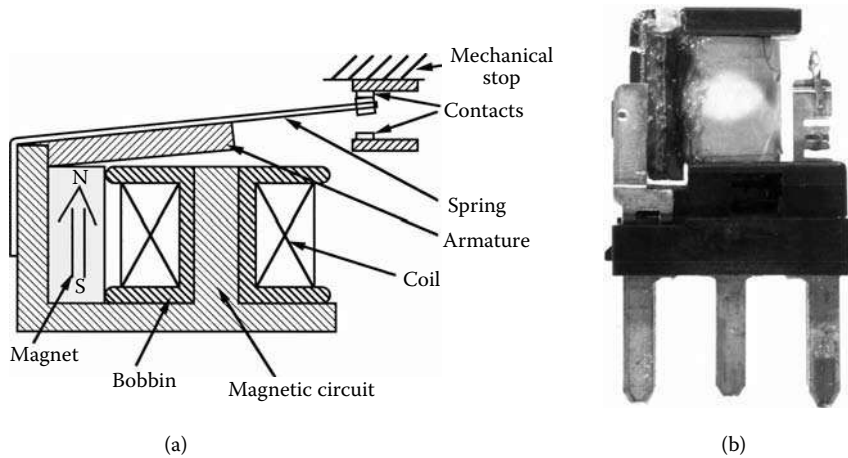
Latching linear actuators represent a growing family of actuators that have latching function. The latching function can be defined as the capability of electromagnetic solenoids to maintain a last position when the power is off. There is a need for latching actuators in the industry because of their energy-saving capability. In the automotive industry, applications include injectors, relays, and fluid control solenoids. In particular, latching relay applications can result in significant energy savings in products such as daytime running lamps; fuel pumps; air-conditioning (A/C) clutch coils; heating, ventilating, air-conditioning (HVAC) blowers; engine cooling fans; and electronically operated transmission solenoids.

The latching function requires the presence of a PM in the magnetic circuit. It also requires that an actuator with its control circuit should have the capability to return the armature to its original position by a return spring action after the magnetic field holding the armature is dismantled (Pawlak et al. 1997, Pawlak et al. 1999).

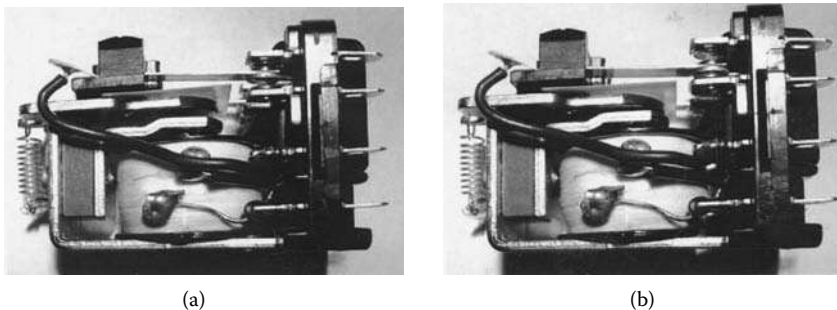
---

### **4.1 Latching Relays**

Both unipolar and bipolar latching relay configurations are discussed in this chapter. A bipolar relay consists of one coil and requires a controller having bidirectional current capabilities. This means more complex electronics, usually an H-switch allowing for bidirectional current, which is more costly than a conventional controller. A unipolar relay consists of two coils and a conventional controller with unidirectional current capabilities. The relay requires two coils, although controller capabilities are less complex compared with a bipolar relay. A conventional bipolar relay can be converted to a bipolar latching relay with the proper placement of a PM to the magnetic circuit. A conventional relay consists of a coil, a pivoted armature, and the electromagnet. For the purpose of the additional latching function, a PM is added (Pawlak et al. 1997). In this configuration, the magnet is located in a space between the coil and the magnetic circuit at the pivot point side, as shown in Figure 4.1. The figure identifies the relay components and shows a cross section of the latching relay based on the conventional relay configuration having Cartesian symmetry. The rectangular-shaped magnet has magnetization with a direction parallel to the axis of symmetry as presented in Figure 4.1(a). The external magnetic circuit is stationary and serves as the main magnetic circuit of the relay. The coil is wound on a bobbin and located around the relay's stationary magnetic core. The rectangular-shaped armature is attached to a flat return spring at the pivot, while the contacts are attached to the other side of the armature. The armature position on both sides is mechanically controlled by the contact locations and is latched on both sides due to the presence of the magnet. The spring is preloaded and with the additional force from spring compression

**FIGURE 4.1**

Bipolar latching relay based on conventional structure: (a) bipolar latching relay components, (b) conventional bipolar relay assembly model converted to latching function. (Courtesy of Delphi Corp.)

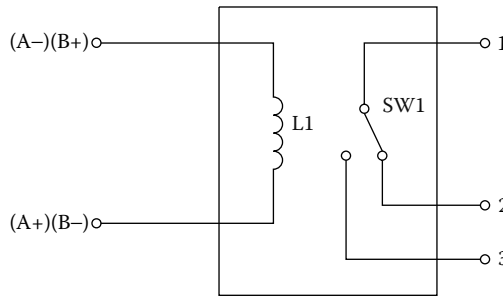
**FIGURE 4.2**

Commercial latching relay based on conventional structure: (a) unlatched position, (b) latched position.

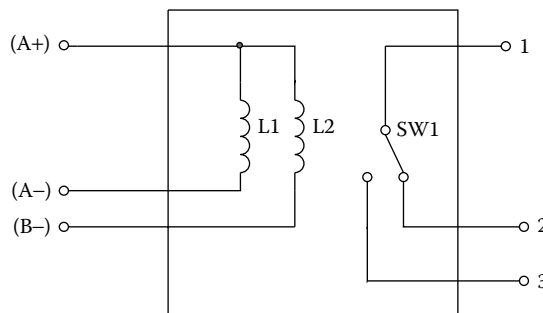
is able to return the armature. Figure 4.2 shows the commercial latching relay having one segmented coil with 10.0 A current rating in two extreme latched and unlatched positions.

Figure 4.3 illustrates the control scheme of the bipolar latching relay having one coil with two terminals and control inputs for both latch *A* and *B* positions, where electrical energy is applied for the armature movement. This controller is more complex and more expensive compared to a unipolar controller because of an H-switch allowing for the bidirectional current to change direction. As indicated by "+" and "-" polarities for latch *A* and "-" and "+" polarities for latch *B*, as shown in Figure 4.3, terminal 2 is connected for latch *A* and terminal 3 is connected for latch *B*.

Figure 4.4 shows the control scheme of the unipolar (dual input) latching relay having two coils with three terminals and control inputs for both latch *A* and *B* positions, where electrical energy is applied for armature movement. One terminal of each coil is connected to the controller ("*A*−" and "*B*−" terminals in Figure 4.4) and the other is connected to form a common terminal ("+" terminals in Figure 4.4). Both coils are energized separately, one at a time and always with the same polarity. It also shows the contact positions. When

**FIGURE 4.3**

Bipolar latching relay control schematic: L<sub>1</sub> is coil inductance, SW1 is an on-off switch, (1) is a common terminal, (2) is the latch A terminal, and (3) is the latch B terminal. (Courtesy of Delphi Corp.)

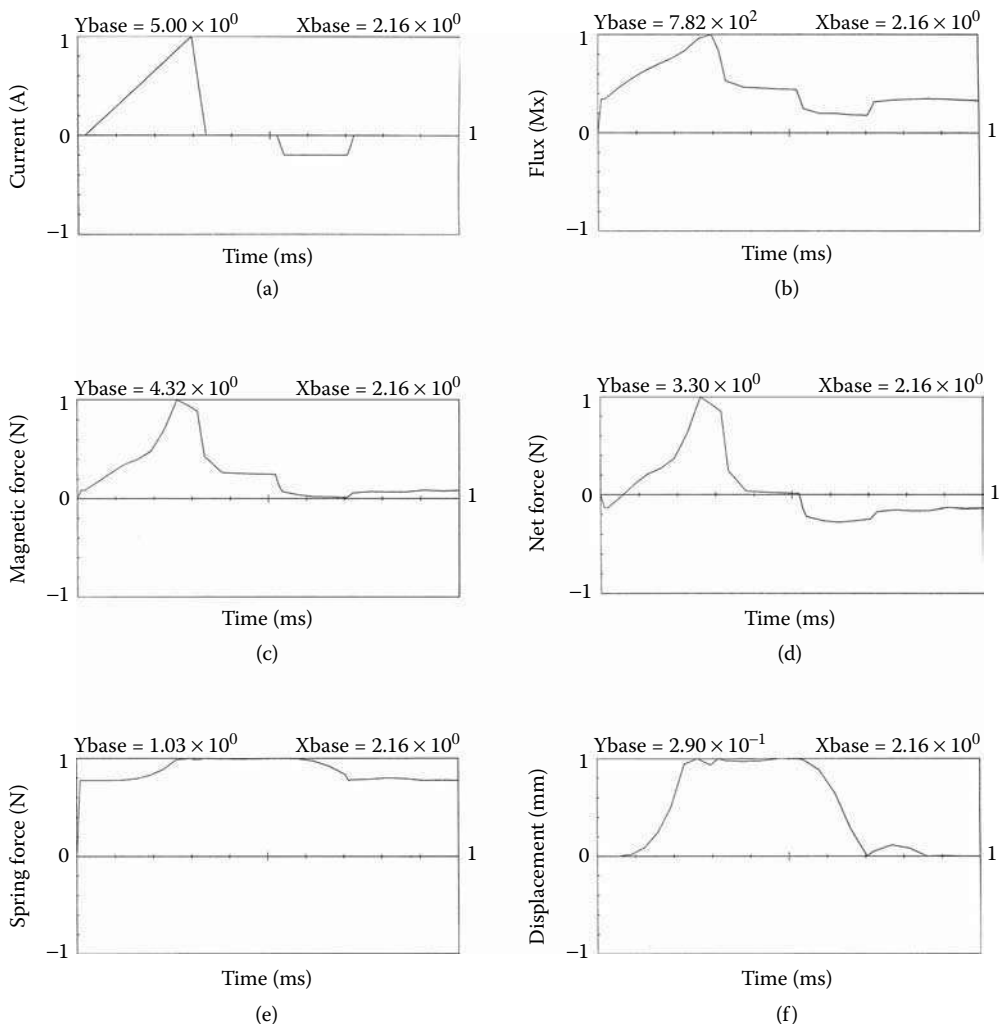
**FIGURE 4.4**

Unipolar latching relay control schematic: L<sub>1</sub> is coil 1 inductance, L<sub>2</sub> is coil 2 inductance, SW1 is an on-off switch, (1) is a common terminal, (2) is the latch A terminal, and (3) is the latch B terminal. (Courtesy of Delphi Corp.)

terminal 1 and terminal 2 are connected, the armature is in the latch A position and when terminal 1 is connected with terminal 3, the armature is in the latch B position.

#### 4.1.1 Dynamics of Latching Relays

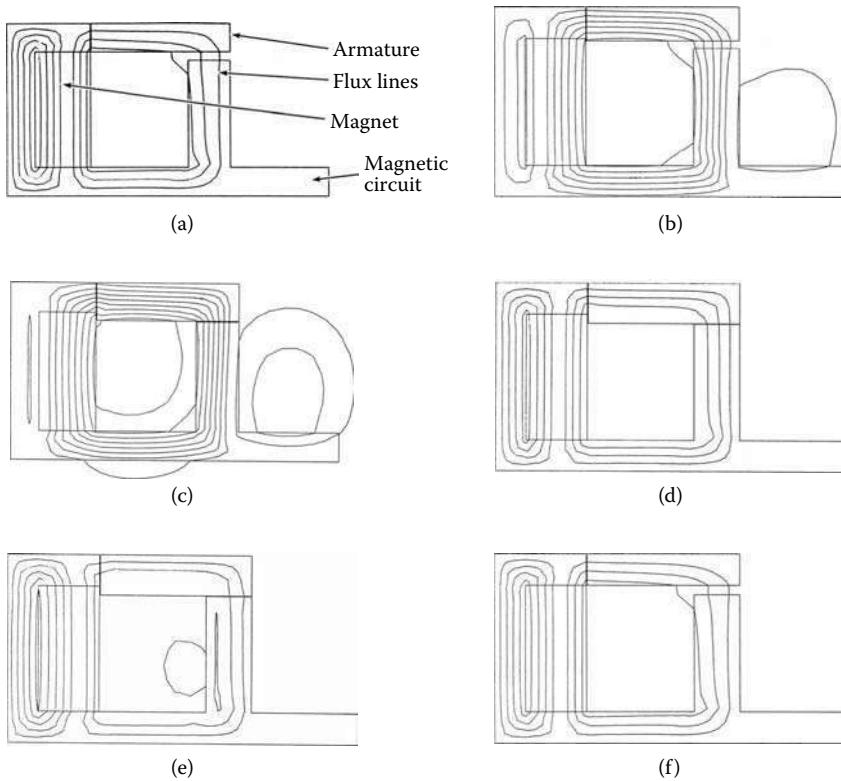
The dynamics analysis of latching relays was conducted using FE software. Because the magnetic structure of the relay has Cartesian symmetry, the pivot motion was replaced with the equivalent axial motion, where the parasitic air gap is negligible in comparison with the main working gap. Figure 4.5 shows the relay's dynamic behavior for the transient current, magnetic flux, magnetic force, spring force, net force, and displacement vs. time, respectively. The control current shown in Figure 4.5(a) identifies the proposed controlled diagram of the relay cycle. Initially, the relay is open and no voltage is applied to the coil. When the voltage is applied to the coil, the current rises, with the slope being a function of coil resistance and inductance. The current reaches its maximum value and the voltage is disconnected. At the same time, the magnetic flux builds up, as presented in Figure 4.5(b), and generates the magnetic force. Both the magnetic flux and the magnetic force are the result of magnet and coil MMFs. When the current builds up in the coil, the magnetic flux increases in the armature and, at a certain point, balances the negative spring force, as presented in Figure 4.5(d) and Figure 4.5(e). At this point, the armature starts moving and closes the air gap, as indicated in Figure 4.5(f). Then the positive voltage is discontinued and the armature stays closed due to PM MMF, which at this point is stronger

**FIGURE 4.5**

Dynamics of latching relay: (a) transient current vs. time, (b) transient magnetic flux vs. time, (c) transient magnetic force vs. time, (d) transient magnetic net force vs. time, (e) transient spring force vs. time, (f) transient displacement vs. time. (Courtesy of Delphi Corp.)

than at the beginning of the cycle because more flux lines cross the main air gap, as shown in Figure 4.6(d). Consequently, a negative voltage is applied, as presented in Figure 4.5(a), which suppresses the magnet flux lines and with the suppressed magnetic force, the spring returns the armature back to its previous position, as indicated in Figure 4.5(f) and Figure 4.6(f), and the cycle is complete.

Figure 4.6(a) through Figure 4.6(f) illustrate the relay's geometry and magnetic flux lines during the dynamic operation, previously described in Figure 4.5. Figure 4.6(a) shows the relay magnetic circuit and flux lines due to PM MMF at the beginning of the cycle at 0.1 ms with no coil excitation. A small portion of magnet flux lines crosses the air gap and the magnet force cannot move the armature. With positive current excitation, more flux is generated and the stronger magnetic force working against the spring force moves the armature, as shown in Figure 4.6(b) and Figure 4.6(c) at 0.2 ms and 0.4 ms, respectively. As illustrated in Figure 4.6(d) at 0.8 ms, with the air gap closed and no current excitation,

**FIGURE 4.6**

Magnetic flux lines for latching relay dynamic operation: (a) magnet flux lines at 0.1 ms, (b) magnet and positive current flux lines at 0.2 ms, (c) magnet and positive current flux at 0.4 ms, (d) magnet flux at 0.8 ms, (e) magnet and negative current flux at 1.2 ms, (f) magnet flux at 1.6 ms. (Courtesy of Delphi Corp.)

more flux lines are attracted toward the main air gap, generating a magnetic force sufficient to keep the armature closed and the spring suppressed. With negative current applied to the coil, the magnetic flux lines are shifted out of the air gap, as shown in Figure 4.6(e) at 1.2 ms, and the armature returns to its previous position, as shown in Figure 4.6(f) at 1.6 ms. After the negative current is discontinued, the PM restores the flux level as well as its distribution, as identified in Figure 4.6(f), at 1.8 ms, back to its original shape at the beginning of the cycle. Compare this with Figure 4.6(a). During dynamic operation, at no time is the magnet exposed to demagnetization forces. This should secure the magnet's normal operation during the entire time of relay's utilization.

#### 4.1.2 Bipolar Latching Relays

The basic concept of a modern latching actuator with magnets in armature is presented in Figure 4.7. The latching relay consists of two components: a stationary electromagnet and a movable armature. The stationary electromagnet consists of an upper and a lower magnetic core assembly as well as a coil with leads. The magnetic core assembly provides a mechanical stop for the armature and a sliding opening for the shaft, while providing for the coil's MMF, its primary flux conducting function. The second mechanical stop is provided by the electrical contacts, as shown in Figure 4.14. Both stops prevent the magnet from direct contact with the magnetic core, thus preventing magnet breakage. The movable

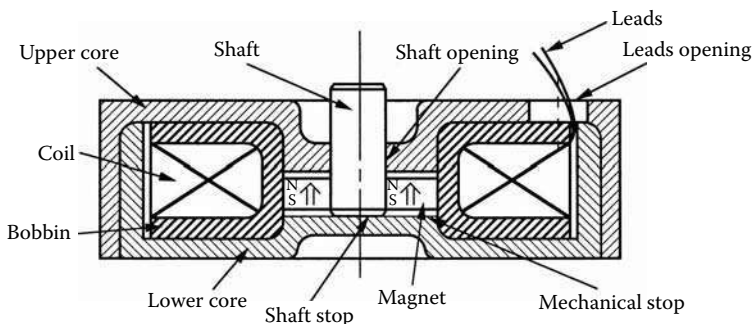


**FIGURE 4.7**  
Bipolar latching relays structure and components. (Courtesy of Delphi Corp.)

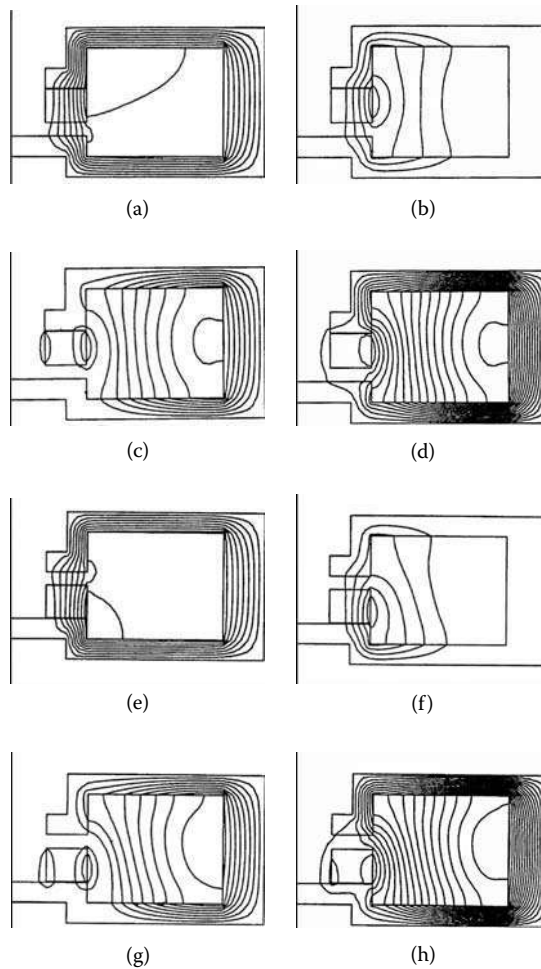


**FIGURE 4.8**  
Bipolar latching relay with magnet in armature components and assembly. (Courtesy of Delphi Corp.)

armature consists of a PM and a shaft. The ring-shaped magnet has axial magnetization providing uniform polarity at the top and an opposite polarity at the bottom. The shaft is mechanically coupled to the ring magnet. The armature is assembled prior to the electromagnetic core assembly.

All the bipolar relay components are shown in Figure 4.7 and Figure 4.8. The armature shaft and the magnet are located inside the housing that secures the armature by providing a slide opening for the shaft and a mechanical stop for the armature. The housing consists of two ferromagnetic core parts — the lower core and the upper core — which are pressed together in the assembly process, encapsulating a coil with a bobbin and two leads. When the lower core is pressed against the upper core, the space for the armature movement is provided and determined by two mechanical stops. The opening in the housing provides a passage for the coil leads. The components presented in Figure 4.8 and Figure 4.14 show means of providing a specially shaped armature shaft that could be made out of nonmagnetic material, preferably stainless steel or plastic, where the shaft's top side would provide mechanical coupling with the ring magnet. The magnet material should be high-energy neodymium or samarium cobalt. If the magnet is based on plastic-molded neodymium, both the shaft and the magnet ring could be manufactured by the same plastic-molding process.

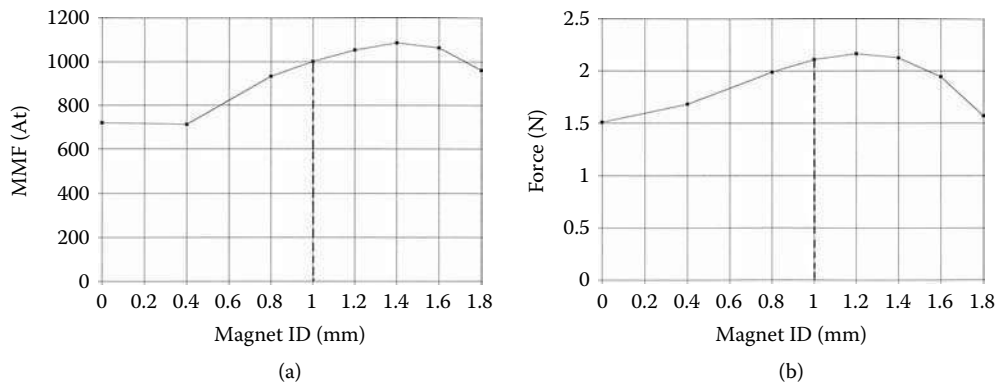
The operation of the latching relays is best demonstrated in Figure 4.9, where different stages of relay operation are illustrated by magnetic flux lines. Initially, the armature is in its upper stable equilibrium position with the presence of the magnetic flux in the magnetic

**FIGURE 4.9**

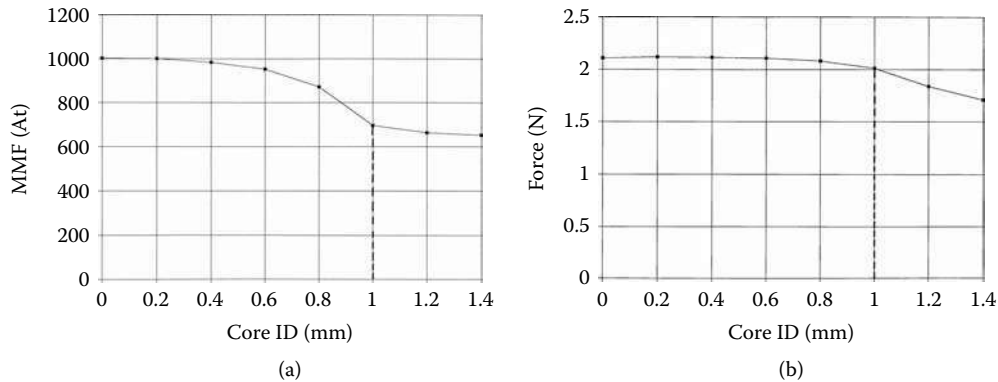
Magnetic flux lines for bipolar latching relay dynamic operation: (a) magnet flux lines at 0.0 At, (b) magnet and positive current flux lines at 100.0 At, (c) magnet and positive current flux at 200.0 At, (d) magnet and positive current flux lines at 300.0 At, (e) magnet flux lines at 0.0 At, (f) magnet and negative current flux at 100.0 At, (g) magnet and negative current flux at 200.0 At, (h) magnet and negative current flux at 300.0 At. (Courtesy of Delphi Corp.)

circuit that is only generated by the PM, as presented in Figure 4.9(a). When the current is applied to the coil, it suppresses the magnet flux lines, as shown in Figure 4.9(b) through Figure 4.9(d) with the current increased to 100.0, 200.0, and 300.0 At, respectively. At this point, the net magnetic forces change their direction and again the repulsive forces are applied, moving the armature to the bottom mechanical stop. At this time, the current is discontinued and the magnet establishes its stable equilibrium position at the bottom, as shown in Figure 4.9(e). With the opposite current applied to the coil, the entire process is reversed and the magnet is forced to move back to its original position, as presented in Figure 4.9(f) through Figure 4.9(h).

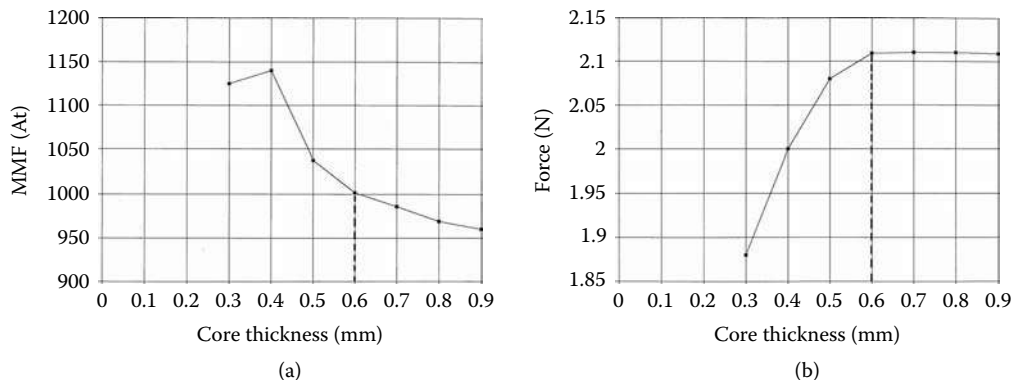
The magnet optimization studies are illustrated in Figure 4.10 through Figure 4.12. Variations in the magnet's inside diameter (ID) affect the latching force developed by the magnet. Figure 4.10(a) shows that the ring magnet develops a higher latching force compared with a disk in which the ID equals zero. There is only one ID of  $1.2 \times 10^{-3}$  m value for the ring magnet that will provide the maximum magnet latching force, as presented

**FIGURE 4.10**

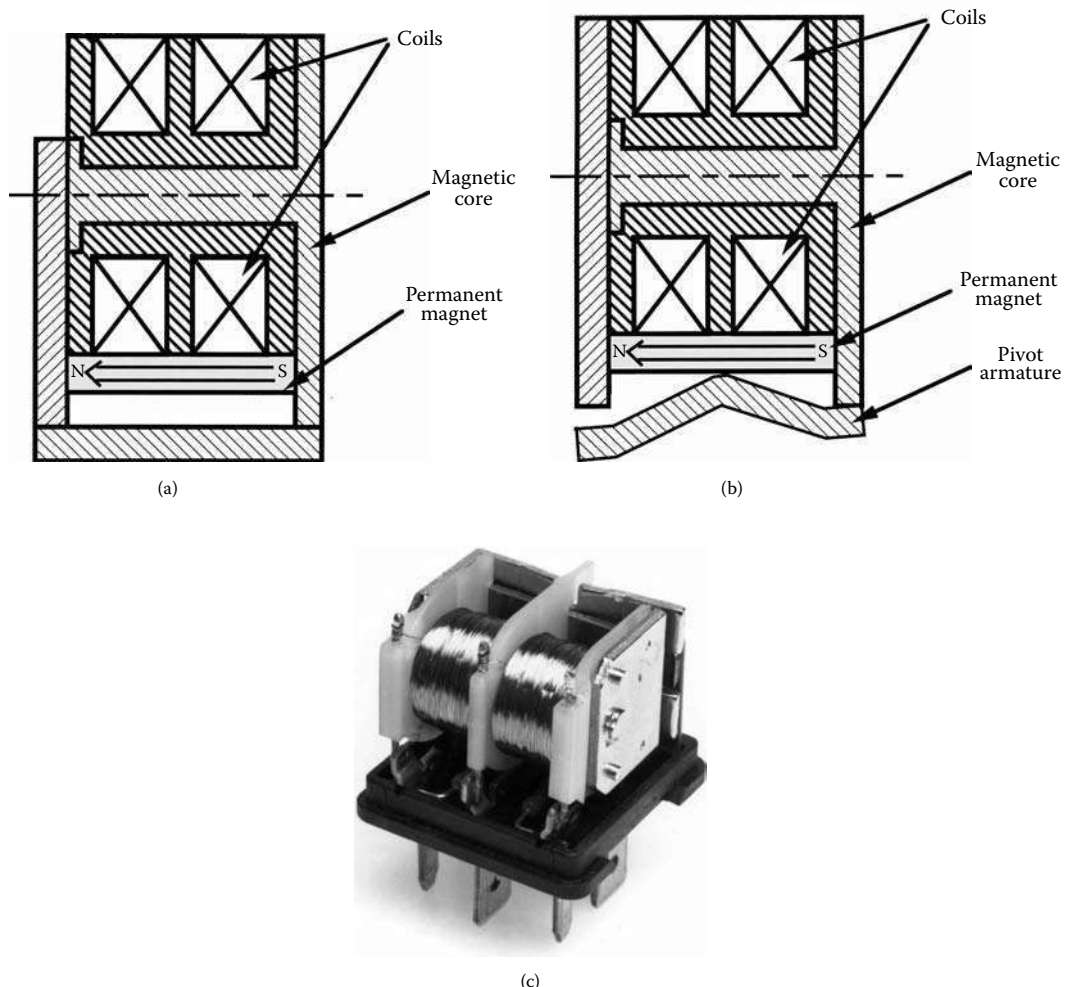
Bipolar latching relay magnet ID optimization study: (a) MMF, (b) latching force. (Courtesy of Delphi Corp.)

**FIGURE 4.11**

Bipolar latching relay core ID optimization study: (a) MMF, (b) latching force. (Courtesy of Delphi Corp.)

**FIGURE 4.12**

Bipolar latching relay core thickness optimization study: (a) MMF, (b) latching force. (Courtesy of Delphi Corp.)

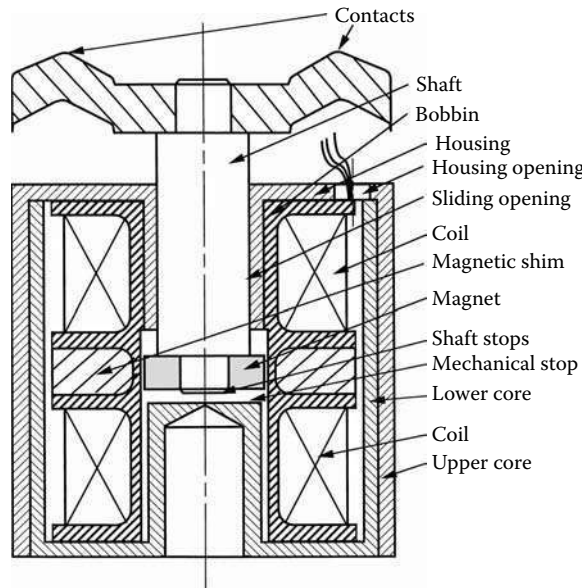
**FIGURE 4.13**

Unipolar conventional latching relay with two coils and pivot armature: (a) unipolar relay with two coils, (b) unipolar relay with two coils and pivot armature, (c) commercial unipolar relay with two coils and pivot armature.

in Figure 4.12(b). For engineering reasons, however, the  $1.0 \times 10^{-3}$  m value was selected, as marked in Figure 4.10(b), Figure 4.11, and Figure 4.12. These figures show the MMF and magnetic force developed in the armature as a function of the iron core thickness. Selected dimensions identified by dotted lines ensure a high relay electromagnetic performance.

#### 4.1.3 Unipolar Latching Relays

If the latching relay presented in Figure 4.1 is duplicated to allow for the second coil to create a unipolar relay structure, it transforms to Figure 4.13. Typically, a conventional relay has a pivot action, which has to be common for both coils. Therefore, one possible solution is to introduce it at the bottom part, as shown in Figure 4.13(b). The configuration with a pivot armature is now commercially available, as illustrated in Figure 4.13(c).

**FIGURE 4.14**

Unipolar latching relay with magnet in armature structure and components. (Courtesy of Delphi Corp.)

A modern concept for unipolar configuration with a movable magnet is presented in Figure 4.14. The latching relay consists of two components: a stationary electromagnet and a movable armature. The stationary electromagnet consists of an upper and a lower magnetic core encapsulating two coils side by side. The latching function is provided by a PM that holds an armature in two stable positions without a spring.

At its latched position, the magnet provides sufficient force for the electrical contacts to be closed or open, depending on the control mode. The coils are energized to repel the magnet's armature. Therefore, when each of the coils is energized, the same polarity exists at the electromagnet's poles and the adjacent magnet side. The relay assembly provides two mechanical stops for the magnetic armature while providing a nonmagnetic contact with the magnetic core. One stop is provided by the shaft because the relay shaft extends from the magnet. The second stop is provided by the contact as it closes before the magnet armature reaches the upper magnetic pole. The movable armature consists of a PM and a shaft. The ring-shaped magnet with an axial magnetization provides a certain polarity at the top and the opposite polarity at the bottom. The shaft is mechanically coupled to the ring magnet. The armature is assembled prior to the electromagnetic core assembly, followed by the magnetic core and coils assembly, and finally a connector is permanently attached to the open side of the shaft. All the parts of the unipolar (dual input) latching relay configuration with the PM in the armature are shown in Figure 4.14. The housing in this design consists of two ferromagnetic core parts, the lower and the upper core, with relatively thin walls allowing for manufacturing using stamping technology. An armature shaft and a magnet are located inside a magnetic housing, which secures the armature by providing a sliding opening for the shaft and one mechanical stop for the armature. With this technology, an additional cylindrical part is needed to provide shaft guidance. The housing parts are pressed together in the assembly process, encapsulating a bobbin with two coils and three leads. When the lower core is pressed into the upper core, the space for the movement is provided by the introduced lower mechanical stop. The opening in the housing creates a passage for the coil leads. A magnetic shim sandwiched between

**FIGURE 4.15**

Unipolar latching relay with magnet in armature components and assembly. (Courtesy of Delphi Corp.)

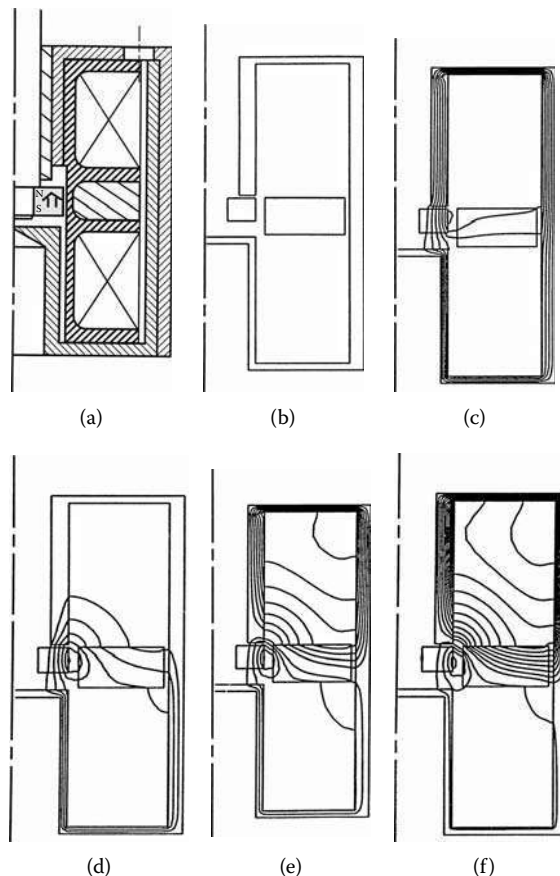
the two coils serves as an additional magnetic circuit, making this device electromagnetically efficient. The detail, presented in Figure 4.14, shows a means of providing a specially shaped armature shaft with shaft stops and contact with the stop, making the armature stop with no magnet or magnetic core contact, thus preventing the magnet from breaking. The shaft is devised such that its bottom position is longer than the magnet's thickness. The distance of the magnet to the magnetic core controls the latching force and is arranged to prevent accidental armature motion for vibration greater than the required 20g acceleration, as presented in Table 4.10. Therefore, the distance of the PM from the lower magnetic core could be different from the distance of the magnet from the upper magnetic core, which is set to provide a sufficient force on the contacts and to protect against vibration. During the lifetime of the relay, the force on the contacts increases over time; because the contact surface is losing material due to wear, the distance from the magnet to the magnetic core is decreasing, providing stronger magnetic force at the contact area. This ability of latching relays to increase contact force helps maintain low-contact resistance, the critical contact parameter. Lower contact resistance, a function of the contact force, should have a positive effect upon contact life, unlike conventional relays where the contact resistance deteriorates (increases) over time. The armature shaft should be made out of a nonmagnetic material, such as stainless steel or plastic, providing additional mechanical coupling with the ring magnet. Any desired magnet material could be utilized in this configuration, depending on the latching force requirements, preferably one based on high-energy neodymium or samarium cobalt. If the selected material is a neodymium-bonded magnet, both the shaft and the ring might be manufactured using the plastic-molded process.

#### 4.1.4 Latching Relay Analysis

Figure 4.15 shows the unipolar relay components and assembly. The unipolar relay configuration with a magnet in an armature, having axial magnetization, is depicted in Figure 4.16(a). The magnetic flux lines in the magnetic circuit are presented in Figure 4.16(c) through Figure 4.16(f) at different dynamic operation stages. Initially, the armature is in its upper stable equilibrium position at the latch A position, as presented in Figure 4.4. When the current is applied to coil B, it is suppressing the magnetic field, as shown in Figure 4.16(c) through Figure 4.16(f). The number of magnetic flux lines increases with the increase of the MMF from 0 to 450.0 At. Figure 4.16(c) through Figure 4.16(f) show the magnet flux lines with a discrete increase of the MMF at 0.0, 150.0, 300.0, and 450.0 At, respectively.

At this point, the net magnetic force changes its direction and the repulsive force is applied, moving the armature to the bottom mechanical stop. Then current is discontinued and the magnet establishes its bottom equilibrium position at the latch B position, as presented in Figure 4.4. With the current applied to coil A, the entire process is reversed and the magnet is moved back to its original latch A position, as presented in Figure 4.4.

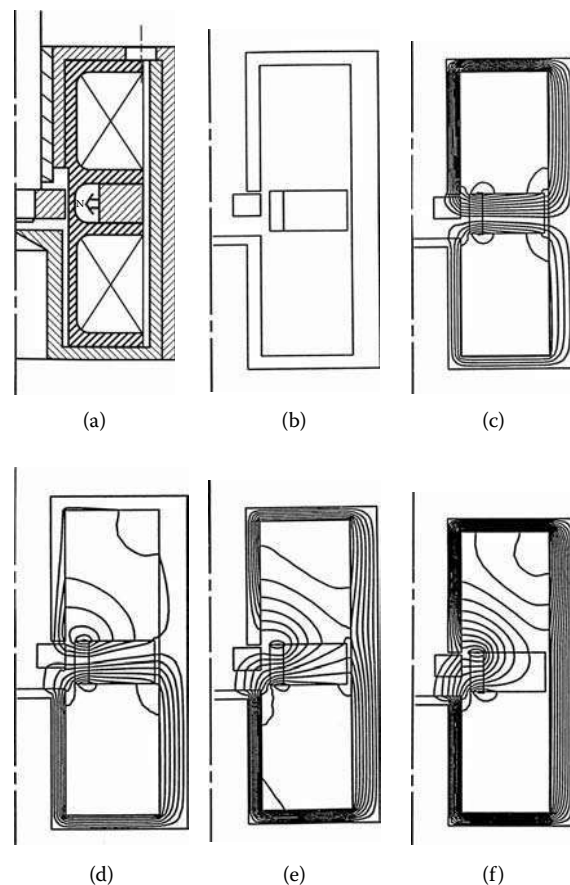
To secure magnet integrity and, therefore, the longer lifespan of the solenoid, a stationary PM location was selected, as presented in Figure 4.17(a). Consequently, Figure 4.17(c)

**FIGURE 4.16**

Flux lines for unipolar latching relay with magnet in armature: (a) relay design, (b) relay configuration, (c) magnet flux lines, (d) MMF = 150.0 At, (e) MMF = 300.0 At, (f) MMF = 450.0 At. (Courtesy of Delphi Corp.)

through Figure 4.17(f) present flux lines of the unipolar relay configuration with the stationary ring magnet position with radial magnetization, in this case, made of the neodymium MQ3. Note that different flux lines distributed between these two designs reveal much better flux utilization in the stationary magnet position configuration. As we can see here, none of the magnetic lines passes the entire housing, but in the movable magnet configuration with axial magnetization, some of the magnetic flux lines that go around the circuit contribute a net zero balance force and only saturate the circuit.

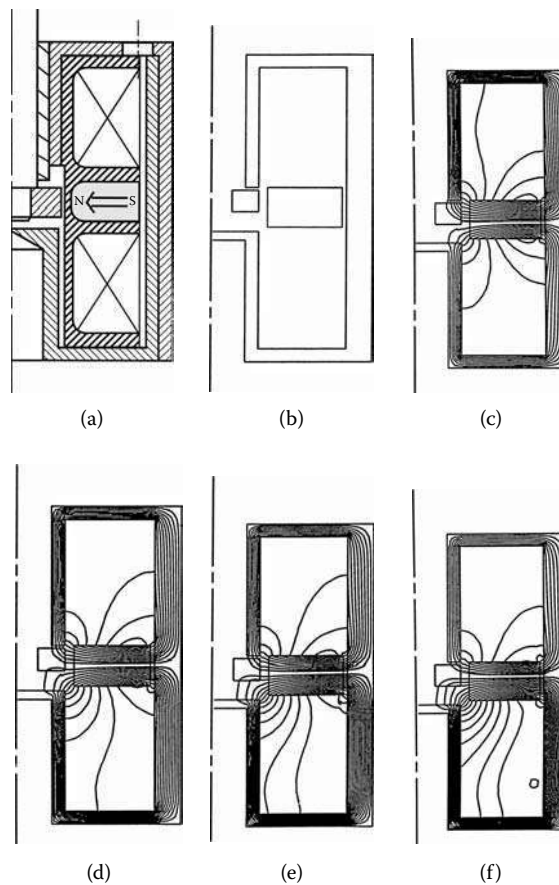
Figure 4.18 shows the unipolar relay components and assembly with a stationary MQ2 magnet. As a result of the lower MQ2 magnet's performance, it occupies the entire space between the coils compared to the configuration presented in Figure 4.17(a). The unipolar relay configuration with a magnet in the armature having radial magnetization is demonstrated in Figure 4.19(a), and the magnetic flux lines in the magnetic circuit at different dynamic operation stages are presented in Figure 4.19(c) through Figure 4.19(f). Flux distribution is similar to the unipolar relay configuration in Figure 4.17.

**FIGURE 4.17**

Flux lines for unipolar latching relay with stationary MQ3 magnet: (a) relay design, (b) relay configuration, (c) magnet flux lines, (d) MMF = 150.0 At, (e) MMF = 300.0 At, (f) MMF = 450.0 At. (Courtesy of Delphi Corp.)

**FIGURE 4.18**

Unipolar latching relay with stationary MQ2 magnet components and assembly with contacts. (Courtesy of Delphi Corp.)

**FIGURE 4.19**

Flux lines for unipolar latching relay with stationary MQ2 magnet: (a) relay design, (b) relay configuration, (c) magnet flux lines, (d) MMF = 150.0 At, (e) MMF = 300.0 At, (f) MMF = 450.0 At. (Courtesy of Delphi Corp.)

#### 4.1.5 Latching Relay Analysis and Tests

An evaluation of latching relays can be based on electromagnetic efficiency, which is defined by the level of MMF necessary for a dynamic operation. Therefore, all analytical studies that lead to MMF reduction are very valuable and result in more electromagnetically efficient structures. Figure 4.20 shows an example of such a study where the MMF is a function of the iron thickness of the magnetic shim sandwiched between the two coils of the unipolar solenoid structure, as presented in Figure 4.14. Without iron, the MMF required is quite high at 500.0 At and, with the presence of iron, the MMF level drops significantly, to below 250.0 At for the  $1.5 \times 10^{-3}$  m thickness of the magnetic shim. Furthermore, shim thickness beyond  $1.5 \times 10^{-3}$  m does not contribute to further MMF reduction. At the same time, the force level stabilizes above 2.0 N and is also independent of the shim thickness beyond this point, as presented in Figure 4.21.

Figure 4.22 shows test results and an analysis comparison of the MMF for several investigated relay configurations. Generally, unipolar relay devices require much less MMF compared with bipolar ones: in some cases, as much as half. Because the value of a current is a function of energy consumption and the number of turns is a function of required space, from both the point of view of packaging and energy consumption, it is

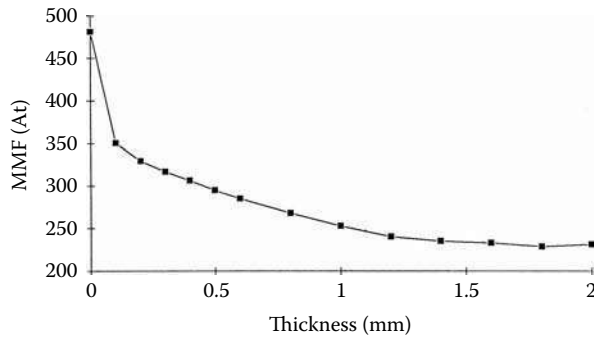


**FIGURE 4.20**  
MMF vs. magnetic shim thickness. (Courtesy of Delphi Corp.)

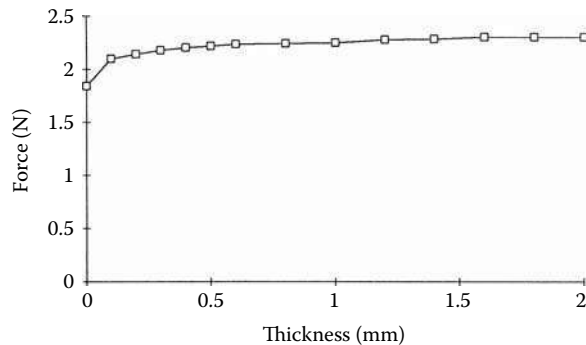


**FIGURE 4.21**  
Force vs. magnetic shim thickness. (Courtesy of Delphi Corp.)

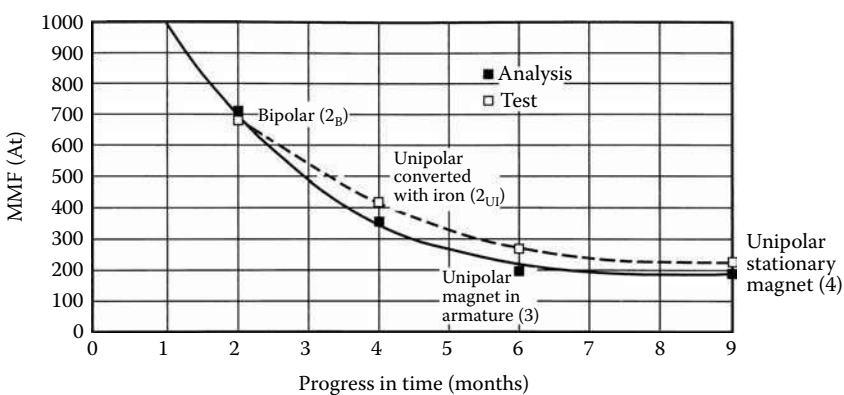


**FIGURE 4.22**  
MMF characteristics: analysis and test comparison. (Courtesy of Delphi Corp.)

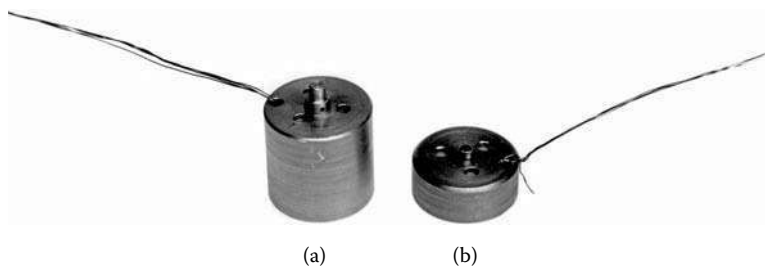
more advantageous to utilize unipolar relay structures. Because energy and packaging are two important issues for latching relays, it is advisable to focus on unipolar relays. This is also a less costly approach for the controller.

**TABLE 4.1**

Latching Relay Dynamic and Static Performance and Requirements

Performance	Test Results						Commercial Reference
	Conventional Stationary	Bipolar Armature	Unipolar Armature	Unipolar Stationary	Unipolar Stationary	Stationary	
Latching relay Magnet location	1	2	3	4	5	4.13(c)	Req.
Progress step no.	4.1(b)	4.7	4.16	4.17	4.19	4.13(c)	none
Figure reference	4.1(b)	4.7	4.16	4.17	4.19	4.13(c)	none
Minimum voltage (V)	17.5	18.0	6.5	9.5	8.0	6.5	<7.0
Pulse width (ms)	2.9	2.0	6.4	3.0	3.2	25.0	none
Latching force (G)	206	193	193	127	120	152	10 g
Armature air gap ( $\times 10^{-3}$ m)	0.36	0.43	0.60	0.94	0.90	1.00	0.50
Maximum current at 7 V(A)	0.33	2.27	0.59	0.54	0.51	0.09	<1.0
Maximum energy fact (A $\times$ ms)	0.96	4.50	3.80	1.60	1.60	2.25	none
MMF at 7 V(At)	266	680	236	216	204	180	none

Source: Courtesy of Delphi Corp.

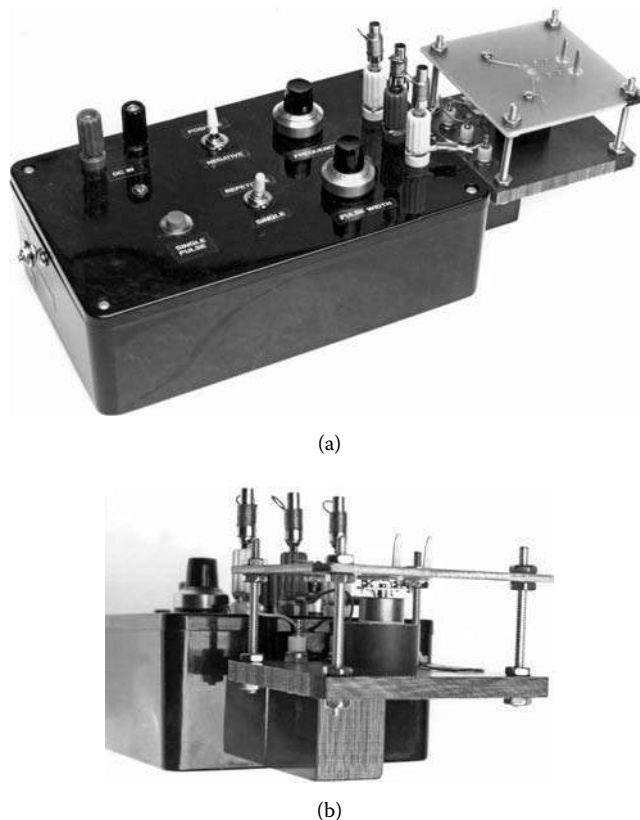
**FIGURE 4.23**

Latching relays assemblies: (a) unipolar, (b) bipolar. (Courtesy of Delphi Corp.)

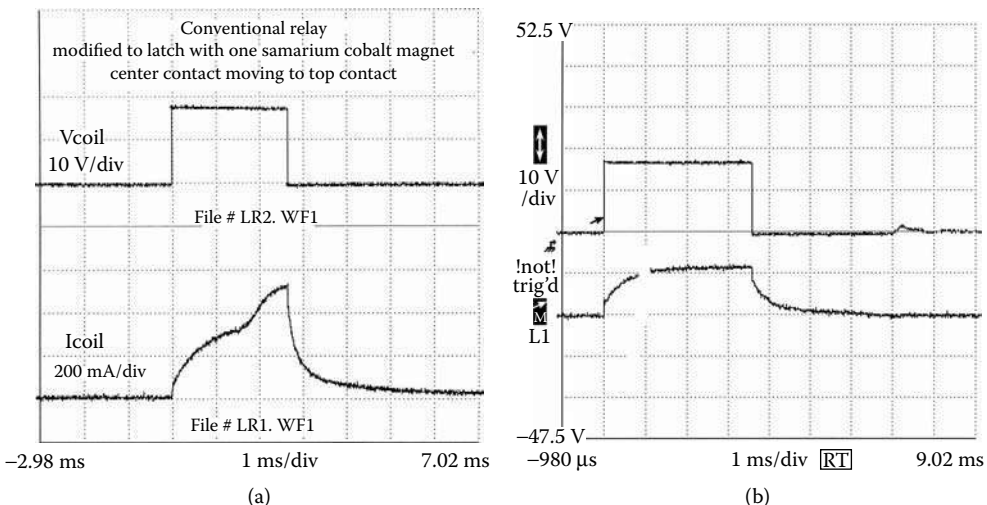
Figure 4.22 reveals the steps involved in minimizing MMF for all investigated bipolar and unipolar latching relay configurations. The beginning of the process, step (1) (Table 4.1 and Figure 4.22), indicates a conventional relay converted to a latching relay [also see Figure 4.1(b) for reference purposes only]. The next step (2<sub>B</sub>) indicates an MMF level of 680.0 At reduced to about 400.0 At, as the unipolar relay is converted from a bipolar relay with iron at step (2<sub>UI</sub>). Consequently, the MMF was reduced to about 200.0 At in step (3) and step (4) (see Figure 4.22), in the search for the most efficient electromagnetic relay.

Figure 4.23 shows two of the investigated relay assemblies, the bipolar and the unipolar models, while Figure 4.24 shows the test fixture with a unipolar model of the configurations incorporated into the test fixture. For static performance, the electromagnetic latching force was determined at the fixed air gap, which varies due to different relay designs. Dynamic tests include both the transient voltage and current, which can determine the travel time as presented in the test fixture, shown in Figure 4.24.

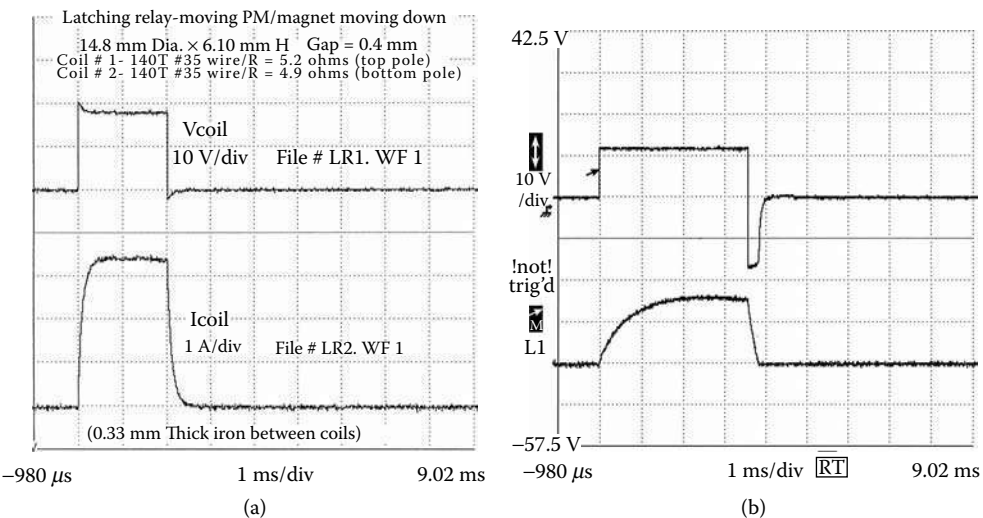
Figure 4.25 through Figure 4.27 present the transient voltage pulse and the transient current for all latching relays discussed above. These data help calculate the maximum energy factor and MMFs for comparison purposes. The relay's open and close travel time corresponds to the minimum input voltage pulse required to activate the relay. The minimum voltage requirement indicates the lowest input voltage signal at which the relay must operate. Figure 4.25 through Figure 4.27 show the transient current for the PWM with 20.0 ms pulse-width and nominal 12.0 V operation. All the requirements, data as well as results from static and dynamic tests of all bipolar and unipolar latching relay configurations, are shown in Table 4.1.

**FIGURE 4.24**

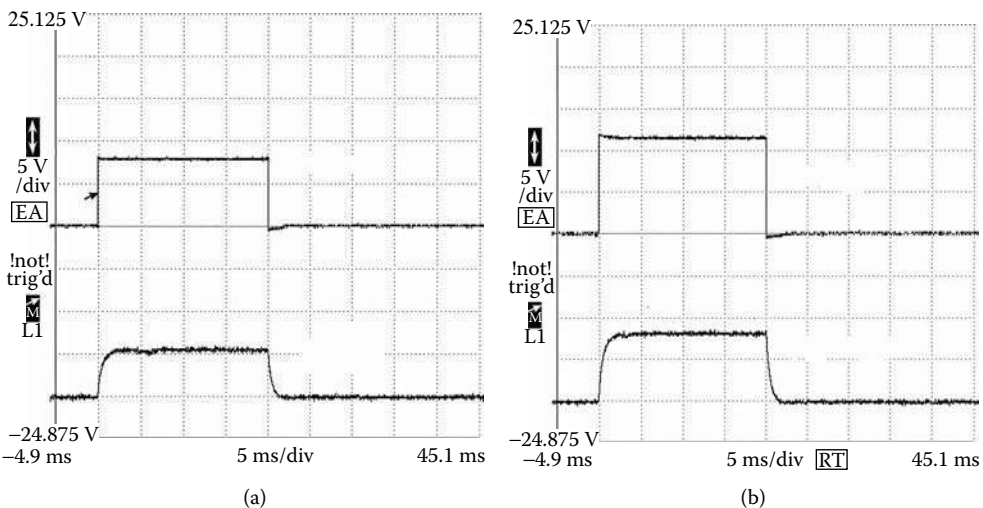
Voltage pulse test fixture with transient current for latching relays: (a) controller and latching relay fixture, (b) latching relay fixture. (Courtesy of Delphi Corp.)

**FIGURE 4.25**

Voltage pulse and transient current for conventional relay with magnet: (a) conventional relay with PM, (b) commercial latching relay. (Courtesy of Delphi Corp.)

**FIGURE 4.26**

Voltage pulse and transient current for modern relay with PM: (a) bipolar relay with magnet in armature, (b) unipolar with MQ3 magnet in armature. (Courtesy of Delphi Corp.)

**FIGURE 4.27**

Voltage pulse and transient current for modern relay with PM: (a) unipolar with MQ2 stationary magnet, (b) unipolar with MQ3 stationary magnet. (Courtesy of Delphi Corp.)

Table 4.2 and Table 4.3 show a comparison of the latching relay's static and dynamic test and analysis results, respectively. The calculated and tested latching forces, MMFs and current levels, are within several percent, indicating a good correlation between the test and analytical results. The dynamics identify that for both the closing and opening, the minimum pulse width of the relay is also in correlation with the FE analysis. A reliability test was performed for a unipolar relay with a magnet in the armature. A total of  $1.5 \times 10^6$  cycles at no-load condition successfully passed. Depending on the current rating, these relays also require a full current load reliability test under 10.0–25.0 A nominal current load conditions.

**TABLE 4.2**

Latching Static Relay Test

Performance	Test Results					
	Unipolar-No-Iron Armature (2B) MQ3	Bipolar Armature (2B) MQ3	Unipolar-Iron Armature (2UI) MQ3	Unipolar Armature (3U) MQ3	Unipolar Stationary (4U) MQ3	Unipolar Stationary (5U) MQ2
Force (G)	193	193	193	193	127	120
Air gap ( $\times 10^{-3}$ m)	0.40	0.40	0.40	0.60	0.94	0.90
Current at 7 V(A)				0.59	0.54	0.51
MMF at 7 V(At)				236	216	204
Current at 12 V(A)	2.27	4.53	2.89	0.79	0.89	0.87
MMF at 12 V(At)	680	680	434	409	399	340

Source: Courtesy of Delphi Corp.

**TABLE 4.3**

Latching Relay Analysis

Performance	Analytical Results					
	Unipolar-No-Iron Armature (2B) MQ3	Bipolar Armature (2B) MQ3	Unipolar-Iron Armature (2UI) MQ3	Unipolar Armature (3U) MQ3	Unipolar Stationary (4U) MQ3	Unipolar Stationary (5U) MQ2
Force (G)	205	205	222	231	189	179
Air gap ( $\times 10^{-3}$ m)	0.43	0.40	0.43	0.60	1.0	1.0
Current at 7 V(A)				0.60	0.47	0.48
MMF at 7 V(At)				240	189	192
Current at 12 V(A)	2.33	4.53	2.40	1.02	0.72	0.71
MMF at 12 V(At)	700	680	360	411	324	284

Source: Courtesy of Delphi Corp.

## 4.2 Latching Solenoids

Latching solenoids feature lower energy consumption and mass than conventional solenoids and, therefore, are used more often in applications for portable devices, such as camcorders and laptop computers, where reduction of energy consumption and low mass are particularly important. For similar reasons, latching solenoids are also very attractive for automotive component applications in spite of their more complex controller and higher cost when compared with conventional solenoids. Other potential applications include latching relays (as described in Section 4.1) and flow control solenoids for an electronically operated transmission and injectors. There are a variety of latching solenoids that can be grouped based on configuration, component location, and applications. Two families of latching solenoids can be identified based on topology and, in particular, on magnet and coil arrangements: one with a moving magnet and the other with a stationary magnet. Latching solenoids with a moving magnet are divided into two subgroups: the first group has a single magnet in the armature and the second has two or more magnets in the armature. Latching solenoids with a stationary magnet can be divided into four different subgroups: (1) a magnet located outside the main magnetic path, (2) a magnet